

AD-A060 722 MASSACHUSETTS INST OF TECH CAMBRIDGE DEPT OF OCEAN E--ETC F/G 13/10
NUMERICAL AND EXPERIMENTAL METHODS FOR THE PREDICTION OF FIELD --ETC(U)
JUN 78 K MIN N00014-76-C-0357
UNCLASSIFIED OE-78-12 NL

UNCLASSIFIED

OE-78-12

N00014-76-C-0357

NL

| OF 3
AD
A060722



AD A060722

LEVEL II

Numerical and Experimental
Methods for the Prediction of
Field Point Velocities
Around Propeller Blades

by

Keh-Sik Moon

DDC
RECEIVED
NOV 9 1978

DDC
RECEIVED
NOV 9 1978
F

This document has been approved
for public release and sale; its
distribution is unlimited.

DDC FILE COPY

Report No. 78-12
June 1978

Massachusetts Institute of Technology
Department of Ocean Engineering
Cambridge Ma 02139

MASSACHUSETTS INSTITUTE OF TECHNOLOGY
DEPARTMENT OF OCEAN ENGINEERING
CAMBRIDGE, MASS. 02139

(2)

⑨ Technical Report

Report No. 78-12

✓ ⑭ OE-78-12

⑥ NUMERICAL AND EXPERIMENTAL METHODS
FOR THE PREDICTION OF FIELD POINT
VELOCITIES AROUND PROPELLER BLADES

by

⑩ Keh-Sin Min

⑪ Jun 1978

✓ ⑫ 211p.

⑯ N00014-76-C-0357

⑯ SR 009 01 01

⑰ SR 009 01 01

Reproduction in whole or in part is permitted
for any purpose of the United States Government.

Approved for public release; distribution unlimited

This research was carried out under the
Naval Sea Systems Command
General Hydromechanics Research Program
Subproject SR 009 01 01, Administered by the
Naval Ship Research and Development Center
Office of Naval Research Contract N00014-76-C-0357
MIT OSP 83456

406 856

50B

78 11 08 038

SECURITY CLASSIFICATION OF THIS PAGE (When Data Entered)

REPORT DOCUMENTATION PAGE		READ INSTRUCTIONS BEFORE COMPLETING FORM
1. REPORT NUMBER 78-12	2. GOVT ACCESSION NO.	3. RECIPIENT'S CATALOG NUMBER
4. TITLE (and Subtitle) NUMERICAL AND EXPERIMENTAL METHODS FOR THE PREDICTION OF FIELD POINT VELOCITIES AROUND PROPELLER BLADES		5. TYPE OF REPORT & PERIOD COVERED Technical Report
		6. PERFORMING ORG. REPORT NUMBER
7. AUTHOR(s) Keh-Sik Min		8. CONTRACT OR GRANT NUMBER(s) N00014-76-C-0357
9. PERFORMING ORGANIZATION NAME AND ADDRESS Department of Ocean Engineering M.I.T., Cambridge, Ma. 02139		10. PROGRAM ELEMENT, PROJECT, TASK AREA & WORK UNIT NUMBERS SR 009-01-01
11. CONTROLLING OFFICE NAME AND ADDRESS Office of Naval Research		12. REPORT DATE June 19, 1978
14. MONITORING AGENCY NAME & ADDRESS (if different from Controlling Office) David Taylor Naval Ship Research and Development Center Bethesda, MD. 20084		13. NUMBER OF PAGES 203
16. DISTRIBUTION STATEMENT (of this Report) This document has been approved for public release and sale; its distribution is unlimited.		15. SECURITY CLASS. (of this report) Unclassified
17. DISTRIBUTION STATEMENT (of the abstract entered in Block 20, if different from Report)		15a. DECLASSIFICATION/DOWNGRADING SCHEDULE
18. SUPPLEMENTARY NOTES		
19. KEY WORDS (Continue on reverse side if necessary and identify by block number) Propeller Theory Vortex Wakes Laser-Doppler Anemometry		
20. ABSTRACT (Continue on reverse side if necessary and identify by block number) Flow characteristics of a series of NSRDC research propellers (propellers 4381, 4382, 4383, 4498) are experimentally investigated applying Laser-Doppler Anemometer technique. This experimental method is significantly different from conventional ones in providing precise quantitative flow information which would be extremely difficult or impossible to obtain with mechanical measuring probes. <i>per</i>		

SECURITY CLASSIFICATION OF THIS PAGE(When Data Entered)

→ The flow characteristics are directly obtained or derived from the measurement of field point velocities.

Also, theoretical study has been made for the prediction of field point velocities utilizing numerical lifting-surface theory and the results are compared to those measured.

It has been found that the agreement is good or at least theory nicely follows the experimental pattern, which indicates the possibility of a simple correlation between measurement and the present theory. ↗

SECURITY CLASSIFICATION OF THIS PAGE(When Data Entered)

NUMERICAL AND EXPERIMENTAL METHODS FOR THE PREDICTION OF FIELD POINT VELOCITIES AROUND PROPELLER BLADES

by

Keh-Sik Min

This report is essentially identical to the thesis submitted by the author on May 5, 1978 in partial fulfillment of the requirements for the degree of Doctor of Philosophy at the Massachusetts Institute of Technology.

Thesis Supervisor: Justin E. Kerwin
Professor of Naval Architecture

ABSTRACT

Flow characteristics of a series of NSRDC research propellers (propellers 4381, 4382, 4383 and 4498) are experimentally investigated applying Laser-Doppler Anemometer technique. This experimental method is significantly different from conventional ones in providing precise quantitative flow information which would be extremely difficult or impossible to obtain with mechanical measuring probes.

The flow characteristics are directly obtained or derived from the measurement of field point velocities.

Also, theoretical study has been made for the prediction of field point velocities utilizing numerical lifting-surface theory and the results are compared to those measured.

It has been found that the agreement is good or at least theory nicely follows the experimental pattern, which indicates the possibility of a simple correlation between measurement and the present theory.

ACKNOWLEDGEMENTS

The author wishes to express herein his foremost gratitude to his thesis supervisor, Professor Justin E. Kerwin of the Department of Ocean Engineering, for the continuous advice, assistance and guidance during the period of the author's graduate study at Massachusetts Institute of Technology.

He also would like to express his appreciation to his thesis committee members, Professors Sheila Widnall and Shaoul Ezekiel of the Department of Aeronautics and Astronautics, and Professor R. J. Van Houten of the Department of Ocean Engineering, for their valuable advice and suggestions.

Special thanks are extended to S. D. Lewis, Research Engineer in charge of the M.I.T. Marine Hydrodynamics Laboratory(variable pressure water tunnel), for his time, effort and invaluable assistance in designing and assembling the apparatus and performing the experiment.

In addition, my gratitude goes to my parents whose confidence in me gave me the strength to finish this work and to my wife, Youngsoo, not only for her typing of the manuscript, but also for her patience, understanding and encouragement throughout the author's graduate study.

Finally, the author wishes to thank all the people who have helped in many ways, directly and indirectly, to bring this work to completion.

TABLE OF CONTENTS

	Page
Report Documentation Page	1
Abstract	2
Acknowledgements	3
Table of Contents	4
List of Tables	6
List of Figures	7
List of Symbols	10
I. Introduction	14
II. Experimental Method	17
II.1. General	17
II.2. Laser-Doppler Anemometry Technique	17
II.3. Considerations for Selection of a System	20
A. Selection of Optical Arrangements and Lenses	22
(1) Fundamental Theory of Dual Beam Mode	25
(2) Direction of Measurement	27
(3) Volume of Measurement	28
(4) Number of Fringes in Measuring Volume	31
(5) Aperture	32
(6) Selection of Lenses	33
B. Particulates	34
C. Size and Type of Laser	35
D. Signal Processors	37
E. Data Analysis	45
F. Other Systems - Frequency Shifting	48
II.4. Errors in LDA	51
II.5. MIT Variable Pressure Water Tunnel and LDA System	61
II.6. Calibration	63

TABLE OF CONTENTS
(continued)

	Page
III. Propeller Model	64
IV. Results of Experiment	65
IV.1. General	65
IV.2. Slipstream Radius	66
IV.3. Hydrodynamic Pitch and Pitch Angle	68
IV.4. Tunnel Free Stream Velocity with Propeller Shaft Housing and Mean Axial Velocity behi.	69
IV.5. Mean Tangential Velocity	70
IV.6. Roll-up Point	71
IV.7. Circulation	72
IV.8. Field Point Velocity	74
IV.9. Blade Boundary Layer	75
V. Numerical Method (Numerical Lifting Surface Theory)	77
VI. Comparison of Field Point Velocities between Theory and Experiment	81
VII. Conclusion and Recommendations	84
References	92

LIST OF TABLES

	Page
1. Comparison of Two Most Common Signal Processing Techniques-Tracker and Counter	95
2. MIT Water Tunnel Laser-Doppler Anemometer System	96
3. Optical Characteristics	97
4. Tunnel Free Stream Measurement by Two Different Methods(ft/sec)	98
5. Calibration Rotor, its Arrangement, Rotating Speed Measurement and Comparison	99
6. NSRDC Research Propellers Principal Design Characteristics	100
7. NSRDC Research Propellers Some Performance Characteristics at Design Condition	102
8. Slipstream Radius	103
9. Percent Contraction of Slipstream at Different Axial Position	104
10. Hydrodynamic Pitch Angle of Tip Vortices	105
11. Hydrodynamic Pitch of Tip Vortices	106
12. Comparison of Circulation Distribution by Different Methods	107
13. NSRDC Prop. 4381(No skew) Estimated Blade Sectional Drag Coefficient	108
14. Comparison of Nondimensional Mean Axial Velocity (Correlation between Theory and Experiment)	109

LIST OF FIGURES

	Page
1. Basic Concept of Laser-Doppler Anemometry	110
2. General Relation between Scattered Light Waves and Doppler Shift	111
3. Reference Beam Mode, Basic Detection Method	112
4. Dual Beam Mode, Basic Detection Method	113
5. Dual Scatter Mode, Basic Detection Method	114
6. Characteristics of Dual Beam Forward Scattering Mode	115
7. Fringe Pattern of Dual Beam Mode	116
8. Generation of Fringe Pattern (light wave interaction)	117
9. Oscilloscope Trace of Particle Traversing Measuring Volume(Typical Photodetector Output)	118
10. Independency of Fringe Spacing on the Refractive Index	119
11. Focused Laser Beam	120
12. Basic Idea of Signal Processing Method of Spectrum Analyzer and Spectrum Broadening	121
13. Dynamic Range and Capture Bandwidth of Tracker Type Signal Processors	122
14. Effect of Noise on Counter	123
15. Frequency Shifting by Acousto-Optics(Bragg) Cell	124
16. Relation between Space-Fixed Coordinate and Moving Coordinate Systems	125
17. MIT Water Tunnel LDA System and Analysis Procedure	126

	Page
18. General Set Up of Propeller and LDA System	127
19. Thickness Distribution of Tunnel Window for Laser Experiment	128
20. Expression of Beam Crossing Point and Comparisons	129
21. Coordinate System adopted at 1973 ITTC for Propeller Motions and Propeller Forces	130
22-25. Slipstream Radius	131-132
26. Relationship between Skew and Ultimate Slipstream Radius	133
27. Relationship between Loading Conditions and Ultimate Slip stream Radius	134
28. Trace of Tip Vortex from a Selected Blade	135
29-32. Hydrodynamic Pitch Angle of Tip Vortices	136-137
33-36. Hydrodynamic Pitch of Tip Vortices	138-139
37-38. MIT Water Tunnel Nondimensional Free Stream Velocity with Prop. Shaft Housing	140
39-40. Mean Axial Velocity Distribution behind Propeller	141
41-44. Mean Vertical Velocity Distribution along the y-axis	142-143
45. Comparison of Mean Tangential Velocity	144
46-49. Initial Slope of Tangential Velocity at Hub Vortex Core Center and Peak Axial Velocity at 95% of Slipstream Radius	145-146
50-53. Fluctuation Pattern of Axial Velocity just inside the Slipstream	147-148
54-57. Mean Tangential Velocity, Vorticity and Circulation Distribution inside the Slipstream	149-150

	Page
58-73. Field Point Velocity - Axial Comp. (General Fluctuation Pattern)	151-158
74-81. Field Point Velocity very close to Tip Vortices - Axial Comp.	159-162
82-84. Velocity Defect due to Blade Boundary Layer	163-165
85. Modeling and Economization of Source and Vortex Systems of Propeller Blade in PUF-2	166
86. Schematic Presentation of Modeling of Vortex Wake System in PUF-2	167
87-142. Comparison of Field Point Velocity (Design Condition)	168-195
143. NSRDC Prop. 4381 (No skew) Oscilloscope Trace of Field Point Velocities - Axial Comp.	196
144-157. Comparison of Field Point Velocity (Off Design Condition)	197-203

LIST OF SYMBOLS

b	Radius of laser beam at the focal point including the intensity greater than e^{-1} of the centerline intensity(e^{-1} waist radius of the laser beam)
C	Propeller blade section chord length
c	Speed of electro-magnetic wave
C_D	Sectional drag coefficient, $C_D = \text{sectional drag} / \frac{1}{2} \rho C_U r^2$
D	Propeller diameter
D_1	Diameter of the initial laser beam(the beam leaving the laser) when all points of intensity greater than e^{-1} (about 36.8%) of the centerline intensity are included
D_2	Same as D_1 but e^{-2} (about 13.5%) intensity are included
d	Distance between splitted beams(bean spacing)
d_a	Aperture diameter
d_f	Distance between fringes(fringe spacing)
d_l	Diameter of laser beam at the measuring volume
d_m	Diameter of measuring volume
\vec{E}	Electric vector of light
F	Focal length(general)
F_r	Focal length of the receiving(collecting) lens
F_t	Focal length of the transmitting(focusing) lens
f	Frequency(general)
f_a	Frequency of travelling acoustic wave

f_D	Frequency detected at photodetector
f_0	Propeller blade section camber
G	Nondimensional circulation strength, $G = \Gamma / 2\pi R U_R$
h_m	height of measuring volume
I	Intensity of laser beam
I_0	Centerline intensity of laser beam
J	Advance coefficient, $J = V_a / n_D$
K_Q	Torque coefficient, $K_Q = Q / \rho n^2 D^5$
K_T	Thrust coefficient, $K_T = T / \rho n^2 D^4$
\vec{k}	wave number vector, $\vec{k} = k \vec{s} = \frac{2\pi}{\lambda} \vec{s}$
l_m	length of measuring volume
M	Magnification factor, Mass
\vec{N}	Normal vector
N_{FR}	Number of fringes
\vec{n}	unit normal vector
n	Propeller revolutions per unit time
P	Propeller blade section pitch
P_w	Hydrodynamic pitch of tip vortices
\vec{p}	Unit polarization vector (specified the direction of \vec{E})
Q	Propeller torque
R	Propeller radius
R_w	Slipstream Radius

\vec{r}	Unit directional vector of scattered light
\vec{s}	Unit directional vector of incident light
T	Absolute temperature, propeller thrust
t_0	Maximum thickness of propeller blade section
U_R	0.7R reference velocity, $U_R = \sqrt{V_a^2 + (0.7wR)^2}$
U_r	Sectional incoming flow velocity $w_r = \sqrt{V_a^2 + (wr)^2}$
V	General expression of velocity
\vec{v}	Velocity vector
V_a	Speed of advance

Greek Letters

β_i	Hydrodynamic pitch angle of propeller blade section
β_w	Hydrodynamic pitch angle of tip vortices
Γ	Circulation strength
ϵ	Half of beam crossing angle $\epsilon = \phi/2$
$\vec{\zeta}$	Vorticity vector
ξ_x	
ξ_r	x, r, θ - component of $\vec{\zeta}$
ξ_t	
η_p	Propeller open-water efficiency $\eta_p = (J/2\pi) \cdot (K_T/K_Q)$

θ_s	Projected skew angle at radius r
θ_w	Angular position of selected tip vortex
λ	Wave length of laser beam
λ_a	Wave length of travelling acoustic wave
n	Refractive index
ρ	Density of water
ϕ	Beam crossing angle, $\phi = 2\epsilon$
ω	Angular velocity

Coordinate Systems and Velocity Components
 (refer to Figure 21)

oxyz	Rotating Cartesian coordinate system
$\bar{x}\bar{y}\bar{z}$	Space-fixed Cartesian coordinate system
xrQ	Polar coordinate system
u, v, w	Velocity components in x, y, z - direction
$\bar{u}, \bar{v}, \bar{w}$	Velocity components in $\bar{x}, \bar{y}, \bar{z}$ - direction
u_x, u_r, u_t	Velocity components in x, r, Q - direction

* Note : These coordinate systems are loosely defined.
 In fact, notation for rotating coordinate system
 (oxyz) is generally used for space-fixed coordinate
 system simply for convenience.

Subscript

G	refers to geometric
E	refers to effective

I. Introduction

A variety of methods is possible to attack hydrodynamic problems. Particularly, two different methods are most widely used to obtain useful information for the flow characteristics around a hydrofoil or propeller blades. One is the series expansion methods of a small parameter. This type of method is known as a singular perturbation problem or "the method of matched asymptotic expansions." The second method is the purely numerical one. Undoubtedly, this method has been becoming of increasing importance with the development of modern computing devices. Therefore, methods employing numerical lifting surface theory are now generally considered as essential for the satisfactory design and performance prediction of marine propellers. Since 1960, a systematic research on these subjects has been carried out at MIT under the direction of Professor Kerwin and, as a result, a series of computer programs has been developed such as MIT PBD*, PINV* and PUF*-series. The newest program, PUF-2, which can be applied to both steady and unsteady cases to determine the hydrodynamic

* Designation of MIT "propeller blade section design", "propeller inverse" and "propeller unsteady force" programs, respectively.

loading on a propeller of prescribed geometry, is believed to be one of the best presently available numerical schemes and to offer the greatest potential for the determination of detailed hydrodynamic loading around blades. In order to verify the overall accuracy and achieve the possible further refinement of the numerical scheme, however, it is necessary to conduct a series of appropriate experiments.

Until very recently, the experimental confirmation of numerical lifting surface theory has been limited to a comparison of overall propeller blade thrust and torque loading. For many years, experimental fluid mechanics has made use of standard mechanical measuring probes to obtain information on fluid velocity. Total-pressure probes, in conjunction with static-pressure probes, have provided the principal means of measuring mean velocity and hot-wire or hot-film anemometers the principal means of measuring instantaneous velocity and, hence, mean velocity, rms velocities and velocity correlations. Mechanical probes will undoubtedly continue to be important to experimental fluid mechanics, but it is obvious that an experiment for the detailed load distribution around a propeller blade with such conventional measuring devices is extremely difficult and costly, if not impossible. The limitations on the conventional mechanical probes make new measuring techniques worthy of careful con-

sideration. Thus, "Laser-Doppler Anemometry Technique" has been introduced as an experimental method expecting to be able to overcome all of the limitations that the mechanical probes have. At the stage of paper survey, the author had encountered several different terminologies used from paper to paper regarding this technique such as laser-Doppler anemometry, laser anemometry, optical anemometry, laser-Doppler velocimetry etc. However, the term "Laser-Doppler Anemometry", or simply "LDA" will be used exclusively in this paper. The strong interest in LDA is evidenced by over thousand papers that have been published on the subject since the first one by Yeh and Cummings in 1964 [1]*, who measured in a fully-developed laminar pipe flow of water. This proliferation of papers is due both to the potential of the technique as well as some of the challenging theoretical considerations associated with it. In this paper, a brief discussion on the basic concept of the LDA technique, necessary components and their functions will first be introduced along with some historical review. Then, the results of measurements and comparison with the numerical output will be discussed next.

* The numbers in [] denote references listed at the end of this paper.

II. Experimental Method

II.1. General

As mentioned in Chapter I, LDA technique has been exclusively used as an experimental method. In section II.2, the basic concept and some considerations for application will be discussed. At the time when the author first began to employ this technique in the flow measurement situations(late 1976), he was unable to find any reference systematically describing general theory and application of LDA technique. Therefore, the author has prepared this material for the purpose of providing some basic knowledge about this technique for the possible future user. In fact, this chapter is not only the summary of the survey of presently available papers in this field, but also the result from the author's own experience. Some understanding of the working theory would be helpful in properly applying the device to a particular flow problem.

II.2. Laser-Doppler Anemometry Technique

Laser anemometry is a technique which utilizes scattered light from particulates in a fluid to measure the velocity of that fluid. When light is scattered from a moving object, a

stationary observer will see a change in the frequency of the scattered light (Doppler shift) proportional to the velocity of the object. In the Laser-Doppler Anemometer, this Doppler shift is used to measure the velocity of particles in a fluid. From the particle velocity, the fluid velocity is inferred. This basic concept is shown schematically in Figure 1. Theoretically, any kind of light can be used as an illuminating light source. However, white light such as room light or day light has too large spectral width to be of any use in such measurements. In practice, a laser beam is almost exclusively used as a light source due to the following properties of the laser beam:

1. monochromatic
2. coherent
3. high intensity
4. linearly polarized
5. easy focusing

In terms of its potential, the advantage which make the laser anemometer very attractive for many fluid measuring applications are:

1. No probe in the fluid.

This is the most obvious advantage. Only the laser

light itself needs to enter the flow field, with a window the only access. This can be vitally important in flows where a probe would cause a disturbance or the fluid is hot, corrosive, or otherwise unsuitable for an immersion of a probe.

2. No flow calibration required.

In theory, the laser anemometer is linear. It will be shown later that the laser light frequency, fluid refractive index at measuring location, and optical geometry uniquely determine the relation(linear) between the particle velocity and the frequency output of the photodetector. This usually eliminates the need for actual velocity calibrations.*

3. Precise measurement of velocity components.

A single component LDA system measures a single component of the particle velocity and is independent of other velocity components. Adding frequency shifting permits measurements in flows when the velocity reverses. With a two component system, the individual components are measured completely independently.

* The overall accuracy is affected by many factors. One of them is the precision of the signal processor(frequency to voltage converter). This can be easily checked with standard electronic test instruments.

4 & 5. Small measuring volume and high frequency response.

These are essential requirements for applications where detailed flow measurements are required. A relatively small measuring volume and inherently fast response gives it the ability to follow rapidly changing velocities in the fluid.

The above advantages must be quantified-particularly the last two. These items will be discussed in section II.3.

A.(1). These characteristics add greatly to the laser anemometer's value as a measurement tool and have made it applicable both to very low velocity flows as well as supersonic flows.

II.3. Considerations for Selection of a System

A complete Laser Doppler Anemometer includes, at the minimum, the following components:

1. laser source
2. transmitting (focusing) optics
3. receiving (light collecting) optics
4. photodetector to convert light signal to eletrical signal
5. signal processor to convert frequency to a voltage

Other components are added to accomplish two component measurements, distinguish flow reversals, provide seeding, etc. Several parameters must be considered for proper selection and application of a laser anemometer to a flow situation. Among these are:

1. the optics arrangement or "mode"
2. whether seeding the flow with particles is required and, if it is, how to do it
3. the size and type of laser
4. the type of signal processor
5. the type of data analysis equipment required

Some of the variables that affect the selection are:

1. whether only one or more than one velocity component is to be measured at one time
2. whether the fluid is liquid or gas
3. the expected fluid velocity range
4. the amount and type of natural particulates in the fluid and the allowable concentration of particulates
5. the accessibility of the measuring point
6. the type of data required, i.e., mean flow, true rms, spectrum, correlations, etc.

Other items, not included above, may well be dominant in a

given measurement situation. The decision on the above items tend to be interrelated and some considerations on the each of items will be discussed in the following.

A. Selection of Optical Arrangements and Lenses

At present, the following three basic "modes" are used.

1. Reference beam
(local oscillator heterodyne arrangement)
2. Dual beam
(fringe system or differential heterodyne arrangement)
3. Dual scatter
(symmetric heterodyne arrangement)

The first two optical arrangements are commonly used, but the third one has not been used as extensively as the others. Most early measurements were made with the "reference beam" optical mode. In this mode, the laser beam is split into an intense scattering beam and a weak reference beam. The reference beam is directed on to a photocathode where it beats with light scattered from the strong beam by particles moving with the flow. The frequency of the scattered light has been altered by the Doppler effect and the interference with the reference beam provides a frequency difference

which is directly proportional to the particle velocity. This arrangement was employed in the pioneer work of Yeh and Cummings and has subsequently been used by many authors. Goldstein and Hagen in 1967 [2], Welch and Tomme in 1967 [3] and Pike, Jackson, Bourke and Page in 1968 [4] are considered as early persons who applied it to turbulent water flows. This system is often useful when the particle concentration is high to give an essentially continuous signal. This simplified the signal processing problem as well as giving an output similar to a hot-wire. However, noise due to multiple particles in the measuring volume as well as other practical limitations of high particle concentration led to development of techniques using low particle concentrations. The "dual beam" optical mode and greatly improved signal processors have now made LDA available for essentially routine measurements in a wide range of applications. Therefore, the dual beam mode is the most commonly used optical arrangement nowadays. One of the earliest application of this mode may be the example by Durst and Whitelaw in 1971 to measure mean and fluctuating velocity components in fully developed channel flow of water [5, 6]. Two different scattering methods can be used with dual beam system. Forward scatter requires the least laser power while backscatter requires only one window and is functionally more convenient. The obvious advantage of dual beam backscatter mode is the

rigidity of a system where the entire anemometer is bolted rigidly together. The disadvantage is the relatively weak scattered light signal when compared to direct forward scatter (signal strength is often only a percent or less of the forward scatter value.) The dual scatter mode has found its primary application in simultaneous measurement of two flow components with a single laser. Although the small acceptable aperture size (due to coherence requirements) limits the signal to noise ratio, the simplicity of the system for two component measurements is attractive in many applications. The most serious disadvantage of the dual scatter arrangement is the small amount of collected light and the resulting poor signal quality. Therefore, more powerful lasers are used to increase the intensity of the scattered light. The basic detection methods of the Doppler frequency for three different modes are described in Figures 3, 4 and 5, respectively. In order to help the understanding of the above Figures, the general relation between scattered light waves and Doppler shift is shown in Figure 2 [7, 8]. Among the three basic modes, the dual beam, forward scattering system is now most popular, since it is generally easiest to use, gives the best signal to noise ratio, and is quite versatile. This is the system that the MIT Marine Hydrodynamics Laboratory has recently acquired mainly for the

study of the flow around model propellers. Therefore, the working theory of dual beam, forward scattering system will be discussed in detail.

(1) Fundamental Theory of Dual Beam Mode

As shown in Figure 6, a basic characteristics of the dual beam mode is the crossing of two laser beams of equal intensity at a point in the fluid to be measured. To achieve this, the laser beam is first separated into two parallel beams of equal intensity that are equidistant from the original beam. These beams are then focused by a lens. Where the two beams cross, they interfere each other to form alternate regions of high and low intensity light, called "fringes", as shown in Figures 6-(c) and 7. These fringes are caused by the light in the two beams cancelling each other in some regions and complementing each other in others. This interference effect is described in Figure 8. As the particle passes through the crossing point in the plane of two beams, these variations in incident light cause variations in the intensity of the scattered light from the particle. If this scattered light from the particle is picked up by a photodetector, it can be converted to an electrical signal whose frequency is proportional to the rate at which the particle is crossing the interference

fringes. A typical photodetector output when observed on an oscilloscope is shown in Figure 9. The laser beams generally have a Gaussian intensity distribution. This causes the amplitude variation, as shown in the Figure 6-(d), with the maximum amplitude occurring in the center of the beam crossing area. The frequency of the signal in Figure 9 is, of course, proportional to the velocity with which the particle is moving across fringes. As shown in Figure 10, the distance between fringes (fringe spacing), d_f , is not affected by the refractive index, but depends only on the wavelength of the laser light, λ , and the intersection angle of the beams, 2ϵ , through the relation:

$$d_f = \frac{\lambda}{2 \sin\epsilon} \quad (1)$$

Multiplying this distance by the output frequency (number of fringes traversed per unit of time) will give the particle velocity:

$$v = f_D \cdot d_f \quad (2)$$

Only the intersection angle and laser wavelength are required for interpreting the frequency in terms of velocity. With lasers, the wavelength is known accurately (error $\leq 0.01\%$ [9]) and an accurate measurement of beam crossing angle is possible for the given optics.

Also, the only velocity measured is the component perpendicular to the "fringes". It should be noted that a 180° ambiguity exists in that the system cannot distinguish "reverse" flow from "forward" flow. Technique for frequency shifting one beam to permit this are discussed in Section II.3.E. An aperture is used on the photodetector so only particles going through the beam crossing area will give a signal. Receiving optics and photodetector with the dual beam system can be placed at any angle and still give same frequency. However, signal quality and intensity will vary greatly. In practice, the receiving optics and photodetector is usually arranged in line with the focusing optics, since this is the location of the strongest signal.

(2) Direction of Measurement

The measurement direction is the vector at right angles to the axis of the optical unit and in the plane of the two beams. In general, any direction in a plane perpendicular to the axis of the optical unit can be selected simply by rotating the beam splitter. The actual measuring location does not move during this rotation. The ability to rotate the beam splitter has several applications:

1. It can be rotated to determine the flow direction
(maximum reading)
2. Readings at $\pm 45^\circ$ to the mean flow can be used to measure \bar{uv} (Reynolds Stress)
3. Readings at $\pm 45^\circ$ can be utilized to obtain an accurate measure of the mean velocity vector

(3) Volume of Measurement

When using LDA, the size of measuring volume affects the accuracy of measurements. It is sometimes very important to minimize the measuring volume. Thin boundary layers, small test sections, accurate positioning, and many other experimental circumstances make a "point" measurement desirable. In this regard, it is necessary to discuss the difference between two measuring volumes, that is, geometric measuring volume and effective measuring volume.

Geometric Measuring Volume

The geometric measuring volume is "shaped" as shown on Figure 6-(b). If the diameter of the laser beam at the measuring volume is d_g and the intersection angle is 2ϵ , then:

$$l_m = \frac{d_\ell}{\sin \epsilon} \quad (3)$$

$$d_m = \frac{d_\ell}{\cos \epsilon} \quad (4)$$

For a diffraction limited lens, one representation of the beam diameter at the focal point is [10, 11]:

$$(d_\ell)_G = \frac{5}{\pi} \cdot \lambda \frac{F_t}{D_1} \quad (5)$$

From Eq. (5), a short focal length and large original beam diameter gives the minimum measuring volume size.

Effective Measuring Volume

If the initial laser beam is plane parallel and has a Gaussian intensity profile, the light waves near the focal waist are also plane parallel and have a Gaussian intensity profile. This wave and optical phenomenon is schematically shown in Figure 11. Due to this Gaussian intensity distribution, the shape of effective measuring volume is ellipsoidal instead of diamond shape. This conclusion has been derived based on the signal at the photodetector rather than appearance. In Figure 11, e^{-1} quantities are used for convenience. They are related to the e^{-2} quantities by [9]:

$$(d_\ell)_E \approx \frac{4}{5} (d_\ell)_G = \frac{4}{\pi} \lambda \frac{Ft}{D_2} \quad (6)$$

In equation (6), the factor of 0.8 is incorporated following the recommendation of [11]. This is the expression of the effective beam diameter at the crossing point for a diffraction limited lens. Therefore, dimensions of the effective measuring volume are:

$$(\ell_m)_E = \frac{(d_\ell)_E}{\sin \epsilon} \quad (7)$$

$$(d_m)_E = \frac{(d_\ell)_E}{\cos \epsilon} \quad (8)$$

$$(h_m)_E = (d_\ell)_E \quad (9)$$

The effective measuring volume is:

$$(vol)_E = \frac{4}{3} \pi \left[\left(\frac{\ell_m}{2} \right) \left(\frac{d_m}{2} \right) \left(\frac{h_m}{2} \right) \right]_E = \frac{\pi (d_\ell)_E^3}{6 \cos \epsilon \sin \epsilon} \quad (10)$$

The dimensions $(\ell_m)_E$ and $(d_m)_E$ basically control the measuring volume size. This, in turn, controls the spatial resolution of the system.

(4) Number of Fringes in Measuring Volume

Figure 6-(c) schematically shows the fringes where the beams cross. The number of fringes is equal to the number of Doppler cycles a single particle will generate. Since d_m is the diameter of the measuring volume, the number of fringes is given by:

$$N_{FR} = \frac{d_m}{d_f} \quad (11)$$

Therefore, the geometric number of fringes is,

$$(N_{FR})_G = \frac{10}{\pi} \frac{F_t}{D_1} \tan\epsilon \approx \frac{5}{\pi} \cdot \frac{d}{D_1} \quad (12)$$

and the effective number of fringes is,

$$(N_{FR})_E = \frac{8}{\pi} \frac{F_t}{D_2} \tan\epsilon \approx \frac{4}{\pi} \cdot \frac{d}{D_2} \quad (13)$$

It is of note that equations (12) and (13) indicate that the number of fringes depends only on the original laser beam diameter and the distance between splitted beams. Of course, equations (12) and (13) are valid only for the very center of the beam crossing point. Towards each end of the length, ℓ_m , the number of fringes would decrease.

(5) Aperture

An aperture is used in front of or as a part of the photodetector. This aperture blocks light coming from locations other than the beam crossing point and thereby improves the signal to noise ratio of the system. In addition, it prevents the possibility of an invalid Doppler signal being generated by mixing of light scattered by a particle in each of the two beams but not at the crossing point. The aperture size is determined by the magnification which is defined as,

$$M = \frac{F_r}{F_t} \quad (14)$$

Therefore, from the previous equations,

$$d_a \approx (d_m)_E \cdot M = \frac{4}{\pi} \frac{\lambda}{D_2} \frac{F_r}{\cos\epsilon} \quad (15)$$

As shown in equation (14), determination of the aperture size depends on the diameter of the beam exiting the laser and the focal lengths of transmitting and receiving lenses. If the focal lengths of transmitting and receiving lenses are same, i.e.,

$$F_t = F_r$$

then,

$$d_a = (d_m)_E \approx (d_l)_E$$

This is the case of the maximum aperture efficiency.

(6) Selection of Lenses

The lens selection depends on:

1. Dimension of test section
2. Flow velocity range
3. Frequency response of signal processor

The focal length of both transmitting and collecting lenses must be long enough to reach the test point corrected for windows and fluids other than air. Velocity range and frequency response of signal processor are the next consideration. Knowing the maximum velocity and the maximum frequency response of signal processor, the desired transmitting lens can be determined by the following relation:

$$f_D = \frac{2V \sin\epsilon}{\lambda} \quad (16)$$

For optimum signal intensity, it is usually best to use the shortest focal length lens that is consistent with the measuring situation and signal processor. Also, it is recommended [9] that transmitting and receiving lenses of the same focal length be used for most applications in order to obtain the maximum aperture efficiency, as shown in section II.3.A.(5).

B. Particulates

The laser anemometer actually measures the velocity of particles in the flow, not fluid velocity, because it measures velocity by detecting light scattered from particles in the fluid. This fact is particularly important in high speed, low pressure flows where only small particles should be sensed since larger ones may not be at the same velocity as the flow. To measure fluid velocity with a laser anemometer, therefore, there must be particles in the flow in sufficient concentration and with proper size to give the required signal. The quality of the data depends strongly on the concentration and type of particulates in the flow. As well as the number of particulates, uniform size particles will also give better results than a wide distribution in size. This is due to the improved signal provided for the signal processor and a reduction in the influence of particle collisions. As a general rule, liquids have adequate concentration and size of particulates for essentially continuous measurements. Also, the relatively high density of most liquids and the low accelerations minimize the importance of particle size. For most gas flows, the number of particulates is insufficient to give data rates high enough to provide an essentially continuous output. Therefore, it is apparent that proper seeding is important

for most measurements in gases. This is without considering the effect of particle size. It should be noted that other characteristics of the particles besides size and concentration can influence the reading. These include refractive index (important in water), rotation, collisions, density, and interaction with the flow. However, size and concentration are the dominant influences in terms of the quality of the data obtained with a laser anemometer[12, 13].

C. Size and Type of Laser

Lasers come in a wide range of sizes, wavelengths and quality. Traditionally, lower power (5 mw or 15 mw) He-Ne lasers have been used for small laboratory type experiment. It has a long tube life, is relatively inexpensive in the smaller sizes, and is readily available from a number of sources. In the larger size it is expensive and its wavelength (6328 \AA) is not optimum for most photomultipliers. In large tunnels and other difficult measurement situations, higher power (over 100 mw) Argon-iron lasers have been used almost exclusively. The wavelength (4880 \AA and 5145 \AA) are in the optimum range for most photomultiplier tubes. Other lasers such as Krypton, YAG and He-Cd lasers might also be considered for some applications. For a specific

application, with sufficient data it should be possible to compute laser power required from the optical configuration and characteristics of the fluid, particulates and photo-detector. In practice, this is very complex and can not be easily defined precisely. However, some generalizations from experience can be made for initial selections.

In the dual beam forward scatter mode, velocities below 200 ft/sec, adequate seeding and less than 300 mm focal length lenses, very good Doppler signals are obtained with good optics and a 5 mw He-Ne laser. Measurements can be made in considerably more adverse conditions, but the signal to noise ratio of the Doppler signal will be somewhat degraded. In backscatter for the above conditions, a larger laser is required for good Doppler signals. A 15 mw unit is adequate for the shorter focal length lenses. In forward scatter, a 15 mw unit works very well with the 600 mm lenses. At shorter focal lengths in forward scatter, velocities up to Mach 1 can be handled nicely with a 15 mw laser. The size, type and wavelength of commercially available lasers is rapidly increasing so the above discussions may soon be outdated. To summarize, for most laboratory experiments a 5 mw or 15 mw He-Ne laser is adequate for good measurements. This is particularly true since forward scatter can generally

be utilized. As backscatter becomes necessary, the focal length increases and/or the velocity goes up, transition to a larger laser such as an Ar-Ion unit becomes necessary. All of the above discussions are for dual beam measurements. Generally, reference beam measurements require somewhat more power for equal signal to noise ratio while dual scatter measurements need considerably more power. With a 5 mw laser, dual scatter measurements should be attempted only with short focal length, relatively low velocities and forward scatter. In dual scatter measurements in the backscatter mode, even the 15 mw laser is inadequate. Therefore, the selection of laser depends not only on the size of the laboratory, but also on the mode of optical arrangements.

D. Signal Processors

The presently available signal processors can be devided into two types:

Special Techniques

Spectrum Analyzer

Analog Correlator

Photon Count Correlator

Frequency to Voltage Converters

Tracker

Counter

Filter Bank

Direct to Computer

Each of the above is the technique for processing signals from the photodetector of a LDA system. The features of various techniques will be briefly discussed.

(1) Spectrum Analyzer

Spectrum analyzers were the first instruments for analyzing LDA signals. Spectrum analyzers generally sweep through the frequency range of interest, displaying the frequencies present as peak on some type of display. They are readily available and permit a good measure of the mean velocity and an estimate of turbulence intensity. Problems with this method include:

1. data is not "real time" (analyzer must sweep through bandwidth of interest)
2. broadening of spectrum due to the finite filter bandwidth
3. broadening of spectrum due to a signal of finite length which includes high order terms
4. broadening of spectrum due to noise

The item 2 above can be corrected. The item 3 need not be a problem with most signal processors when only one particle at a time is in the measuring volume, but will show up on a spectrum analyzer. Figure 12 shows the basic idea of signal processing method of spectrum analyzer and spectrum broadening.

(2) Analog Correlator

Correlators sample the signal. Standard analog correlators have been used very little for LDA work, probably because they are too slow, particularly at high frequencies. However, within its frequency range, the analog autocorrelator will give both mean velocity and a measure of turbulence intensity. In this regard, this information is similar to a spectrum analyzer.

(3) Photon Count Correlator

The photon count correlator is basically the same as the analog correlator with a special input section for pulse counting instead of analog voltage levels. It operates on individual photon pulses and would convert the pulse frequency to a digital word. The reason for a special instrument is the need for speed. The photon correlator will operate at very low light intensities. This is its primary advantage. It

permits measurements where other techniques do not have an adequate signal. If light intensity is too high, individual photon pulses cannot be resolved. However, one can almost always decrease light intensity, while the opposite is not true. Mean flow and turbulence intensity are available from this technique, but time information on flow signal is not readily available. For frequency to voltage converter type signal processors, some important characteristics should be mentioned prior to the discussions. They are:

1. number of Doppler cycles required for accurate measurement
2. capture bandwidth
3. slew rate
4. dynamic range
5. ability to extract signal from noise
6. measurement accuracy

The items 2 and 4 above are particularly important from the operational view point.

(4) Tracker

Tracker is basically a combination of tracking filter and frequency to voltage converter. Typically, this type of signal processors has been used where the particle concen-

tration is high, since it is easier to use with multiple particles in the measuring volume and with relatively noisy signals. The fundamental limitation of any tracker type signal processors is the "Capture" range. If the change of velocity between one particle and the next particle is greater than the "Capture" range of the unit, it will not track the new value and any succeeding values that remain outside the capture range. This happens particularly when a combination of low particle concentrations and large changes in velocity occur. Figure 13 illustrates the dynamic range and capture bandwidth. From Figure 13 the following operational points can be derived:

1. operation should be towards full scale for optimum extraction of the signal from noise
2. operation should be towards the bottom of the range for maximum capture bandwidth

With high particle concentration in the fluid, noise due to varying particle phase will be present. A low pass filter should always be used to minimize this noise by filtering out frequencies above those of interest. Unfortunately, all of this phase noise can not be filtered out, since it is essentially "white" noise. Practically, there are limits to both accuracy and minimum output noise levels on trackers even with

ideal input signals, and this greatly restricts the turbulence measurements when the intensity is high.

(5) Counter

A counter measures the time interval for a fixed number of cycles, N, of the Doppler signal. The inverse of this time interval is then velocity. This type of signal processors has been applied in the flow situations of high velocity, low particle concentration. It is often used in difficult measuring situations with the large laser. A counter does not have a "Capture" range, since any signal within its entire frequency range can be "Captured". The accuracy of the system mostly depends on the accurate zero crossing measurements. For a single particle and low background noise, N cycle of the Doppler signal represent the correct frequency for the velocity present. With multiple particles, phase changes can give a significant error over N cycle, particularly if N is small. Also, the "pedestal" or DC component of the Doppler burst must be removed for accurate zero cross counting. Ideally, it can be done without limiting the dynamic range of the instrument. Generally, the following methods are utilized to remove the pedestal:

1. high pass filter
2. optical pedestal removal
3. frequency shifting
4. filter bank

If the method of filtering is used to removed the pedestal, the frequency range and hence the "Capture" range will be limited by the filter. Furthermore, improper filtering may be the another source of error. Figure 14 schematically describes the effect of noise on zero crossing measurements. A comparison of some characteristics between presently available commercial tracker type and counter type signal processors is shown in Table 1. This comparison has been made because they are the most common techniques.

(6) Filter Bank

The filter bank consists of many individual filters. Output essentially looks for filter that is resonating and identifies it as frequency. The problems in this type of signal processors are:

1. several cycles are required for resonance
2. accuracy is limited by the number of filters

The filter bank signal processors are effectively real time spectrum analyzers.

(7) Direct to Computer

A fast analog to digital converter with subsequent computer

data processing can also be used. The converter essentially puts the "raw" Doppler signal into digital form for use in a computer. The data is then sorted out by proper programming. Disadvantages of this kind of signal processing method are:

1. limited frequency of analog to digital converter
2. large amounts of computer time and data storage required

Summary

If signal strength is adequate, most well designed signal processors will work for most flows. It is the author's opinion that the special techniques work better in turbulence measurements, although they do not give an instantaneous velocity value. Furthermore, photon correlators will operate at very low light levels. The tracker, counter and filter bank are all methods to obtain a nearly "instantaneous" conversion of the frequency to voltage. Tracker can give better results for lower signal/noise ratio, are easier to use and cost less than counter type processors. In highly turbulent flows with low particle concentration (mostly gases with natural seeding), a tracker may not work at all and a counter must be used. Counters will handle a wider variety of flows than trackers. The above comments are related to the signal processors now available. Certainly, the practical implementation of both techniques will be greatly improved in the future.

E. Data Analysis

The fact that laser anemometer actually measures the particle velocity, not fluid velocity, gives special problems in data analysis. Particles are distributed randomly in the fluid and the naturally occurring particles vary in size and concentration. Intentional seeding permits control of size and concentration but still leaves a random spatial distribution. Perhaps this is the single most important complication of the LDA technique. In addition, the signal, as far as any realizable signal processor is concerned, is essentially discontinuous even with a high particle concentration due to widely varying amplitude. In many applications, the signal is actually intermittent due to the absence of particles in the measuring volume. The choice of the best method of data analysis depends on many, often interrelated factors such as:

Particle concentration (Burst Density)

Particle size

Spatial / Temporal Resolution

Signal to noise ratio

Signal processing method

Signal validation method

Type of information required

Among the factors, the single most important one is the

particle concentration. The statistics of high density signals are fundamentally different from low density signals. Most data analysis systems such as rms meters, spectrum analyzers, correlators, and even voltmeters for mean flow are designed to operate on continuous data. Therefore, it is ideal when the output of the signal processor on a laser anemometer can be considered continuous. This depends primarily on the data rate. For mean flow, the fact that the processor holds the last reading helps considerably. When this happens, there are at least two ways of time averaging the data. One way is to average the signal over all time regardless of the signal validity. This corresponds to low pass filtering the data. The other way is to average the signal over only those intervals in which the signal was valid. While this approach is intuitively more correct, it is also more difficult to implement. In the case of high burst density signals, there is little difference between the two types of averages. For most purposes, therefore, it is sufficient to approximate the latter by the former for high burst density signals. However, this may not be true of low burst density signals. For turbulent flow, true rms is normally the first parameter measured after the mean flow. Here, the validity of assuming a continuous measurement depends on the data rate and the frequencies that

contain the primary energy. Certainly, on the average, several data points per cycle are required for frequencies that represent a significant part of the total turbulent energy. For most turbulence, most of the energy is in the lower frequencies so that mean velocity and turbulence intensity can frequently be measured assuming high data rates. The use of continuous data procedures for spectral analysis depends directly on the number of data points. Again, at the maximum frequency of interest, it is necessary to have, on the average, several data points per cycle for good data. For correlation with time delay, the correlation curve will be biased if a new data point has not occurred at the minimum time increment utilized in the correlation. A detailed analysis including both the samples per second and the distribution of these samples is necessary to precisely define the validity of the data when assuming a continuous output. The fact the sample points are not equally spaced can actually be utilized to improve the effective response without separately keeping track of time intervals if an appropriate estimator is used[14]. For low burst density signals, the best method of taking data is to take individual data points as they occur. It is important to notice that low burst density means a low probability of more than one particle in the measuring volume at a time.

There still can be a sufficiently high data rate to follow the flow characteristics of interest. At low data rates, maximum data utilization is obtained when both time data and velocity data are utilized. Here, the term, "low data rate", generally means a rate so low that even the large scale fluctuations in flow are not recognizable on, say, an oscilloscope trace of the signal processor output. With an on-line computer, the computer clock can be used to measure the time interval between data points. Combining this with the velocity measurement represented by each data point permits complete statistical analysis of the results.

F. Other Systems

There are numerous modifications of the three basic systems that can be utilized for special measurement requirements. These may indicate the flexibility of the laser anemometer. However, only the frequency shifter will be discussed here.

Frequency Shifting

The standard laser anemometer system has a 180° direction ambiguity. In other words, it cannot tell whether the flow is forward or backward. This becomes a limitation in a number of

measurements. In order to expand the applications of laser anemometry, a frequency shifter is used. Proper application of the frequency shifter permits measurements in reverse flow as well as assisting in other difficult applications. In principle, it can be utilized with any mode. In practice, it has been used primarily with the dual beam and reference beam modes. In the reference beam mode, the frequency of the scattered light is compared with that of a reference beam. At zero flow, the two light frequencies are equal and the frequency output of the photodetector (difference between reference beam frequency and scattered light frequency) goes to zero. If the reference beam is frequency shifted, for example, 40 MHz, then the photodetector output at zero flow is 40 MHz. The frequency output will be higher for particle velocities in one direction and lower for the other direction. Essentially, the resulting system gives a zero offset that permits bi-directional measurements with a laser anemometer. In the dual beam mode, two beams of the same frequency interfere with each other where they cross and this interference causes a stationary fringe pattern. If one beam is shifted in frequency relative to the other, the fringes can be thought of as "moving". If the difference in frequency of the two beams is 40 MHz, a stationary particle in the measuring volume will then give a 40 MHz signal from the photodetector picking up

the scattering light. Movement in the same direction as the moving fringes will lower the frequency while movement in the opposite direction will raise it. Again, the result is equivalent to a zero offset. In short, this technique can be summarized as "shifting the frequency of the light of one of the heterodyne signals by f_s so that zero velocity will give frequency f_s at the photodetector. Techniques for frequency shifting include acousto-optic (Bragg) cells and rotating diffraction gratings. Both techniques work well, but acousto-optic (Bragg) cell technique is more widely used due to the small range of maximum shift frequency of present rotating diffraction grating technique. The principles of the Debye-Sears effect form the basis of acousto-optics cells, which may be used to divide a light beam into several beams with different frequencies and directions. Bragg cell is a particular case of these cells operating to yield one beam with a frequency and direction different from the incident beam. As shown in Figure 15, the incident light beam passes through a medium in which acoustic waves are travelling. Depending on the angle, the acoustic frequency (normally 40 MHz) is either added or subtracted from the light frequency. The intensity of the light in each refracted beam depends on several parameters including the cell dimensions, the acoustic and light frequencies, the absorbing medium, the electrical power used

to drive the crystal and the angle between the acoustic wave fronts and the incident beam. In practice, the intensity of the two beams coming out (zeroth order and first order) can be equalized. Frequency shifting is a very useful tool in LDA. The specific applications of frequency shifting are:

1. Flow reversals in the mean flow direction
2. Turbulence components perpendicular to the mean flow
3. Pedestal removal by frequency shifting
4. Optimizing the frequency range on signal processor

II.4. Errors in Laser Doppler Anemometry

The errors that are associated with measurements using laser anemometry come from many theoretical and practical limitations. They can be listed as:

- A. velocity fluctuations within the volume
- B. mean velocity gradients across the volume
- C. finite transit time of the particles through the volume
- D. low particle concentration
- E. signal/noise ratio
- F. precision of the signal processors

The items A, B and C above are theoretical limitations associated with finite measuring volume [15, 16]. The items A and B

effects similar to those found in using a hot-wire anemometer.

A. Fluctuations in particle movement within the measuring volume can influence the resulting mean and turbulence data.

B. Likewise, a finite measuring volume can affect mean flow measurements in steep velocity gradients.

Furthermore, for uniform particle concentrations, the number of data points will be higher at high velocities. Summing individual data points will lead the result to the high velocity side.

C. The effect of finite transit time of the particles through the volume basically derives from the fact that when a spectrum analysis is done on the output of the photodetector of an LDA, there is a spectral broadening. If one considers that the Doppler signal for a single particle has a beginning and an ending, this in itself must generate higher frequency variations that show up as spectral broadening even in laminar flow. This, then gives a "minimum" turbulence intensity that can be measured. How much spectral broadening affects the various types of signal processors is somewhat controversial. With a very noise free Doppler signal,

a system measuring time between zero crossing (counter type) would seem to be independent of the transit time ambiguity when only one particle is in the control volume at any one time. Similarly, with a similar signal, a system reading the signal while it still has good amplitude and holding that reading (tracker type) would also seem to be free of the transit time ambiguity. However, there is probably never only one particle in the control volume even though one dominates due to size. Also, one never has a truly noise free signal.

The items D, E and F are practical limitations.

- D. Low particle concentration will affect the time averaged mean velocity. A simple average of output data will not give the correct average value.
- E. The effect of poor signal/noise ratio is the most important practical limitation on measurement accuracy. The signal to noise ratio of the Doppler signal affects the accuracy of any signal processor, particularly for measurements of turbulent flow. In the counter, the effect of noise is clearly seen when either the data rate goes down or the number of count is decreased. In the tracker, a poor signal noise ratio also results in a decreased

sample rate as well as some degradation in the tracking accuracy and stability. There are numerous sources of noise. They can be divided into two categories:

Inherent Sources of Noise

- (1) Variations of fluid velocity across the measuring volume
- (2) Multiple particle signals
- (3) Shot noise
- (4) Brownian motion

Extraneous Sources of Noise

- (5) Reflected light waves from the laser
 - (6) Light waves from the environment
 - (7) Noise from frequency shifting
 - (8) Optical noise
 - (9) Signal processor noise
-
- (1) Noise from the variation of fluid velocity

This is a source of noise associated with the measuring volume size. This is one of some unique sources of the laser anemometer, when compared with the hot wire anemometer. This

noise source is not present with a hot wire which averages variations of heat transfer over its length. Whereas the laser, measuring on individual particles, reacts much differently.

(2) Noise from multiple particle signals

This is a second inherent source of noise - commonly called "Doppler ambiguity"[16]. The combination of varying Doppler signal amplitudes and random phases between signals from different particles results in artificial variations in the frequency seen by the signal processor. This noise is not a problem at low particle concentrations, but becomes significant when the probability of multiple particles in the measuring volume is high. This phenomenon particularly limits the minimum turbulence that can be measured. Several methods are available to reduce the effect of Doppler ambiguity. A low pass filter should be used so that only the frequencies of interest are observed. As discussed previously, however, all of this noise cannot be filtered out since it is essentially "white" noise. Cross correlating two independent measurements at the same point in the fluid will give a correlation independent of the ambiguity noise [17]. From this, a transform can be used to obtain spectrum. In addition to

filtering, an alternate technique has been suggested[18]. Since the ambiguity spectrum is equivalent to white noise, its influence can be determined by measuring the rms of the signal using different low pass positions. Once established, it can be subtracted. Among the three methods discussed, the most common and popular method is the use of a filter.

(3) Shot Noise

This is the noise associated with the discrete emission of photo-electrons. If the only light hitting the photodetector is scattered by a single signal producing particle, the dark current in the photodetector is zero and there is no noise in the electronics following the photodetector, then, the only remaining source of noise is the shot noise associated with the electron current flow produced by the signal itself. The mean square of the shot noise fluctuations is proportional to the mean photo current. This signal-to-shot noise ratio serves as a measure of the performance of a LDA, and it is the first priority to insure adequately large values of this in designing or specifying a LDA.

(4) Noise due to Brownian motion

This can be another possible source of noise. As briefly discussed in reference 6, this effect can be a problem when

flow velocity is very low. The molecular speed due to Brownian motion is proportional to the following relation,

$$v \sim \sqrt{T/M} \quad (17)$$

For gases, molecular weight is so small that the molecular speed is enormous and, hence, the frequency at the measuring volume due to this motion often reaches the order of 10^9 MHz. This is the reason why LDA measurement is not possible without particles. For liquids, this effect is much less than for gases, but still gives high order of frequency.

(5) and (6) Noise due to reflected light waves from the laser and light waves from the environment

These items are related to the components of light waves at the photo detector. The total electric vector at the photo detector may consider of:

- a) light waves scattered from one or more illuminating beams by one or more particles
- b) "reference" light waves from the laser
- c) extraneous light waves from the laser reflections
- d) extraneous light waves from the environment (i.e. room light, radiation from flames, etc.).

Each type of light wave contributes to the photo current, but

only a) and b) produce signals containing useful velocity information. Laser light reflected or scattered by walls may interfere with light scattered by particles to produce noise. This effect is particularly severe when measurements are made very close to walls. Also, light waves from the environment can interfere with the signal producing light waves. It occurs often in practice particularly when the intensity of scattered light waves by particles is weak.

(7) Noise from frequency shifting

As discussed previously, acousto-optic (Bragg) cell technique is more widely used among two common techniques for frequency shifting. However, Bragg cell generates some noise due to high frequency vibration (40 MHz) of local oscillator to produce travelling acoustic waves. Usually, this contribution to overall noise effect is regarded as small.

(8) Optical noise

Poor optics design can be another source of noise. The poor quality optics, for example, can generate the unparallel fringes or cause the beams to cross outside the working range in the dual beam system. If the fringes are not parallel, then a particle going through different portions of the measuring

volume will give different frequencies even when traveling the same velocity. The result is the same as a mean velocity gradient. In addition to the above effects, the optics whose surface is not sufficiently smooth would cause the same noises at those discussed in items (5) and (6).

(9) Signal processor noise

The last noise source to be discussed here is the signal processor itself. The minimum possible noise is that with a continuous signal from a generator as the source. This gives a measure of the minimum attainable output noise with a given signal processor. Often, a discontinuous signal that is amplitude modulated will give more output noise than a continuous signal. This is a good representation of the Doppler signal when the particle concentration is light. A heavy particle concentration, including Doppler ambiguity, is difficult to simulate with signal generators. However, in this case the signal processor is not usually the major source of the noise. The processor can reduce the noise through either not following the rapid frequency changes or through output low pass filtering.

F. Sometimes, the precision of the signal processors can be an important practical limitations. For example, the relation between input frequency and output voltage should

be linear for tracker or counter type signal processors.

Since this effect is so obvious that no further discussion will be necessary.

Summary

For turbulence or RMS measurement, all of the above limitations are all interrelated and precise quantitative error analysis is practically impossible. For mean velocity measurement, the error due to phase noise may be systematically reduced for periodic signals by averaging signals of successive periods (waveform analysis). The true signals add while the noise reduces to zero on average. In most cases of mean velocity measurement with reasonable signal/noise ratio, therefore, the following items are considered to be major factors which affect the accuracy:

1. accuracy of laser wavelength
2. accuracy of beam crossing angle
3. accuracy of frequency shifting system
4. precision of signal processors

For most presently available commercial systems, the usual error ranges are 0.01%, 0.1%, 0.01% and 0.4% for the above items 1, 2, 3 and 4, respectively[19]. From the above information, therefore, the accuracy of most mean velocity measurement is expected to be within 99%.

II.5. MIT Variable Pressure Water Tunnel and LDA Systems

In spite of the remarkable potentials and advantages, however, the actual application of the Laser-Doppler Anemometry technique to the propeller tunnel is greatly restricted by the characteristics of tunnel itself. Fortunately, the MIT water tunnel is extremely ideal for laser measurements for the following reasons:

1. test section is square with complete accessibility on all four sides.
2. the size of the test section is large enough to accomodate hydrodynamic models, and small enough to allow the use of low-powered lasers.
3. the optical systems can be rigidly mounted on a single movable base which passes underneath the test section.

MIT water tunnel has the following characteristics:

Section shape	: Square Section
Inside dimension	: 20"
Outside dimension	: 24"
Tunnel window	: 44" x 16" x 2" plexiglass
Free stream velocity range	: 0 - 30 FPS

The MIT water tunnel LDA system including signal process and data analysis equipment has the capability of measuring and storing the velocity at a fixed point in space at a large number of time intervals between two blade passages. Combining these results for a sequence of fixed measurement points, it is possible to construct the velocity field in propeller fixed coordinates as shown in Figure 16. The MIT water tunnel LDA system and some of its characteristics are shown in Tables 2 and 3, and Figures 17 and 18. In addition to the tunnel characteristics, there is another important point in the practical application of LDA system. It is the quality of tunnel window (particularly transmitting side window) in the sense of thickness distribution and surface smoothness. As far as thickness problem is concerned, what is important is not the absolute thickness, but the uniformity of thickness. The thickness of window should be sufficiently uniform for the accurate positioning of beam crossing point and for the perfect crossing of the beams. Furthermore, its surface should be sufficiently smooth to prevent excessive surface scattering of the laser beams. Sample measurements of tunnel window thick-

ness distributions are shown in Figure 19. Figure 20 shows the relations between distances for two different transmitting lenses and comparisons between some measured and calculated distances.

II.6. Calibration

In section II.4., it has been concluded that the overall error of the system would not be greater than 1%. To check the validity of this conclusion, two comparisons were made. The first one was the comparison of tunnel free stream measurement between LDA system and existing device (manometer), and some typical results are shown in Table 4. Since this is the simplest case of flow measurement situations, both should work well. As shown in Table 4, the agreement between two different measurements is excellent. In order to make a comparison for more complicated measurements, a special device, so-called "calibration rotor" was prepared. This rotor was installed on the propeller shaft and rotated at several different RPM to measure the rotating speed. Dimension of the rotor arrangement and results are shown in Table 5. As shown in Table 5, the agreement is

very good at lower RPM (lower than 1200). At higher RPM (higher than 1200), however, agreement is poor and the measurements by two different methods are continuously diverging with increasing RPM. It was really embarrassing and hard to explain at first. However, it was found that the RPM meter (counter) did not work properly above 1200 RPM. This explained everything and the accuracy of LDA measurement was confirmed.

III. Propeller Model

A set of four NSRDC research propellers were chosen for this study. They are Propellers 4381, 4382, 4383 and 4498, and were designed by lifting-surface methods with varying skew and warp[20, 21]. These propellers are considered to be the first model marine propellers designed to study the effects of skew systematically. The first three propellers belong to one series, which were designed for uniform flow with all parameters held constant except skew (and pitch and camber corrections due to skew)[20].

The propeller 4498 belongs to the other series[21], which differs from the previous series in the view point of rake. However, all of these propellers have the same radial distribution of chord length and thickness, and were designed to have the same loading distribution for uniform flows at the design advance condition of $J = 0.889$. Therefore, this set of propellers is ideal in the study of the effect of large changes in skew and rake without extraneous influences. The detail geometric and performance characteristics of these propellers can be found in references 20 and 21. For convenience, however, the principal design and some performance characteristics are reproduced in Tables 4 and 5.

IV. Results of Experiment

IV.1. General

The earliest and simplest measurements were made early in December, 1976, when all of the necessary components had arrived and were assembled on a temporary wooden base. These were measurements of tunnel free stream velocities. Since then, a successful procedure of measuring technique has been developed and established through a series of trial measurements such as rotating speed of a specially prepared

rotor, tunnel wall boundary layer and some field point velocities for several different propellers. The preliminary test results had not only showed the accuracy and excellent repeatability, which may be the two most important factors in an experiment, but also confirmed the possibility of successful measurements of the precise quantitative flow informations around propeller blades, which would be extremely difficult or unsuccessful with conventional measuring devices. The preliminary results are partly reported in reference 19 and will not be discussed here. Only the information directly obtained or derived from a series of laser measurements for the propellers introduced in Chapter III will be discussed in the subsequent sections. In this study, results are presented following the coordinate system adopted at 1973 ITTC convention, which is shown in Figure 21.

IV.2. Slipstream Radius

The conventional way of measuring slipstream radius basically relies on flow visualization. In this method, propeller tip vortices are first made visible by a suitable reduction in tunnel pressure and radius(or diameter) itself is next measured either by a sighting telescope focused on

the tip vortices or by photographing them. This visual method is regarded as a reasonable one, but not the best method, since it has been noticed that the shape of tip vortices are somewhat affected by the tunnel pressure. With the LDA system, however, this can be directly measured without reducing the tunnel pressure. In this measurement, it has been found that the fluctuational transition from free stream to slipstream is extremely sharp. This transition occurs within the width of only about two percent of propeller radius depending on the loading condition. Since this information forms a basis of several other derived quantities, the measurements were carefully performed at two or three different positions, for instance, approaching from the top (along the negative z-axis with $y = 0$) and from the side (along the $\pm y$ -axis with $z = 0$), and averaged. For most cases, however, they are surprisingly close each other and averaging was not really necessary. The slipstream radius measurements are shown in Table 8 and Figures 22 through 25. It may be noted from the above Figures that most of contraction occurs within the axial distance of one radius from the propeller tip. More specifically, about 55%, 75% and 90% of total contraction occur at the axial distance of $0.2R$, $0.5R$ and $1.0R$ from the propeller tip for all propellers and for all loading conditions. Table 9

shows the contraction ratio with respect to total contraction at the axial distance of 0.2, 0.5 and 1.0 radius. It may be also noted that there is an interesting relation between skew and ultimate slipstream radius, that is, the ultimate slipstream radius is almost linearly increasing with increasing skew, as shown in Figure 26. The relation between loading condition and ultimate slipstream radius is shown in Figure 27.

IV.3. Hydrodynamic Pitch and Pitch Angle

With the LDA system, at least two methods are available to find hydrodynamic pitch and pitch angle of tip vortices. One way is to trace the tip vortex from a selected propeller blade to find an axial-angular relation of that vortex(vortex trace method). This can be done through a series of plots of field point velocity close to the slipstream at different axial positions. Figure 28 is one typical example describing this method. The other method is to use the relation between axial and tangential velocity components with respect to the rotating coordinate system(velocity method). To do this, the mean velocity components with respect to space fixed coordinate system were first measured and converted to those with respect to rotating coordinate system. Both

methods work well leading to the results with good agreement. However, the vortex trace method is preferred, because the result from the velocity method tends to be somewhat dispersed, while that of the vortex trace method is quite smooth. Also, the visual method can be used to find these quantities, but its result is less accurate due to the reason explained in section IV.2. The hydrodynamic pitch and pitch angle of tip vortices obtained from the vortex trace method are shown in Tables 10 and 11, and Figures 29 through 36.

IV.4. Tunnel Free Stream Velocity with Propeller Shaft Housing and Mean Axial Velocity behind Propeller

Theory assumes no propeller shaft. Actually, there must be a shaft and it generates wake. This may explain the reason why the axial component of field point velocity predicted by theory near the hub vortex is always considerably higher than that of measured, which will be shown later. In order to estimate the effect of wake, tunnel free stream velocities were measured with propeller shaft housing and dummy hub. They are shown in Figures 37 and 38. Next, the mean axial velocities from one side of free stream to the other side of free stream through the hub vortex core center were measured at several different axial positions. They are shown in Figures 39 and 40. Their patterns of velocity defect are

compared to be very similar and it can be roughly concluded that radial region of $0.5R$ is under the influence of the wake. Also, a spanwise load distribution can be deduced from the mean axial velocity measurement. A comparison between Figures 39 and 40 shows the higher load distribution near the tip for highly skewed propellers* than for plain propellers. This can be confirmed by the comparison of radial circulation distributions obtained either by the solutions of Boundary Value Problem or by the tangential velocity measurements. The methods of obtaining circulation distribution will be discussed in section IV.7.

IV.5. Mean Tangential Velocity

In fact, this velocity is measured along the y -axis($z=0$). Therefore, it would be more precise to state as "vertical velocity measurement along the y -axis". However, this is equivalent to tangential velocity, particularly to mean tangential velocity. Figures 41 through 44 show the mean vertical velocity measurements along the y -axis. Their usefulness will be shown later. The mean tangential velocity

* This conclusion applies only to the present propeller series, and implies that the present design method does not call for enough pitch reduction at the tip.

and the instantaneous tangential velocities are almost identical, that is, fluctuation is very small in tangential velocity except very close to tip vortices. Figure 45 shows the comparison of mean tangential velocity between plain and highly skewed propellers measured at the roll-up point.

IV.6. Roll-Up Point

The position of roll-up point for the hub vertex system can be found by investigating the initial slope of tangential velocity through the hub vortex. Similarly, that of the tip vortex system can be found by examining either the peak axial velocity or the fluctuation pattern of axial velocity very close to tip vertices. As shown in Figures 46 through 49, both the initial slope of tangential velocity and the peak axial velocity at 95% of slipstream radius are almost linearly increasing with increasing axial distance from the propeller, finally reaching a maximum value at a certain axial position, and then slowly decreasing due to diffusion of vorticity. The axial position with a peak value is considered to be the roll-up point. Thus determined position of roll-up points all fall within $0.9R - 1.0R$ from the propeller tip. As mentioned above, another way for finding the roll-up point of the tip vorticity is to examine the fluctuation pattern of

axial velocity very close to slipstream radius. As shown in Figures 50 through 53, the fluctuation pattern of axial velocity at 95% of slipstream radius first becomes regular at a certain axial position, which is the same axial position as that of peak velocity. Experience reflects that the exact position of the roll-up point is not crucial.

IV.7. Circulation

The tangential velocity measurement is particularly useful to find out the circulation strength and distribution. Both initial slope and definition of vorticity together with the information of tangential velocity distribution* can be used to calculate circulation strength. In (x, r, θ) - cylindrical coordinate system, vorticity is expressed by,

$$\vec{\zeta} = (\zeta_x, \zeta_r, \zeta_\theta) = \nabla \times \vec{v}$$

$$= \frac{i}{r} \left[\frac{\partial}{\partial r} (ru_t) - \frac{\partial u_r}{\partial \theta} \right] + \frac{\dot{e}_r}{r} \left[\frac{\partial u_x}{\partial \theta} - \frac{\partial}{\partial x} (ru_t) \right] + \dot{e}_\theta \left[\frac{\partial u_r}{\partial x} - \frac{\partial u_x}{\partial r} \right]$$
(17)

To simplify this expression, assumptions are made that:

- 1) the flow is axially symmetric

* This method was originally suggested by Prof. Widnall to estimate hub vortex core size.

- 2) there is no change in tangential velocity with change in axial distance after roll-up point
- 3) there is no change in radial velocity with change in axial position after roll-up point

The first assumption is true for mean velocity, and the mean velocity was actually used. The second and third assumptions are reasonable for the portions after roll-up point. In fact, radial velocity is negligibly small after roll-up point except extremely close to hub vortex core center. With the above assumptions, the vorticity equation is reduced to the form of.

$$\vec{\zeta} = (\zeta_x, 0, \zeta_t) \quad (18)$$

where,

$$\zeta_x = \frac{1}{r} \frac{\partial}{\partial r} (r u_t) \quad (19)$$

$$\zeta_t = - \frac{\partial u_r}{\partial r} \quad (20)$$

The circulation distribution is obtained by the integration of vorticity as,

$$\Gamma = \iint_S \vec{\zeta} \cdot \vec{n} \, ds \quad (21)$$

Thus obtained results are shown in Figures 54 through 57. In order to have some general aspect, the circulation strengths have been calculated by several different methods

and are shown in Table 12. Table 12 also shows a comparison of circulation strength between PUF-2 and experiment (vorticity integration). Their agreement is good for a plain propeller, but becomes less good as skew increases. This may explain the less good agreement in propeller thrust between test and theory for highly skewed propellers.

IV.8. Field Point Velocity

The ultimate goal of this study is to develop a prediction method of field point velocity numerically and experimentally. In this regard, the application of LDA technique is quite successful and the field point velocity measurement has essentially become a routine work. In fact, most of previously discussed informations have been derived from the velocity measurements. For this study, time-averaged field point velocities per propeller revolution or for three blade periods at over thousand field points have been measured and stored in the form of plot. Here, it is reminded that the position of field points is expressed following the ITTC convention shown in Figure 21 and that these measured velocities with respect to space-fixed coordinate system can easily be converted to those for propeller fixed (rotating) coordinate system using the relation derived in Figure 16. Some examples

of measurements are shown in Figures 58 through 81. For convenience, however, most of measurements around propeller blade are presented in Chapter VI along with numerical outputs for comparison. Figures 58 through 73 show the typical fluctuation pattern of axial velocity at upstream and downstream locations rather close to the propeller blade. Figures 74 through 81 show the particular fluctuation pattern of axial velocity slightly inside($0.95R_w$) and outside($1.05R_w$) of slipstream. In fact, these Figures show the velocity jump across the tip vortices. This velocity jump was once used to estimate the tip vortex strength. The detail method will not be discussed here. It is simply mentioned that this method yields the value very close to that by initial slope of mean tangential velocity method shown in Table 12, section IV.7. Also, the transition from initial to ultimate fluctuation pattern of axial velocity slightly inside the slipstream is shown in Figures 50 through 53.

IV.9. Blade Boundary Layer

For the velocity measurements inside the slipstream, rather unexpected, but consistent patterns(dents) have been encountered. Figures 82, 83 and 84 are those for the measured axial velocity clearly showing a dent for each blade period.

Although it seemed more convincing for them to be explained by viscous effect, there still remained a possibility that they were caused by vortex systems, because theory occasionally produces dents. Through the careful investigation of both the numerical scheme and measurements, however, the conclusion has been reached that those are really velocity defects caused by the blade boundary layer. The dents in theory come from the modeling of vortex system. In the present numerical method, as will be discussed in Chapter V, propeller blades are replaced by surfaces with spanwise and chordwise vortex segments, one with fine spacing and the others with coarse spacing. The purpose of such arrangements is to reduce the computation time. The occasional dents in theory are due to this unequal arrangement of vortex segments. Numerical calculation at carefully chosen field points does not produce these dents. Furthermore, if the dents are caused by vortex systems, then their pattern can not be so consistent as shown in Figures 82, 83 and 84 with the variations of radial and axial positions. The dots in Figures 82 and 83 are potential flow approximations. They are constructed first by plotting the theoretical values and by bringing down to match the measurements, just like DC voltage change. This information of velocity distribution in the wake can be used to estimate the blade sectional drag by applying momentum

balance for the properly chosen control surface. This method of determining sectional drag is not only very useful, but also often the only practical way. With this method, a rough estimation of the blade sectional drag coefficient has been made neglecting the contribution from the static pressure and rotational motion, and the results are shown in Table 13. As shown in Table 13, the estimated sectional drag coefficient becomes higher toward propeller tip. This result implies that the incorporation of presently adopted sectional drag coefficient to the numerical scheme may not be fully justified, even though the average value of estimated coefficient and presently adopted coefficient are very close each other. Here, it should be noted that the estimation is somewhat affected by the approximation of potential flow. Although those values are not expected to be immediately useful, they are at least valuable to confirm that the strange patterns are really velocity defects due to boundary layer.

V. Numerical Method (Numerical Lifting Surface Theory)

For the numerical prediction of field point velocities, the Field Point Velocity Program (FPV-9) has been prepared. This program is essentially the same as the Propeller Unsteady Force Program (PUF-2) in the sense of utilizing the sub-

routines used in PUF-2. In fact, PUF-2 is a consequence of the last several year's research carried out by several people. Although FPV-9 has been prepared for the case of steady flow, it may be extended to unsteady case without much difficulty. This program is composed of two major programs - The Boundary Value Problem Program (BVP) and the Velocity Program. First, the propeller geometry is read in as an input in the Boundary Value Problem Program. The analytical lifting surface theory employs the source and vortex sheets (continuous distribution) as a model to represent propeller blades, and the trailing vortex sheets to represent propeller wake. Obviously, such a modelling is not practical in a numerical scheme. Therefore, the continuous distributions of sources and vortices are replaced by concentrated source and vortex line segments as shown in Figure 85. The vortex spacings on blades are uniform both in the chordwise and spanwise directions. The roll-up procedures to the tip and hub vortices, and the contraction of the slipstream have been accounted for in the present modelling of the trailing vortex wake system, which schematically is shown in Figure 86. Since the problem is basically linear, the thickness and lifting problems can be separated. Applying the standard method, the thickness problem is solved by distributing sources at each chordwise section. The source strengths are determined by the mean inflow velocities obtained from the

lifting line theory. Thus determined source strength is used exclusively with the assumption that the thickness problem is not sensitive to the circumferential variation of inflow velocity. The lifting problem is solved utilizing the existing formulation for the lifting surface theory, that is,

Integral equation for the unknown vortex strength

Boundary condition

Kelvin's condition

Kutta condition

The integral equation is the well-known Cauchy principal type singular equation and particular caution is required in the procedure of discretization. The boundary condition (tangency condition) is satisfied on the blade camber surface as,

$$\vec{N} \cdot \vec{V} = 0$$

where,

$$\vec{V} = \vec{V}_{\text{inflow}} + \vec{V}_{\text{source}} + \vec{V}_{\text{vortex (bounder + trailer + wake)}}$$

Kelvin's theorem is applied to locally relate the trailing vortices to spanwise vortices. By this procedure, the number of unknowns is reduced. Finally, the Kutta condition is required to ensure smooth tangential flow at the trailing edge. From

the previous tests and experiences, one-point linear Kutta condition is adopted. Therefore, the strength of the lost vortex element in a chordwise panel is linearly dependent on the strengths of the adjacent vortices on the blade and in the wake. This choice is regarded as optimum, particularly for unsteady cases. The integral equation is, by discretization, transformed into a system of linear algebraic equations for the unknown strength of the spanwise vortices. Upon solving this system of equations and utilizing the above conditions, the vorticity distribution over the blades and wake is obtained. In order to reduce the computation time as briefly mentioned in section IV.9, the number of discrete vortex elements of the other blades and wakes is considerably reduced as shown in Figure 85. However, the calculated velocity would not be noticeably affected by this economization, particularly for the field points close to a propeller blade, since the induced velocity due to vortex is inversely proportional to the distance and the distance between blades is sufficiently far. Now, the Velocity Program calculates the field point velocity as a function of advance coefficient at the specified field points, by calculating the induced velocities from the individual source and vortex elements, and summing up all the contributions including inflow velocity. Also, the same economization scheme as in BVP program is

applied in calculating the contributions from other blades and wakes. In summary, the particular features of the present numerical scheme may be listed as follows:

1. Incorporation of roll-up procedure
2. Incorporation of contraction of slipstream
3. Boundary condition being satisfied on the camber surface (except thickness effect)
4. One point linear Kutta condition
5. Economization

VI. Comparison of Field Point Velocities between Theory and Experiment

Figures 87 through 142 show the field point velocities as measured and as calculated. To be fair enough, approximately equal number of Figures with good agreement and with less good agreement has been selected from over 200 comparisons made, and they are presented in order of upstream, very close to leading edge, very close to trailing edge and downstream for each four propellers. As shown in these Figures, the agreement at upstream field is always excellent for the propellers 4381, 4382 and 4383 and good for the propeller 4498. One exception is the discrepancy in minimum velocity as shown in Figures 88, 103, 129 and 131, as examples. This

difference is considered to come from both the imperfection of theory and the averaging process through Educator. Theory tends to exaggerate the effect of vortex, particularly when field points are closer to vortex segments, while slight change in propeller RPM caused either by torsional vibration of propeller shaft or by change of RPM in driving motor would chop off the sharp change in velocity through the averaging process*. This phenomenon can actually be seen if we visualize both the raw and averaged signal on the oscilloscope, as shown in Figure 143. In Figure 143, the upper figure is the raw signal directly from the signal processor (tracker) and the lower one is time-averaged signal through the Waveform Educator. The agreement in near field to propeller blade inside slipstream is generally good, or at least theory does nicely follow the experimental pattern. Here, it is emphasized that a particular care should be taken in making a numerical prediction of field point velocities inside the slipstream, particularly for the region from the trailing edge to the roll-up point. As indicated earlier, the numerical output is extremely sensitive to the location of field points due to the nature of Cauchy principal type integral equation. For the numerical prediction at arbitrary field points in

* This phenomenon was previously predicted by Prof. Ezekiel.

this region, therefore, it is strongly recommended that a series of initial calculations be made first at the geometric center of vortex grids and that proper interpolation be applied next. To find out the position of geometric center of vortex grids, a special program has been prepared, or the Velocity Program will print out both Cartesian and polar coordinates of these points with the proper indication of built-in option. Furthermore, experience reflects that the position of initial input field points (geometric center of vortex grids) should be as precise as at least five decimal places. This is one of limitations of present numerical scheme. In fact, most of velocity measurements inside the slipstream shown in the Figures in this section were made at the imaginary geometric center of vortex grids inside the tunnel for direct comparison with theory. The velocity prediction with present numerical scheme is getting worse with increasing axial distance from the propeller due to the presently adopted vortex wake model, that is, the helix of ultimate wake is treated as line segments instead of streamlines. However, the primary interest is in the velocity prediction at the near field to propeller blades. Far field velocity prediction is expected to be greatly improved when a new wake model*

* This model is being prepared by Prof. Kerwin.

is ready. So far, comparisons and discussions have been limited to the result of design condition. Even for off design conditions, considerable amounts of measurements (though much less than those for design condition) were made and some of them are shown in Figures 144 through 157 with calculated values for comparison. Although it is difficult to make general comments due to a limited number of comparisons, it seems that the agreement is still good for the moderately loaded condition($J=0.6$), but it becomes considerably worse for the heavily loaded condition($J \approx 0.3$). Specifically, measurement shows back flow around the tip region as shown in Figure 147 as an example, but theory does not predict this. The first impression is that present theory may not be adequate for the prediction of field point velocity at heavily loaded condition.

VII. Conclusions and Recommendations

Through this study, the following conclusions are made.

1. The application of LDA technique is quite successful. The previously virtually impossible measurement has essentially become a routine work. This technique can also be utilized in many different flow measurements as well as propeller measurement.

2. The slipstream radius may be a function of many factors such as loading condition, skew, rake, etc. For the present series of propellers, the ultimate slipstream radius almost linearly increases with increasing skew or increasing advance coefficient. With this study alone, however, it is not possible to derive a generally applicable relationship. This may be quite possible after investigating a wider variety of propellers with the variations including number of blades, initial geometry, blade area ratio, etc.
3. The ultimate hydrodynamic pitch and pitch angle seem to be basically determined by design pitch and pitch angle and affected very little by skew.
4. For all loading conditions, most of contraction of slipstream (approximately 90%) occurs within the axial distance of one radius from the propeller plane.
5. Roll-up occurs at the axial distance of 0.8-1.0 radius from the propeller tip for design condition. This axial position of roll-up for moderately loaded condition seems to be almost the same as for design condition, but that for heavily loaded condition is not clear.
6. From items 4 and 5, it can be concluded that there is a close relation between the position of roll-up and the con-

traction ratio of slipstream. More specifically speaking, the roll-up points are approximately the same as the positions of 90% contraction of slipstream.

7. The circulation distribution and strength obtained by BVP program are somewhat affected by input wake data such as axial position of roll-up, slipstream radius at roll-up point, hydrodynamic pitch and pitch angle, etc. Tests show that these variations of circulation distribution and strength have almost no effect on the overall propeller blade thrust and torque (output of PUF-2). However, field point velocity prediction is affected as same degree of the variations.

8. The calculated circulation strength is always higher than the experimentally determined strength. The difference is small and agreement is good for the plain propeller, but the difference becomes greater as skew increases. This result may explain the less good agreement in thrust between theory and experiment for highly skewed propellers.

9. The roughly estimated sectional drag coefficient based on experimental measurements becomes higher toward tip instead of getting lower. It is implied by this result that the incorporation of presently adopted sectional drag coefficient to the

numerical scheme may not be fully justified, even though the average value of estimated coefficient and presently adopted coefficient used in the theory are very close each other.

10. For the field point velocity, over 200 comparisons were made between theory and experiment. Most of them are for the design condition. From these comparisons, the following conclusion has been derived:

For the design condition, the agreement is always excellent for upstream and outside slipstream. For the near field inside the slipstream including points very close to trailing edge, the agreement is generally good, or at least theory nicely follows the experimental pattern. For far field inside slipstream, the agreement is not as good, but this region is not of much concern. For the moderately loaded condition, generally similar conclusion can be made to that for design condition. For the heavily loaded condition, the agreement is still not bad for upstream and near field inside slipstream (not very close to trailing edge), but considerably worse than that for design and moderately loaded conditions. Particularly, measurement shows rather strong back flow around tip, but theory does not predict this. The first impression is that present theory may not be adequate for the prediction of field point velocity for heavily loaded condition. However, it should be noted

that the above conclusions for moderately loaded and heavily loaded conditions are derived from a limited number of comparisons and may be treated as tentative ones.

11. The figures of field point velocity comparison for near field inside slipstream show rather regular parallel shift-up of the numerical results from measurements, which seems more strongly related to radial position than to axial position. This suggests that there may be a general correlation factor between measurement and present theory. With this idea, the correlation factor for the axial component of field point velocity has been briefly investigated and shown in Table 14. As shown in Table 14, the correlation factors for two different propellers at given radial positions are remarkably close(except in the immediate vicinity of the hub vortex) in spite of big difference in relative axial position from propeller blades. The factor shown in Table 4 (as a function of radial position) may be directly useful for this series of propellers, although the analysis discussed here is extremely simple.

With the above conclusions, it is recommended that further research be conducted in the following areas:

1. More investigation of the viscous effect

The author believe that it is worth carrying out more investigation for the viscous effect. The viscous effect seems to be greater for lower advance coefficient (higher loading condition), judging from blade boundary layer pattern. Furthermore, the relation between blade boundary layer and geometric characteristics, particularly skew, should be carefully studied. Due to centrifugal force, the particles tend to be pushed outward and, hence, boundary layer tends to be thicker toward tip. This phenomenon is particularly important for highly skewed propellers, since a considerable part of the leading edge may be already inside the boundary layer. The study of this effect may be the key to the solution of less good agreement problem in thrust between theory and experiment for highly skewed propellers. For effective investigation, the author recommends that a more realistic boundary layer pattern be first constructed by combining axial and tangential patterns and converting angular scale to linear scale, and that comparison of thus constructed patterns be made between plain and highly skewed propellers.

2. Correlation study

For the present series of propellers, correlation between theory and measurement has been briefly studied and a correlation factor has been derived as a function of radial position. It seems to be quite meaningful. However, it is not expected to be generally applicable. The accuracy of numerical prediction of field point velocities will be improved if further study on this subject is carried out to determine generally applicable relation between measurement and present theory.

3. Off-Design Condition

Most of the measurements and comparisons in this study are made for the design condition and the conclusion is that the agreement is good. However, it is difficult to make general conclusion for off-design condition. Therefore, further measurements and comparisons are recommended for off-design conditions, particularly for the heavily loaded condition, to investigate the applicability of the present numerical method for the prediction of field point velocity and to improve the theory.

4. Other Components of velocity

In this study, no comparison has been made for other components of velocity such as radial or tangential components. The radial component is usually considered to be small. However, measurement shows that this is not always true. Even for the design condition, almost the same order of free stream velocity was measured very close to blade and hub vortex. For the heavily loaded condition, the radial component is usually greater than free stream velocity very close to the suction side of the blades. Although the agreement between theory and measurement for axial component is good, that for the other components is not known. The comparison of the other components remains to be done.

References

1. Yeh, Y. & Cummings, H.Z., "Localized Flow Measurements with an He-Ne Laser Spectrometer", *Appl. Phys. Letters* 4, 176, 1964.
2. Goldstein, R.J. & Hagen, W.F., "Turbulent Flow Measurements Utilizing the Doppler Shift of Scattered Laser Radiation", *Phys. Fluids* 10, 1349, 1967.
3. Welch, N.E. & Tomme, W.J., "Analysis of Turbulence from Data Obtained with a Laser Velocimeter", *AIAA Paper No. 67-179*, 1967.
4. Pike, E.R., Jackson, D.A., Bourke, P.J. & Page, D.I., "Measurement of Turbulent Velocities from the Doppler Shift in Scattered Laser Light", *J. Phys. E:Sci. Instrum.* 1, 111, 1968.
5. Durst, F. & Whitelaw, J.H., "Integrated Optical Units for Laser Anemometry", *J. Phys. E:Sci. Instrum.* 4, 804, 1971.
6. Durst, F. & Whitelaw, J.H., "Measurements of Mean Velocity, Fluctuating Velocity and Shear Stress Using a Single Channel Anemometer", *DISA Inf.* 12, 11, 1971.
7. Born, M. & Wolf, E., "Principles of Optics", Pergamon Press, Oxford, 1970.
8. Kerker, M., "The Scattering of Light and Other Electromagnetic Radiation", Academic Press, New York, 1969.
9. Laser Anemometry ...
Theory, Application and Technique,
Thermo-Systems, Inc., 1977.

10. Durst, F. & Whitelaw, J.H., "Optimization of Optical Anemometers", Proc. Roy. Soc. A324, 157, 1971.
11. Durst, F. & Whitelaw, J.H., "Light Source and Geometrical Requirements for the Optimization of Optical Anemometry Signals", Opto-Electronics 5, pp. 137-151, 1973.
12. Berman, N.S., "Fluid Particle Considerations in the Laser Doppler Velocimeter", Arizona State University, Tempe, Report ERC-R-73017, 1972.
13. Berman, N.S., "Particle-Fluid Interaction Corrections for Flow Measurements with a Laser Doppler Flow Meter", NASA CR 124254, 1973.
14. Mayo, W.T., Shay, M.T. & Riter, S., "Digital Estimation of Turbulence Power Spectra from Burst Counter LDV Data", Proc. of 2nd Int. Workshop on Laser Velocimetry, Purdue University, 1, 16, 1974.
15. Edwards, R.V., Angus, J.C., French, M.J. & Dunning, J.W.Jr., "Spectral Analysis of the Signal from the Laser Doppler Flow Meter: Time-Independent Systems", J. Appl. Phys. 42, 837, 1971.
16. George, W.K. & Lumley, J.L., "The Laser-Doppler Velocimeter and its Application to the Measurement of Turbulence", Journal of Fluid Mechanics, Vol. 60, pp. 321-362, 1973.
17. Van Maanen, H.R.E., "Reduction of Ambiguity Noise in Laser Doppler Velocimeter by a Cross Correlation Technique", presented at LDA Symposium, Technical University of Denmark, 1975.

AD-A060 722 MASSACHUSETTS INST OF TECH CAMBRIDGE DEPT OF OCEAN E--ETC F/G 13/10
NUMERICAL AND EXPERIMENTAL METHODS FOR THE PREDICTION OF FIELD --ETC(U)
JUN 78 K MIN

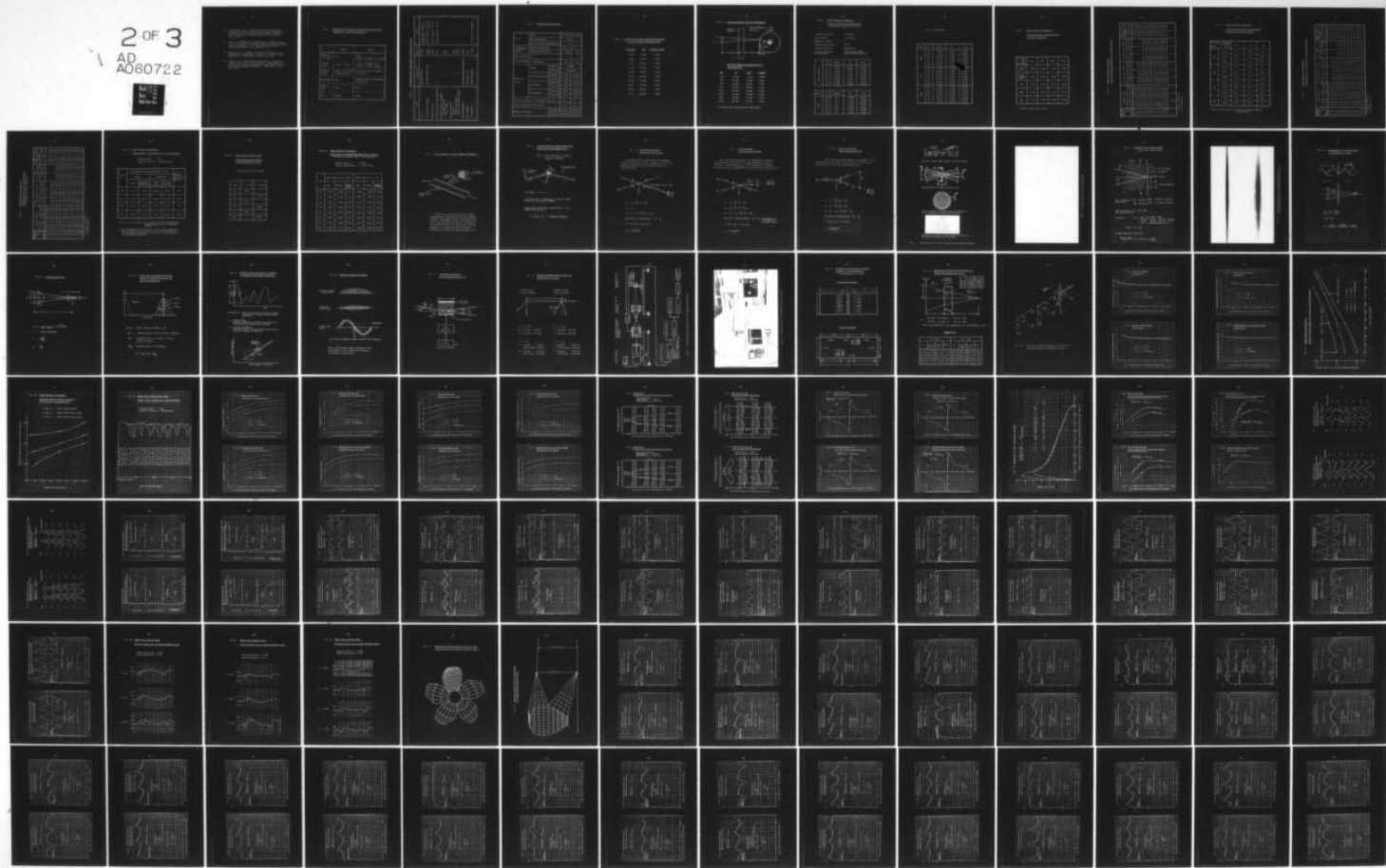
UNCLASSIFIED

OE-78-12

N00014-76-C-0357

NL

2 OF 3
AD
A060722



18. George, W.K., Jr., "The Measurement of Turbulence Intensities using Real-Time Laser Doppler Velocimeter", Proceedings of the Second International Workshop on Laser Velocimeter, Perdue University, pp. 511-520, March, 1974.
19. Min, K., "Numerical and Experimental Method of Prediction of Field Point Velocities around a Propeller Blade", Research Proposal, to the Department Headquarters of Ocean Engineering, M.I.T., March, 1977.
20. Boswell, R.J., "Design, Cavitation Performance, and Open-Water Performance of a Series of Research Skewed Propellers", NSRDC Report 3339, March, 1971.
21. Nelka, J.J., "Experimental Evaluation of a Series of Skewed Propellers with Forward Rake : Open-Water Performance, Cavitation Performance, Field-Point Pressures and Unsteady Propeller Leading", NSRDC Report 4113, July, 1974.

Table 1 Comparison of Two Most Common Signal Processing Techniques - Tracker and Counter

	Tracker	Counter
Required S/N ratio	Low	High (lowered by proper filtering)
Dynamic Range	2 KH _Z - 50 MH _Z	1 KH _Z - 100 MH _Z if not limited by input filters
Capture Range	10% of full scale tracking range	not exist if not limited by filters
Slew Rate	Good	Limited only by processing time (1 μ s)
Ease of Use	Good	Fair
Cost	Medium	High

Table 2 MIT Watertunnel Laser-Doppler Anemometer System

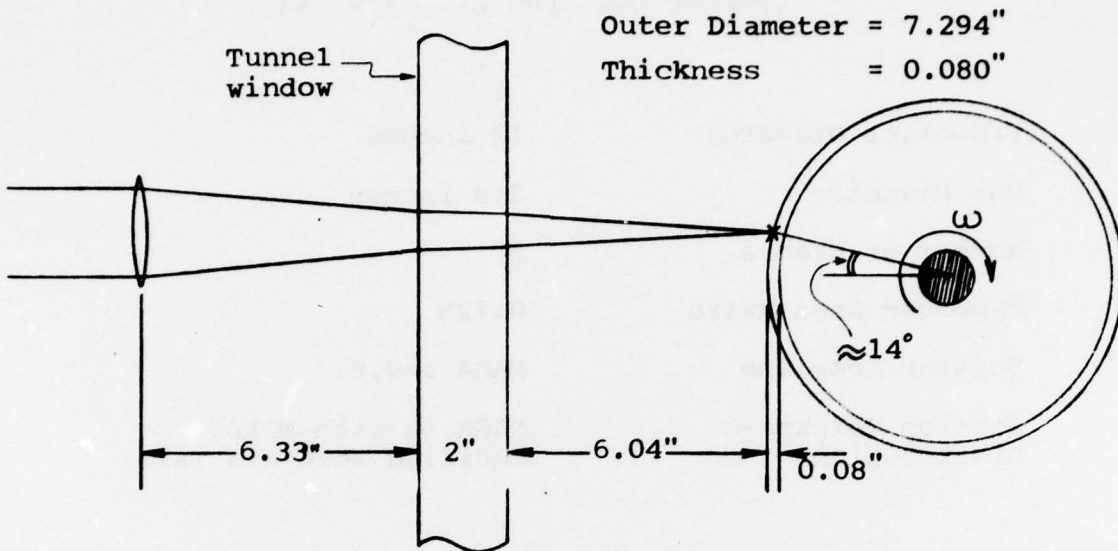
Item	Manufacturer	Model No.	Remark
Laser	Spectra Physics	124A	He-Ne Laser (15 mw) Wavelength = 632.8 nm
Transmitting Lenses	Thermo-Systems, Inc.	918F 919V	Focal Length = 309 mm 481 mm
Receiving Lens	"	938B	Focal Length = 310 mm
Scattered Light Focusing Lens	"	935	Focal Length = 200 mm
Photomultiplier Assembly	"	962	
Photomultiplier	"	965	
Power Supply	"		
Signal Processor	"	1090	
Tracker	"	1057	
Signal Conditioner	"	1091	
Monitor and Power Supply	"		
Waveform Educter	Princeton Applied Research	TDH-9	
Oscilloscope	Tektronix, Inc.	561B	
X-Y Recorder	Hewlett Packard	7044A	25 cm x 40 cm Maximum

Table 3 Optical Characteristics

Lasef	Type	15 mw He-Ne laser		
	Wave Length(nm)	632.8		
	Initial Beam Diameter(D_2 ,mm)	1.1		
Transmitting (focusing) lenses	Focal Distance(mm)	309	481	
	Crossing Angle(deg.)	8.88	5.72	
Beam Spacing(mm)		50		
Distance between Fringes(μm)		4.087	6.341	
Measuring Volume	Shape	Geometric	Diamond	
		Effective	Ellipsoid	
	Beam Diameter(mm)	Geometric	0.556	
		Effective	0.226	
	Length(mm)	Geometric	7.309	
		Effective	2.924	
	Diameter(mm)	Geometric	0.568	
		Effective	0.227	
Effective Number of Fringes(nearest 100)		100	100	
Actual Aperture Diameter(mm)		0.25	0.15	
Doppler Frequency	MHz/MPS	0.24467	0.15770	
	MHz/fps	0.07458	0.04807	

Table 4 Tunnel Free Stream Velocity Measurement
by Two Different Methods(ft/sec)

<u>Manometer</u>	<u>LDA</u>	<u>Manometer/LDA</u>
9.00	9.049	0.995
11.34	11.378	0.997
13.05	13.067	0.999
13.73	13.762	0.998
14.44	14.376	1.004
16.70	16.695	1.000
17.28	17.194	1.005
18.62	18.528	1.005
19.66	19.527	1.007
20.77	20.647	1.006

Table 5 Calibration Rotor and its Arrangement

Rotating Speed Measurement(ft/sec)
and Comparison

<u>RPM</u>	<u>$R\omega$</u>	<u>LDA*</u>	<u>$LDA/R\omega$</u>
250	8.644	8.713	1.008
500	17.287	17.264	0.999
750	25.931	25.977	1.002
1000	34.575	34.600	1.001
1250	43.219	43.028	0.996
1500	51.862	51.098	0.985
1750	60.506	55.624	0.919
2000	69.150	59.294	0.857

* Corrected for 14 degree off angle effect

Table 6 NSRDC Research Propellers

Principal Design Characteristics
 (Reproduced from [20] and [21])

Propeller Diameter	12 inches
Hub Diameter	2.4 inches
Number of Blades	5
Expanded Area Ratio	0.725
Section Meanline	NACA $a=0.8$
Section Thickness Distribution	NACA 66 with NSRDC modified Nose and Tail

Basic Geometry	r/R	$\tan \beta_i$	C/D	t_o/C
	0.2	1.8256	0.174	0.2494
	0.3	1.3094	0.229	0.1562
	0.4	1.0075	0.275	0.1068
	0.5	0.8034	0.312	0.0768
	0.6	0.6483	0.337	0.0566
	0.7	0.5300	0.347	0.0421
	0.8	0.4390	0.334	0.0314
	0.9	0.3681	0.280	0.0239

Prop.	r/R	θ_s (deg.)	P/D	f_o/C
4381	0.3	0.0	1.3448	0.0368
	0.4	0.0	1.3580	0.0348
	0.5	0.0	1.3361	0.0307
	0.6	0.0	1.2797	0.0245
	0.7	0.0	1.2099	0.0191
	0.8	0.0	1.1366	0.0148
	0.9	0.0	1.0660	0.0123

Table 6 (continued)

Prop.	r/R	θ_s (deg.)	P/D	f_o/c
4382	0.3	4.655	1.4332	0.0370
	0.4	9.363	1.4117	0.0344
	0.5	13.948	1.3613	0.0305
	0.6	18.378	1.2854	0.0247
	0.7	22.747	1.1999	0.0199
	0.8	27.145	1.1111	0.0161
	0.9	31.575	1.0270	0.134
4383	0.3	9.293	1.5124	407
	0.4	18.816	1.4588	0.0385
	0.5	27.991	1.3860	0.0342
	0.6	36.770	1.2958	0.0281
	0.7	45.453	1.1976	0.0230
	0.8	54.245	1.0959	0.0189
	0.9	63.102	0.9955	0.0159
4498	0.3	9.293	1.5124	0.0407
	0.4	18.816	1.4588	0.0385
	0.5	27.991	1.3860	0.0342
	0.6	36.770	1.2958	0.0281
	0.7	45.453	1.1976	0.0230
	0.8	54.245	1.0959	0.0189
	0.9	63.102	0.9955	0.0159

Table 7 NSRDC Research PropellersSome Performance Characteristics
at Design Condition

Prop. No. Charact.	4381	4382	4383	4498
Advance Coeff.	0.889	0.889	0.889	0.889
Thrust Loading Coeff.	0.686	0.686	0.686	0.686
K_T^*	0.208	0.218	0.231	0.246
$10K_Q^*$	0.419	0.441	0.472	0.536
η_p	0.702	0.699	0.692	0.649

* NSRDC revised test result.

Table 8 NSRDC Research Propellers

Slipstream Radius(Fraction of Prop. Radius)

Prop. No.	4381(No skew)				4382(36 deg. skew)				4383(72 deg. skew)				4498(72 deg. skew & No rake - warped)	
	-x/R	J	0.322	0.600	0.889*	0.285	0.600	0.889*	0.252	0.600	0.889*	0.600	0.889*	
0.05	0.932	0.944	0.948	-	-	-	-	-	-	-	-	0.966	0.972	
0.10	0.913	0.927	0.932	-	-	-	-	-	-	-	-	0.952	0.958	
0.20	0.889	0.905	0.914	0.964	0.972	0.978	-	-	-	-	-	0.934	0.940	
0.30	0.872	0.891	0.902	0.930	0.946	0.957	-	-	-	-	-	0.921	0.927	
0.40	0.858	0.880	0.893	0.909	0.928	0.939	0.964	0.969	0.978	0.978	0.978	0.911	0.917	
0.50	0.847	0.872	0.886	0.892	0.913	0.926	0.938	0.943	0.953	0.953	0.953	0.903	0.910	
0.60	0.837	0.865	0.880	0.880	0.902	0.915	0.923	0.930	0.940	0.940	0.940	0.897	0.905	
0.80	0.823	0.856	0.870	0.861	0.884	0.898	0.904	0.911	0.919	0.919	0.919	0.888	0.898	
1.00	0.814	0.849	0.863	0.848	0.871	0.886	0.892	0.900	0.913	0.913	0.913	0.883	0.894	
1.25	0.806	0.843	0.857	0.839	0.861	0.877	0.882	0.891	0.906	0.906	0.906	0.879	0.891	
1.50	0.801	0.838	0.853	0.835	0.856	0.873	0.877	0.886	0.902	0.902	0.902	0.877	0.890	
1.75	0.798	0.835	0.851	0.832	0.854	0.871	0.874	0.884	0.899	0.899	0.899	0.876	0.890	
2.00**	0.796	0.832	0.849	0.830	0.853	0.871	0.872	0.882	0.898	0.898	0.898	0.876	0.890	
2.50**	0.795	0.830	0.848	0.828	0.852	0.870	0.870	0.881	0.898	0.898	0.898	0.875	0.890	

* Design Condition

** Extrapolation

Table 9 NSRDC Research Propellers

Percent Contraction of Slipstream*
at Different Axial Position

Prop. No.	Axial Distance from the Tip J	0.2R	0.5R	1.0R
4381	0.322	54.1	74.6	90.7
	0.600	55.9	75.3	88.8
	0.889	56.6	75.0	90.1
4382	0.285	52.1	75.4	92.6
	0.600	48.2	72.3	92.7
	0.889	45.5	71.9	93.4
4383	0.252	55.1	77.1	92.6
	0.600	55.6	77.7	93.8
	0.889	54.6	79.2	94.1
4498	0.600	52.8	77.6	93.6
	0.889	54.5	81.8	96.4

* Basis of Percentage : total(or ultimate) amount
of contraction.

Table 10 NSRDC Research Propellers

Hydrodynamic Pitch Angle of Tip Vortices(deg.)

Prop. No.	4381(No skew)			4382(36 deg. skew)			4383 (72 deg. skew)			4498(72 deg. skew & No rake - warped)		
	J	0.322	0.600	0.889*	0.285	0.600	0.889*	0.600	0.889*	0.600	0.889*	
-x/R	0.05	12.31	15.06	16.89	-	-	-	-	-	15.28	17.26	
	0.10	12.86	15.38	17.27	-	-	-	-	-	15.77	17.71	
	0.20	13.81	15.99	17.80	13.43	15.65	16.90	-	-	16.57	18.43	
	0.30	14.53	16.51	18.24	14.23	16.24	17.61	-	-	17.18	19.04	
	0.40	15.11	16.97	18.62	14.88	16.78	18.29	15.86	16.80	17.68	19.56	
	0.50	15.60	17.37	18.96	15.39	17.22	18.70	15.68	17.77	18.08	19.98	
	0.60	16.04	17.77	19.29	15.82	17.63	19.18	17.27	18.47	18.41	20.29	
	0.70	16.43	18.11	19.69	16.19	17.97	19.51	17.74	18.99	18.70	20.54	
	0.80	16.81	18.45	19.86	16.49	18.28	19.81	18.12	19.40	18.91	20.73	
	1.00	17.49	19.06	20.35	16.94	18.75	20.34	18.58	20.02	19.21	21.00	
	1.25	18.12	19.59	20.83	17.36	19.21	20.86	19.01	20.52	19.46	21.21	
	1.50	18.48	19.97	21.21	17.61	19.53	21.21	19.27	20.80	19.60	21.29	
	1.75	18.70	20.19	21.51	17.78	19.72	21.39	19.39	20.98	19.67	21.30	
	2.00**	18.82	20.32	21.68	17.89	19.84	21.45	19.46	21.08	19.70	21.30	
	2.50**	18.90	20.40	21.70	18.00	19.90	21.50	19.50	21.10	19.70	21.30	

* Design Condition

** Extrapolation

Table 11 NSRDC Research Propellers

Hydrodynamic Pitch of Tip Vortices
 (Fraction of Prop. Diameter)

Prop. No.	4381 (No skew)			4382 (36 deg. skew)			4383 (72 deg. skew)			4498 (72 deg. skew & No rake - warped)		
	J	0.322	0.600	0.889*	0.285	0.600	0.889*	0.600	0.889*	0.600	0.889*	0.889*
-x/R												
0.05	0.639	0.798	0.904	—	—	—	—	—	—	—	—	—
0.10	0.655	0.801	0.901	—	—	—	—	—	—	0.845	0.961	0.984
0.20	0.687	0.814	0.922	0.723	0.855	0.934	—	—	—	0.873	0.984	1.005
0.30	0.710	0.829	0.934	0.741	0.865	0.955	—	—	—	0.894	1.012	1.024
0.40	0.728	0.844	0.945	0.756	0.878	0.971	0.865	0.928	0.960	0.926	1.039	1.051
0.50	0.743	0.857	0.956	0.767	0.889	0.984	0.888	0.939	0.986	0.939	1.049	1.060
0.60	0.756	0.871	0.966	0.779	0.898	0.996	0.908	0.956	0.996	0.956	1.068	1.078
0.70	0.769	0.884	0.977	0.789	0.908	1.007	0.924	1.006	0.949	1.006	1.066	1.076
0.80	0.781	0.922	0.987	0.798	0.917	1.017	0.936	1.017	0.956	1.017	1.068	1.078
1.00	0.806	0.922	1.006	0.808	0.929	1.032	0.950	1.045	0.967	1.045	1.066	1.076
1.25	0.828	0.943	1.026	0.824	0.942	1.050	0.964	1.065	0.983	1.065	1.086	1.090
1.50	0.842	0.957	1.040	0.832	0.952	1.064	0.973	1.077	0.981	1.077	1.090	1.093
1.75	0.849	0.965	1.052	0.839	0.962	1.071	0.977	1.083	0.983	1.083	1.093	1.096
2.00*	0.852	0.968	1.060	0.842	0.967	1.075	0.979	1.087	0.984	1.087	1.094	1.097
2.50*	0.855	0.970	1.060	0.845	0.969	1.077	0.980	1.089	0.984	1.089	1.094	1.097

* Design Condition

** Extrapolation

Table 12 NSRDC Research PropellersComparison of Circulation by Different Methods

Propeller RPM = 900

Advance Coeff.(J) = 0.889(Design)

Prop. No.	Nondimensional Circulation(G) × 1000				% Diff.* between PUF-2 and Exp.(Vort. Integ.)	
	Theory		Experiment			
	PUF-2	Lifting** Line(Lerbs Criterion)	Integ. of Vorticity	Initial slope of Tang. Vel.		
4381	12.32	10.12	11.94	10.44	3.16	
4382	12.46	10.68	11.98	10.34	4.01	
4383	12.66	11.24	12.03	11.60	5.24	
4498	12.77	12.04	12.14	11.81	5.19	

* Basis of Percentage : Circulation Strength determined by Experiment(Vorticity Integration Method)

** With measured thrust as input. Since these propellers have unloaded tips relative to the Lerbs' optimum, the latter would be expected to result in a lower value of the maximum circulation.

Table 13 NSRDC Prop. 4381(No skew)

Estimated Blade Sectional
Drag Coefficient($\times 10^3$)

Advance Coeff.(J) = 0.889

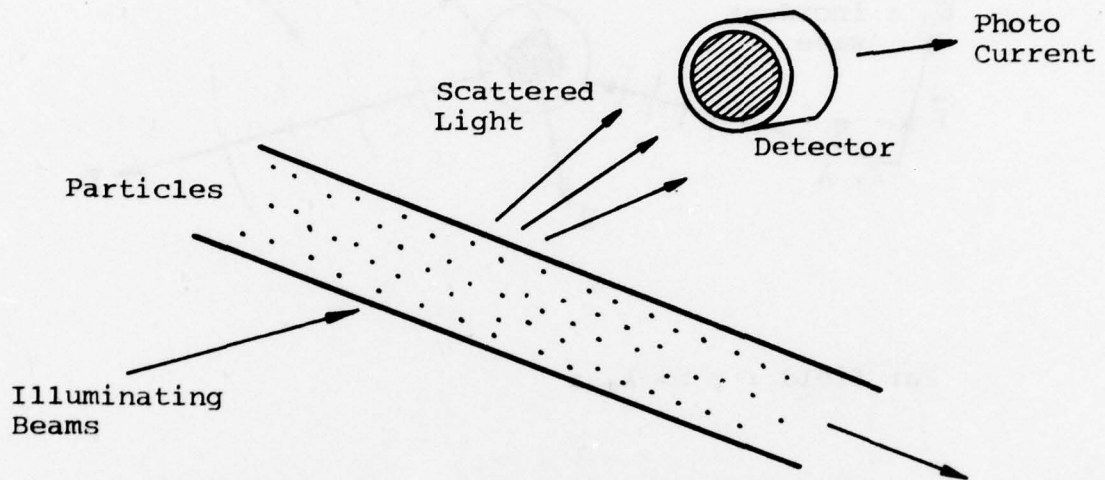
r/R	$x = -0.3R$	$x = -0.4R$
0.3	5.361	-
0.4	-	7.120
0.5	7.621	-
0.6	-	8.291
0.7	9.223	-
0.8	-	10.959

Table 14 NSRDC Research PropellersComparison of Nondimension Mean Axial Velocity
(Correlation between Theory and Experiment)

Advance Coeff.(J) = 0.889

Speed of Advance(V_a) = 13.335 ft/sec

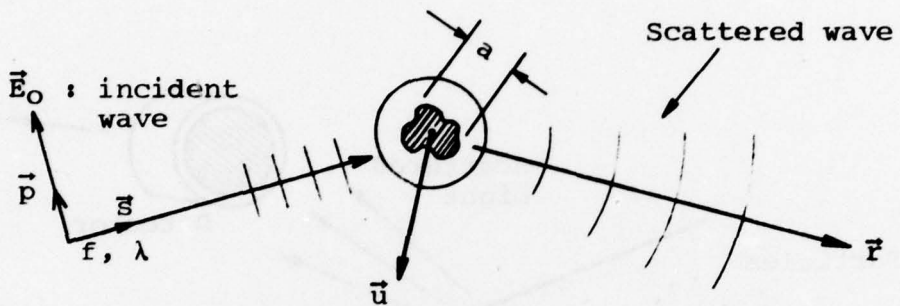
r/R	Prop. 4381 at $x = -0.4R$			Prop. 4383 at $x = -0.5R$		
	Exp.	Theory	<u>Exp.</u> <u>Theory</u>	Exp.	Theory	<u>Exp.</u> <u>Theory</u>
0.1	0.187	1.394	0.13	0.389	1.399	0.28
0.2	0.986	1.392	0.71	1.009	1.399	0.72
0.3	1.185	1.386	0.86	1.178	1.398	0.84
0.4	1.282	1.382	0.93	1.258	1.387	0.91
0.5	1.328	1.378	0.96	1.302	1.385	0.94
0.6	1.338	1.374	0.97	1.324	1.379	0.96
0.7	1.314	1.345	0.98	1.324	1.365	0.97
0.8	1.252	1.266	0.99	1.294	1.304	0.99

Fig. 1 Basic Concept of Laser-Doppler Anemometry

Light waves scattered from the illuminating beams by moving particles are Doppler shifted. The Doppler shift information, and hence the velocity information is contained in the photo current of the detector and the problem is to relate the photo current to the particle velocities, beam geometry, etc.

Fig. 2 General Relation between Scattered Light Waves and Doppler Shift

Ref. : Born and Wolf in 1970[7]
Kerker in 1969[8]



Far field : $r \gg \lambda, a$

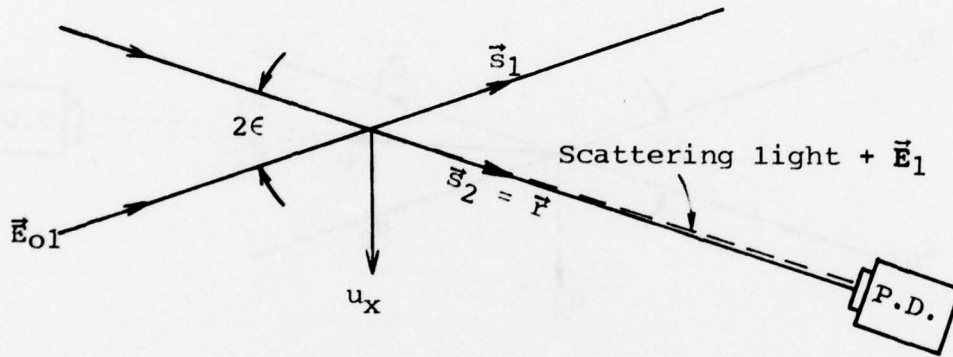
Scattered wave is spherical in the far field
(true for any particle shape.)

Light waves scattered in direction of \vec{r} are
Doppler shifted by :

$$\Delta f = \frac{\vec{u}}{\lambda} \cdot (\vec{r} - \vec{s}) : \text{Doppler frequency}$$

Fig. 3 Reference Beam Mode
Basic Detection Method

Reference beam method compares the Doppler shifted frequency of light scattered from an illuminating beam with the unshifted light of a reference beam.



$$f_1 = f_o + \frac{\vec{u}}{\lambda} \cdot (\vec{r} - \vec{s}_1)$$

$$f_2 = f_o$$

$$f_o = f_1 - f_2 = \frac{\vec{u}}{\lambda} \cdot (\vec{r} - \vec{s}_1)$$

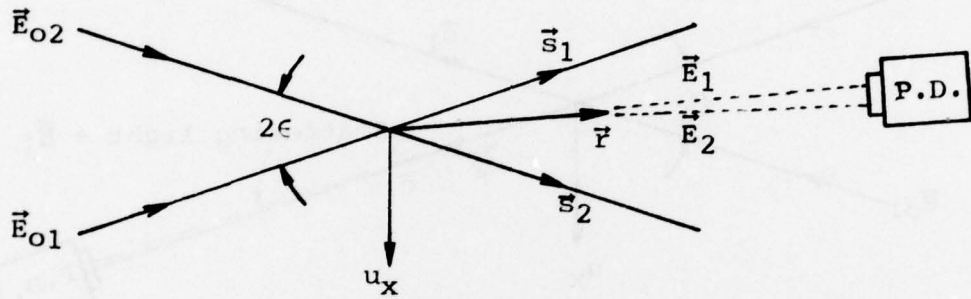
Direction of Measurement : $\vec{r} - \vec{s}_1$

$$\vec{u} \cdot (\vec{r} - \vec{s}_1) = 2 u_x \sin \epsilon$$

$$\therefore f_D = \frac{2 u_x \sin \epsilon}{\lambda}$$

Fig. 4 Dual Beam Mode
Basic Detection Method

Dual beam method compares the frequencies of Doppler shifted waves scattered in the same direction from two different illuminating waves. The difference or Doppler frequency, f_D , is independent of the direction of observation.



$$f_1 = f_o + \frac{\vec{u}}{\lambda} \cdot (\vec{r} - \vec{s}_1)$$

$$f_2 = f_o + \frac{\vec{u}}{\lambda} \cdot (\vec{r} - \vec{s}_2)$$

$$f_D = f_1 - f_2 = \frac{\vec{u}}{\lambda} \cdot (\vec{s}_2 - \vec{s}_1)$$

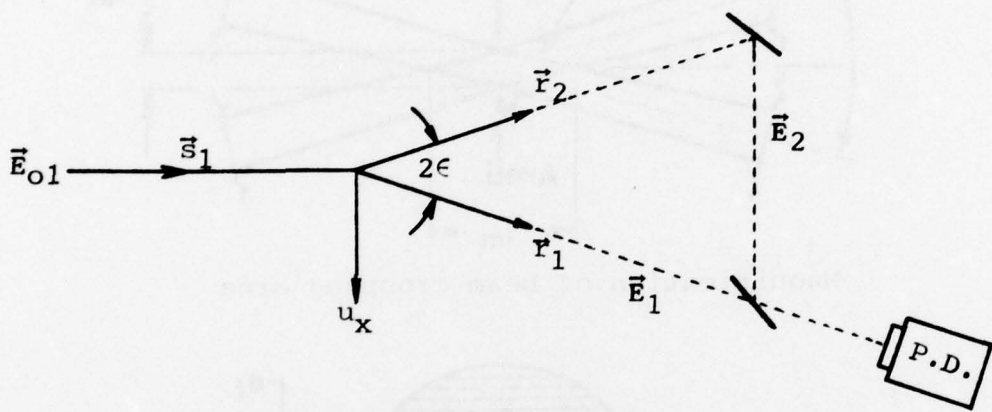
Direction of Measurement : $\vec{s}_2 - \vec{s}_1$ (independent of the direction of observation)

$$\vec{u} \cdot (\vec{s}_2 - \vec{s}_1) = 2 u_x \sin\epsilon$$

$$\therefore f_D = \frac{2 u_x \sin\epsilon}{\lambda}$$

Fig. 5 Dual Scatter Mode
Basic Detection Method

Dual scatter method compares the Doppler shifted frequencies of two light waves scattered in different directions from the same illuminating wave.



$$f_1 = f_o + \frac{\vec{u}}{\lambda} \cdot (\vec{r}_1 - \vec{s}_1)$$

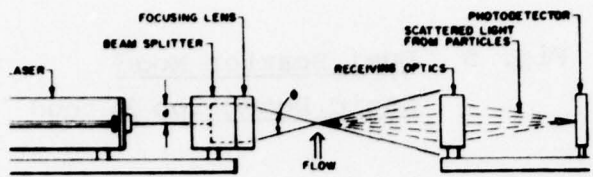
$$f_2 = f_o + \frac{\vec{u}}{\lambda} \cdot (\vec{r}_2 - \vec{s}_1)$$

$$f_D = f_1 - f_2 \approx \frac{\vec{u}}{\lambda} \cdot (\vec{r}_1 - \vec{r}_2)$$

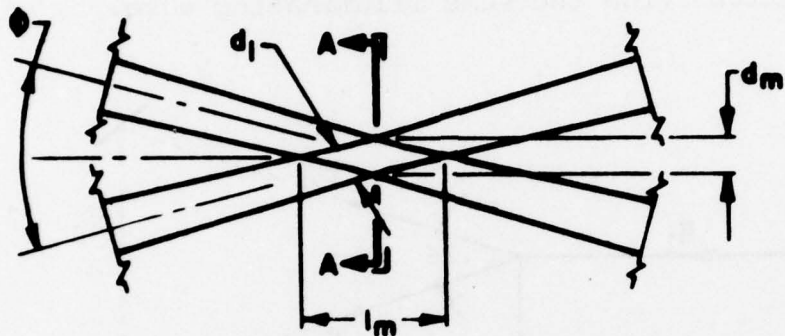
Direction of Measurement : $\vec{r}_1 - \vec{r}_2$

$$\vec{u} \cdot (\vec{r}_1 - \vec{r}_2) = 2 u_x \sin\epsilon$$

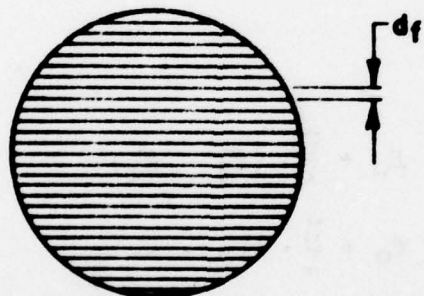
$$\therefore f_D = \frac{2 u_x \sin\epsilon}{\lambda}$$



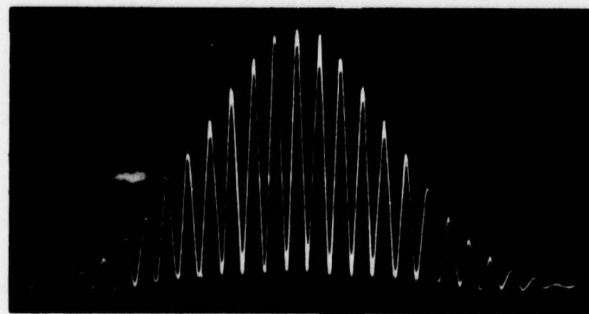
Set up of dual beam forward scattering mode



Magnification of beam crossing area



Light intensity distribution at section A-A'
(Fringe pattern at beam crossing point)



Amplitude variation in the beam crossing area
(Gaussian intensity distribution)

Fig. 6 Characteristics of Dual Beam Forward Scattering Mode

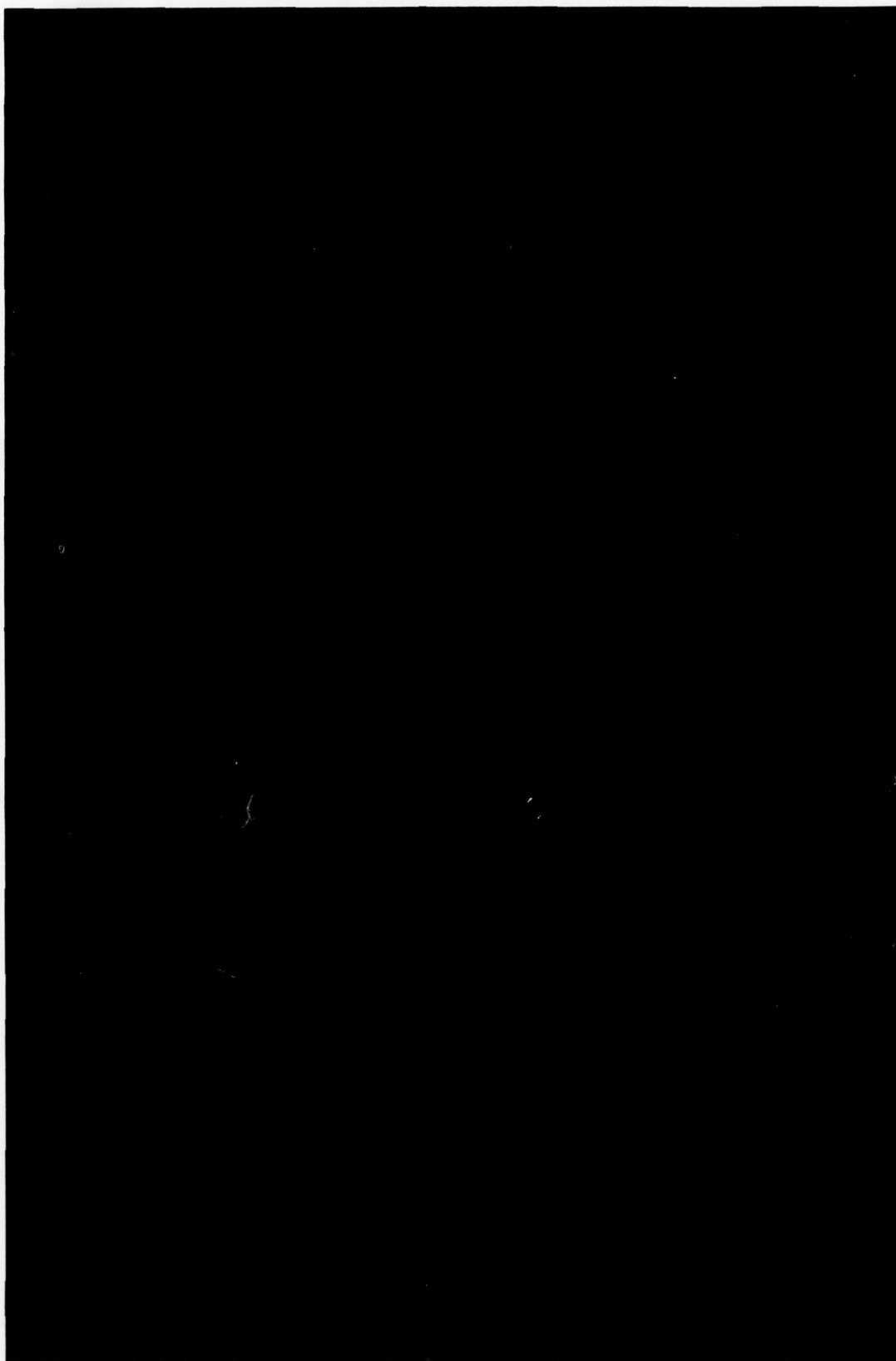
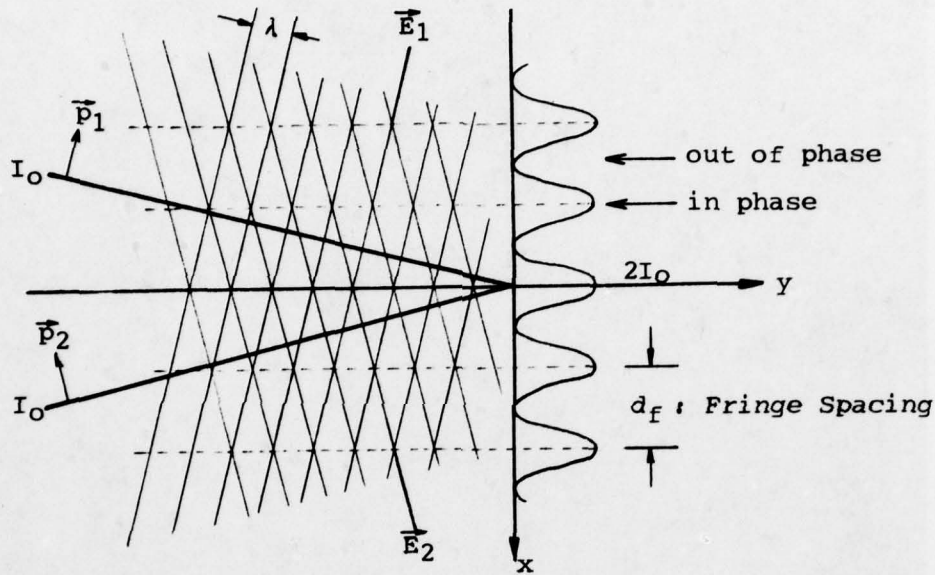


Fig. 7 Fringe Pattern of Dual Beam Mode

Fig. 8 Generation of Fringe Pattern
(light wave interference)



Two interfering : $\vec{E}_1 = \sqrt{I_0} \vec{p}_1 e^{i[\omega t - k(x\cos\epsilon + y\sin\epsilon)]}$
light waves $\vec{E}_2 = \sqrt{I_0} \vec{p}_2 e^{i[\omega t - k(-x\cos\epsilon + y\sin\epsilon)]}$

Electric Vector : $\vec{E} = \vec{E}_1 + \vec{E}_2$
(by superposition)

Intensity : $I(x) = (\vec{E}_1 + \vec{E}_2) \cdot (\vec{E}_1^* + \vec{E}_2^*)$
 $= \vec{E}_1 \cdot \vec{E}_1^* + \vec{E}_2 \cdot \vec{E}_2^* + \vec{E}_1 \cdot \vec{E}_2^* + \vec{E}_2 \cdot \vec{E}_1^*$
 $= 2I_0 [1 + \vec{p}_1 \cdot \vec{p}_2 \cos(2kx\sin\epsilon)]$

where $k = 2\pi/\lambda$

Fringe Spacing is given by,

$$\frac{4\pi d_f \sin\epsilon}{\lambda} = 2\pi \longrightarrow d_f = \frac{\lambda}{2 \sin\epsilon}$$

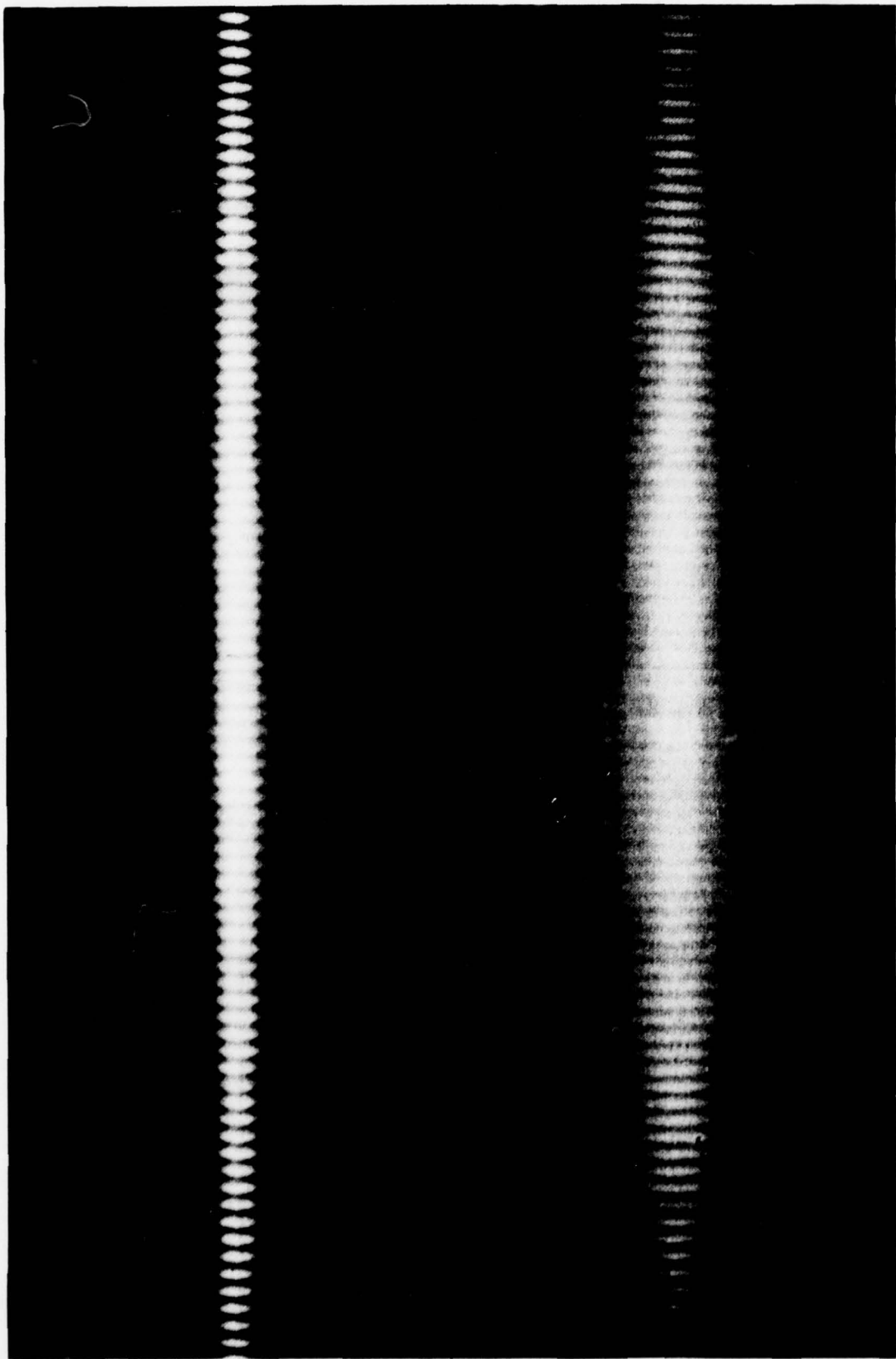
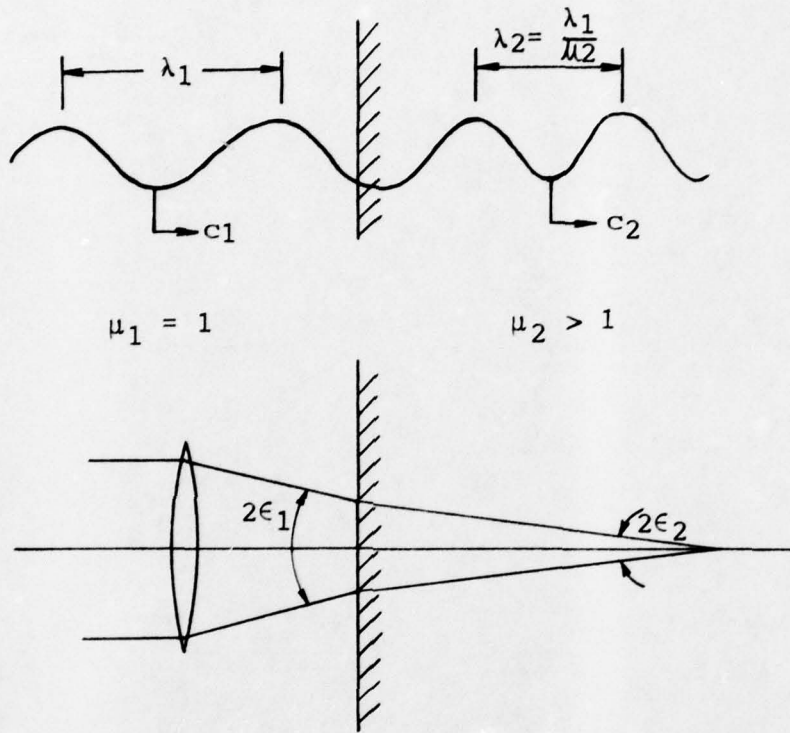


Fig. 9 Oscilloscope Trace of Particle Traversing
Measuring Volume(Typical Photodetector Output)

Fig. 10 Independency of Fringe Spacing
on the Refractive Index



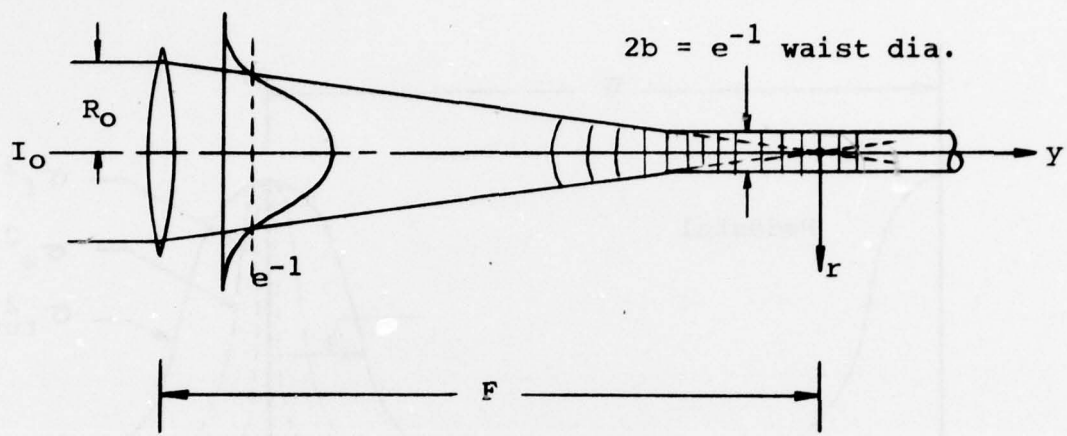
$$\mu_1 = 1$$

$$\mu_2 > 1$$

$$\frac{\mu_2}{\mu_1} = \frac{c_1}{c_2} = \frac{\sin \epsilon_1}{\sin \epsilon_2}$$

$$\mu_1 \lambda_1 = \mu_2 \lambda_2$$

$$d_f = \frac{\lambda_2}{2 \sin \epsilon_2} = \frac{\lambda_1 / \mu_2}{2 \sin \epsilon_1 / \mu_2} = \frac{\lambda_1}{2 \sin \epsilon_1}$$

Fig. 11 Focused Laser Beam

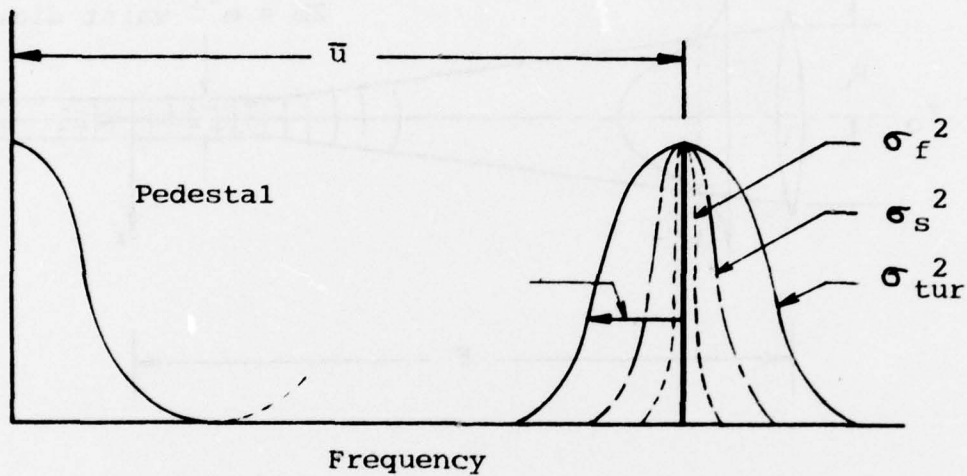
$$I(r) = \frac{P}{\pi(b^2 + \alpha^2 y^2)} e^{-\frac{r^2}{b^2 + \alpha^2 y^2}}$$

P = total beam power

$$b = \frac{F\lambda}{2\pi R_o}$$

$$\alpha = \frac{R_o}{F}$$

Fig. 12 Basic Idea of Signal Processing
Method of Spectrum Analyzer and
Spectrum Broadening



— : "Ideal" signal in laminar flow

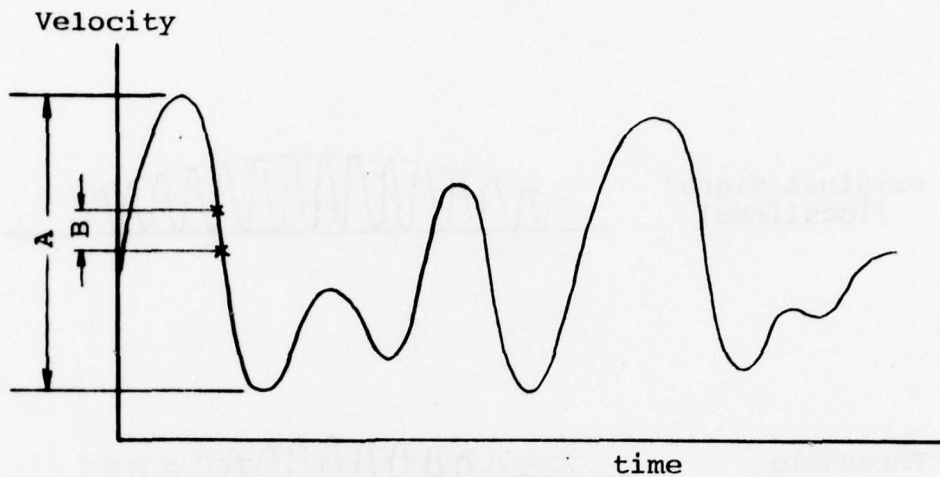
σ_f^2 : Broadening due to finite filter bandwidth

σ_s^2 : Broadening due to a signal of finite length and noise

σ_{tur}^2 : Broadening due to turbulence

$$\sigma^2 = \sigma_f^2 + \sigma_s^2 + \sigma_{tur}^2$$

**Fig. 13 Dynamic Range and Capture Bandwidth
of Tracker Type Signal Processors**



Assumption : Ideal system where system is always following the signal properly (high slew rate)

A = Dynamic Range
(maximum change in velocity the system can follow with no manual range change)

B = $\frac{1}{2}$ Capture Bandwidth
(maximum velocity change between data points that the system can measure)

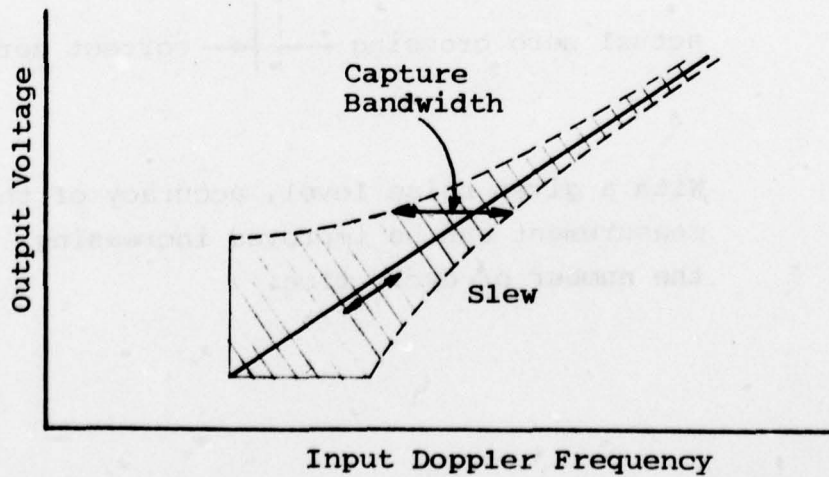
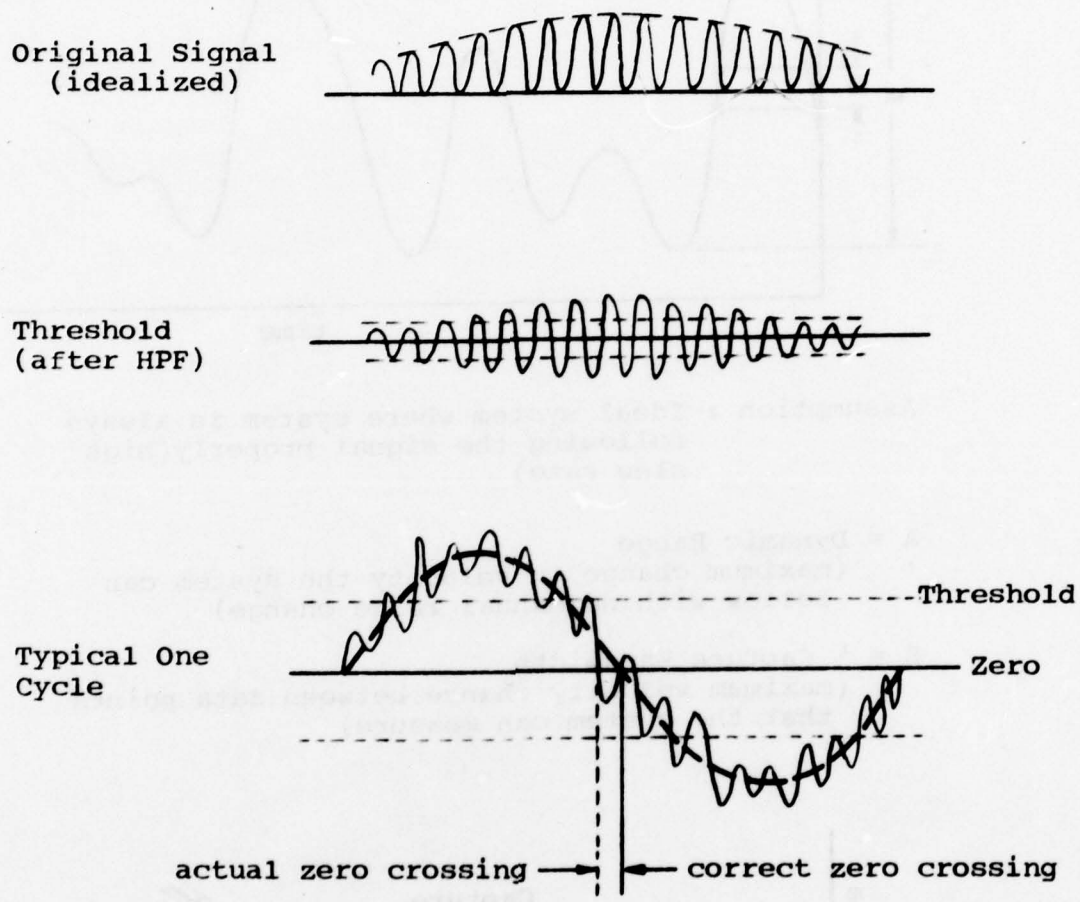


Fig. 14 Effect of Noise on Counter



With a given noise level, accuracy of the measurement can be improved increasing the number of cycle time.

Fig. 15 Frequency Shifting by
Acousto-Optics(Bragg) Cell

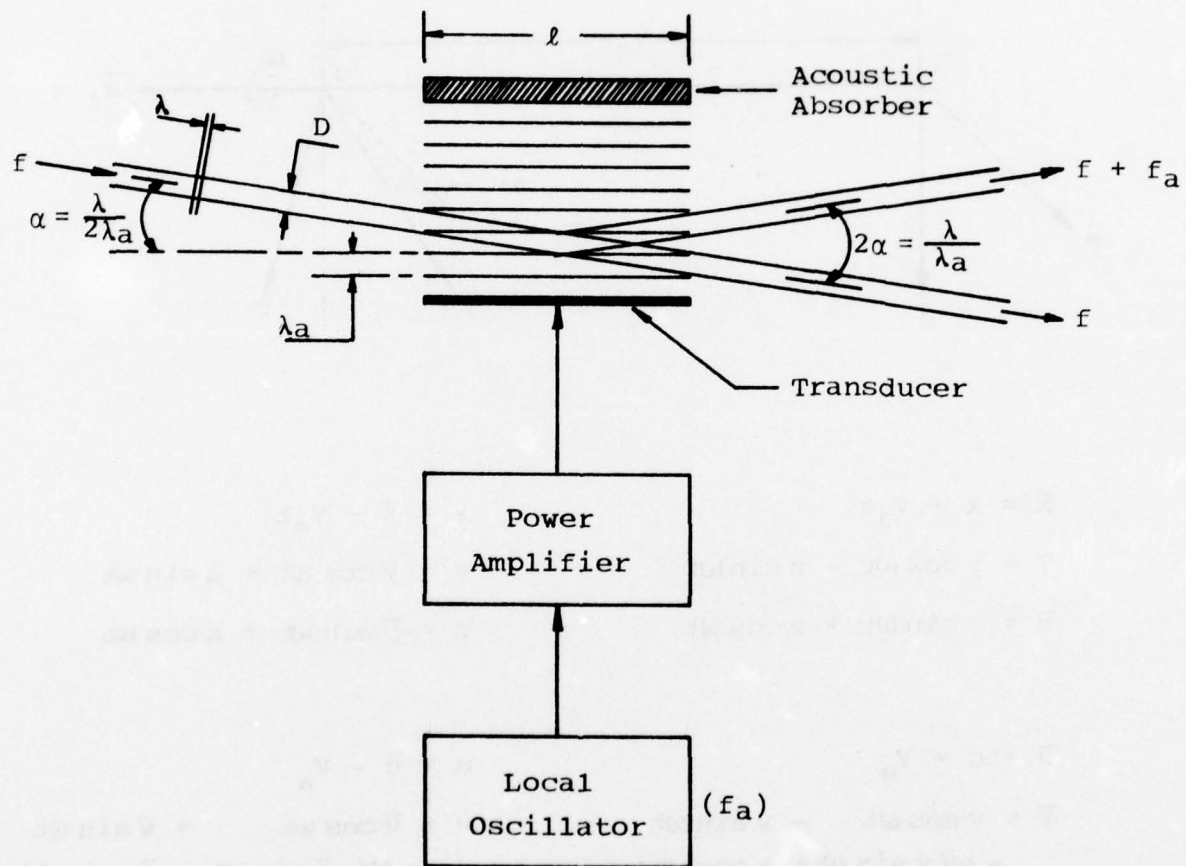
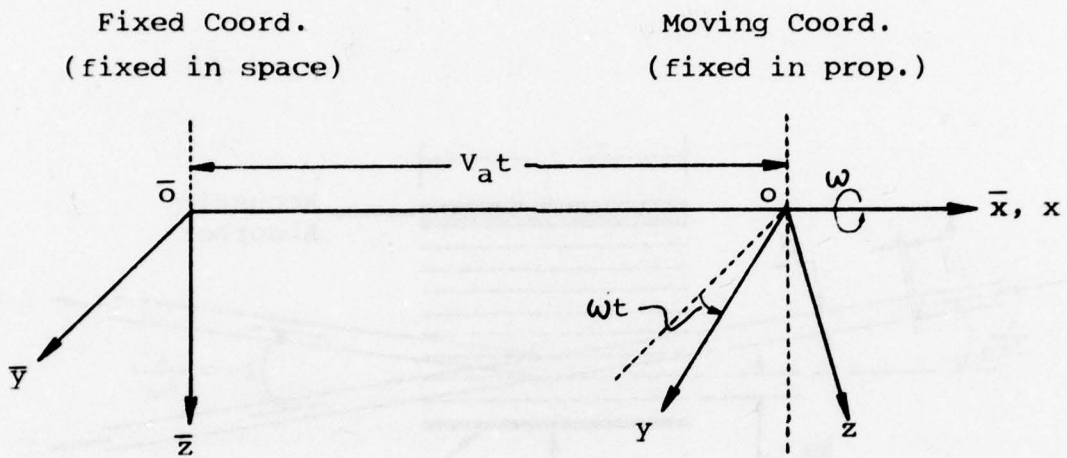


Fig. 16 Relation between Fixed Coord. and Moving Coord. Systems



$$\bar{x} = x + v_a t$$

$$\bar{y} = y \cos \omega t - z \sin \omega t$$

$$\bar{z} = y \sin \omega t + z \cos \omega t$$

$$x = \bar{x} - v_a t$$

$$y = \bar{y} \cos \omega t + \bar{z} \sin \omega t$$

$$z = -\bar{y} \sin \omega t + \bar{z} \cos \omega t$$

$$\bar{u} = u + v_a$$

$$\bar{v} = v \cos \omega t - w \sin \omega t - \omega(y \sin \omega t + z \cos \omega t)$$

$$\bar{w} = v \sin \omega t + w \cos \omega t + \omega(y \cos \omega t - z \sin \omega t)$$

$$u = \bar{u} - v_a$$

$$v = \bar{v} \cos \omega t + \bar{w} \sin \omega t + \omega(-\bar{y} \sin \omega t + \bar{z} \cos \omega t)$$

$$w = -\bar{v} \sin \omega t + \bar{w} \cos \omega t - \omega(\bar{y} \cos \omega t + \bar{z} \sin \omega t)$$

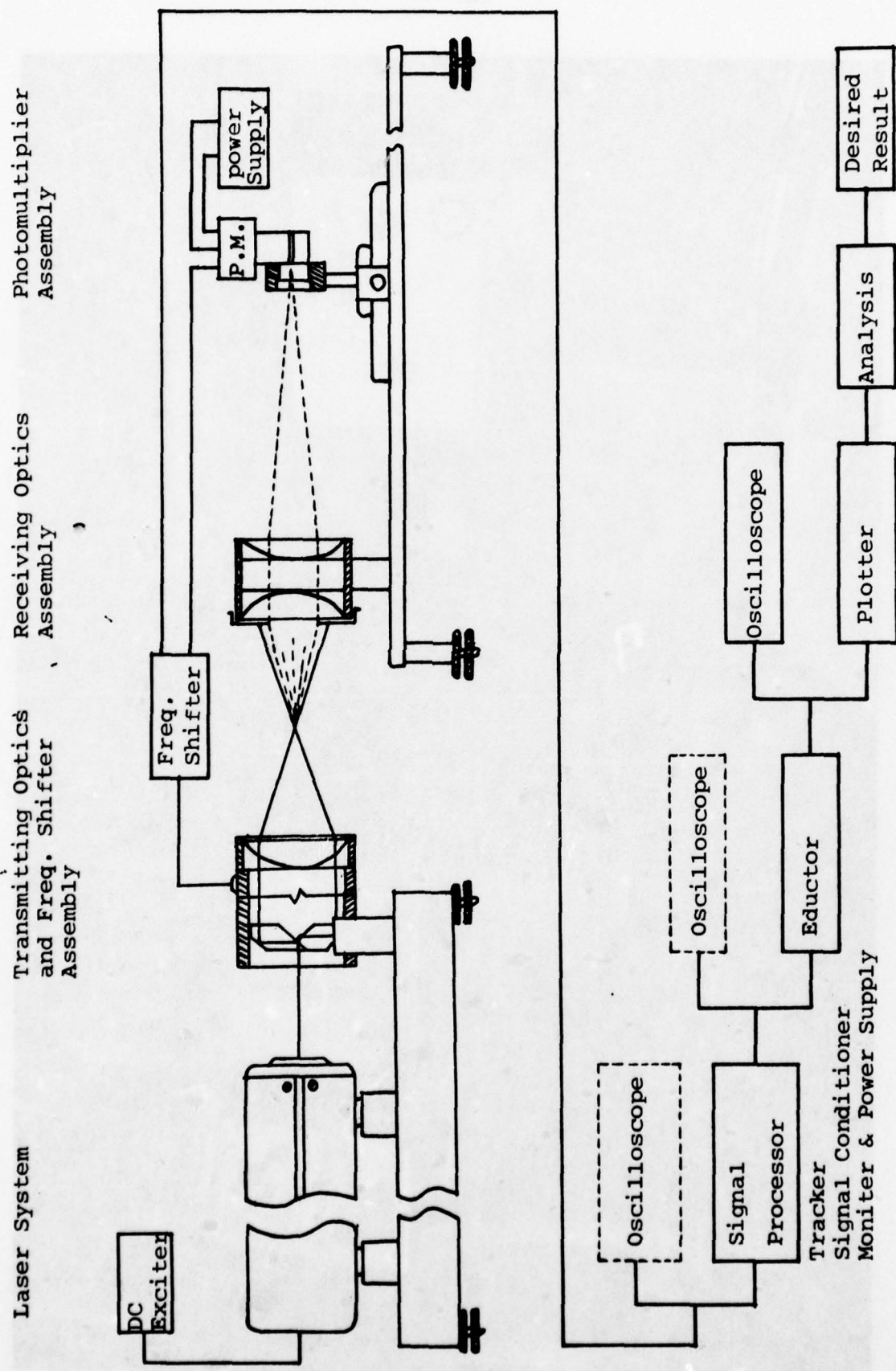


Fig. 17 MIT Watertunnel LDA System and Analysis Procedure

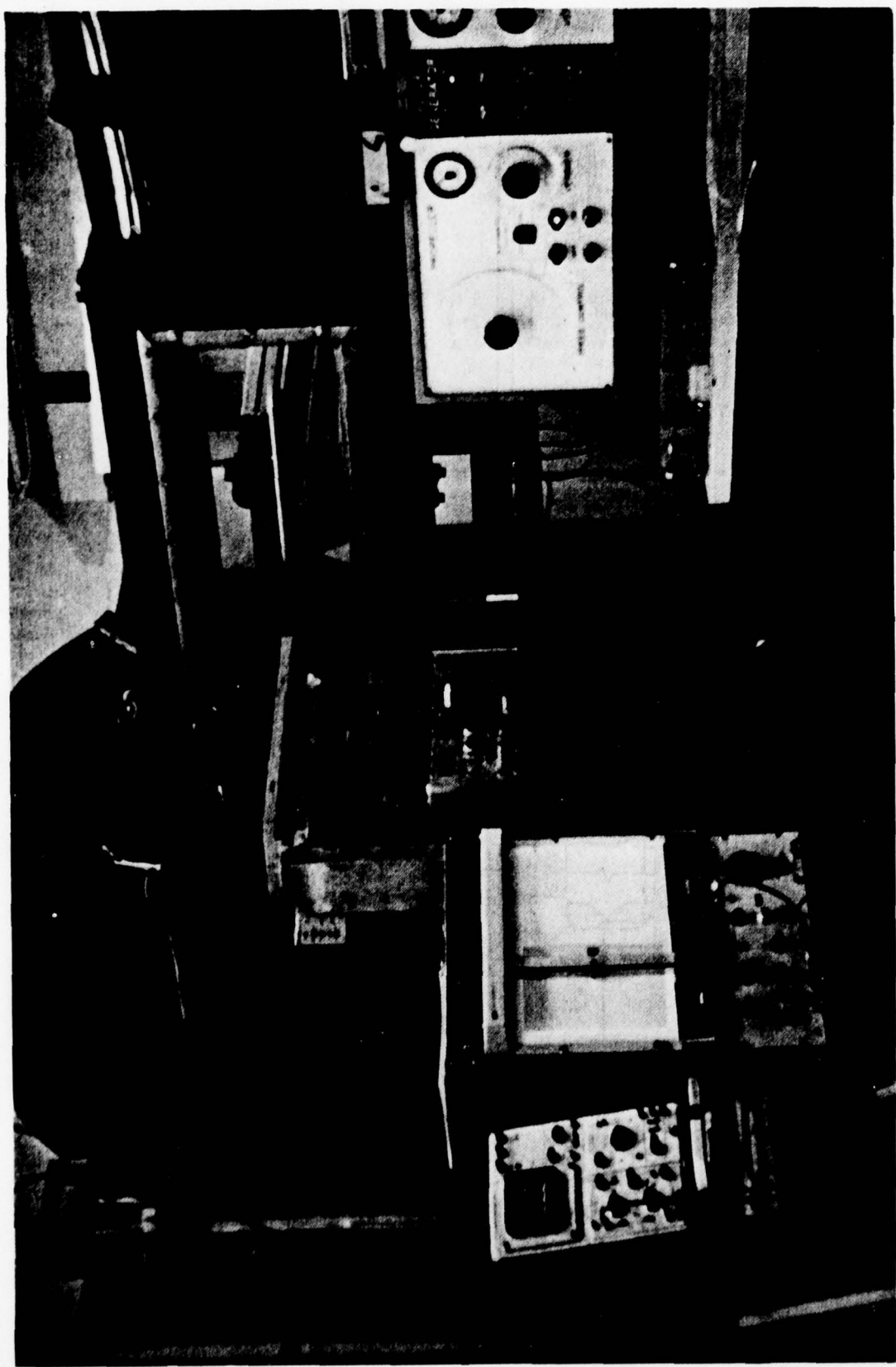
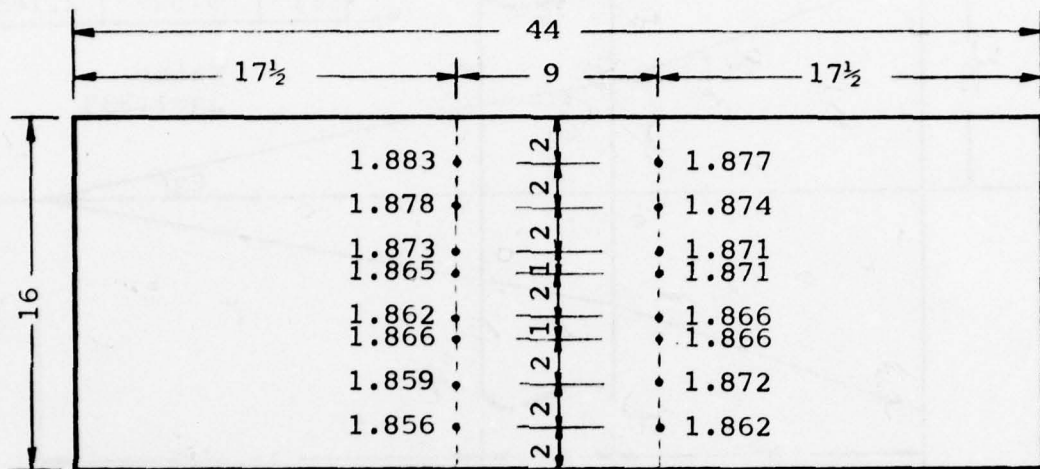


Fig. 18 General Setup of Propeller and LDA system

Fig. 19 Thickness Distribution of Tunnel Window for Laser Experiment
 (all dimensions in inches)

Transmitting Window



Receiving Window

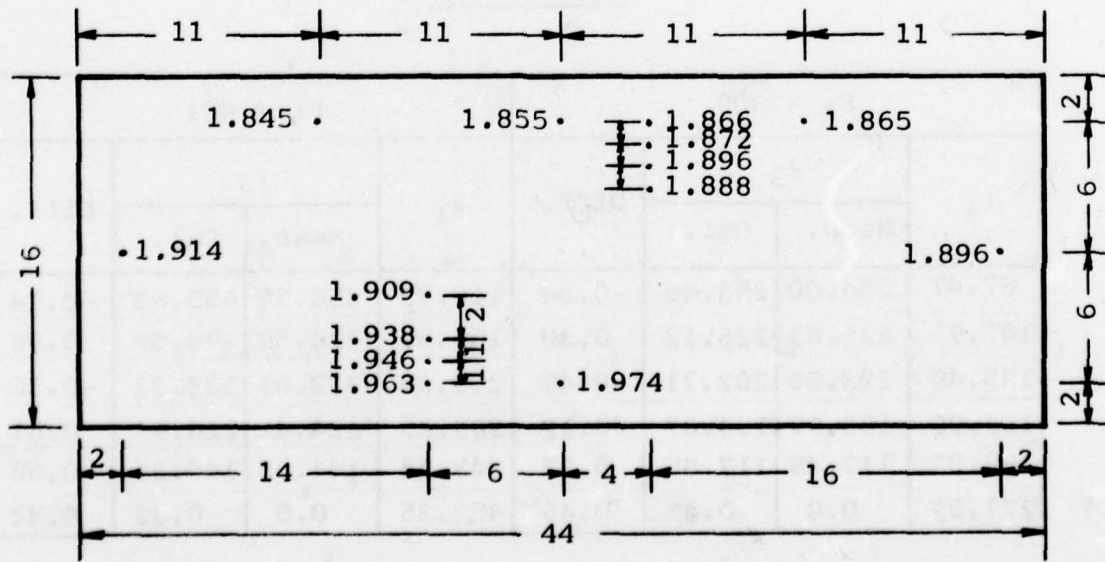
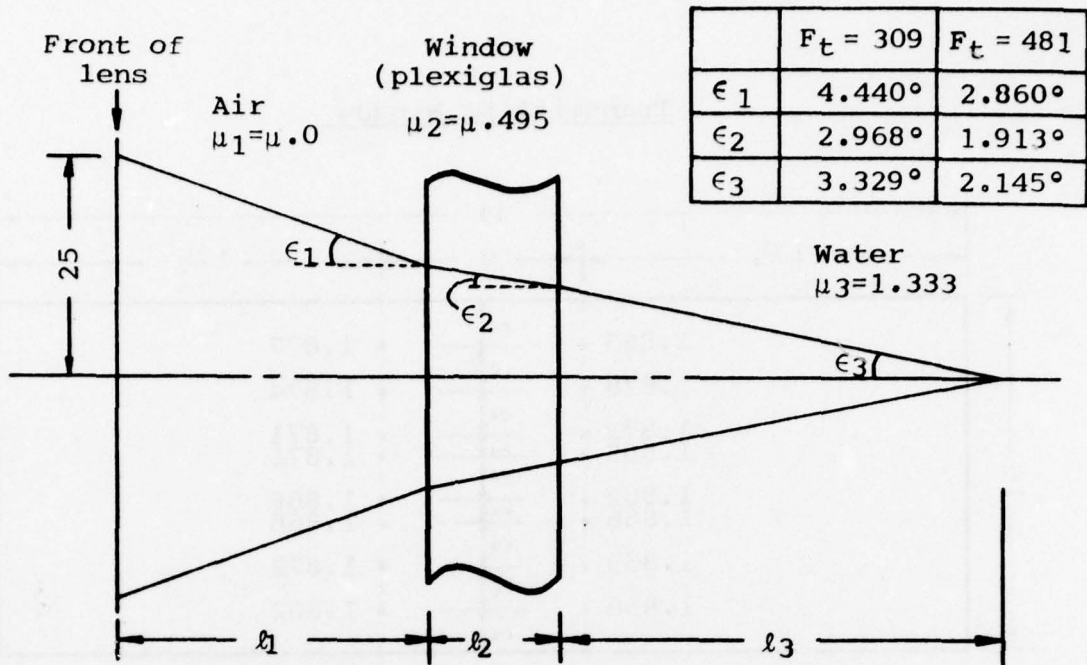


Fig. 20 Expression of Beam Crossing Point and Comparisons(Dimensions in mm)



	$F_t = 309$	$F_t = 481$
ϵ_1	4.440°	2.860°
ϵ_2	2.968°	1.913°
ϵ_3	3.329°	2.145°

$$\ell_3 = \begin{cases} 370.209 - (1.3348) \ell_1 & \text{for } F_t = 309 \\ 603.495 - (1.3337) \ell_1 & \text{for } F_t = 481 \end{cases}$$

with $\ell_2 = 47.498(1.87")$ and Correction for lens mounting case.

Comparisons

$F_t = 309$				$F_t = 481$			
ℓ_1	ℓ_3		Diff.	ℓ_1	ℓ_3		Diff.
	Meas.	Cal.			Meas.	Cal.	
87.47	254.00	253.46	-0.54	110.72	456.57	455.83	-0.74
107.95	225.82	226.12	0.30	156.59	394.59	394.65	0.06
125.49	203.20	202.71	-0.49	203.33	332.61	332.31	-0.30
162.08	153.99	153.87	-0.12	283.85	224.41	224.92	0.51
189.07	117.48	117.85	0.37	343.54	144.65	145.31	0.66
277.01	0.0	0.45	0.45	452.25	0.0	0.32	0.32

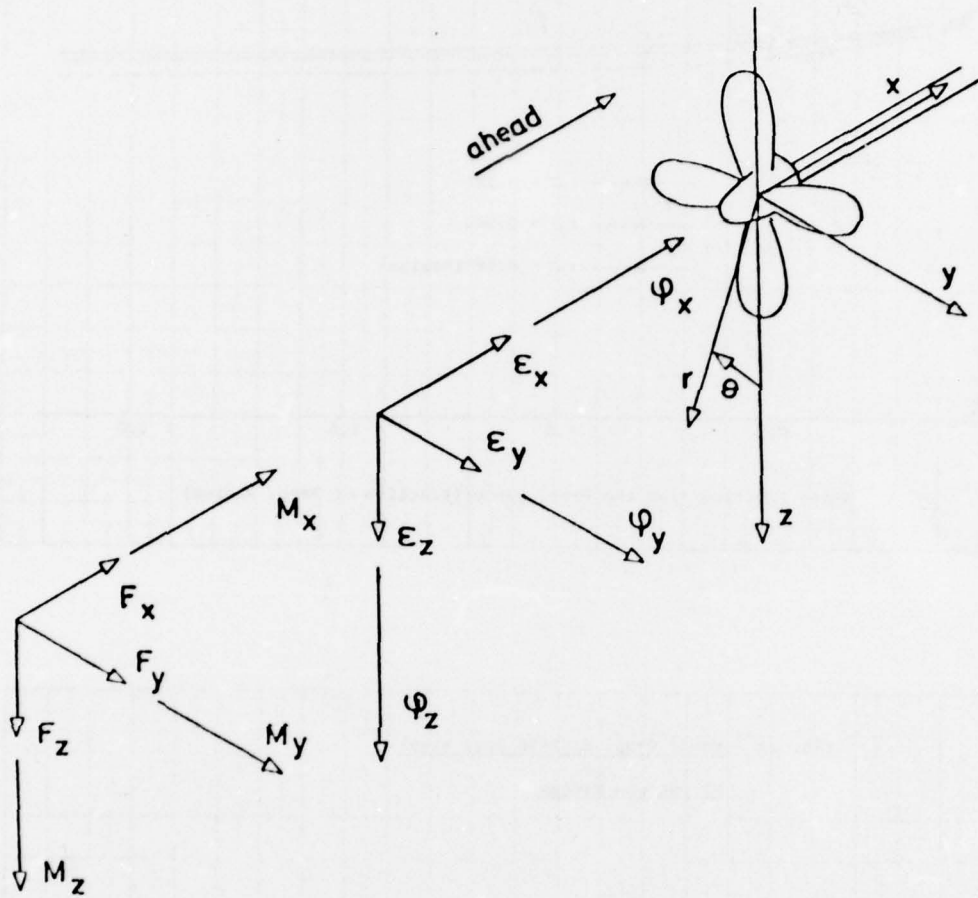
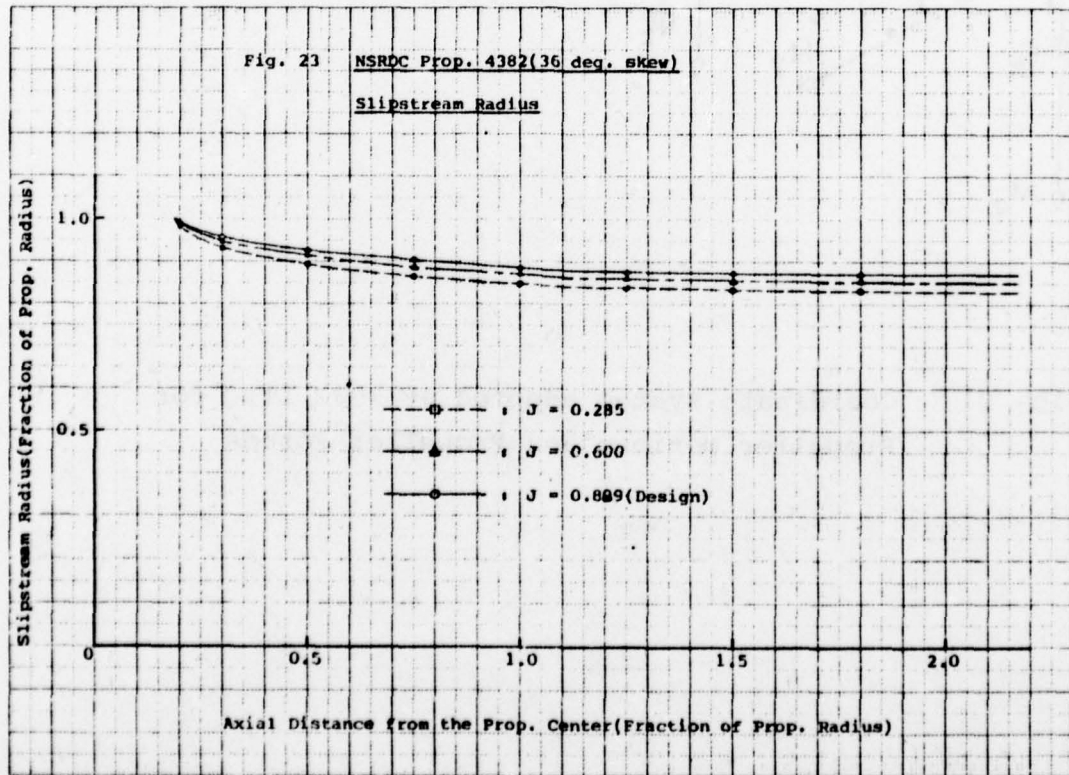
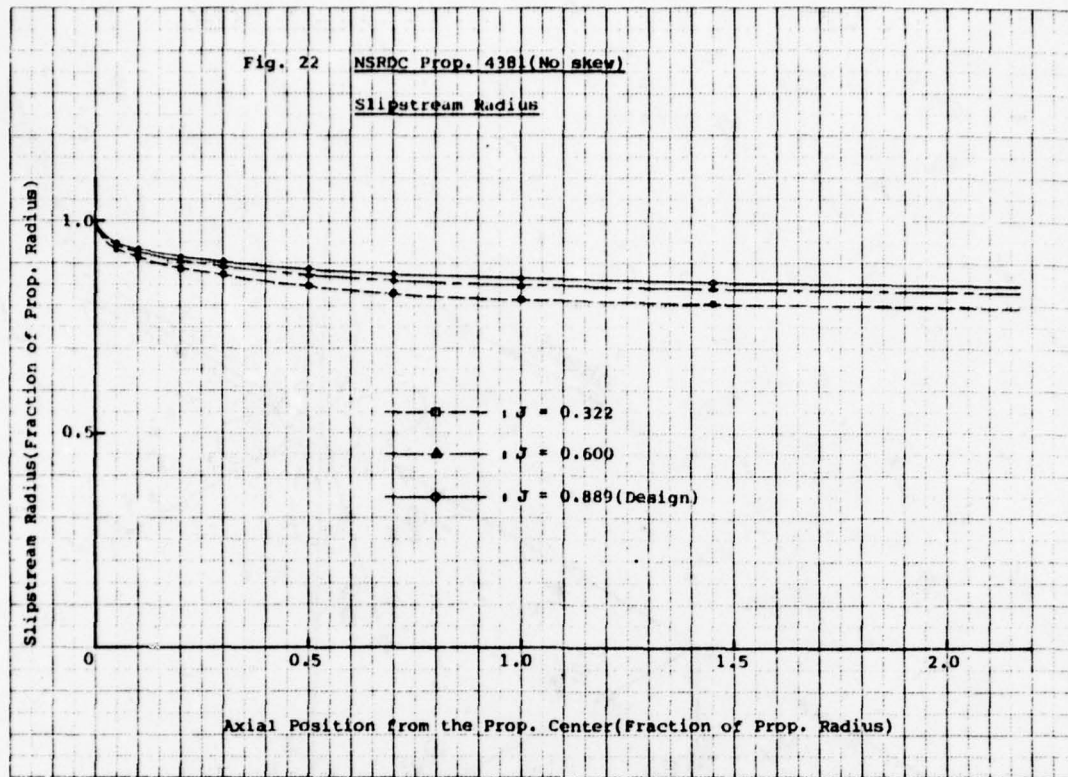


Fig. 21 Coordinate System adopted at 1973 ITTC for Propeller Motions and Propeller Forces



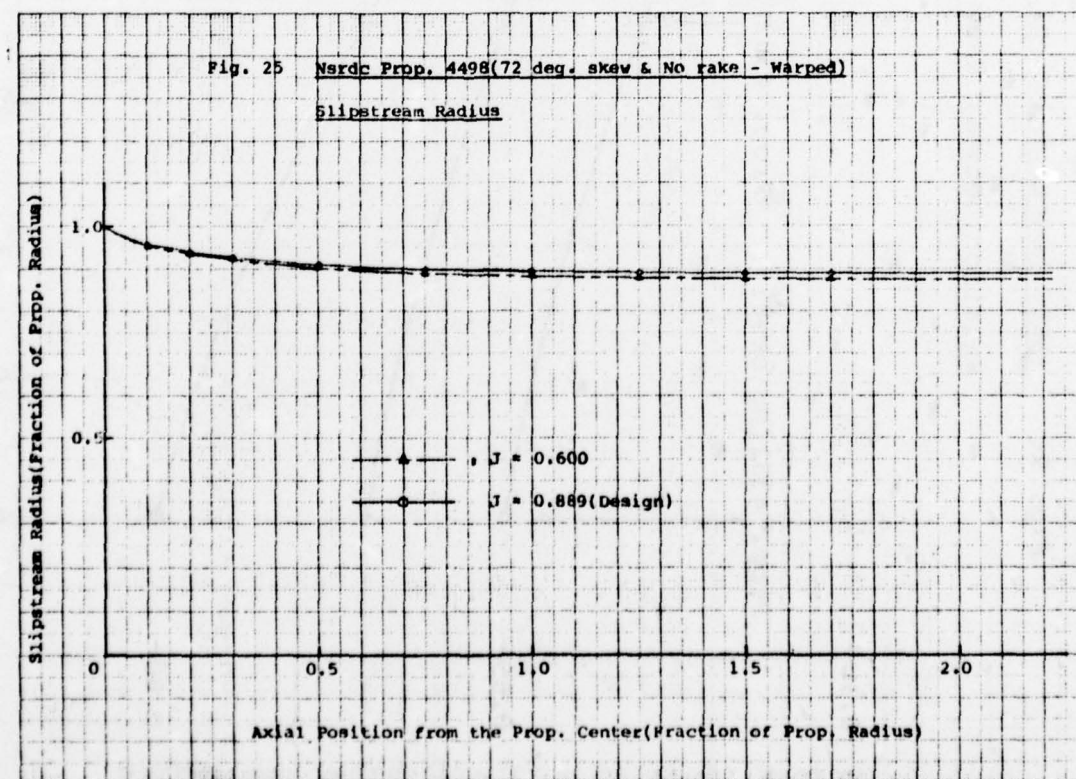
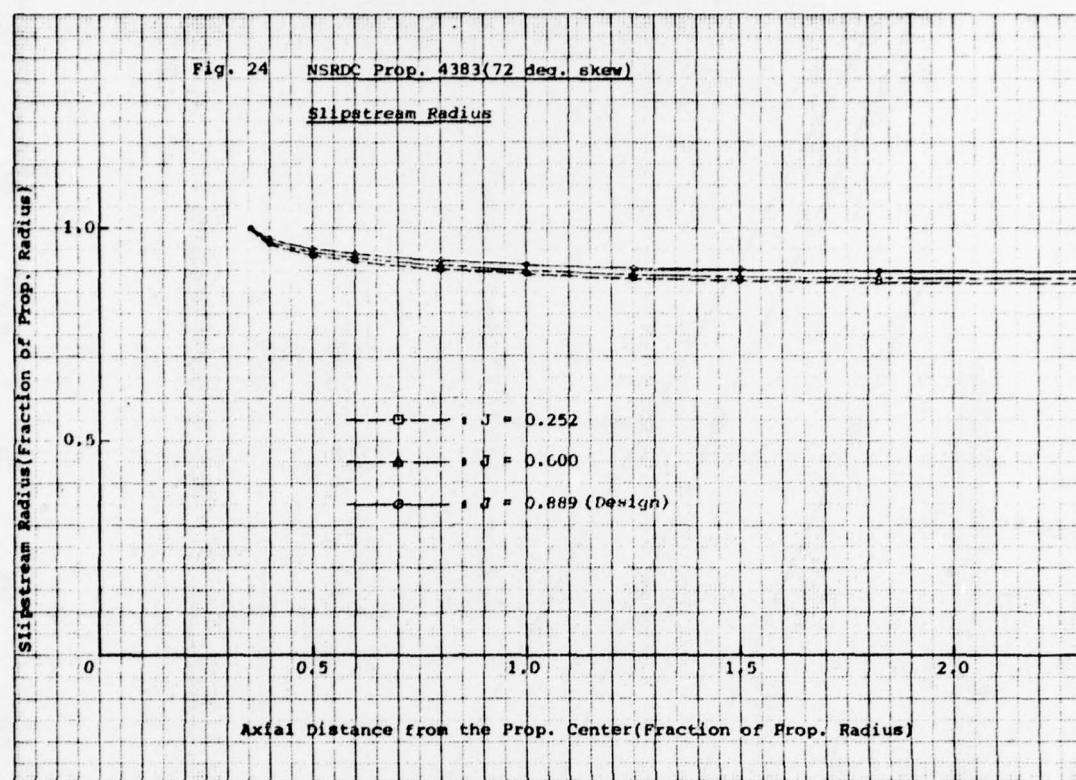


Fig. 26

NSRDC Research Propellers

Relation between Skew and Ultimate Slipstream Radius

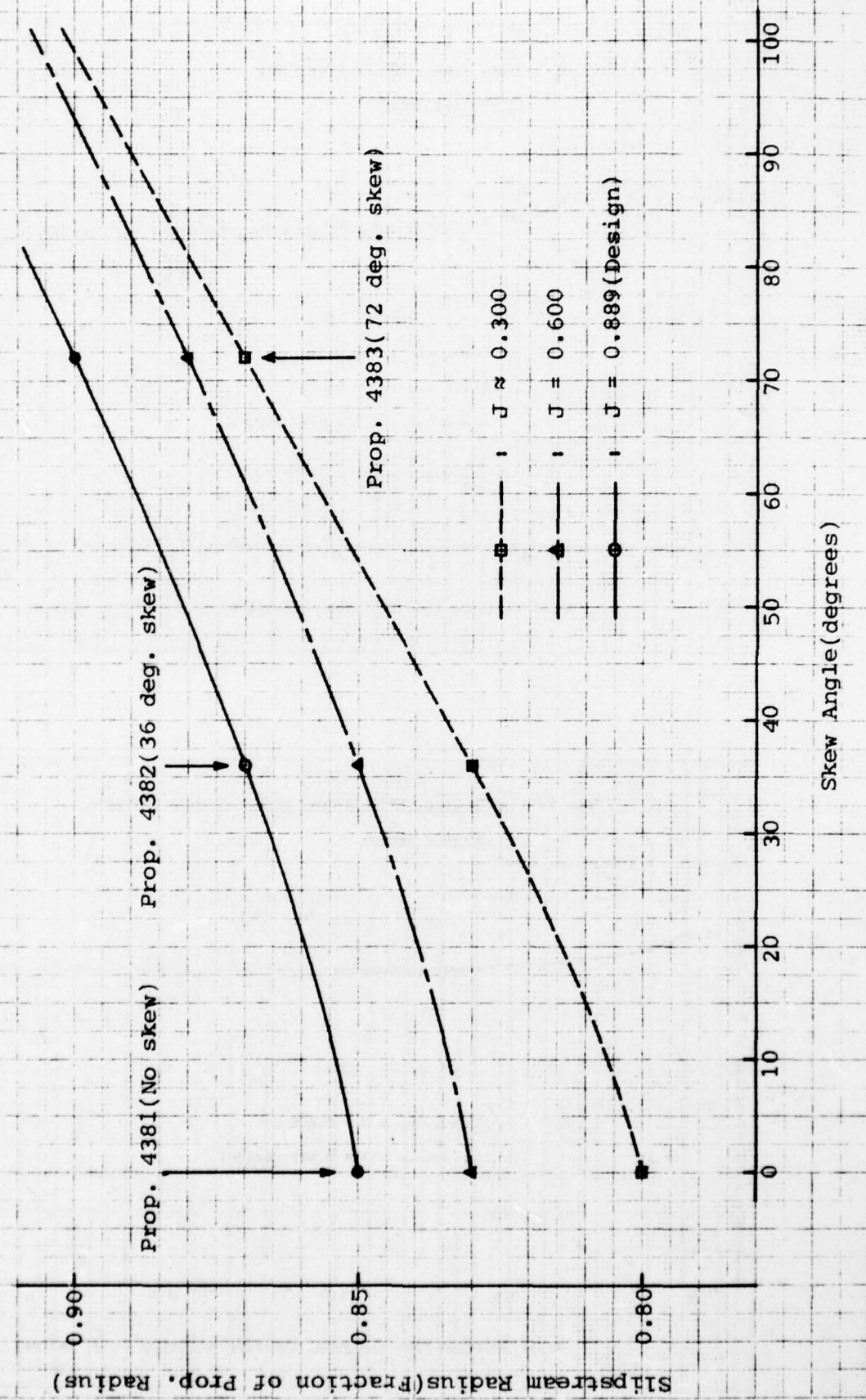


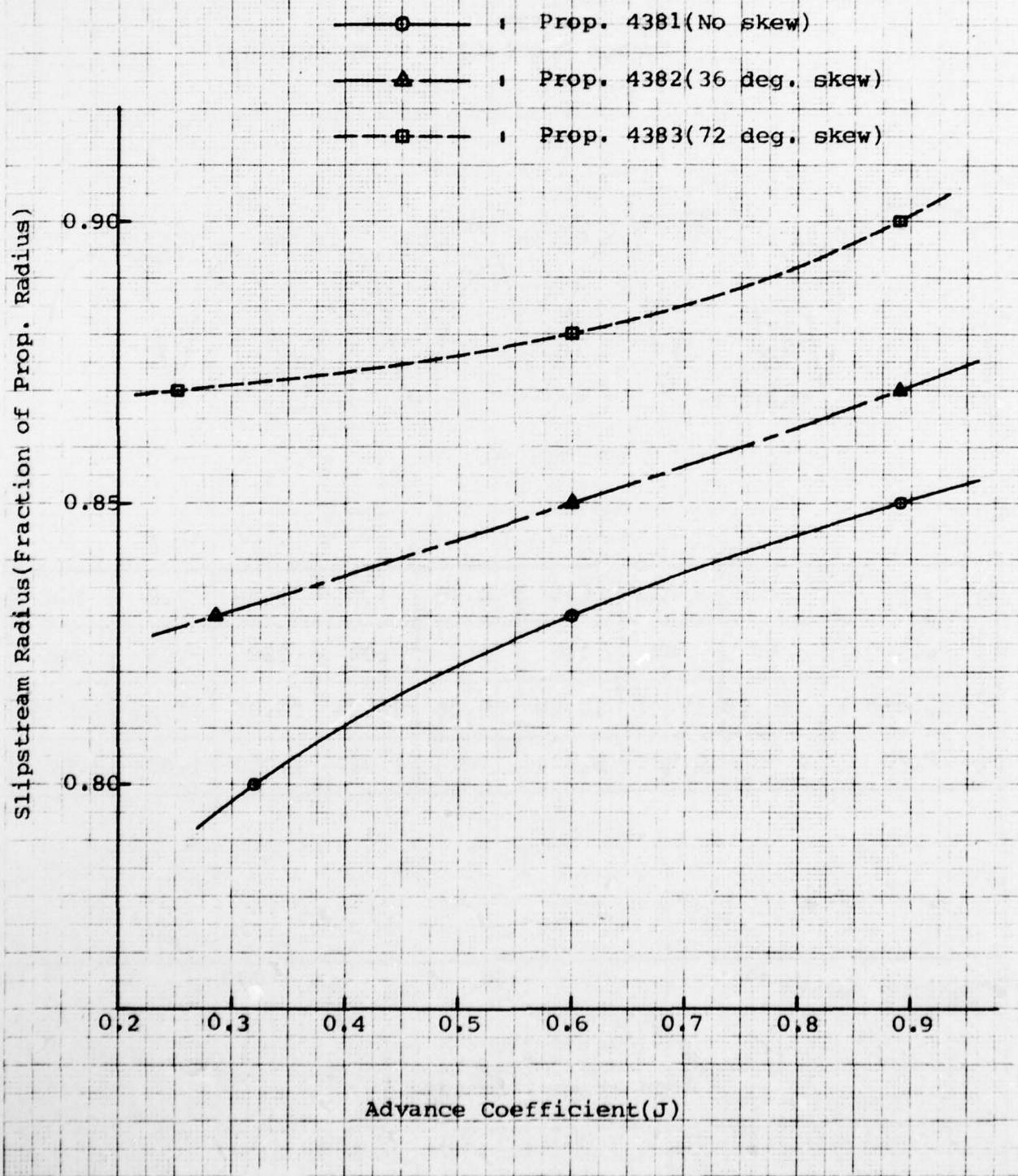
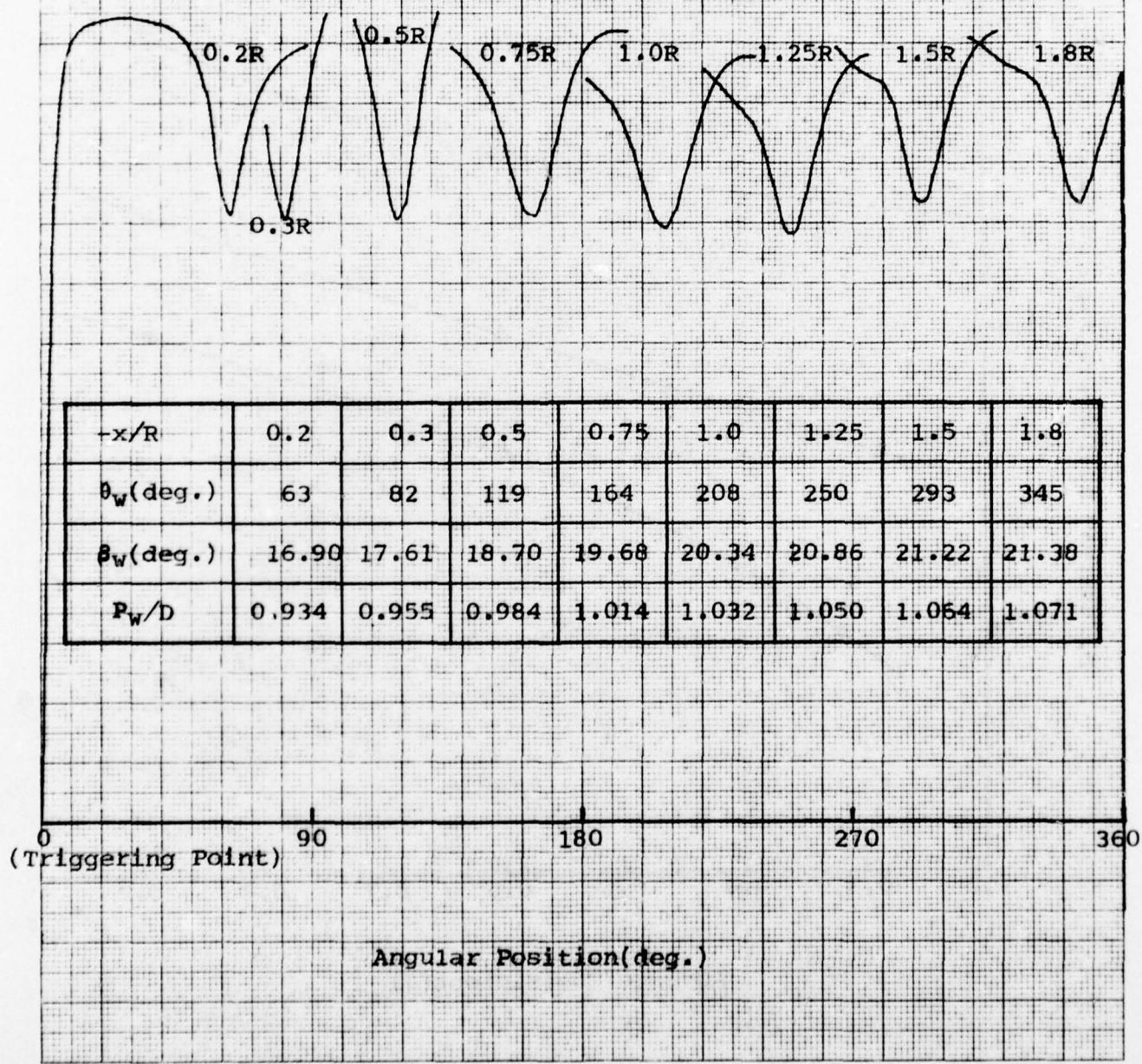
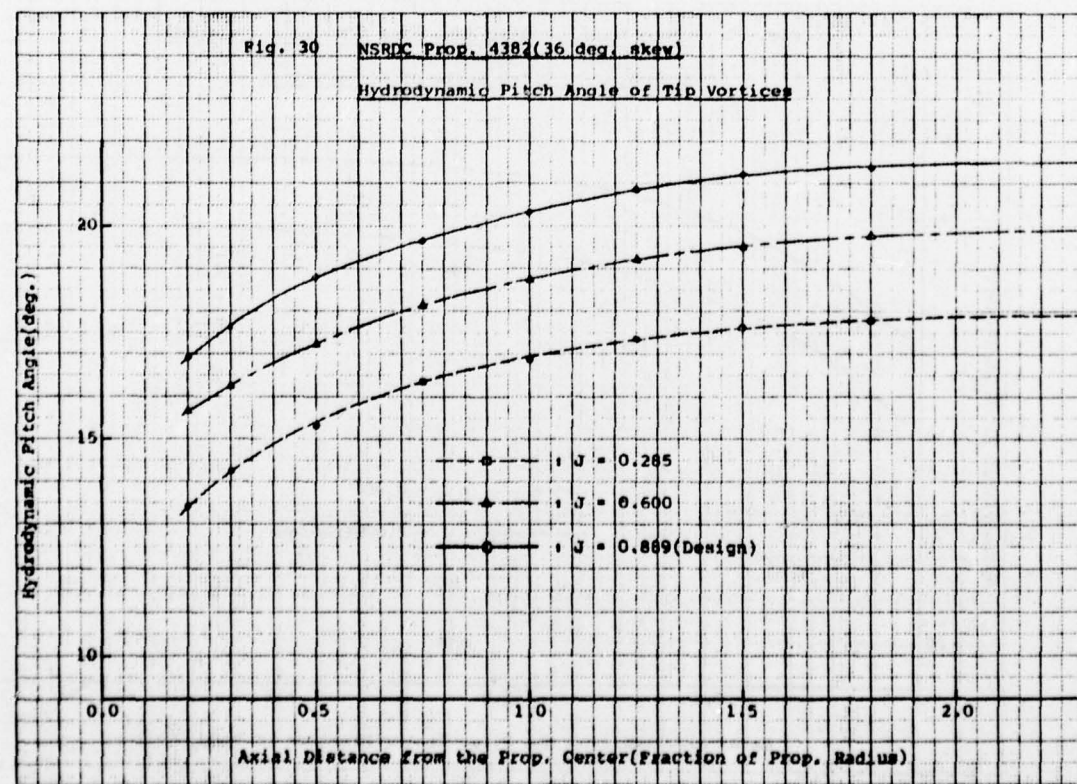
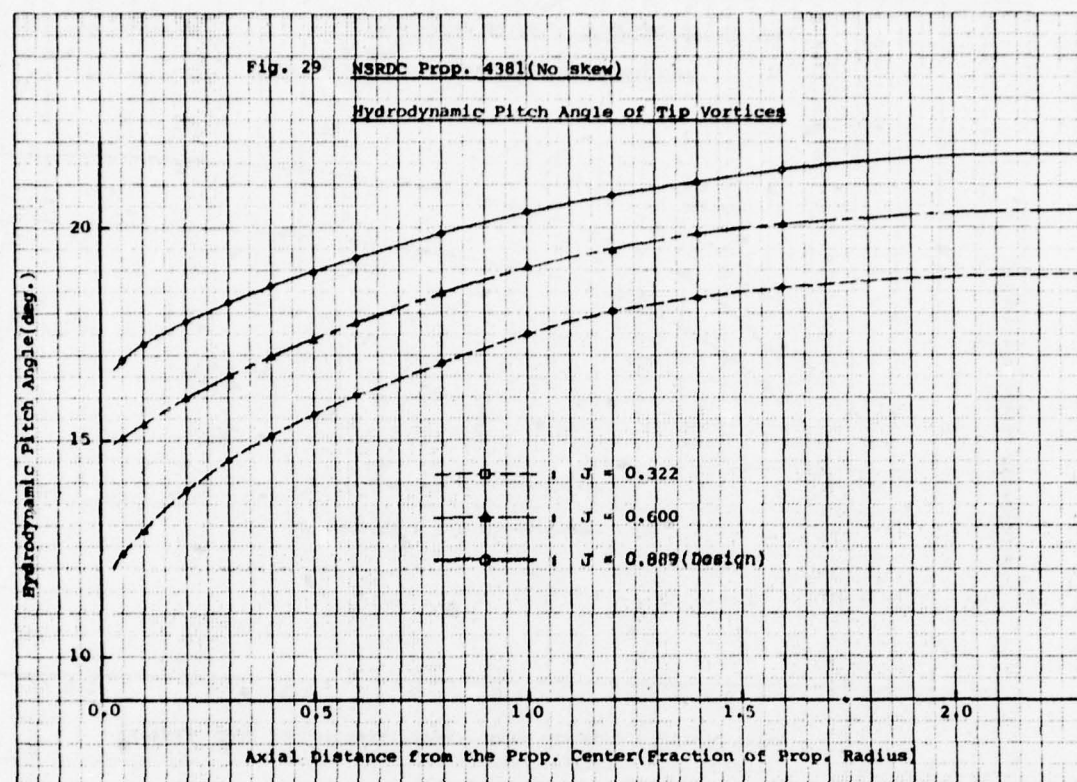
Fig. 27 NSRDC Research PropellersRelation between Loading Condition
and Ultimate Slipstream Radius

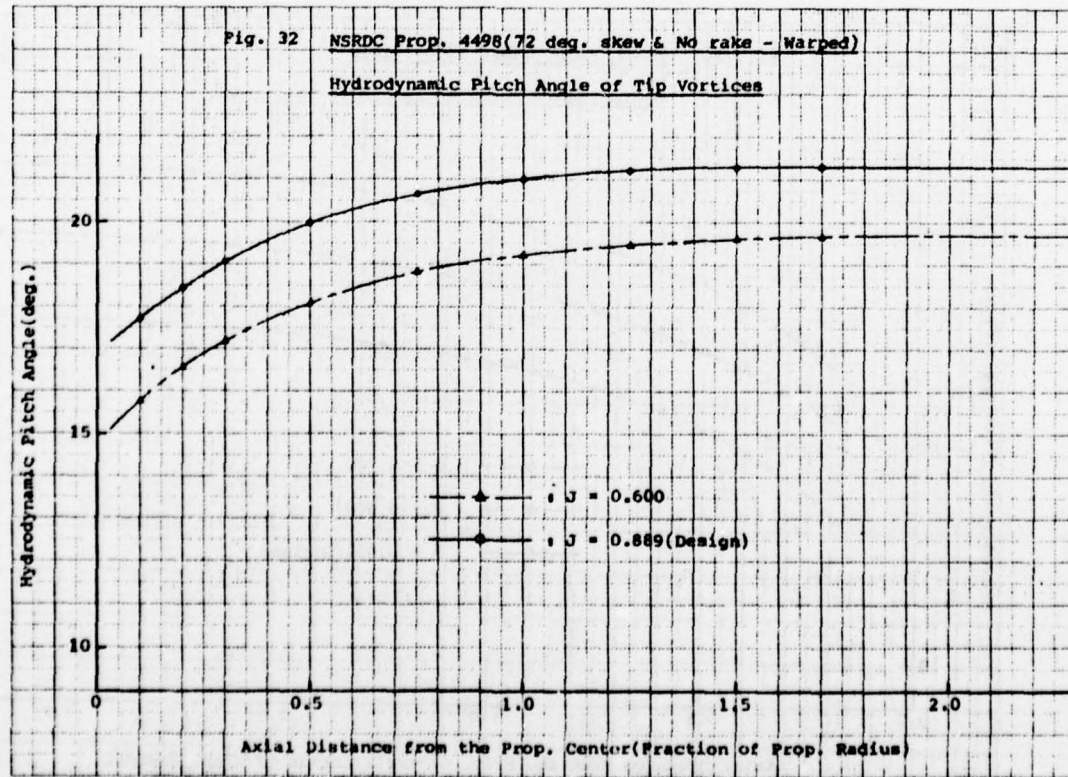
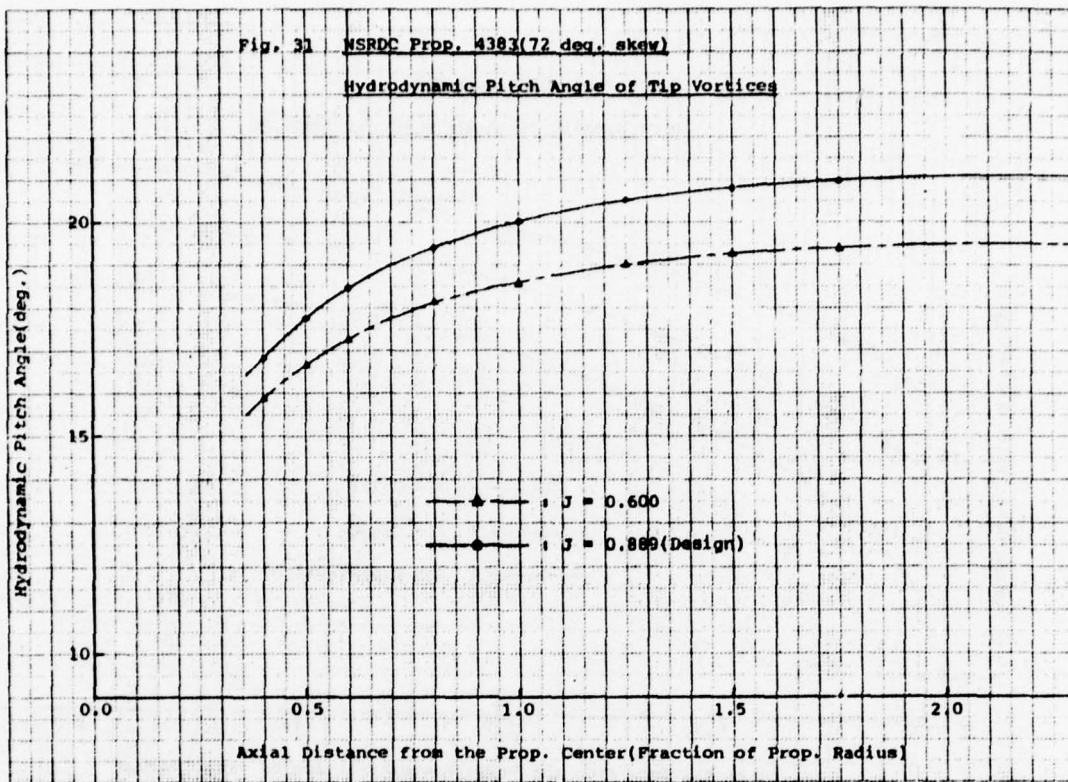
Fig. 28 NSRDC Prop. 4382 (36 deg. skew)

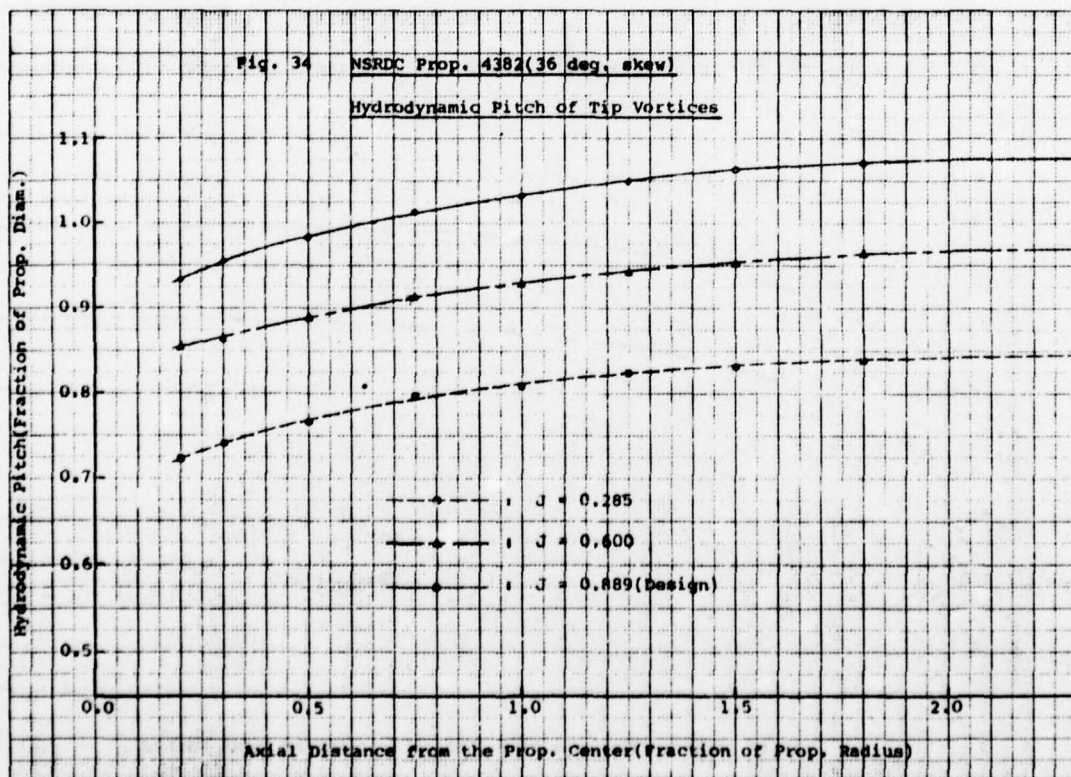
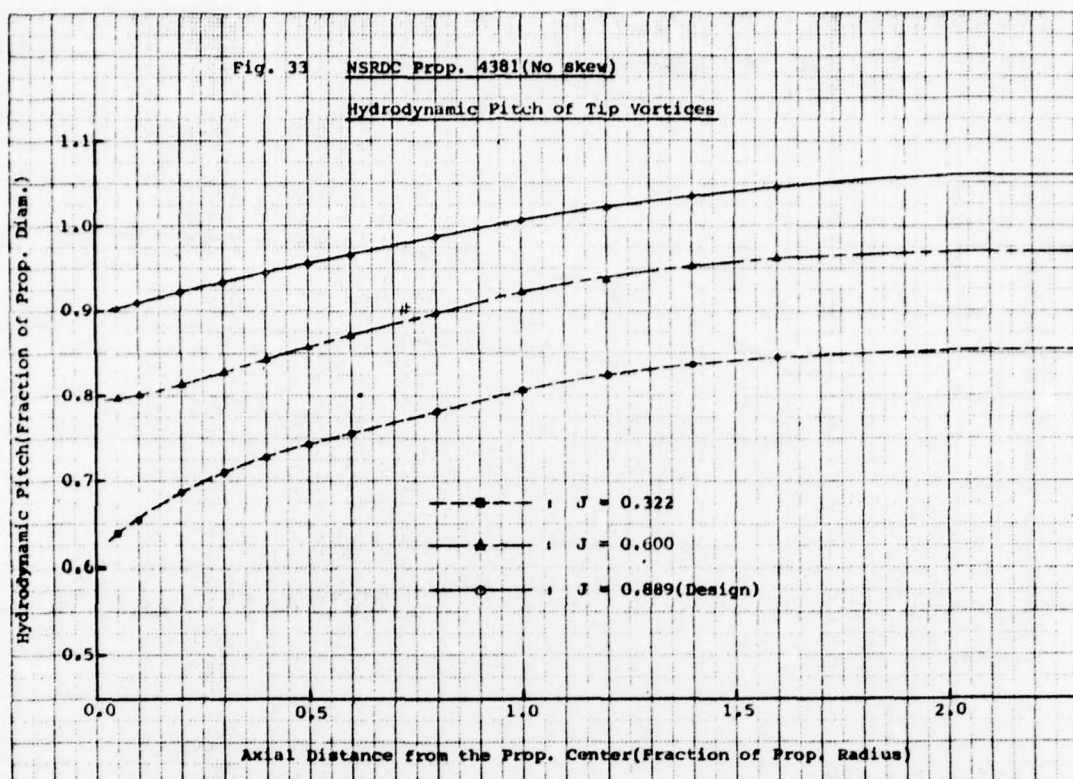
Trace of Tip Vortex from a Selected Blade

Propeller RPM = 900
 Advance Coeff. (J) = 0.889 (Design)









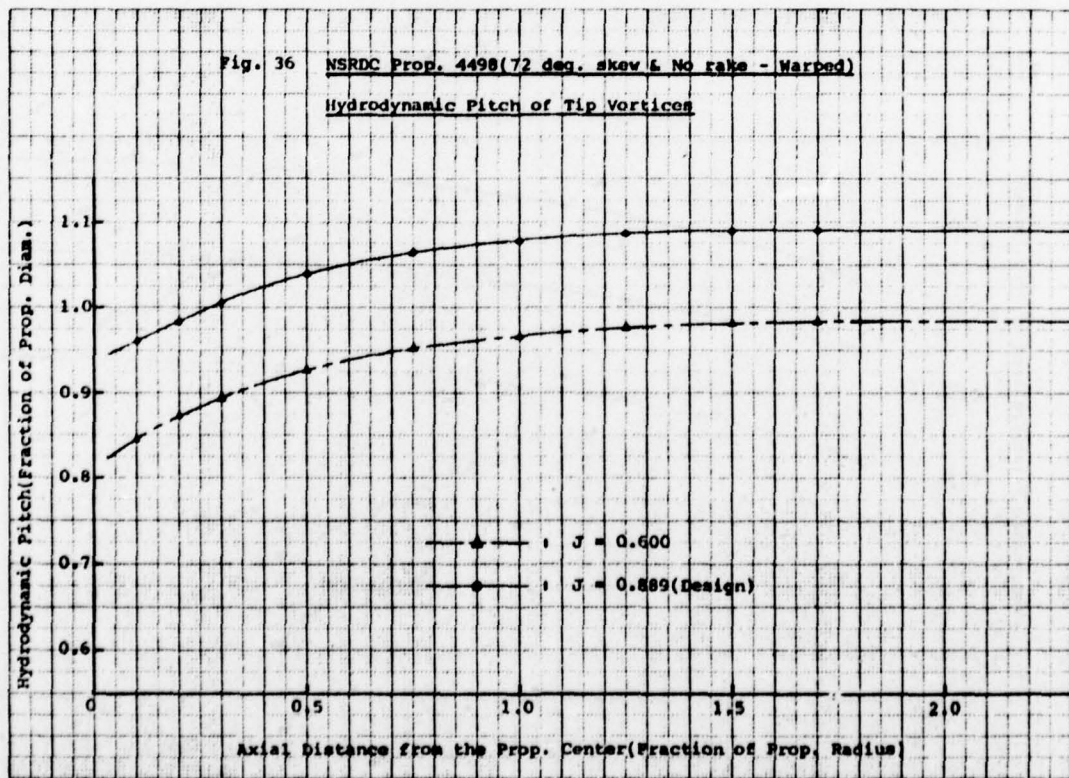
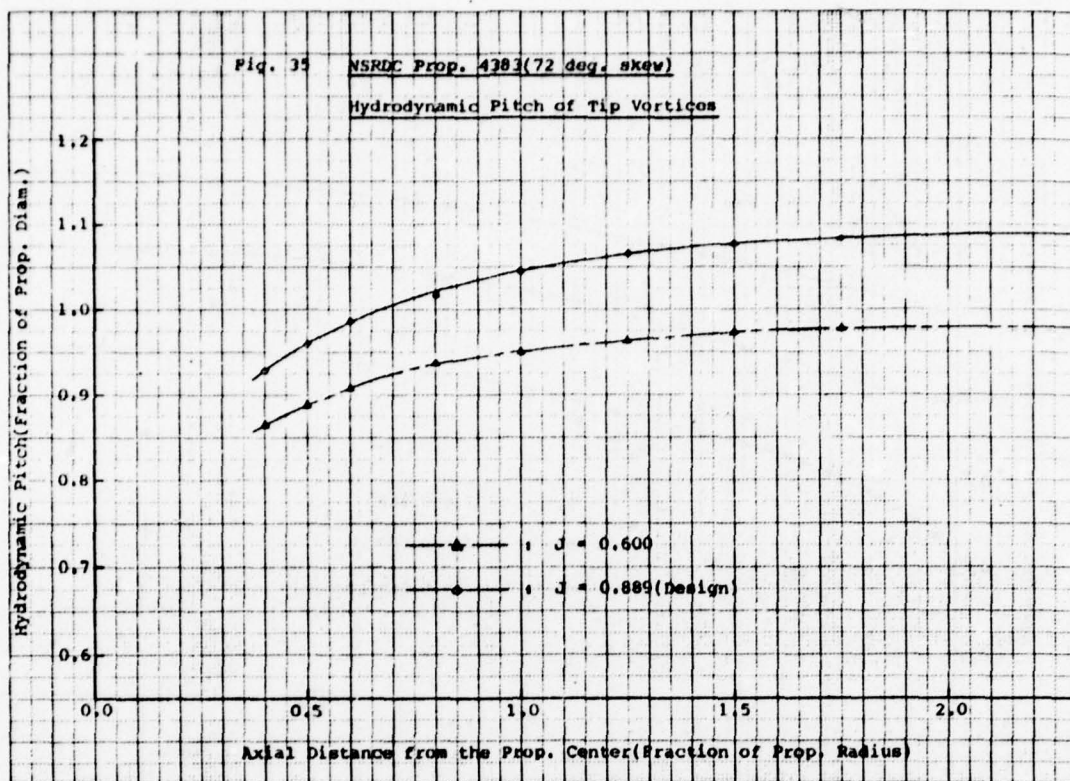


Fig. 37 MIT Water Tunnel

Nondimensional Free Stream Velocity with Prop. Shaft Housing

Dummy Hub Not Rotating
 Dummy Hub Radius(r) = 1.2 inches
 Impeller RPM = 200
 Free Stream Velocity(U) = 13.114 ft/sec

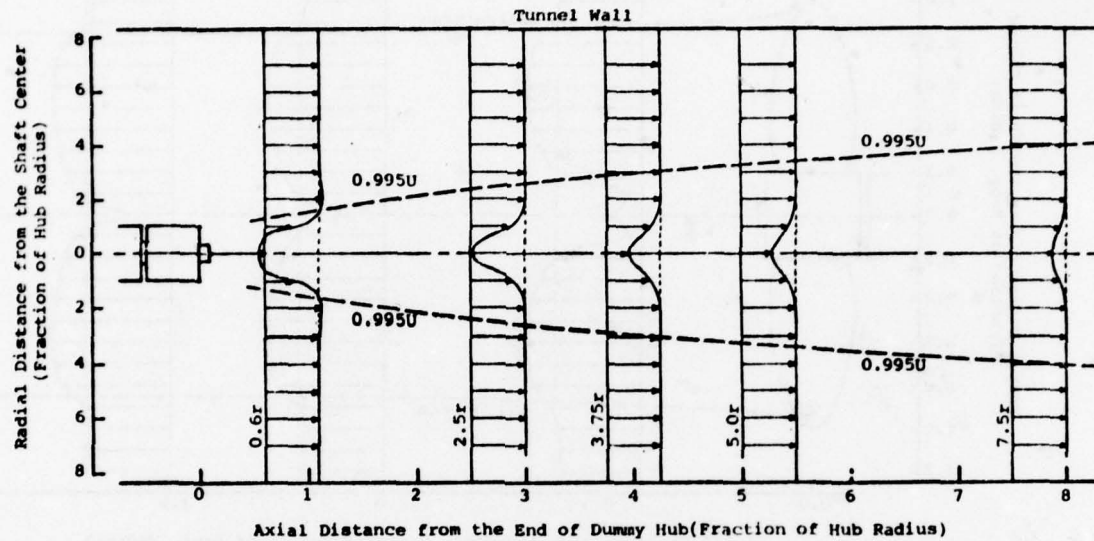


Fig. 38 MIT Water Tunnel

Nondimensional Free Stream Velocity with Prop. Shaft Housing

Dummy Hub Rotating(900 RPM)
 Dummy Hub Radius(r) = 1.2 inches
 Impeller RPM = 200
 Free Stream Velocity(U) = 13.114 ft/sec

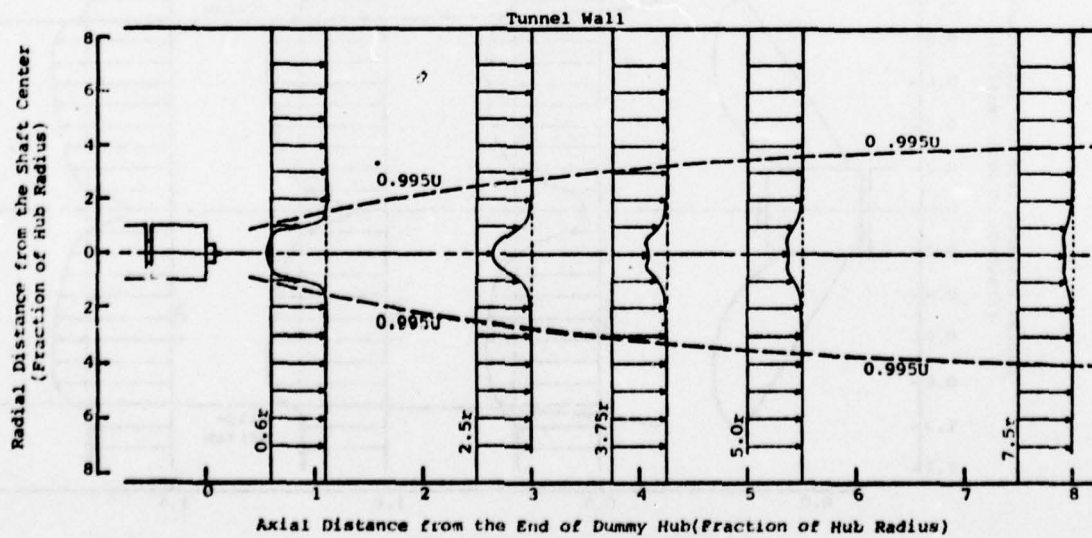


Fig. 39 NSRDC Prop. 4381(No skew)
Axial Velocity Distribution behind Propeller

Advance Coeff.(J) = 0.889
 Speed of Advance(V_a) = 13.335 ft/sec

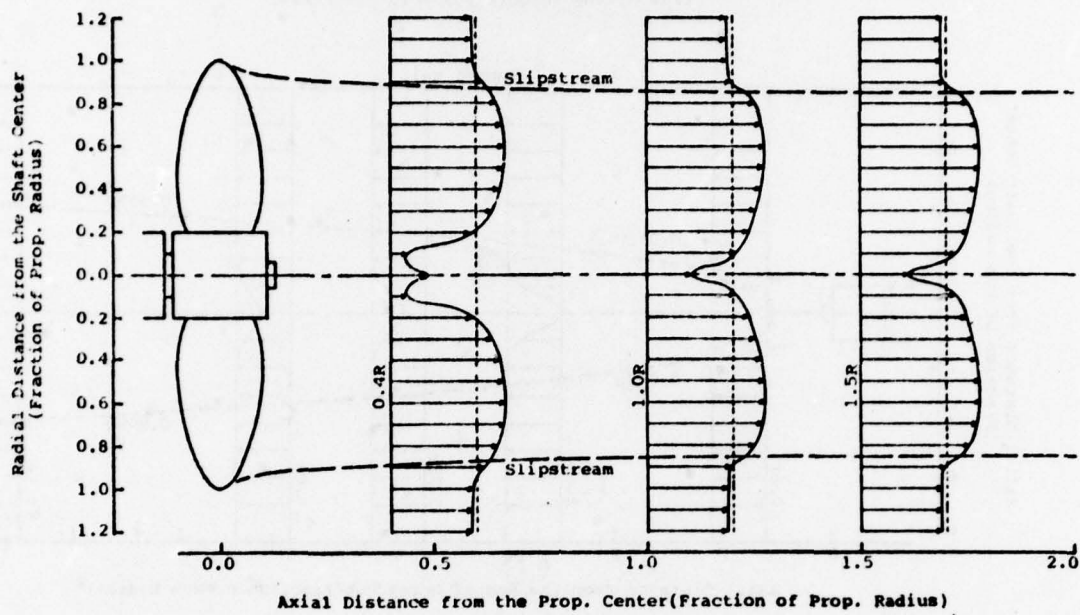
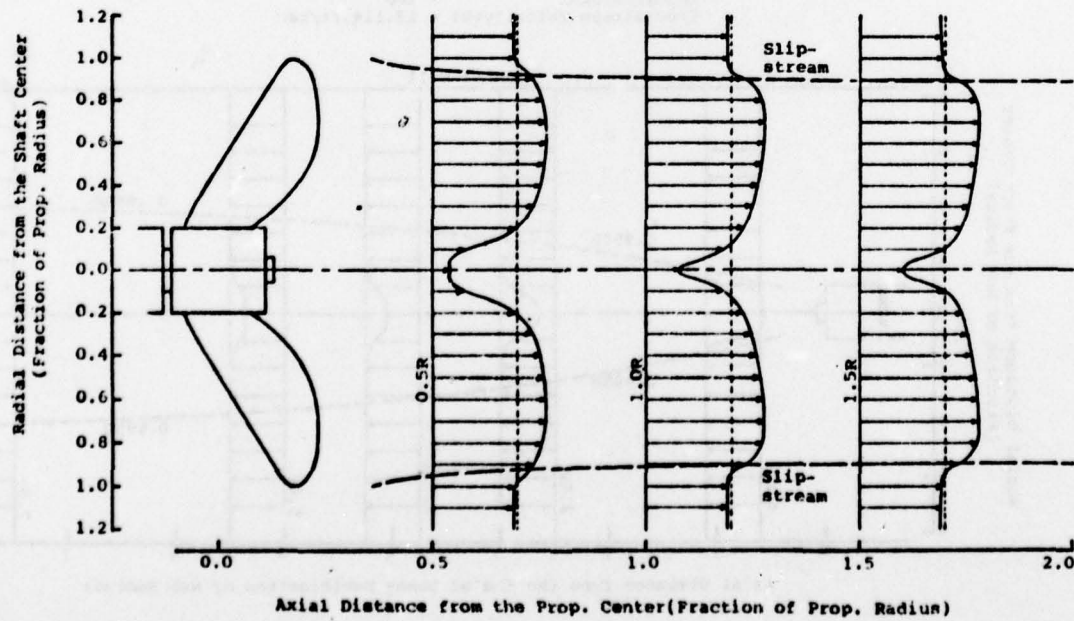
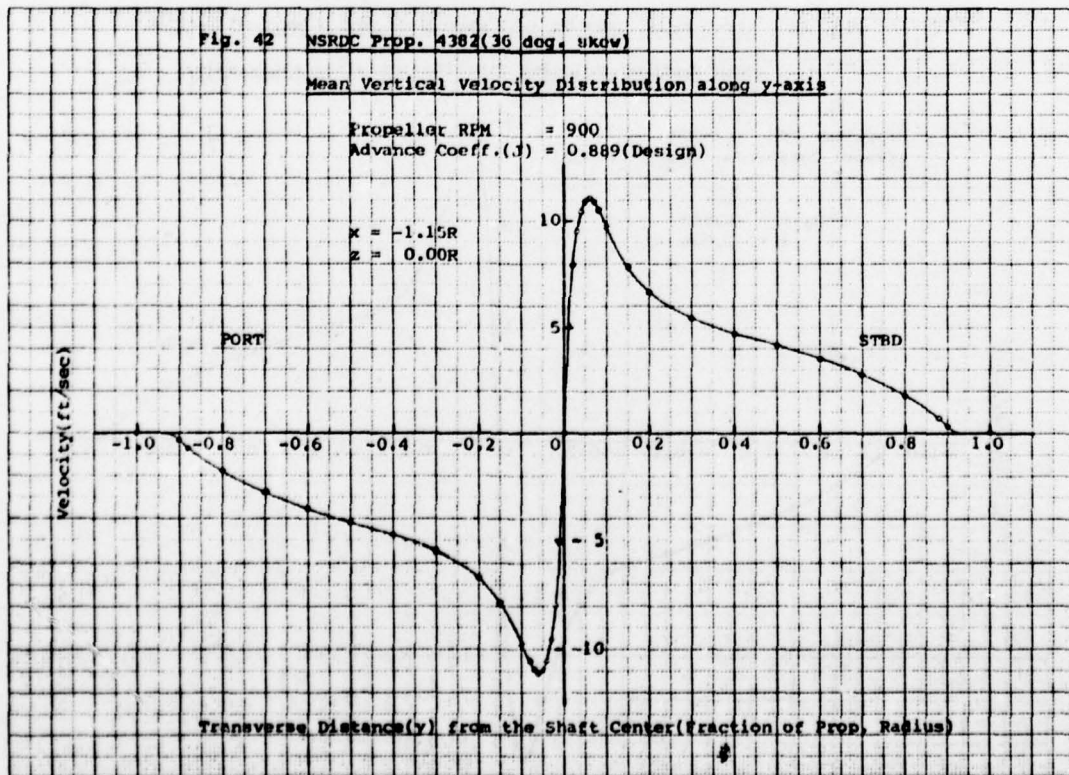
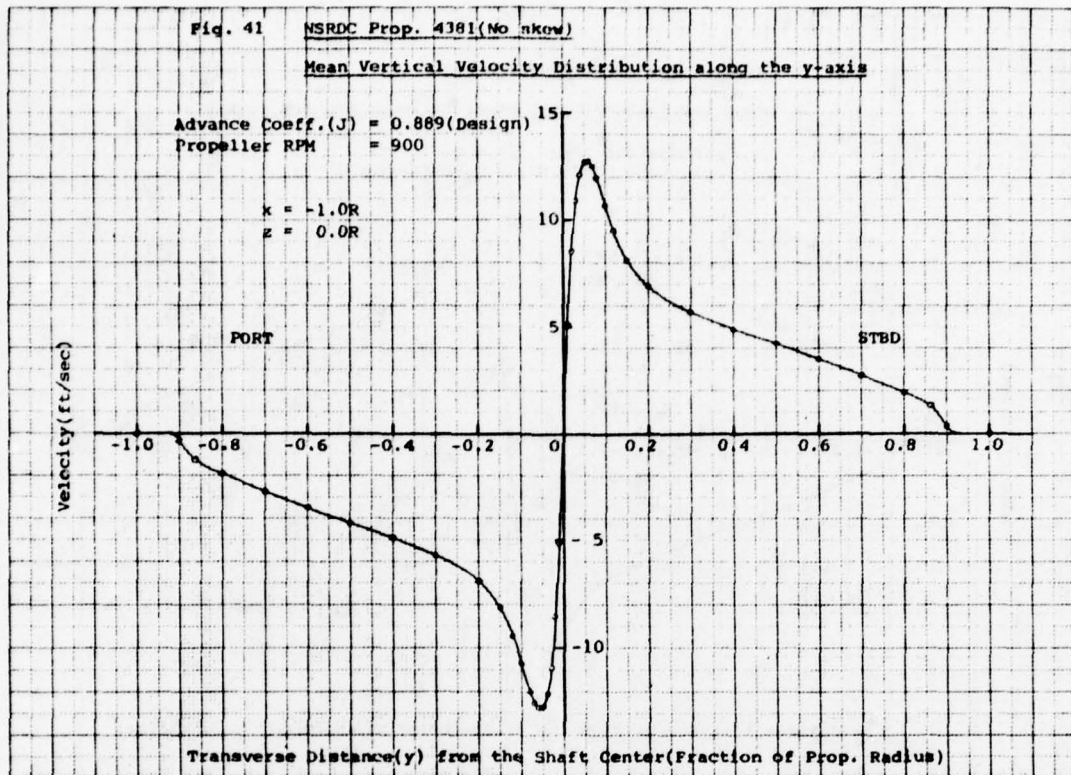


Fig. 40 NSRDC Prop. 4383(72 deg. skew)
Axial Velocity Distribution behind Propeller

Advance Coeff.(J) = 0.889
 Speed of Advance(V_a) = 13.335 ft/sec





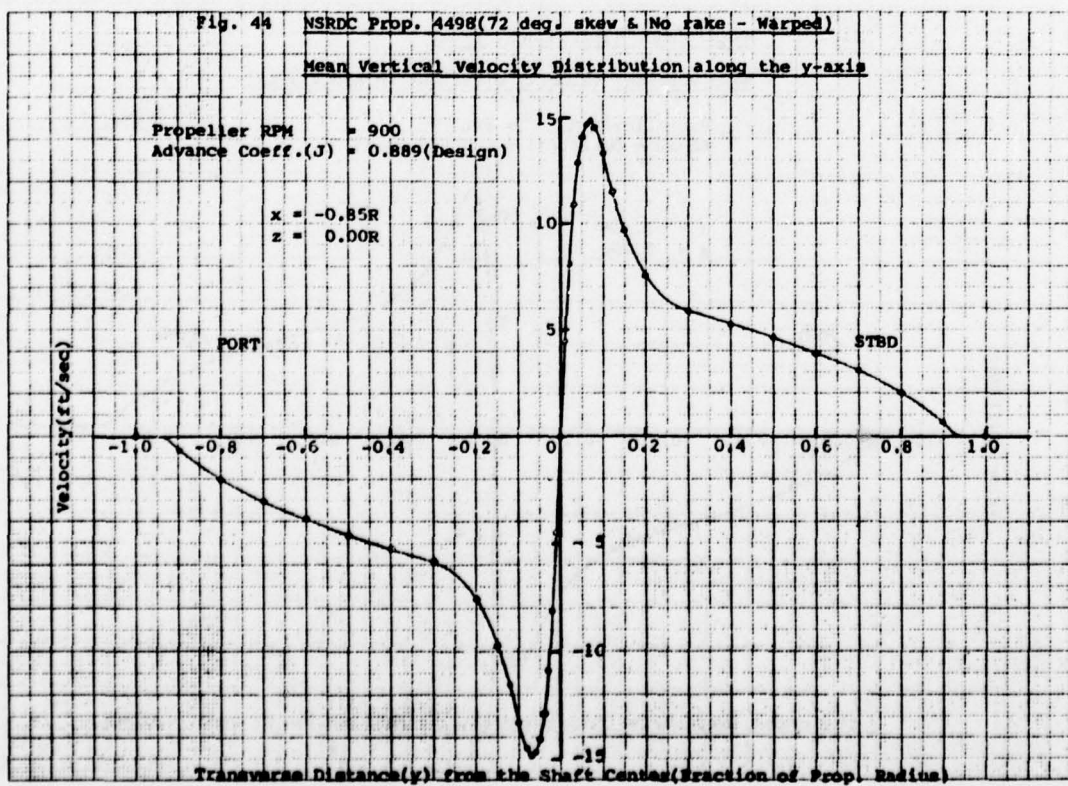
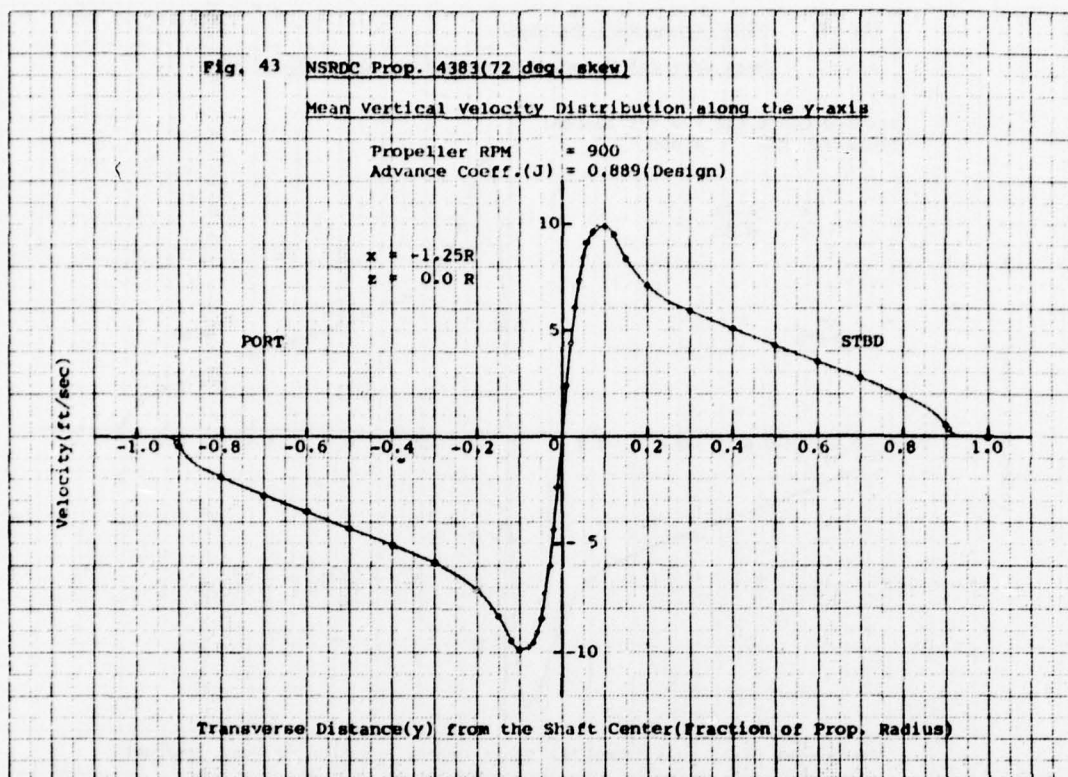
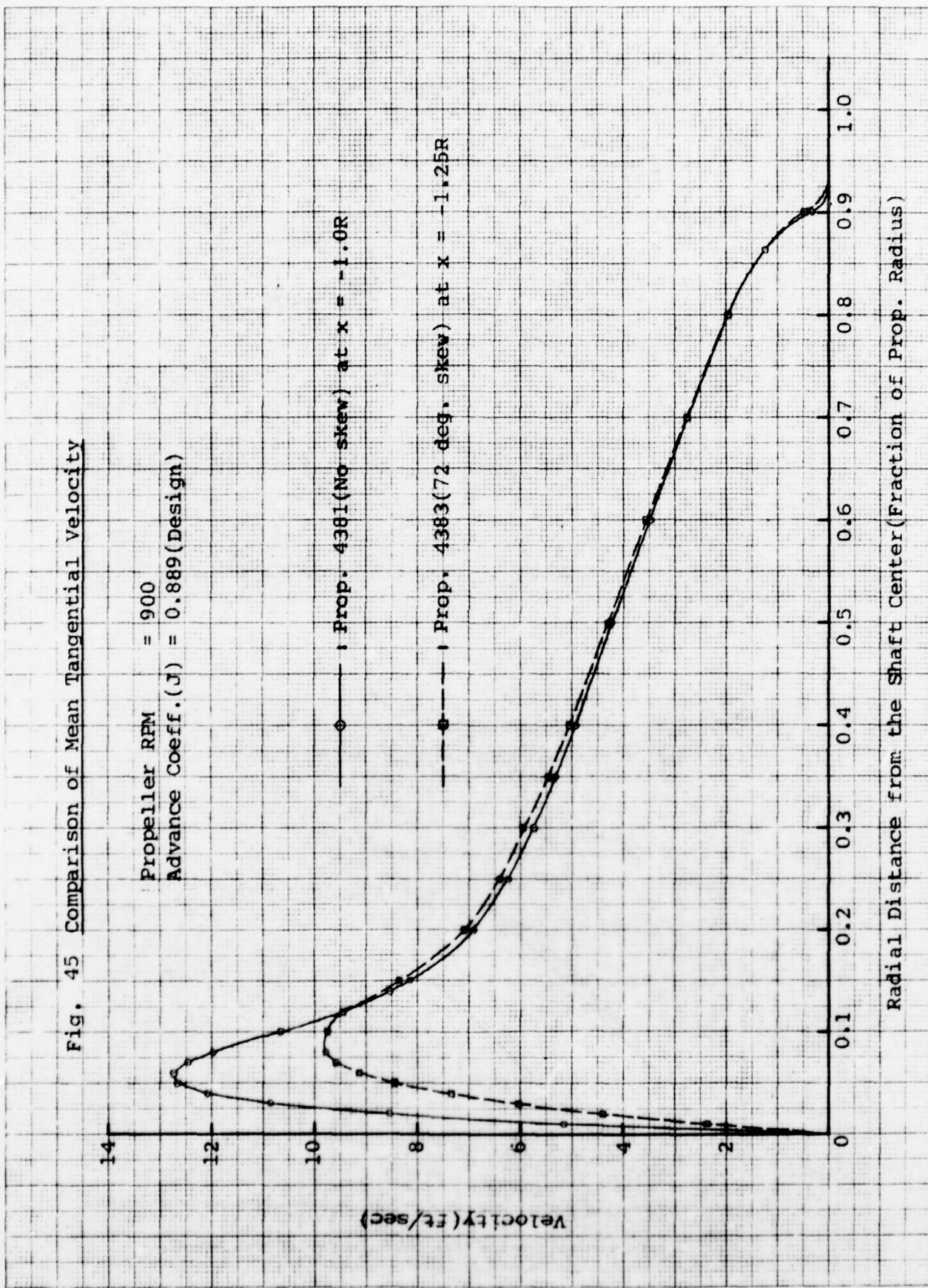
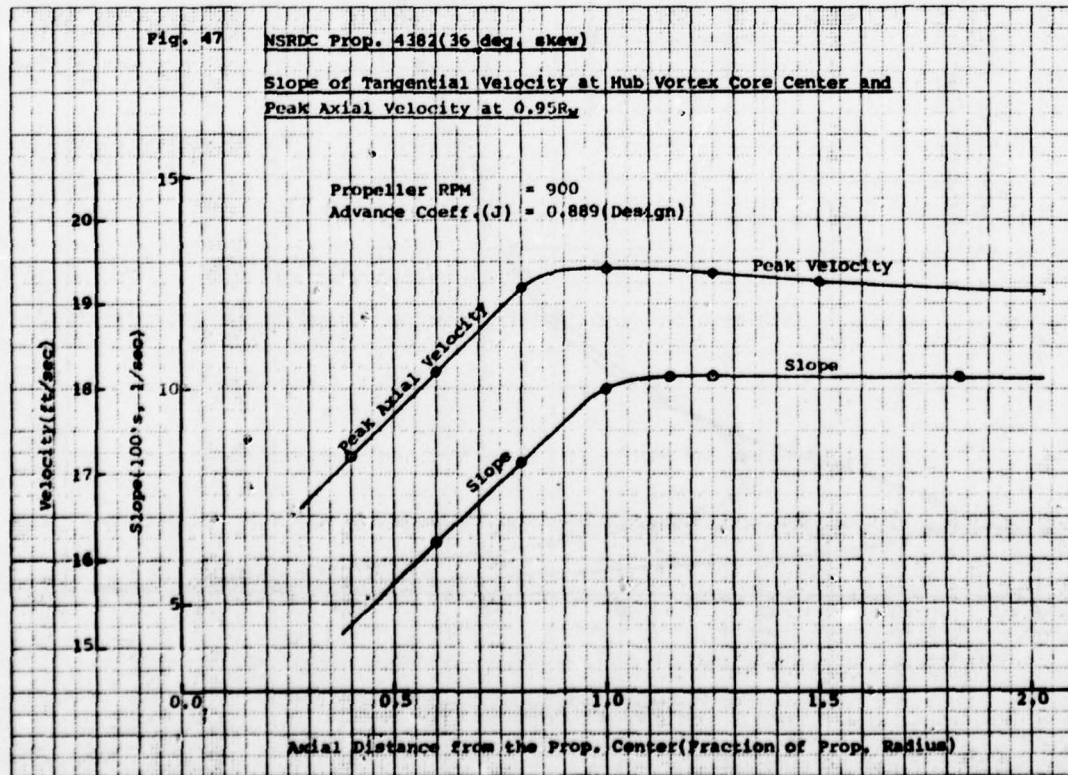
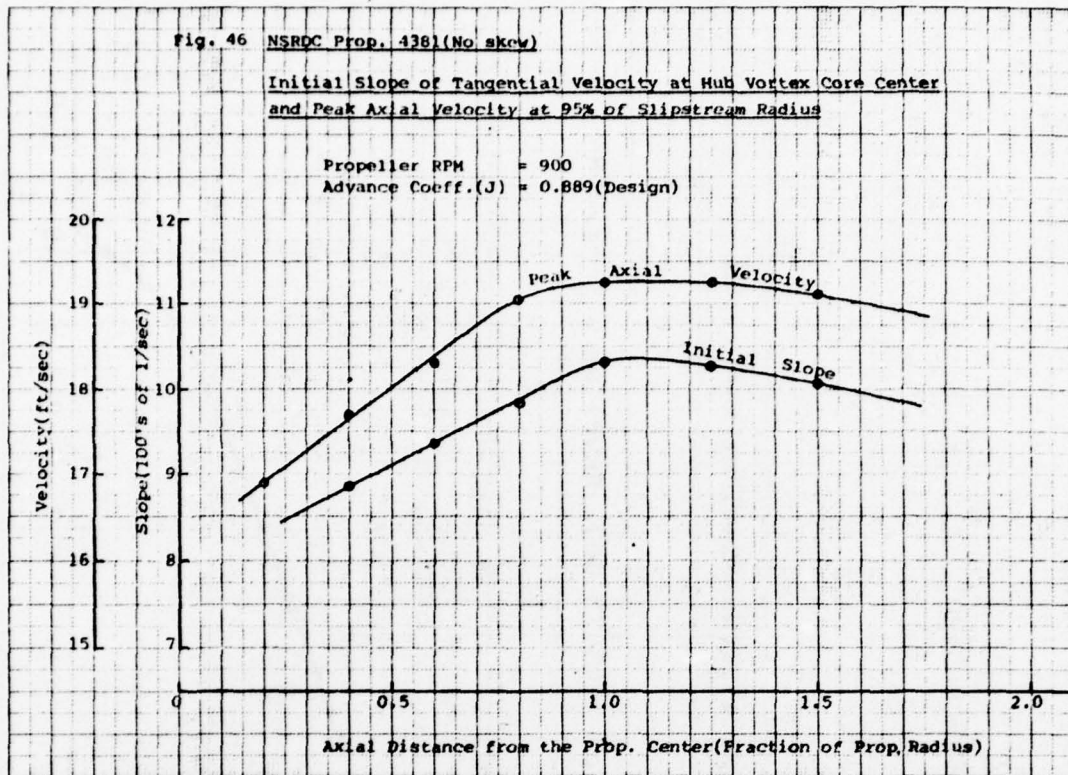


Fig. 45 Comparison of Mean Tangential Velocity





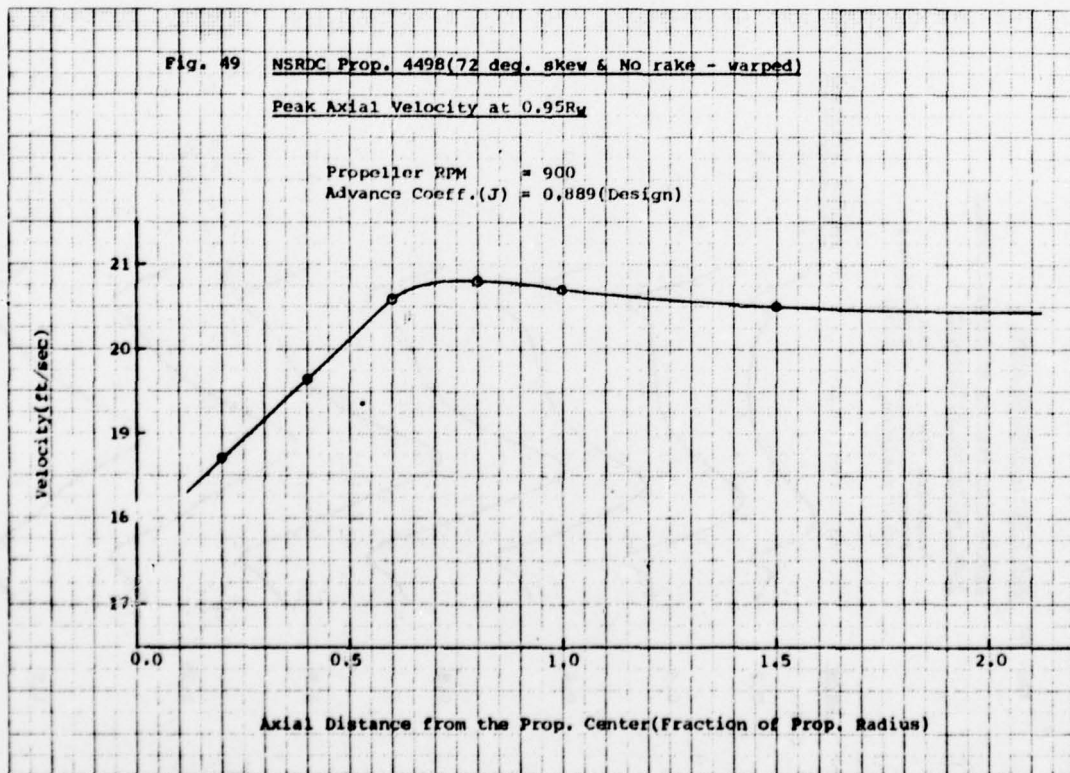
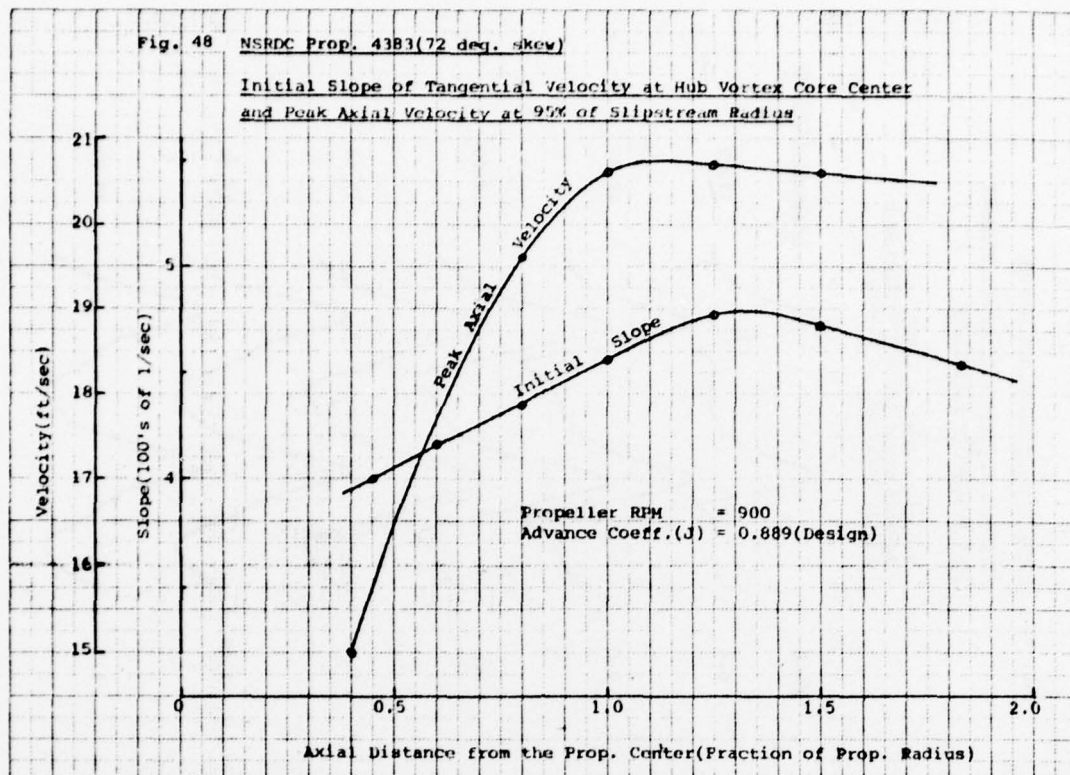


Fig. 50 NSRDC Prop. 4381(No skew)
Fluctuation Pattern of Axial Velocity
just inside the Slipstream

Propeller RPM = 900
 Advance Coeff. (J) = 0.889 (Design)
 Radial Position = $0.95 R_N$

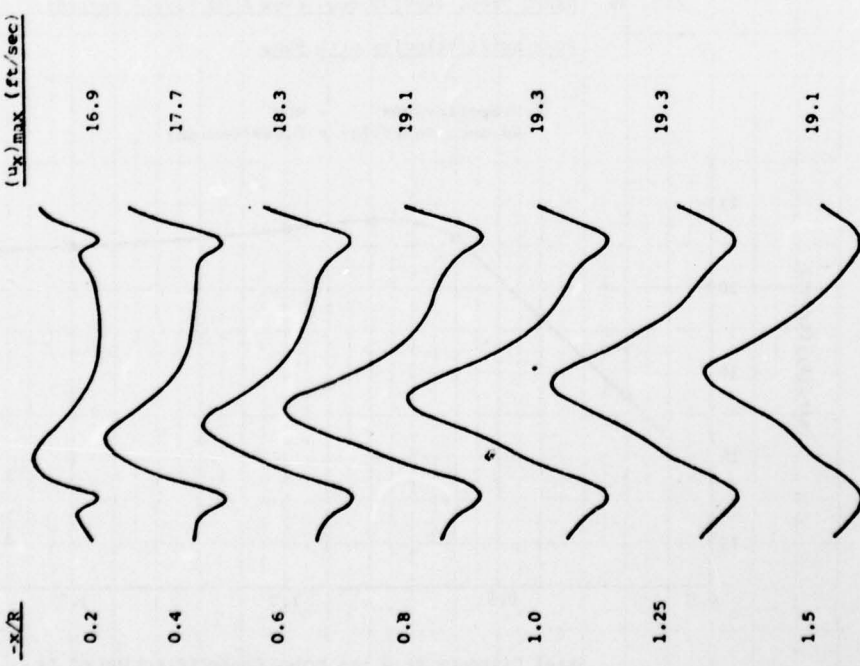


Fig. 51

NSRDC Prop. 4382(36 deg. skew)
Fluctuation Pattern of Axial Velocity
just inside the Slipstream

Propeller RPM = 900
 Advance Coeff. (J) = 0.889 (Design)
 Radial Position = $0.95 R_N$

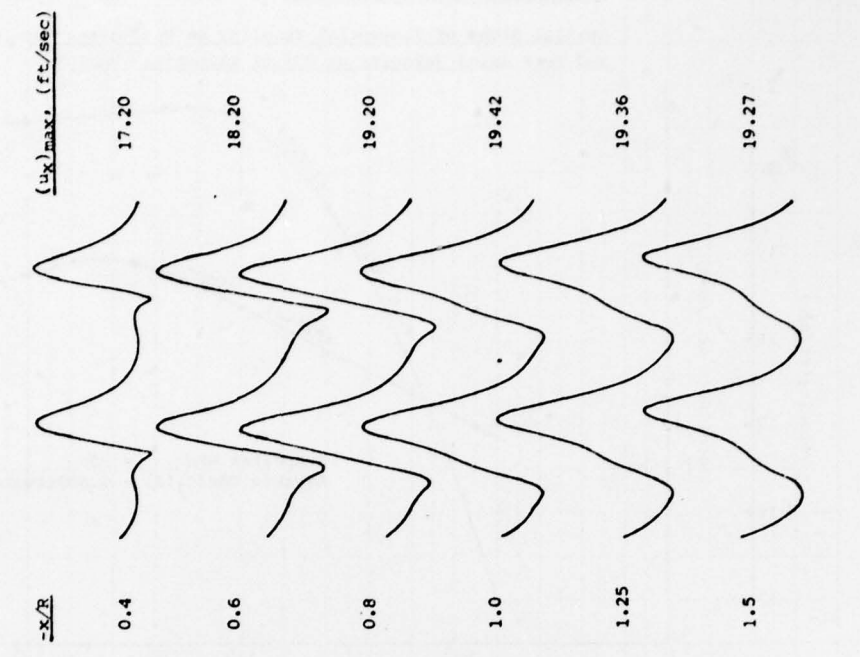


Fig. 52 NSRDC PROP. 4383(72 deg. skew)
Fluctuation Pattern of Axial Velocity
 just inside the Slipstream

Propeller RPM = 900
 Advance Coeff. (J) = 0.889 (Design)
 Radial Position = $0.95 R_w$

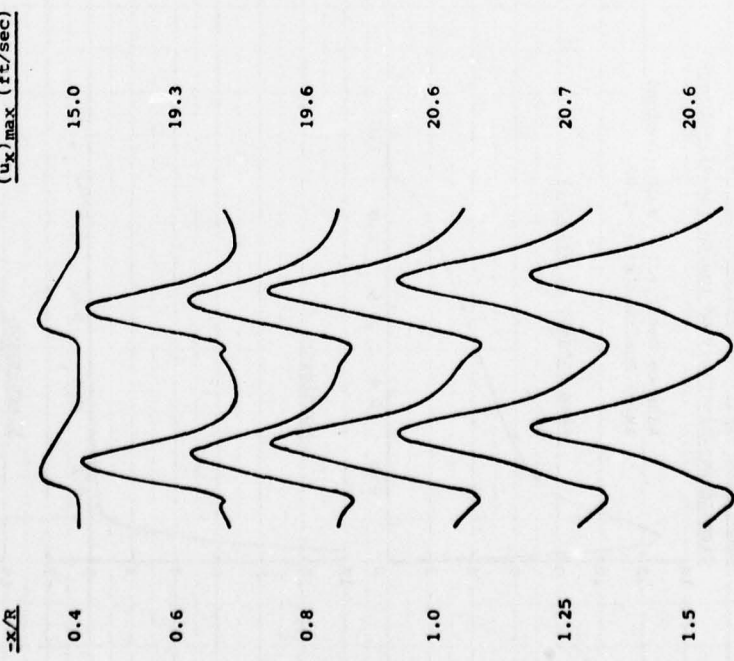
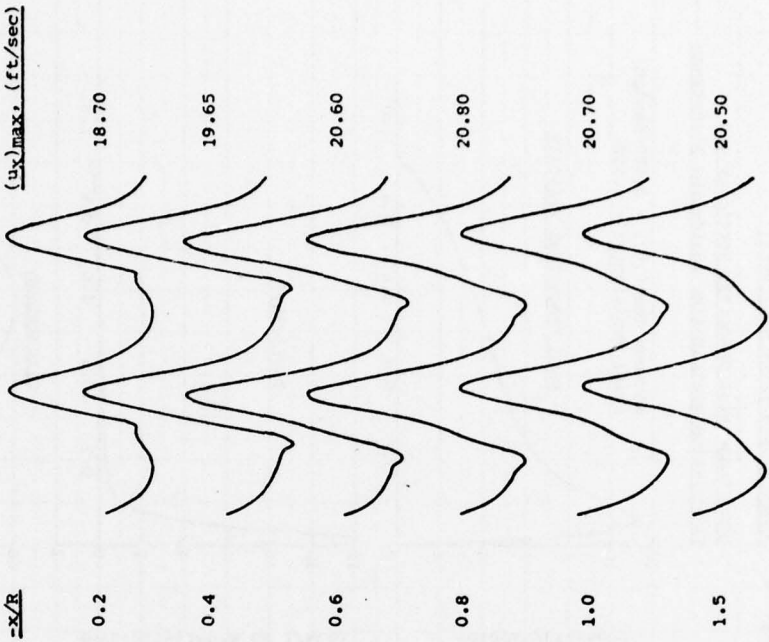
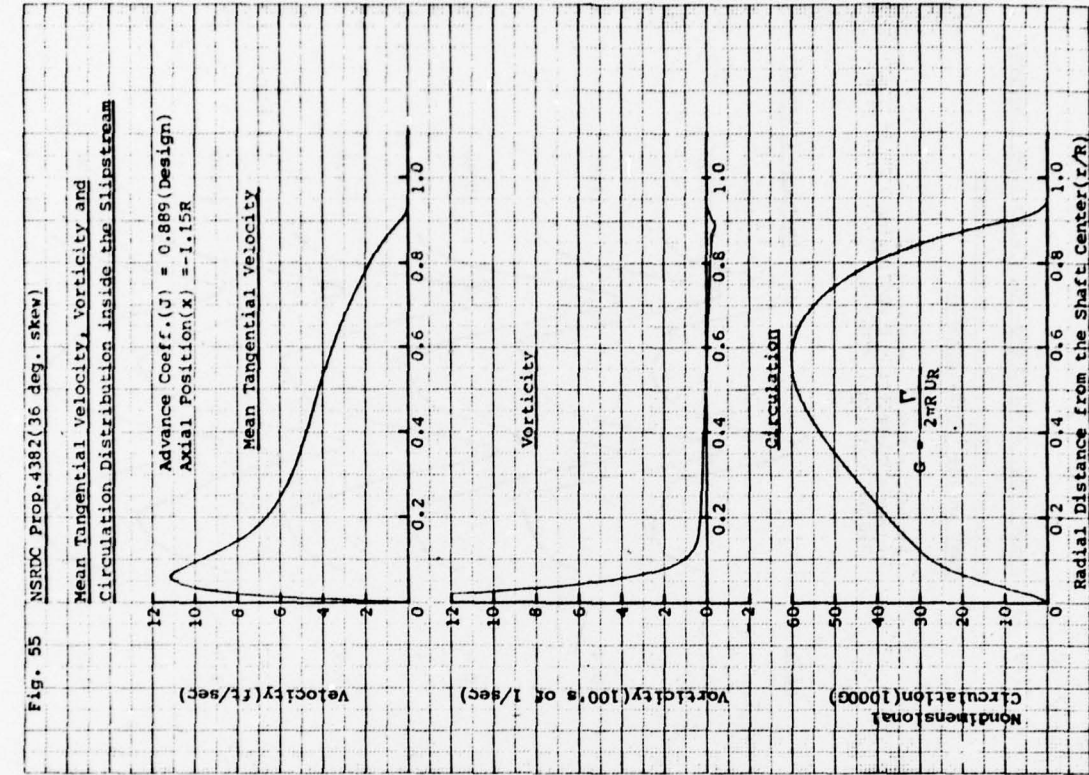
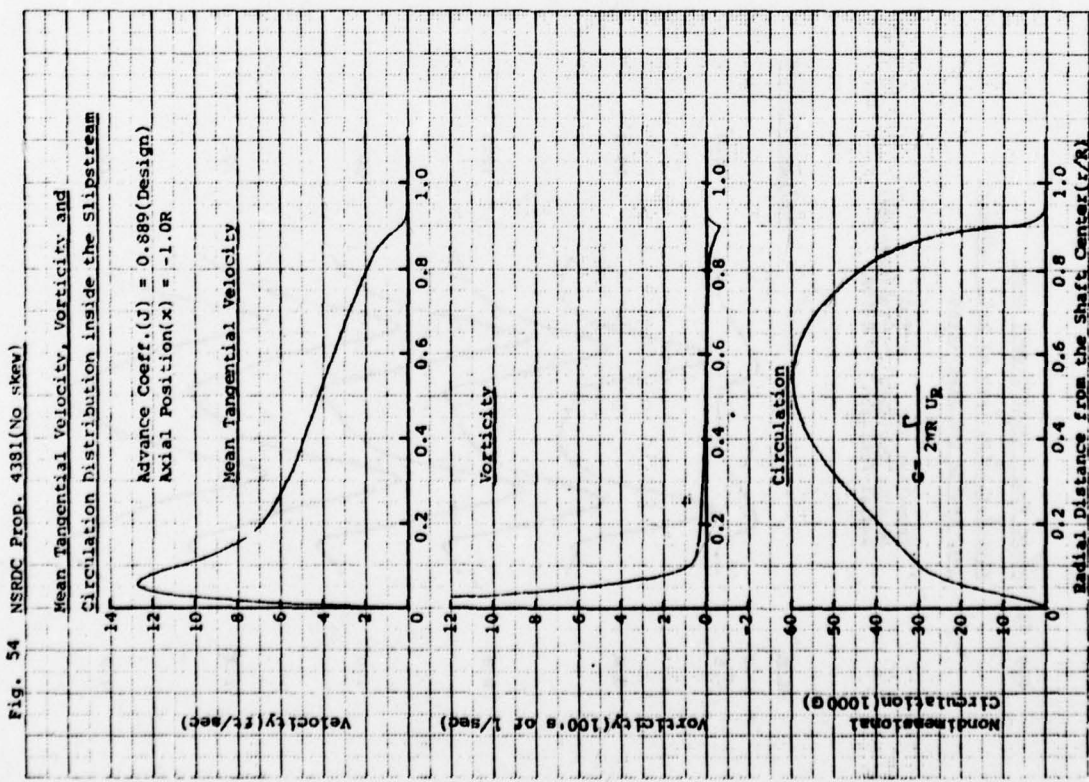
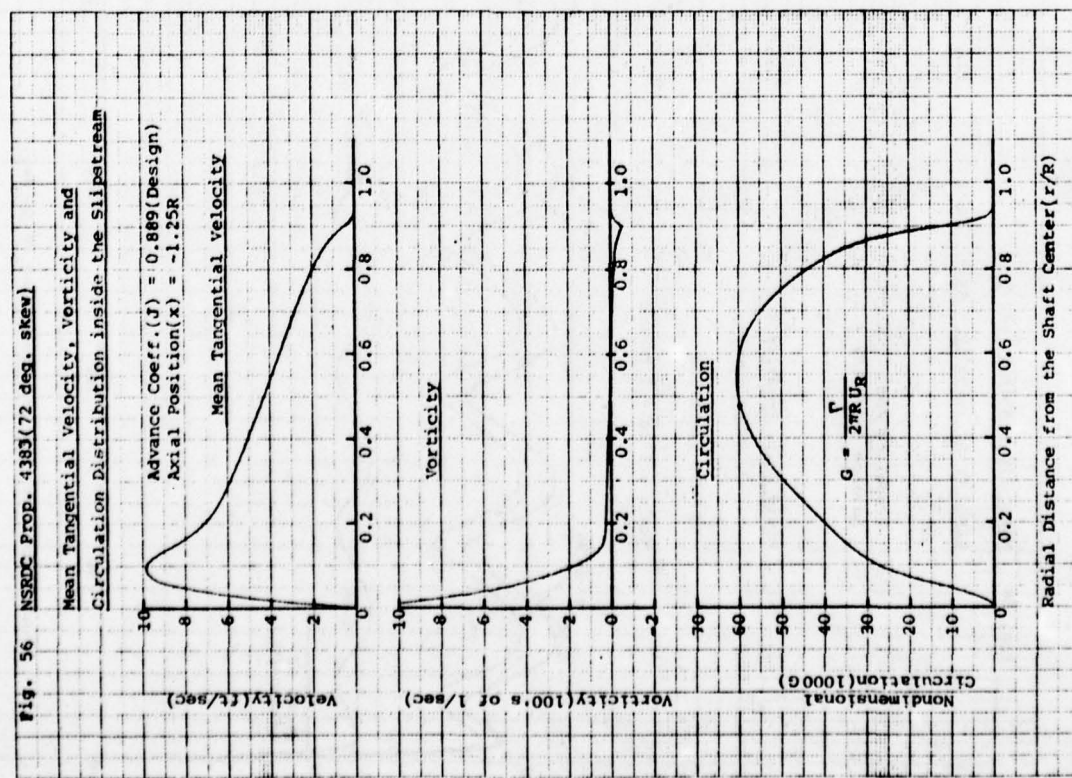
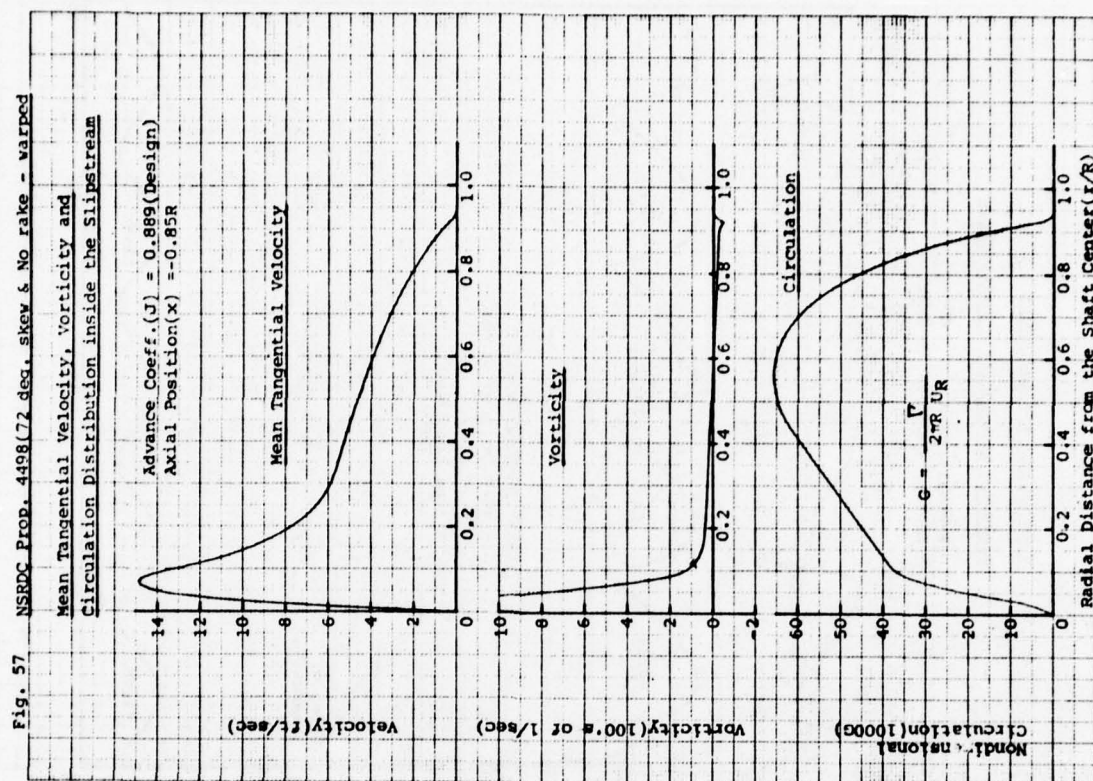


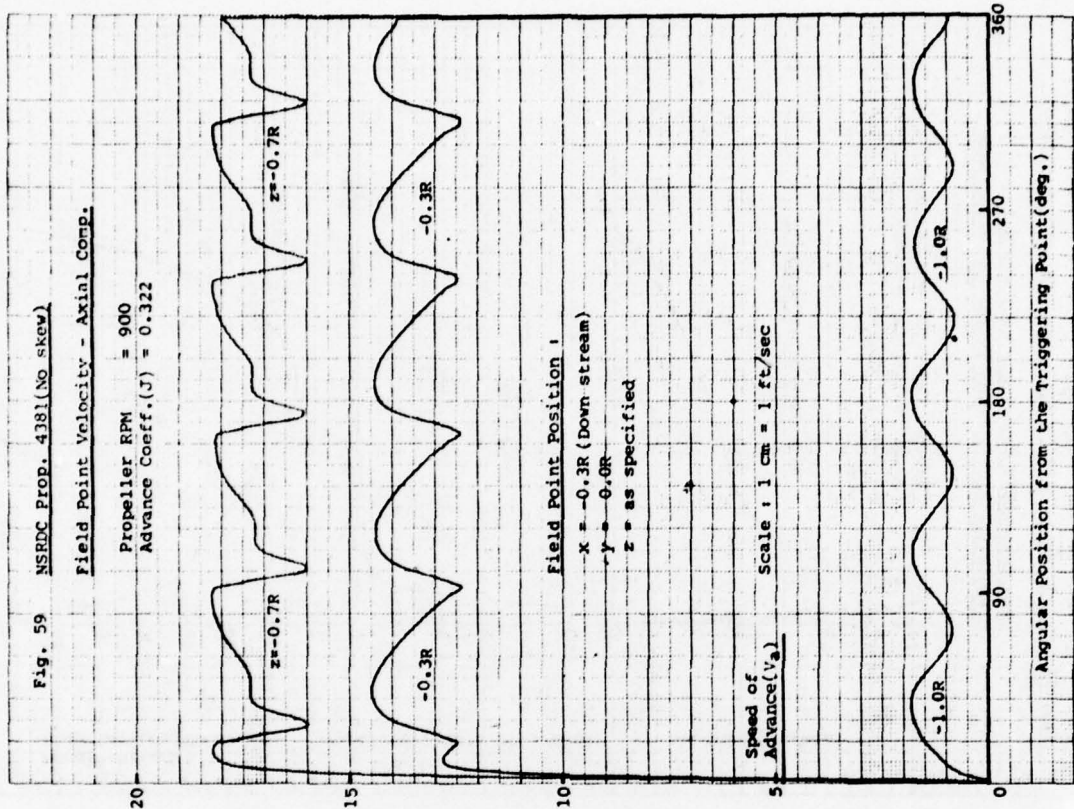
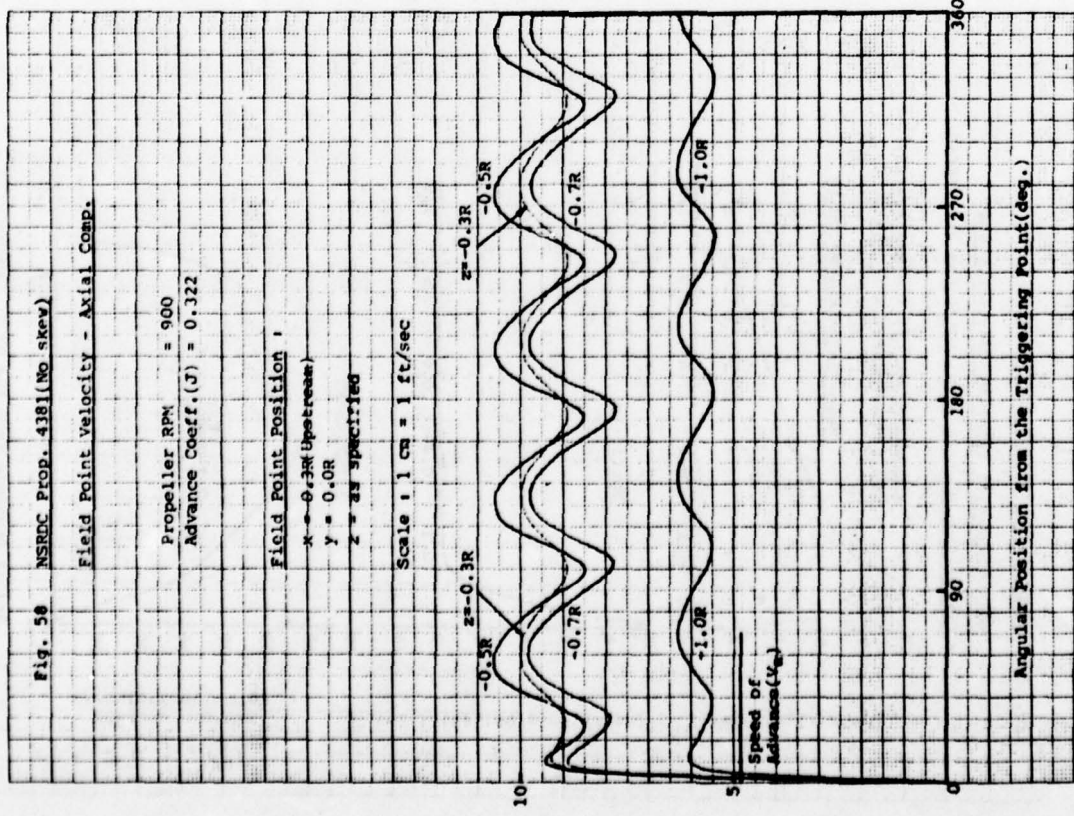
Fig. 53 NSRDC PROP. 4498(72 deg. skew & No rake - Warped)
Fluctuation Pattern of Axial Velocity
 just inside the Slipstream

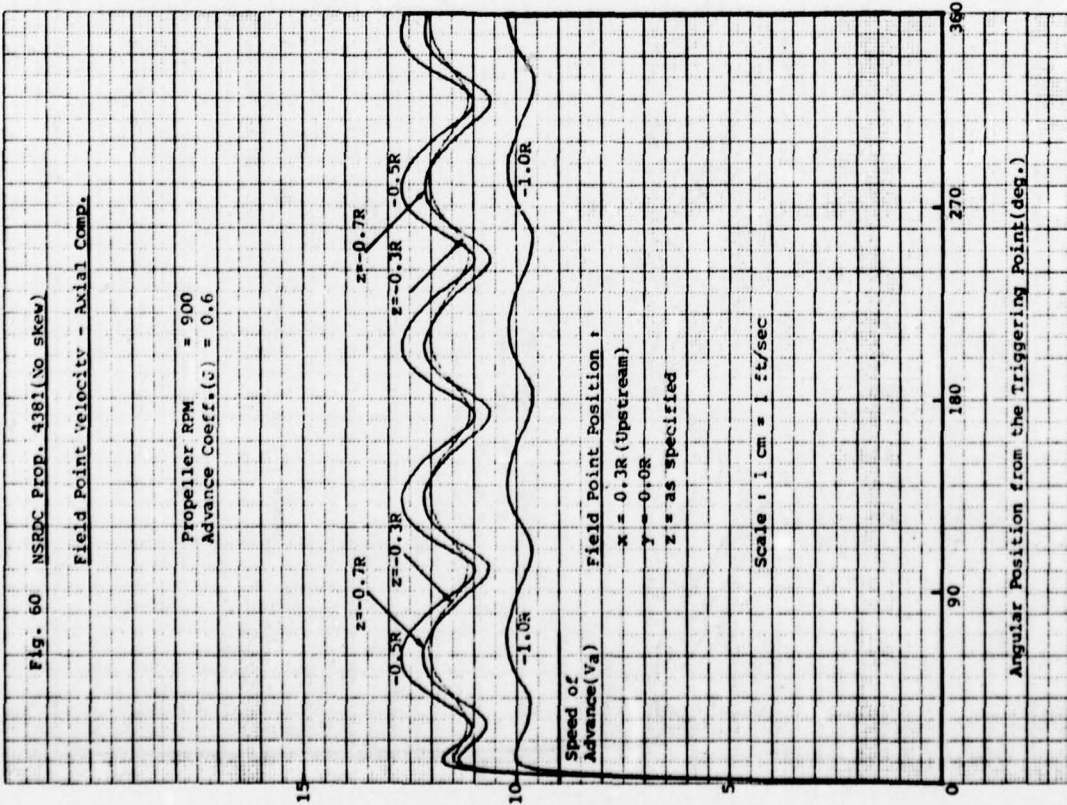
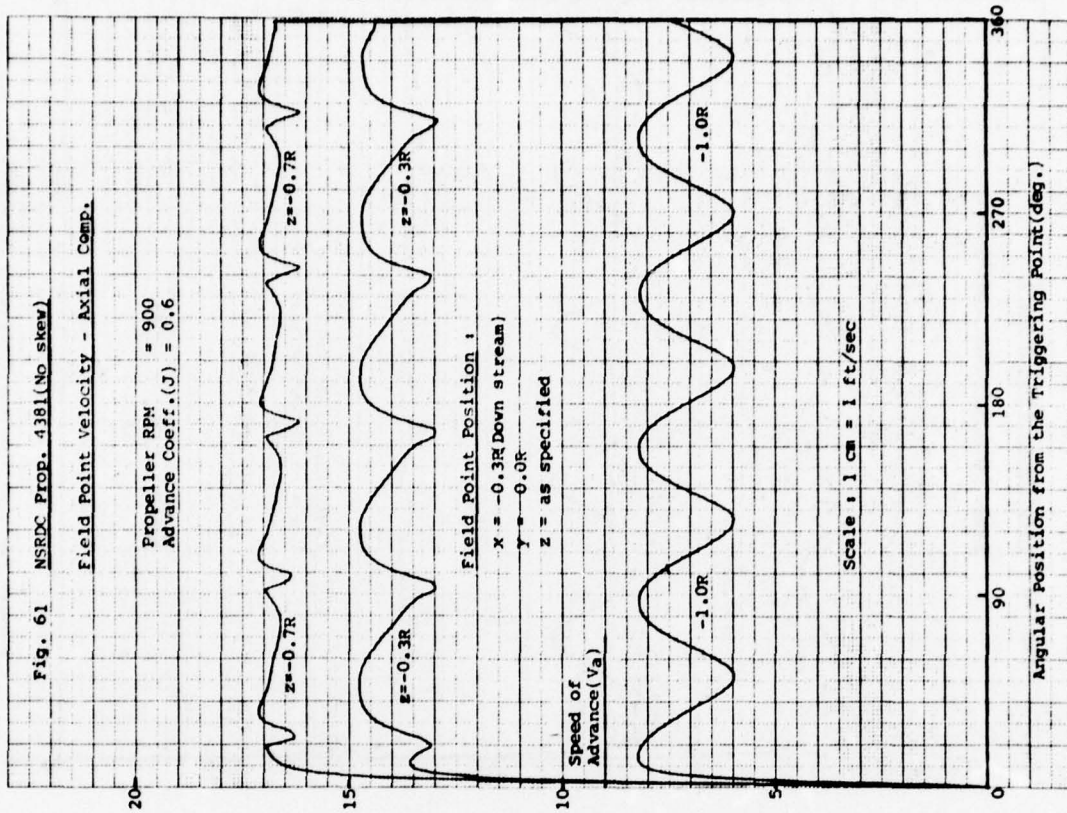
Propeller RPM = 900
 Advance Coeff. (J) = 0.889 (Design)
 Radial Position = $0.95 R_w$

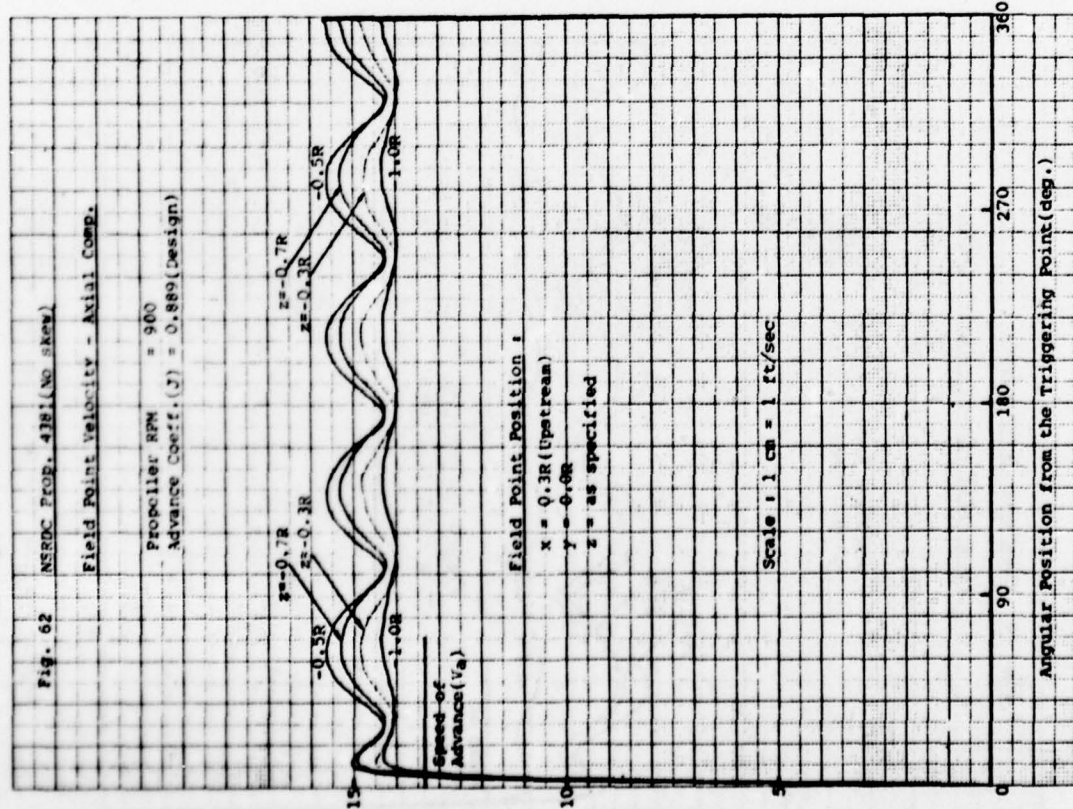
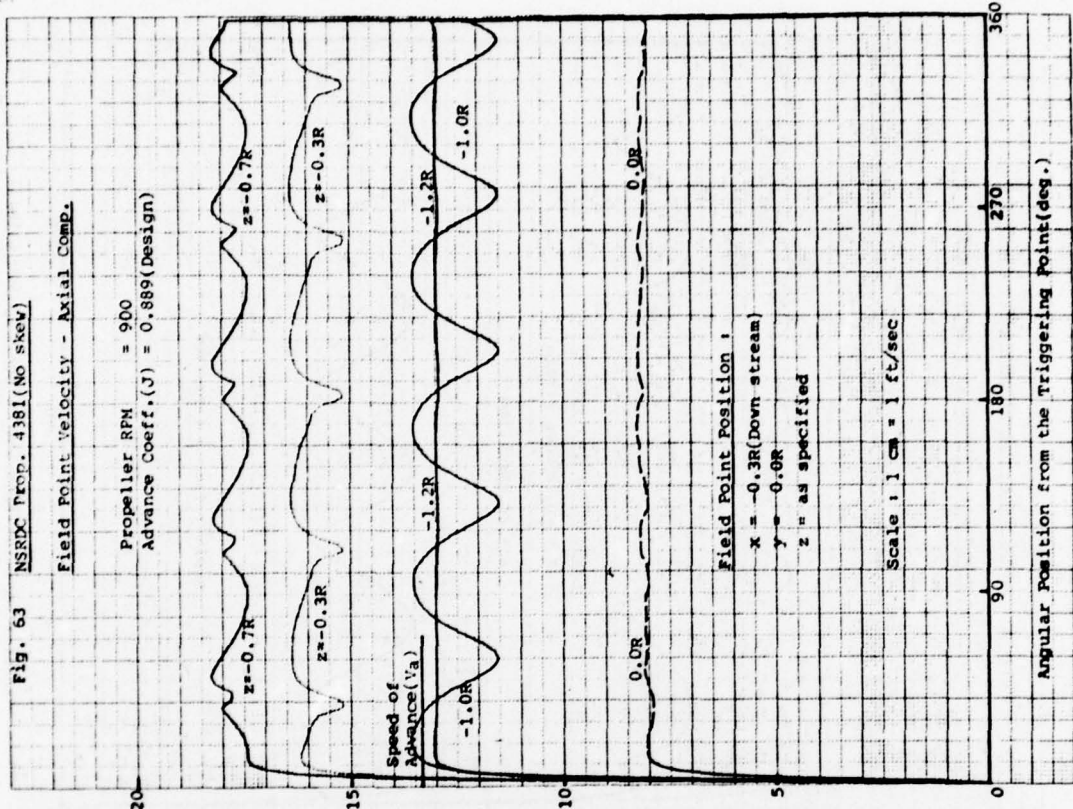


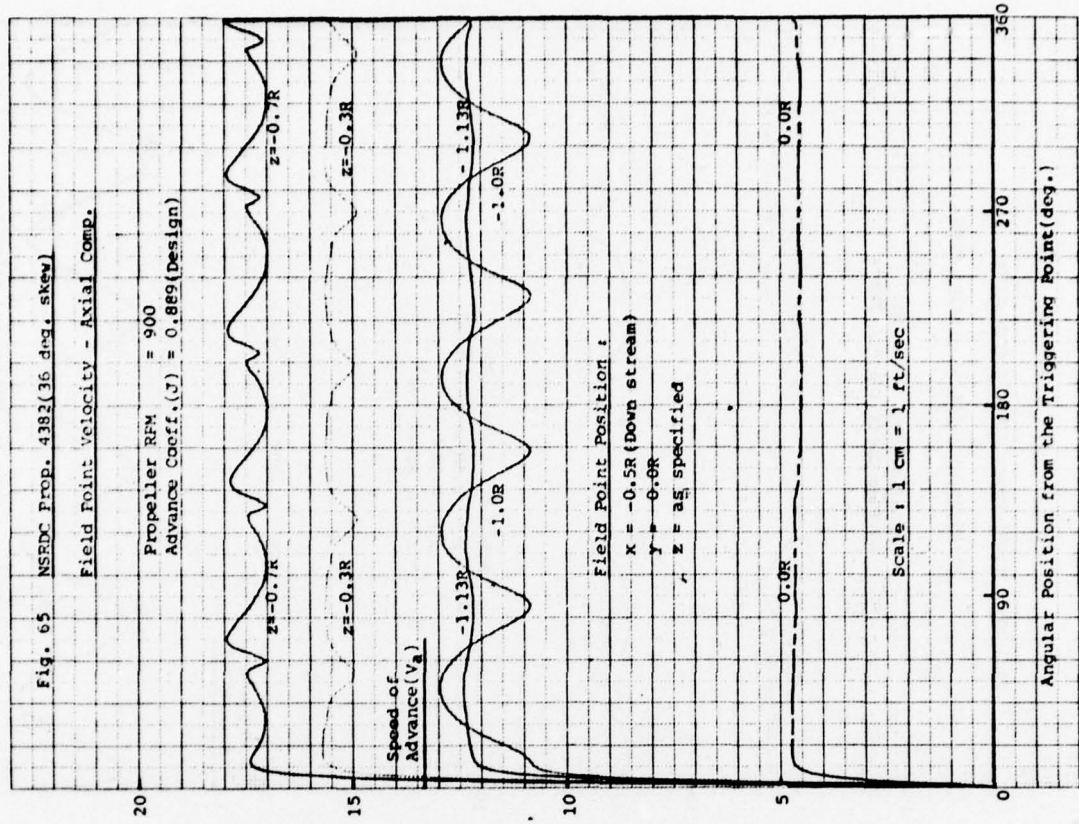
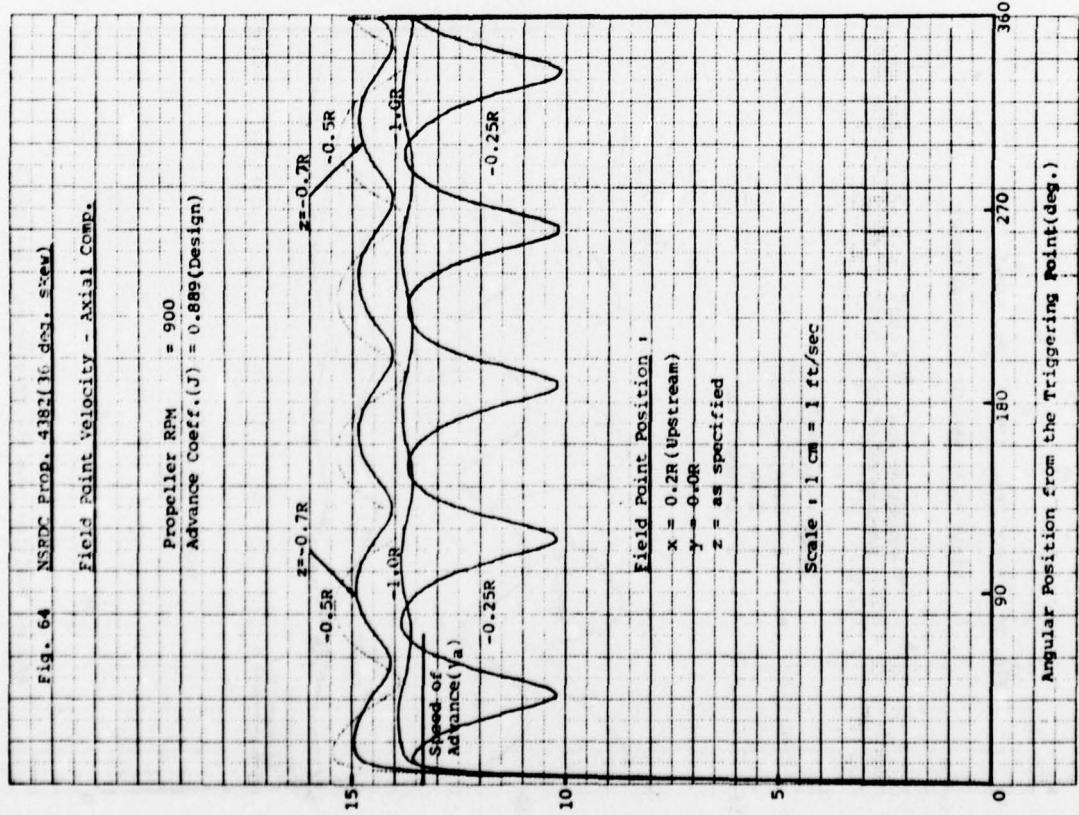


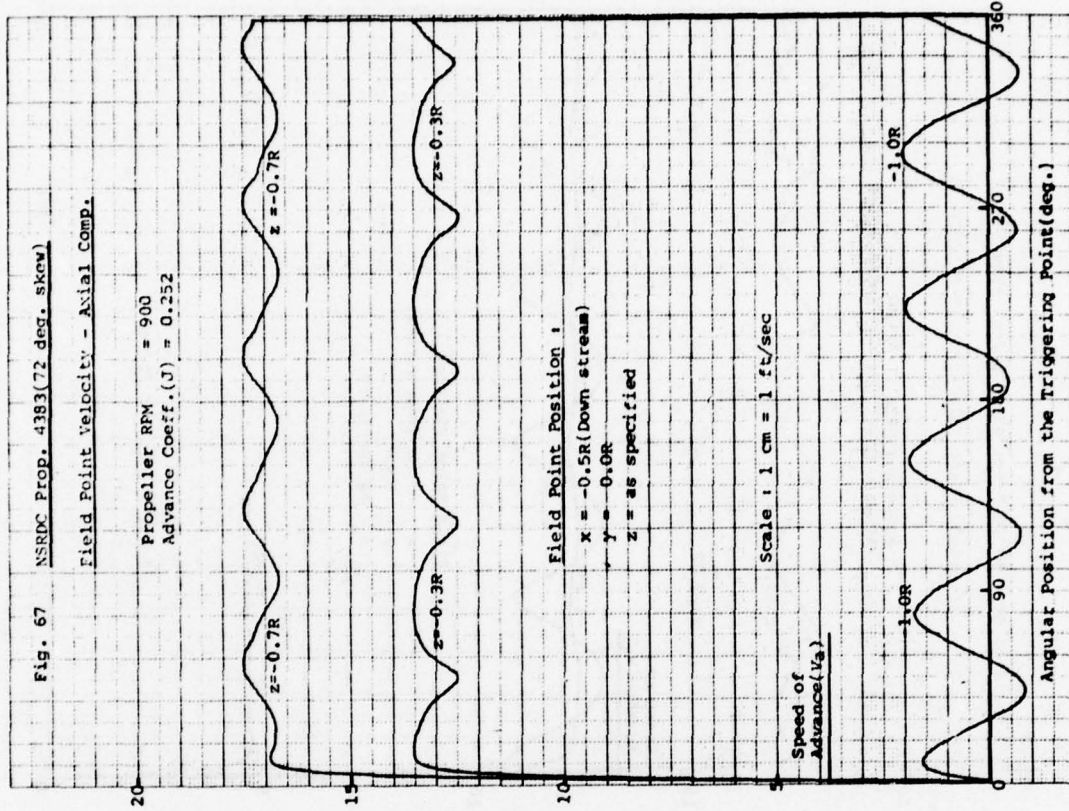
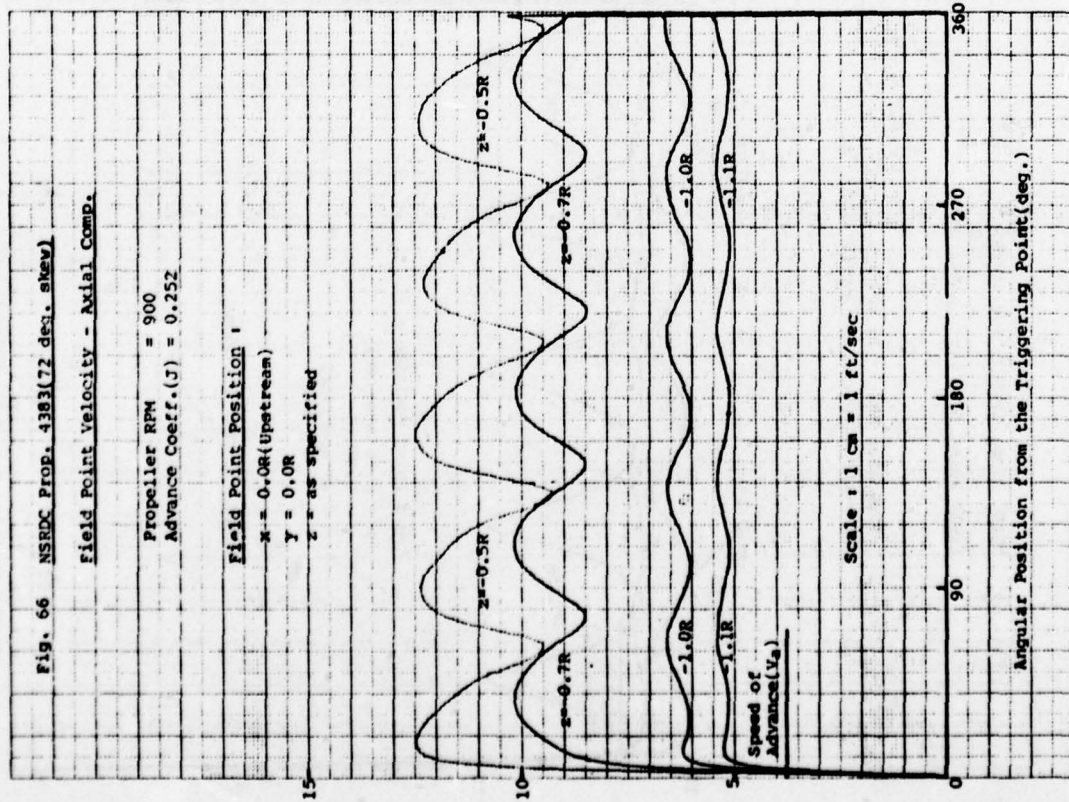


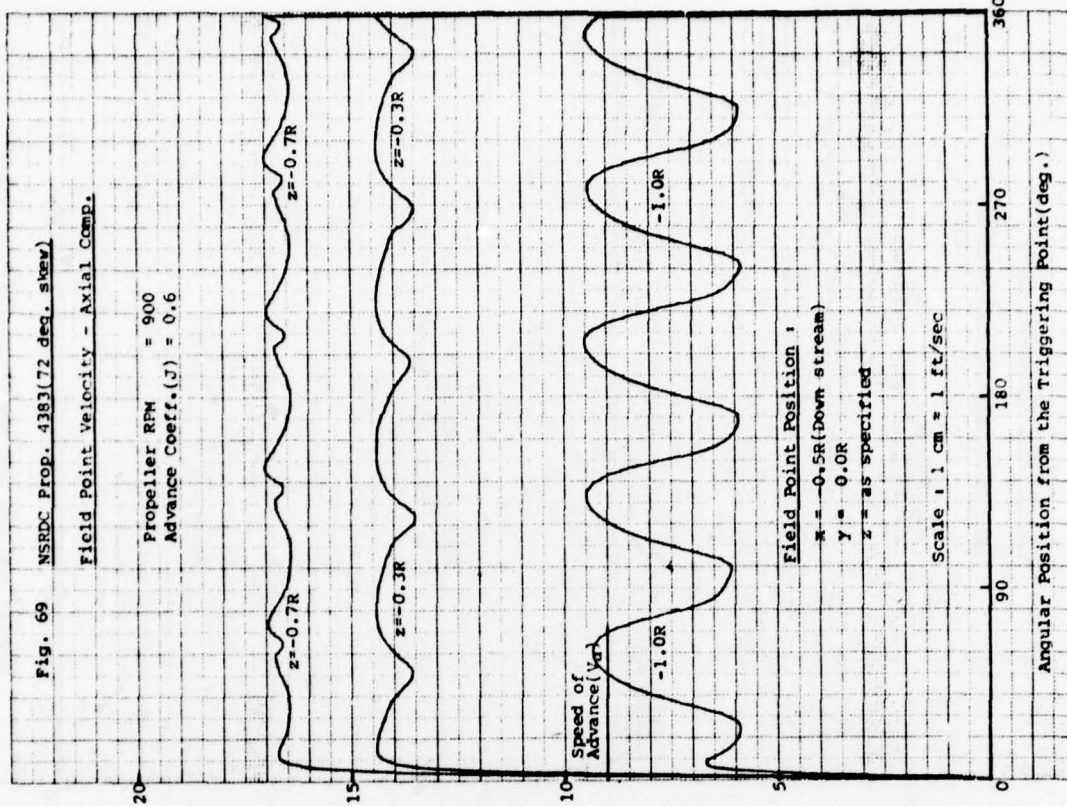
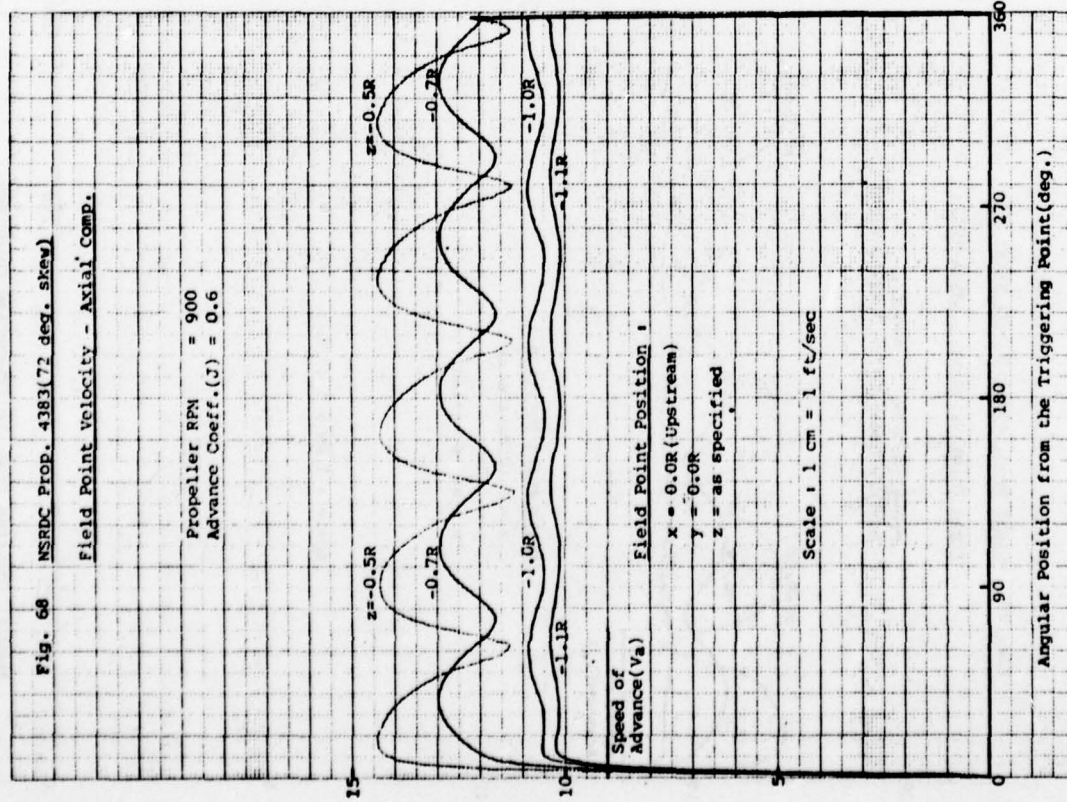


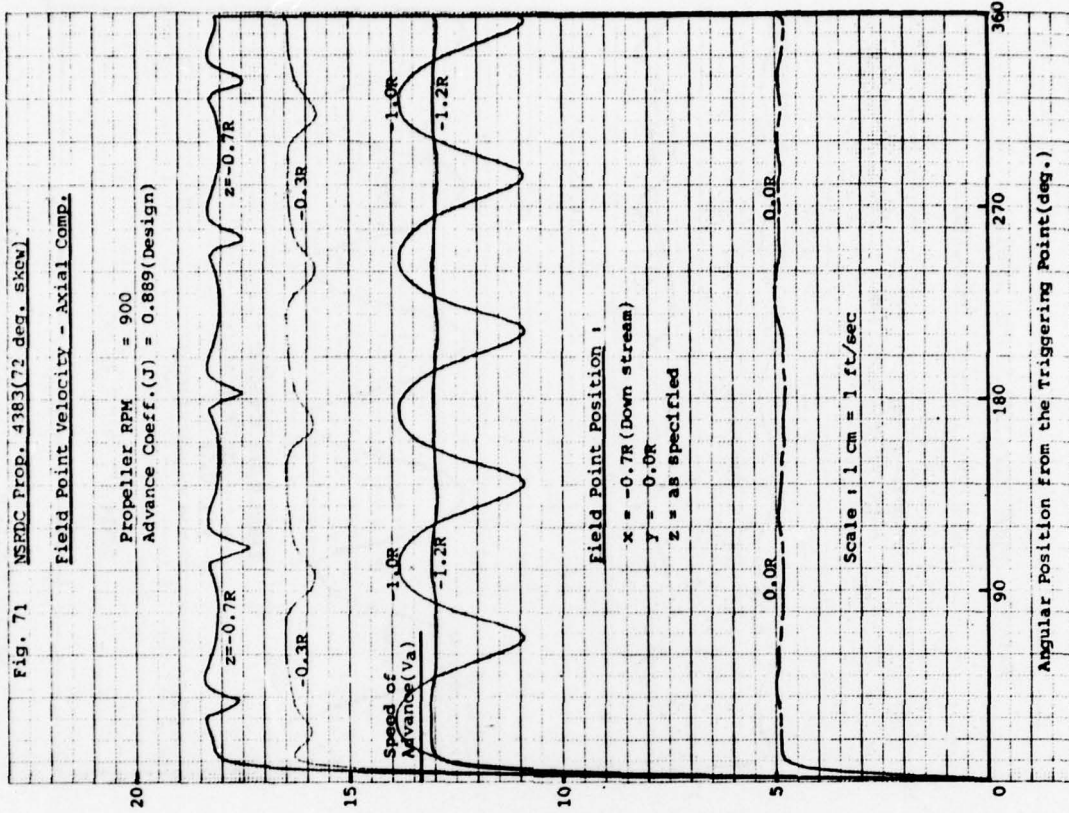
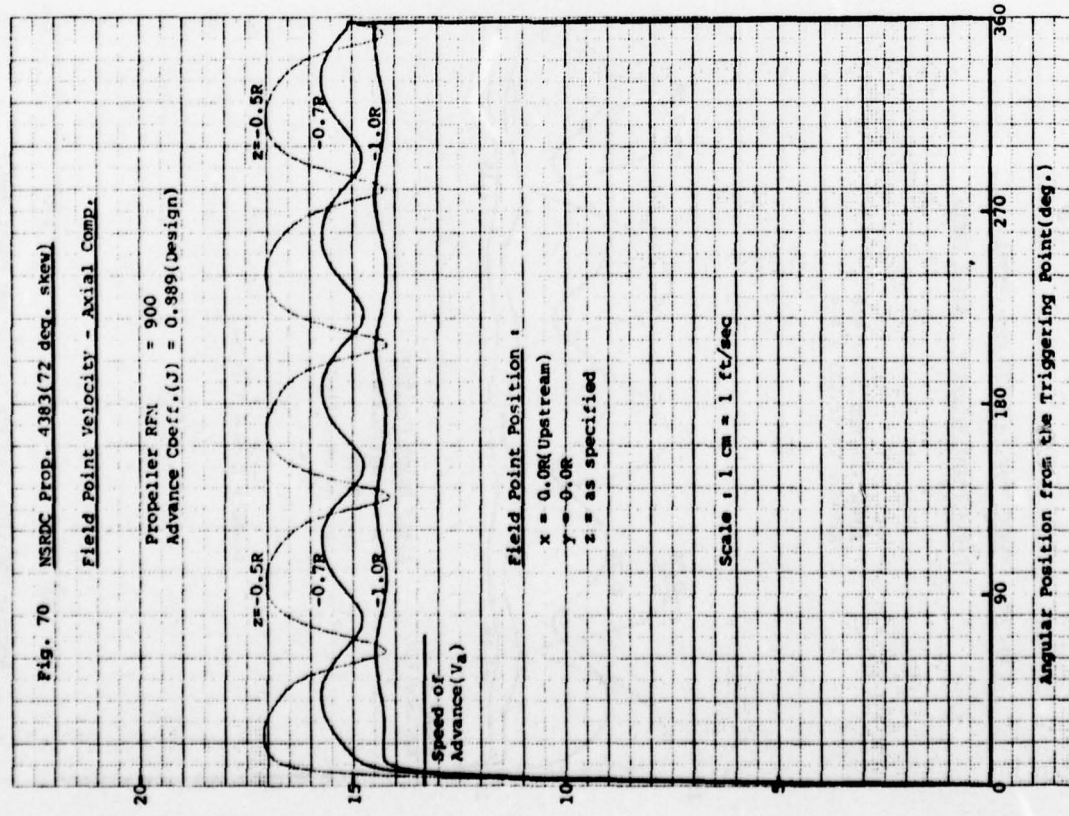


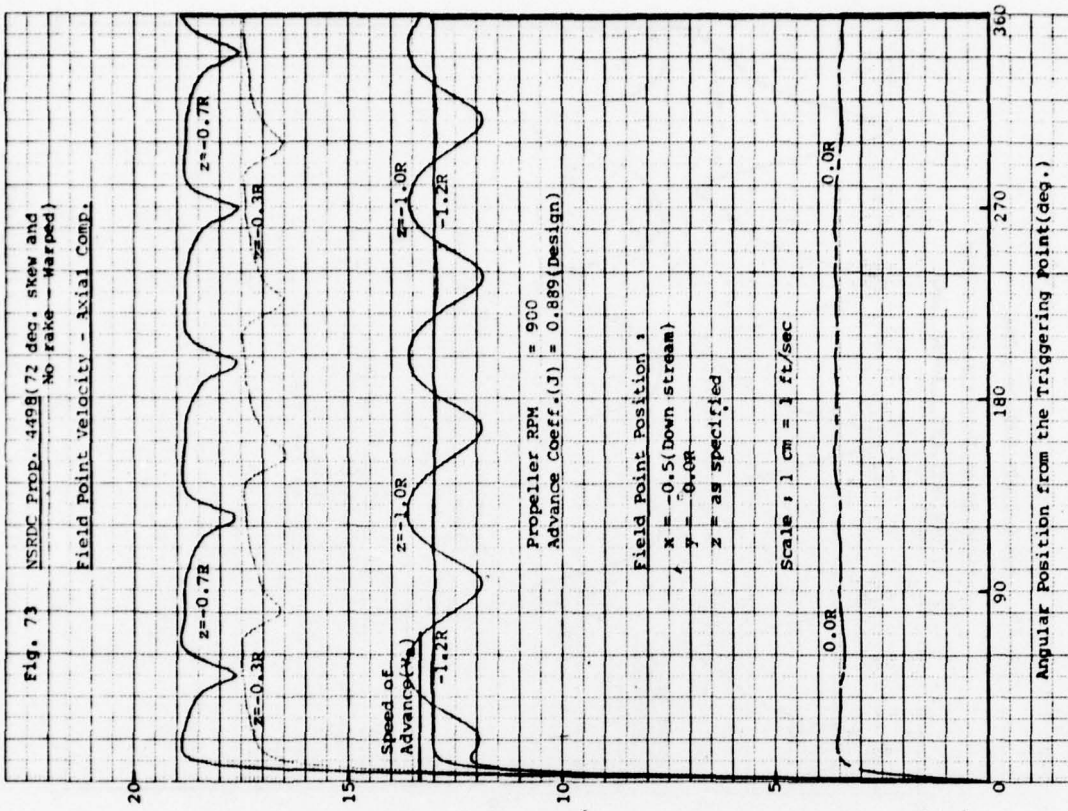
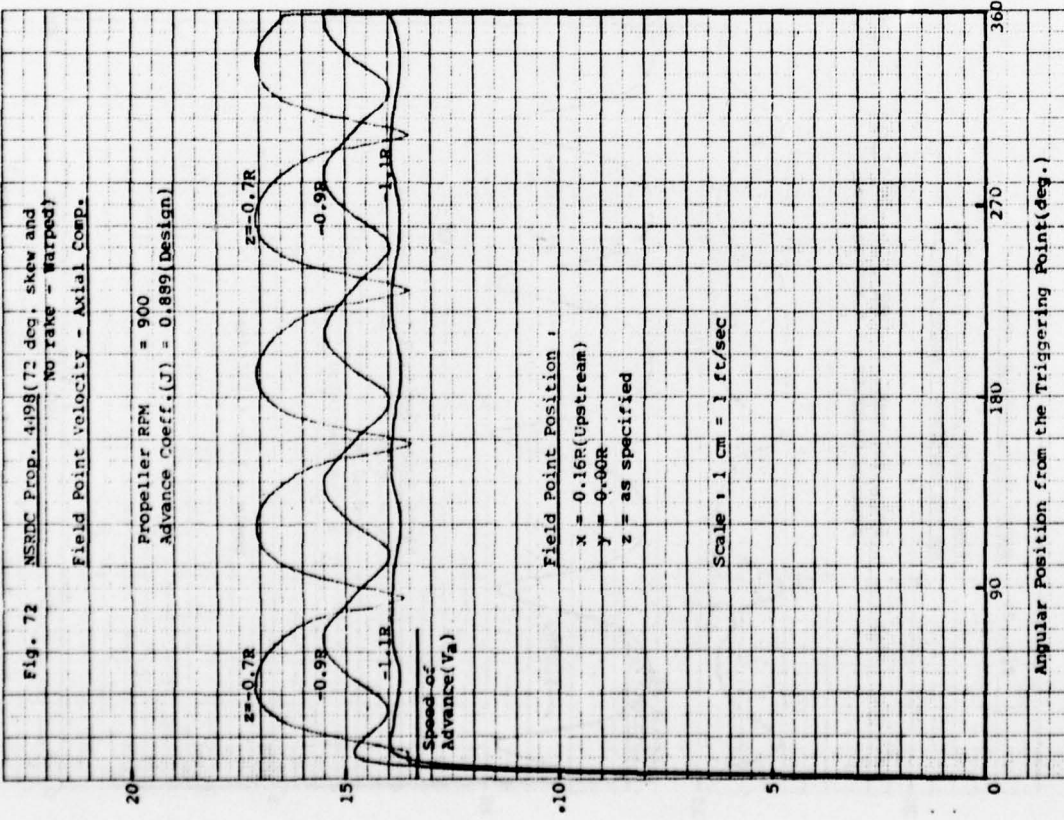


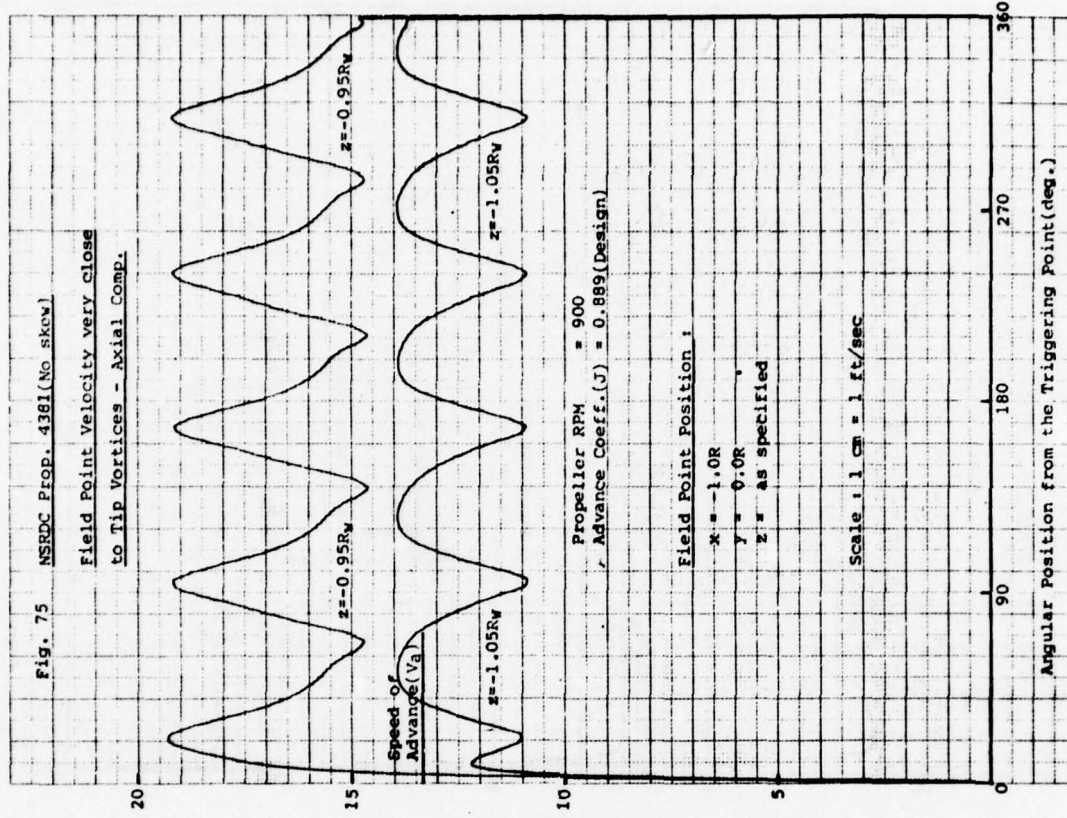
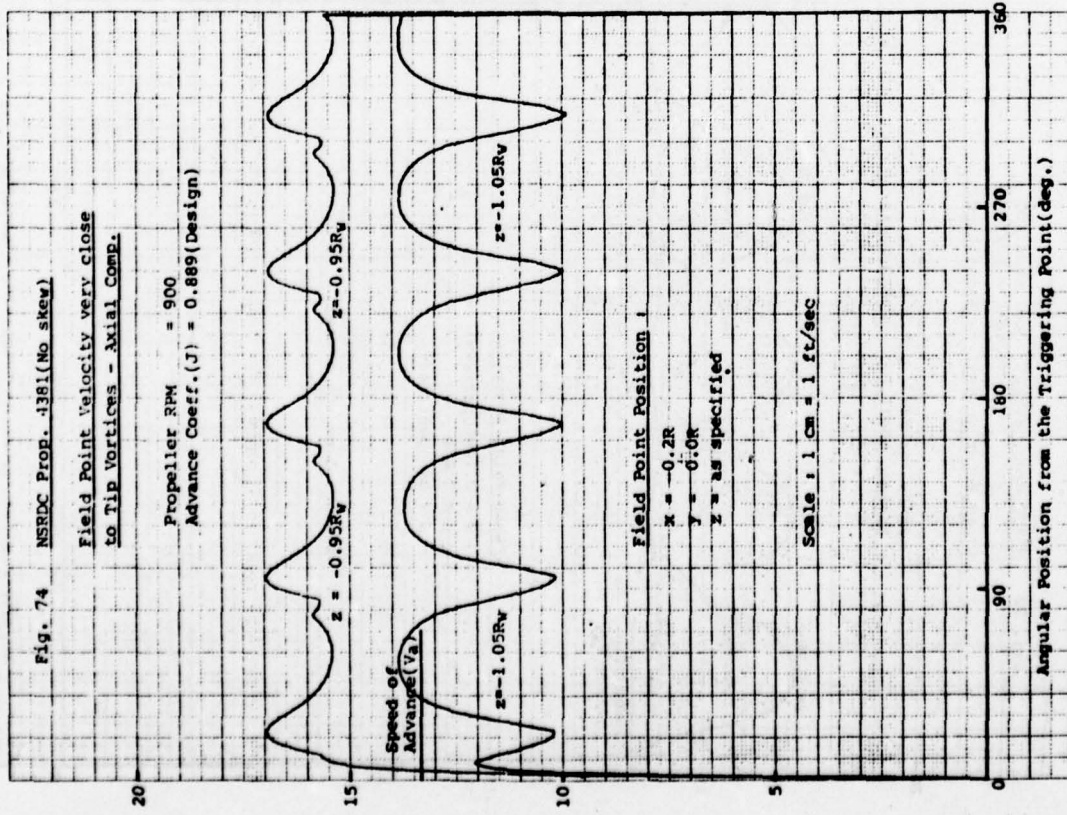


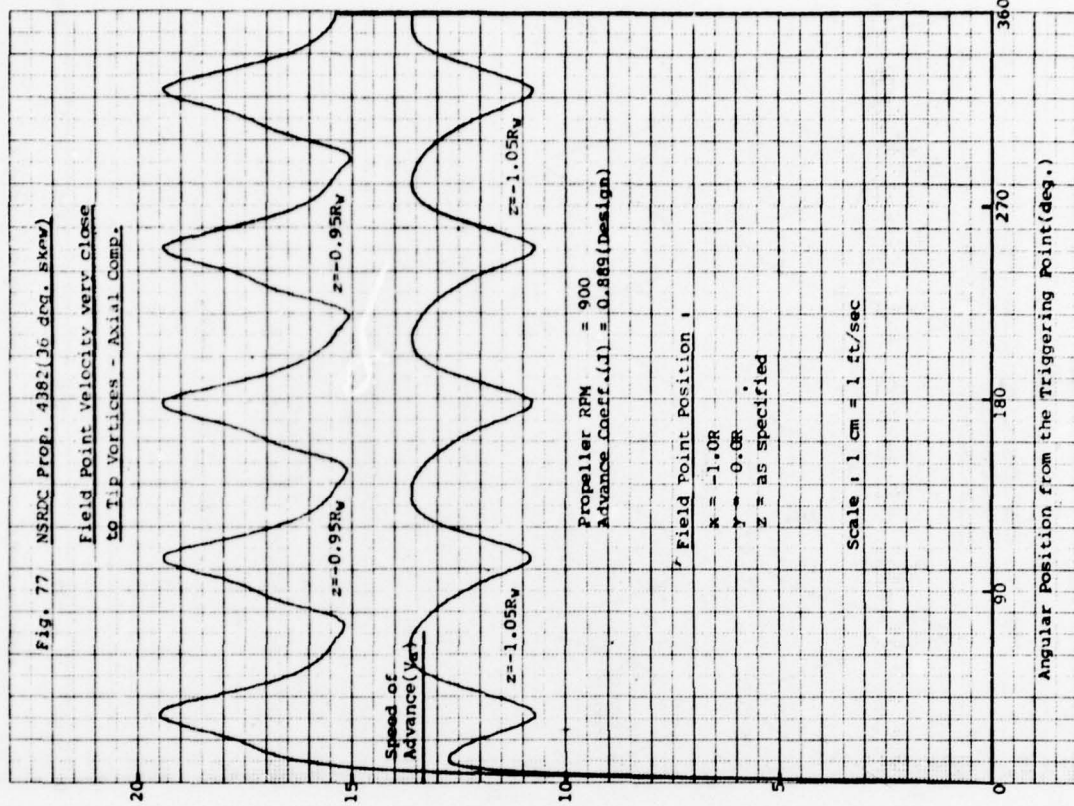
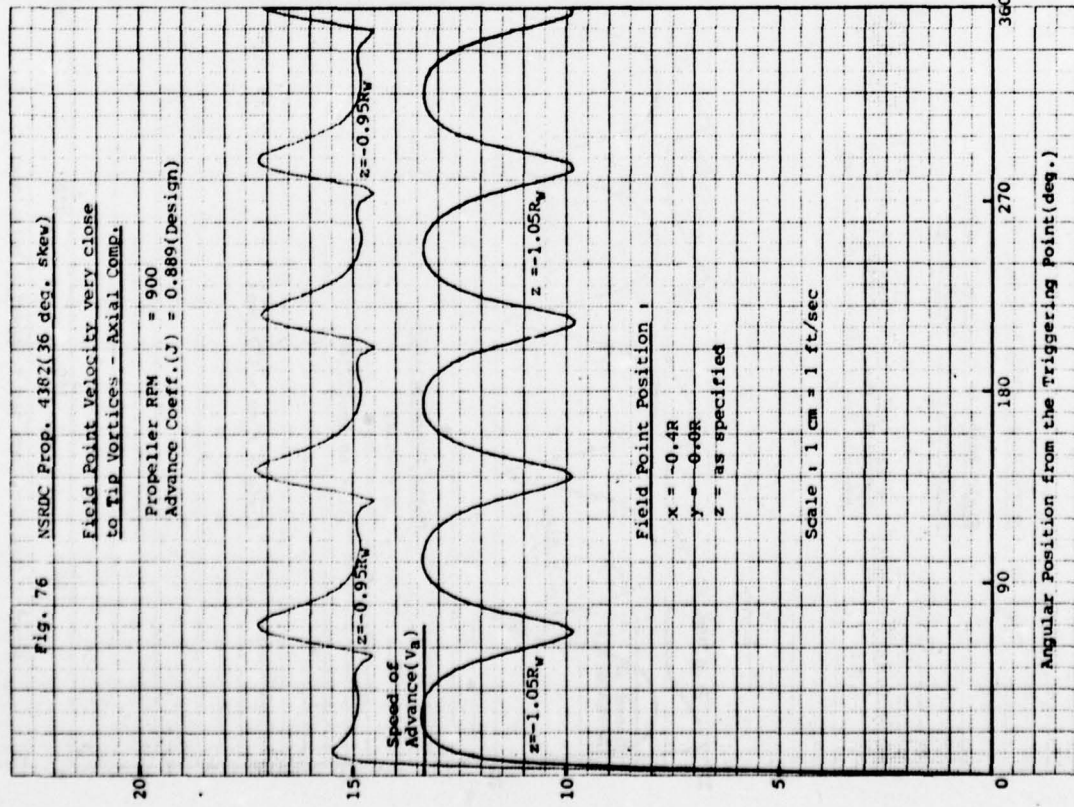


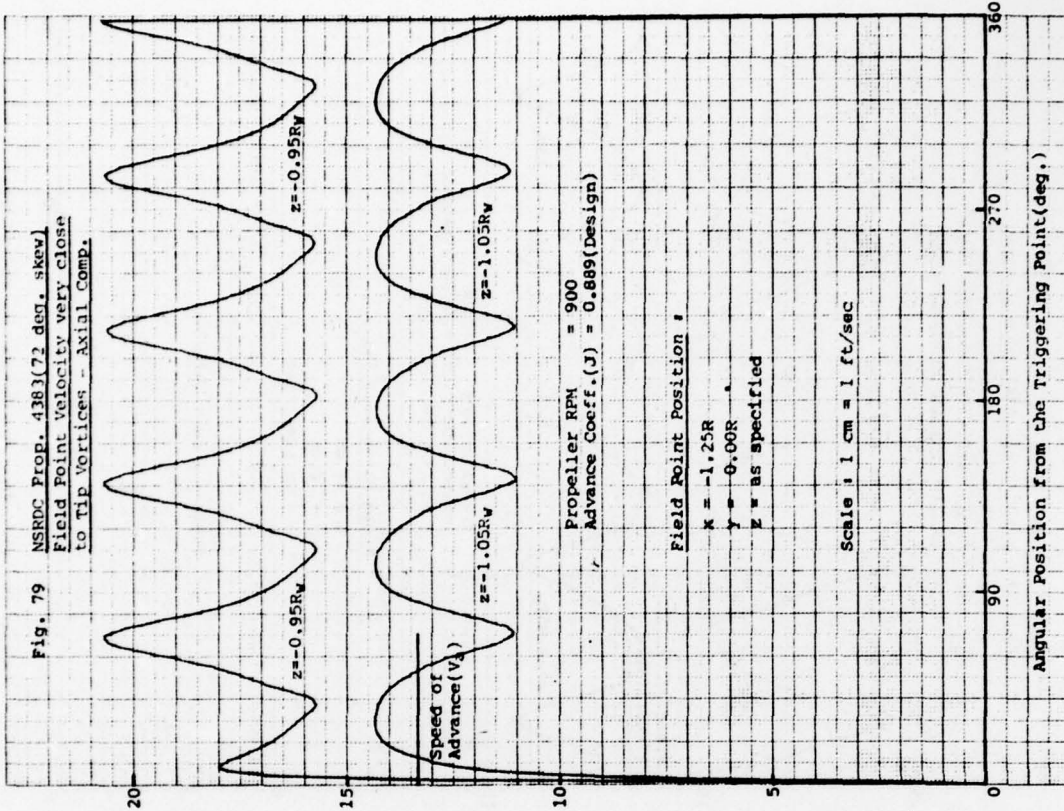
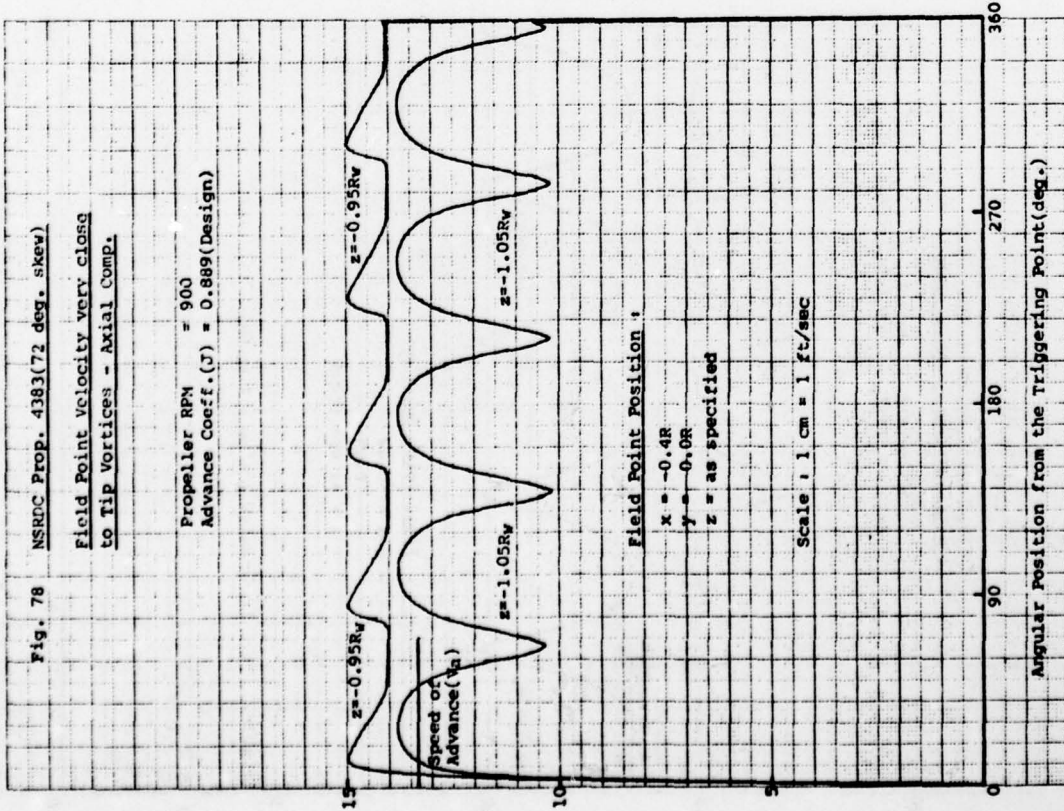












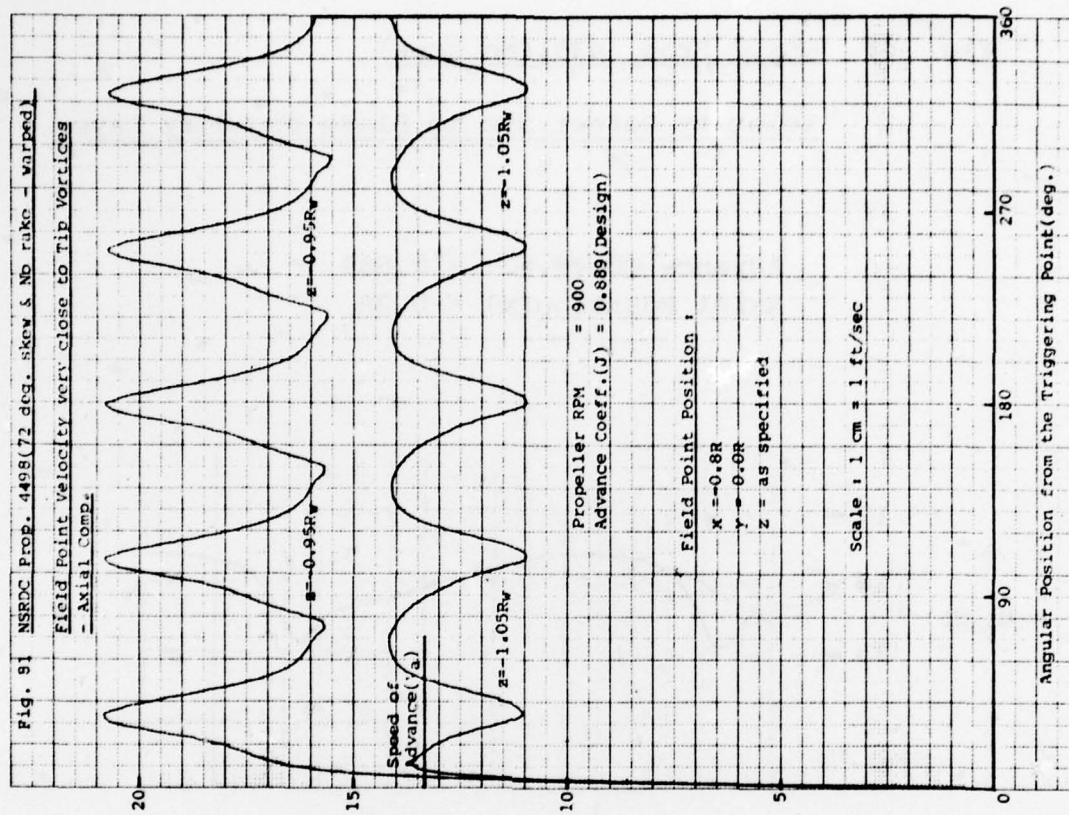
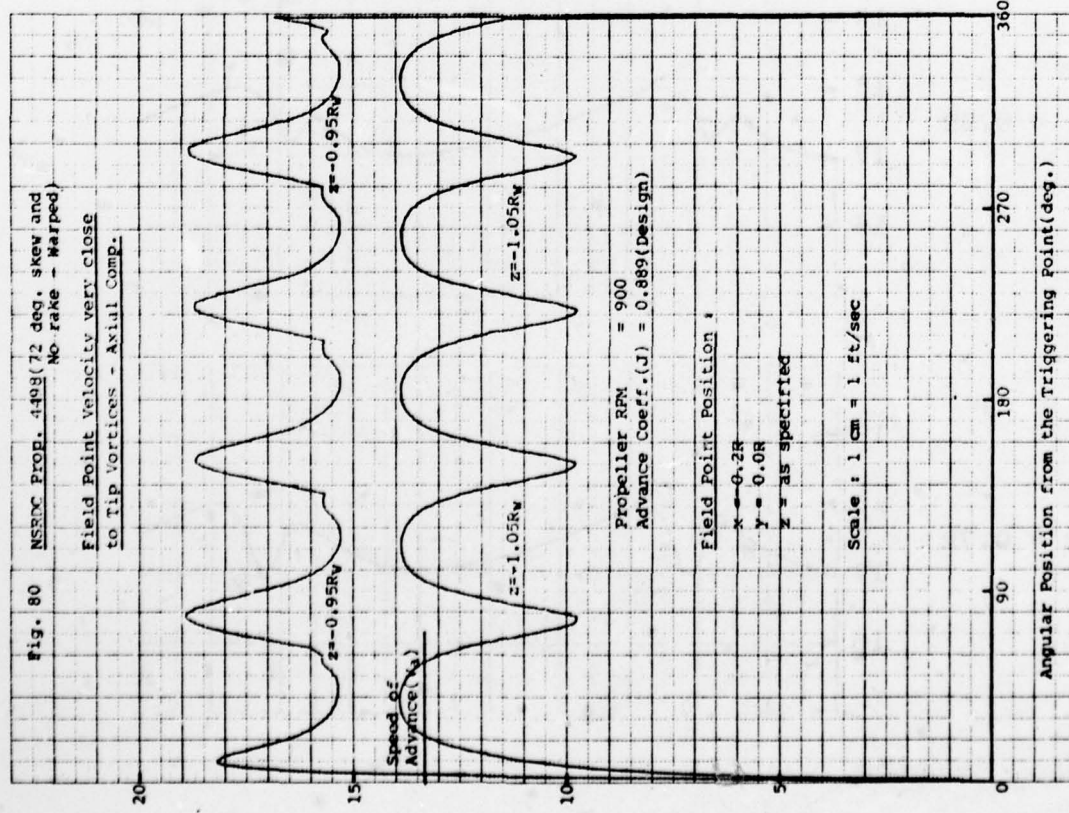


Fig. 82 NSRDC Prop. 4381(No skew)Velocity Defect due to Blade Boundary Layer

Advance Coeff.(J) = 0.889
Axial Position(x) = -0.3R

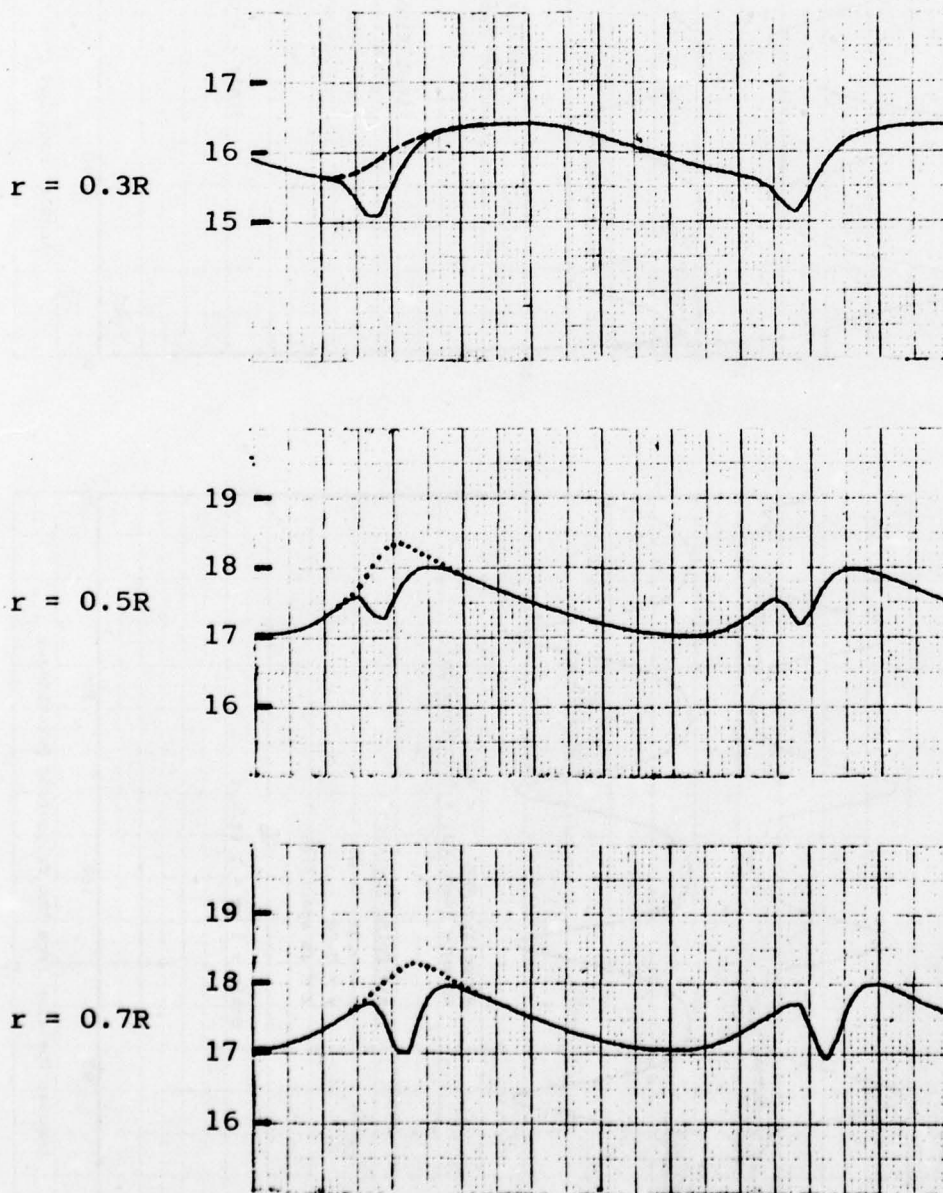


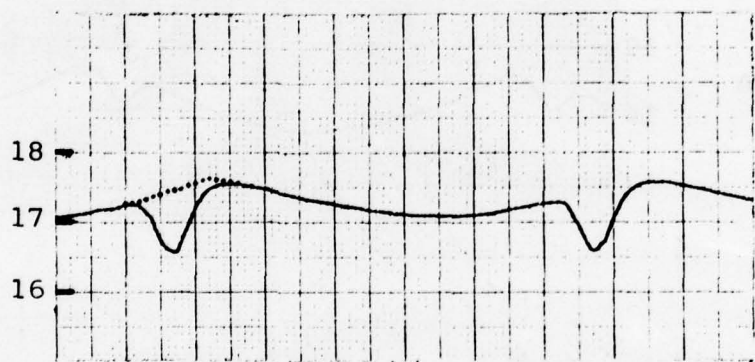
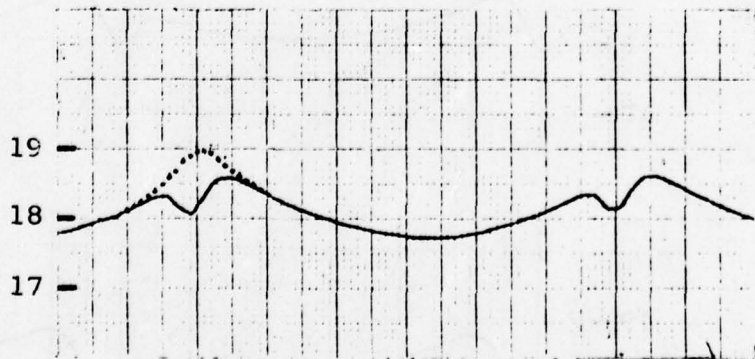
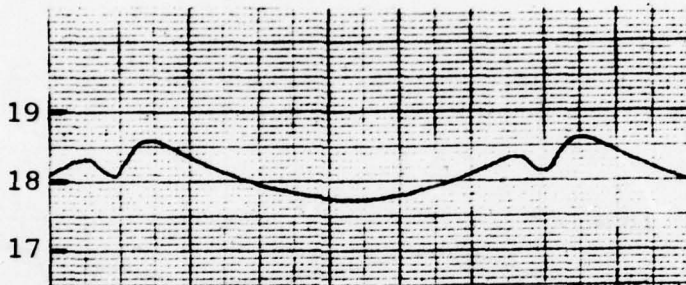
Fig. 83 NSRDC Prop. 4381 (No skew)Velocity Defect due to Blade Boundary LayerAdvance Coeff. (J) = 0.889Axial Position (x) = -0.4 $r = 0.4R$  $r = 0.6R$  $r = 0.8R$ 

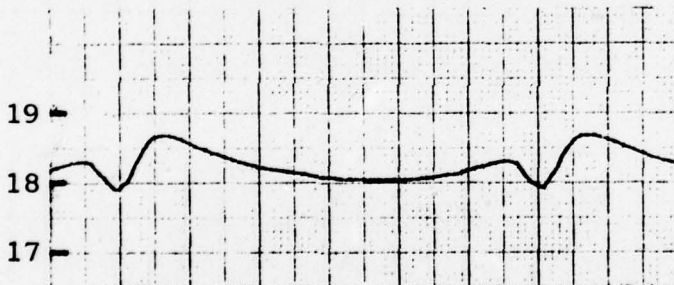
Fig. 84 NSRDC Prop. 4381 (No skew)Velocity Defect due to Blade Boundary Layer

Advance Coeff.(J) = 0.889
Radial Position(r)= 0.6R

$x = -0.4R$



$x = -0.6R$



$x = -0.8R$



$x = -1.0R$



Fig. 85 Modeling and Economization of Source and
Vortex Systems of Propeller Blade in PUF-2

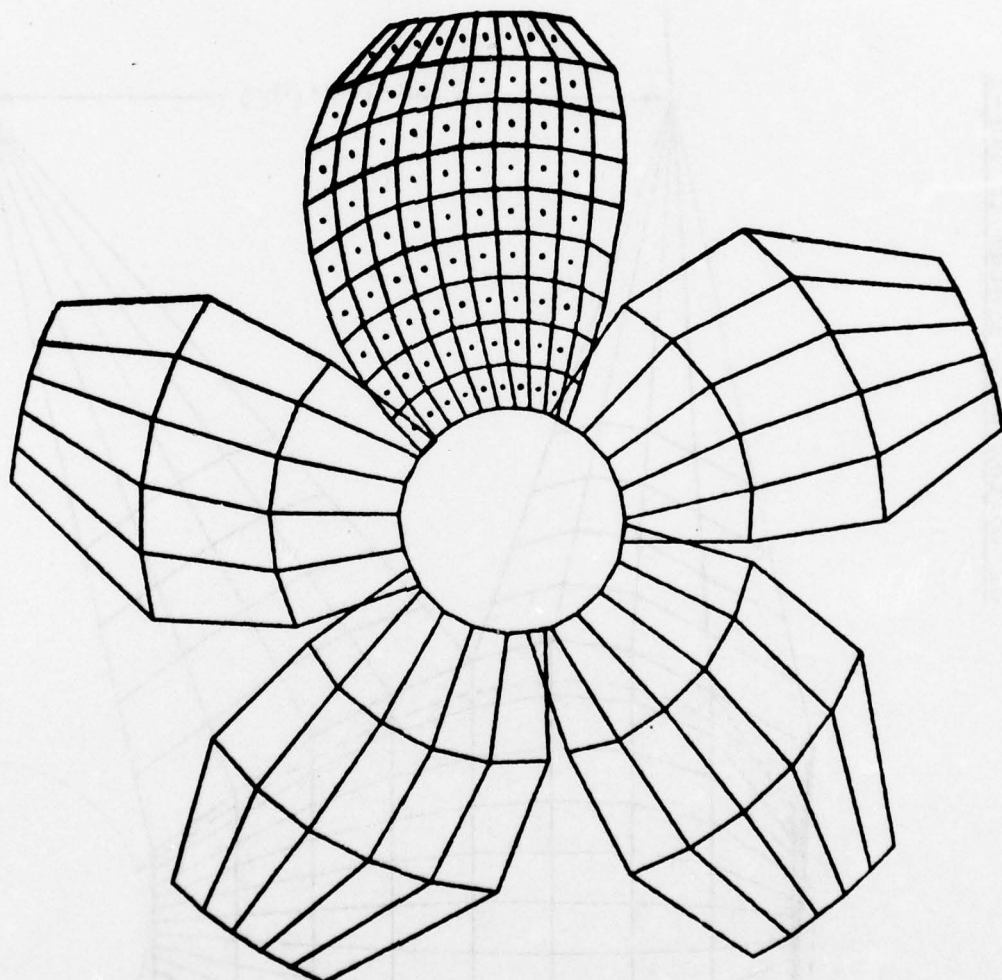
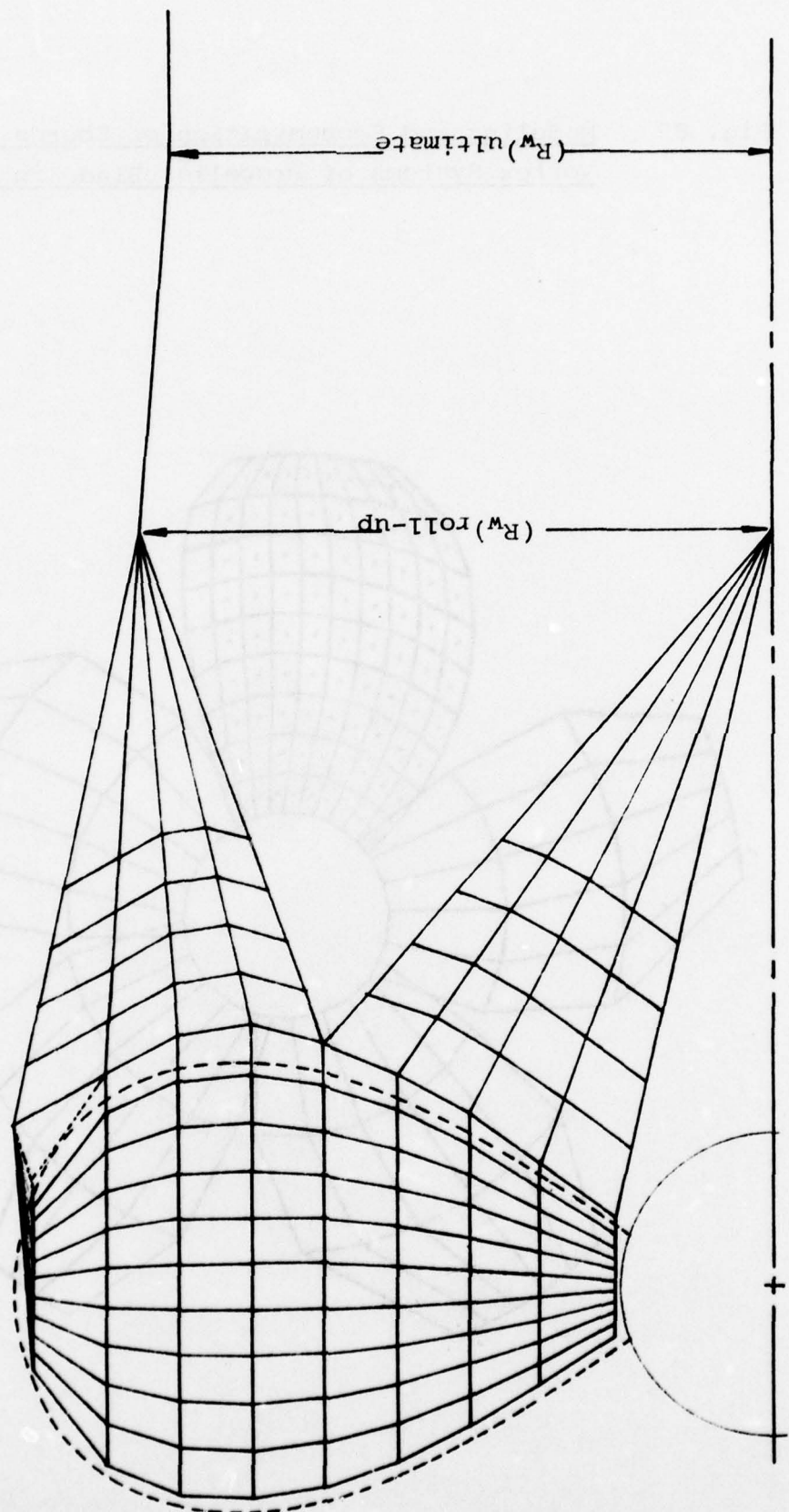
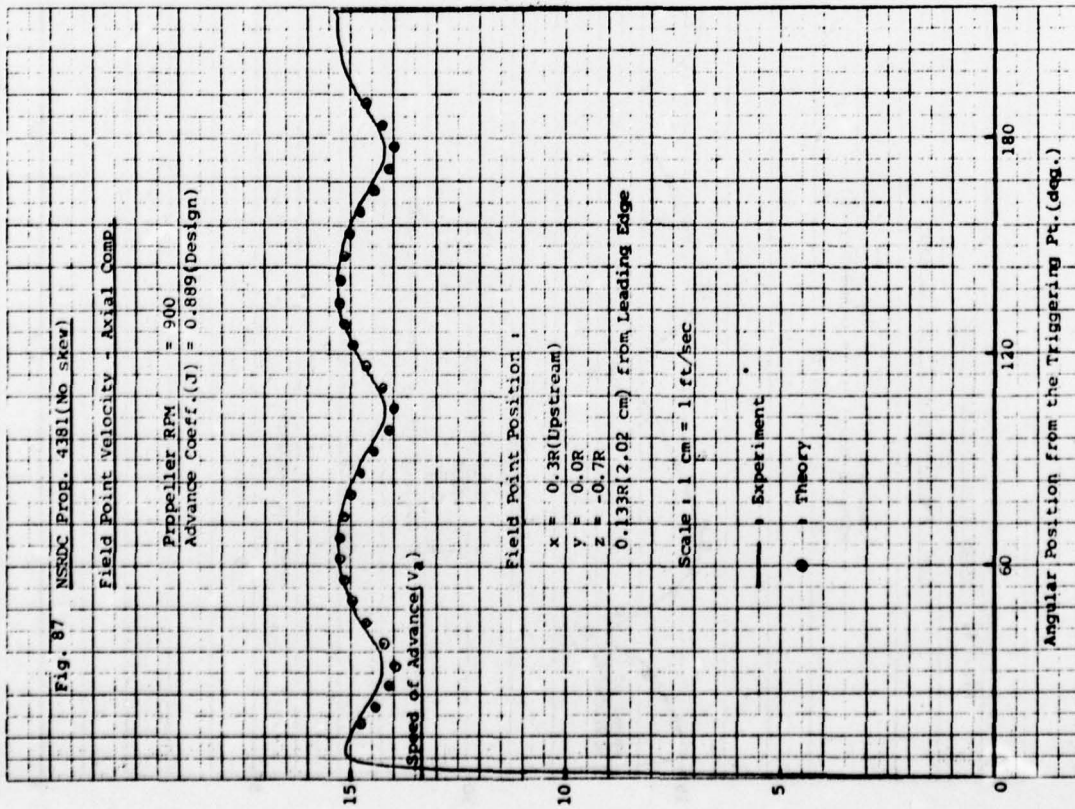
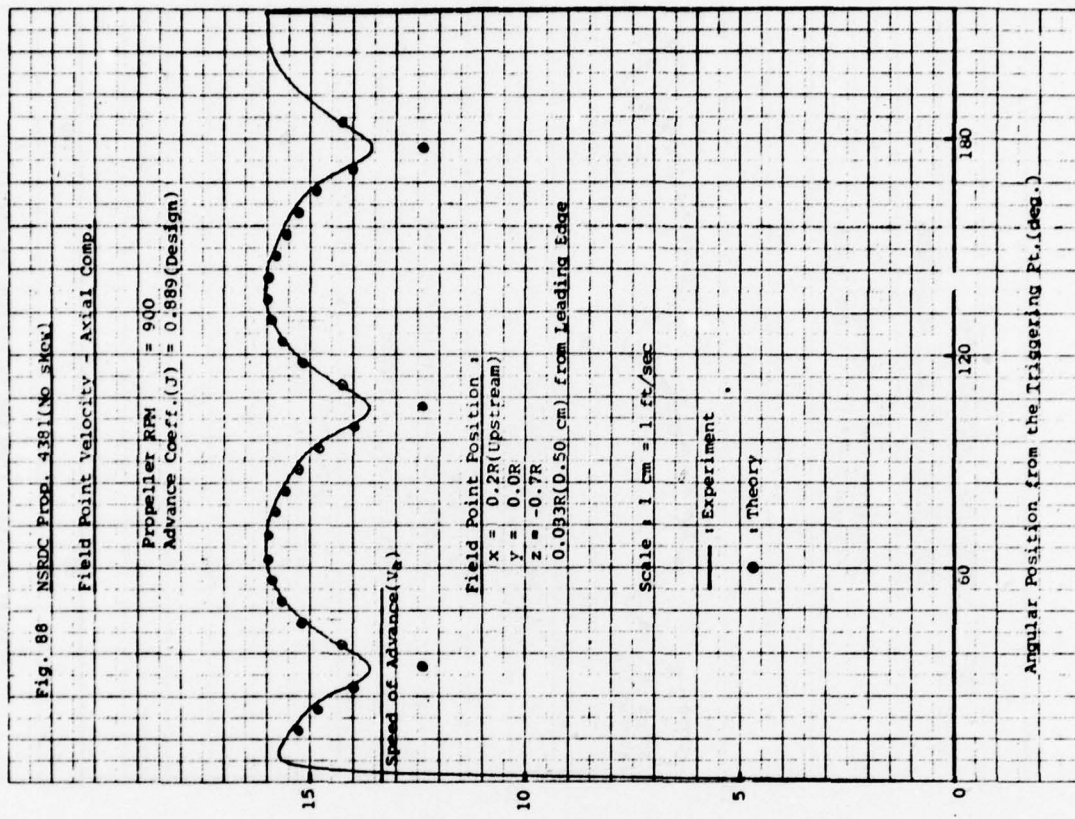
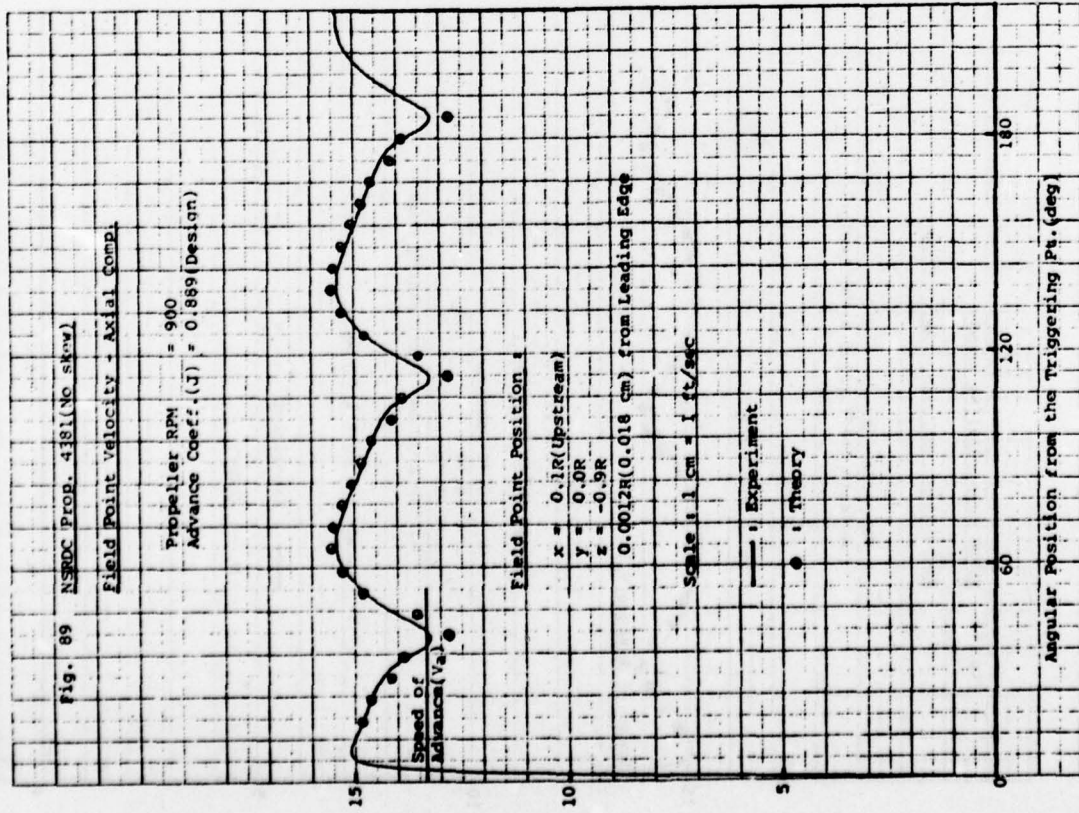
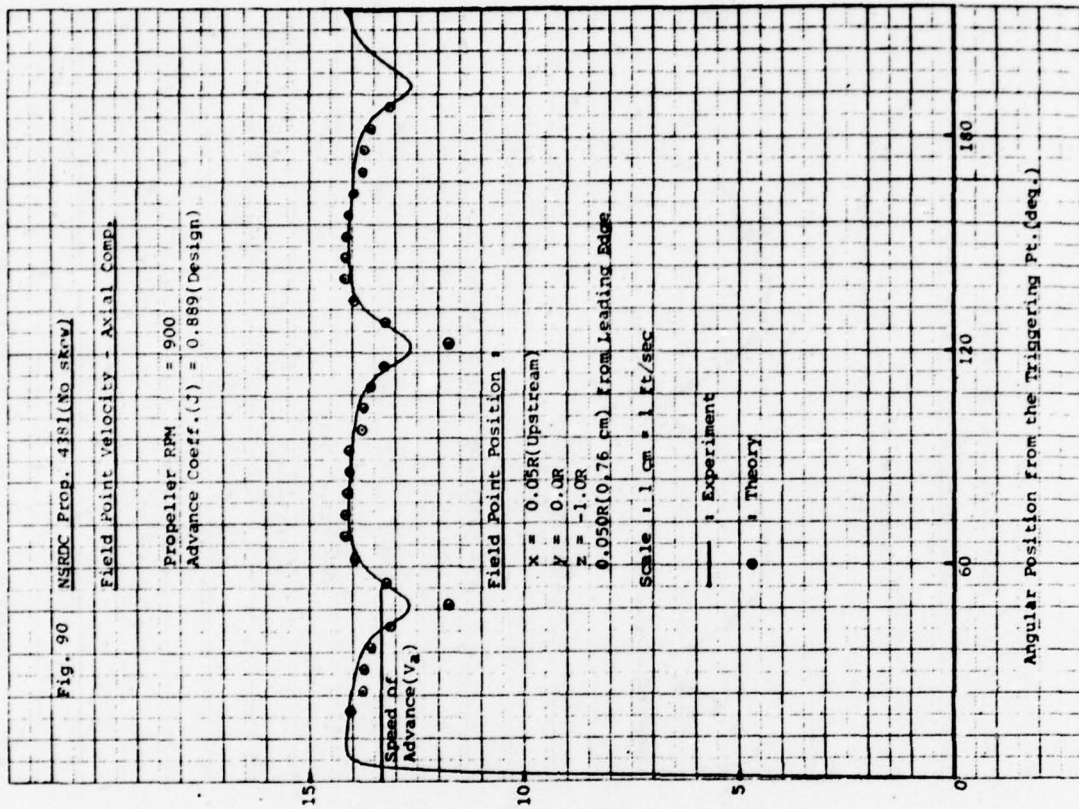
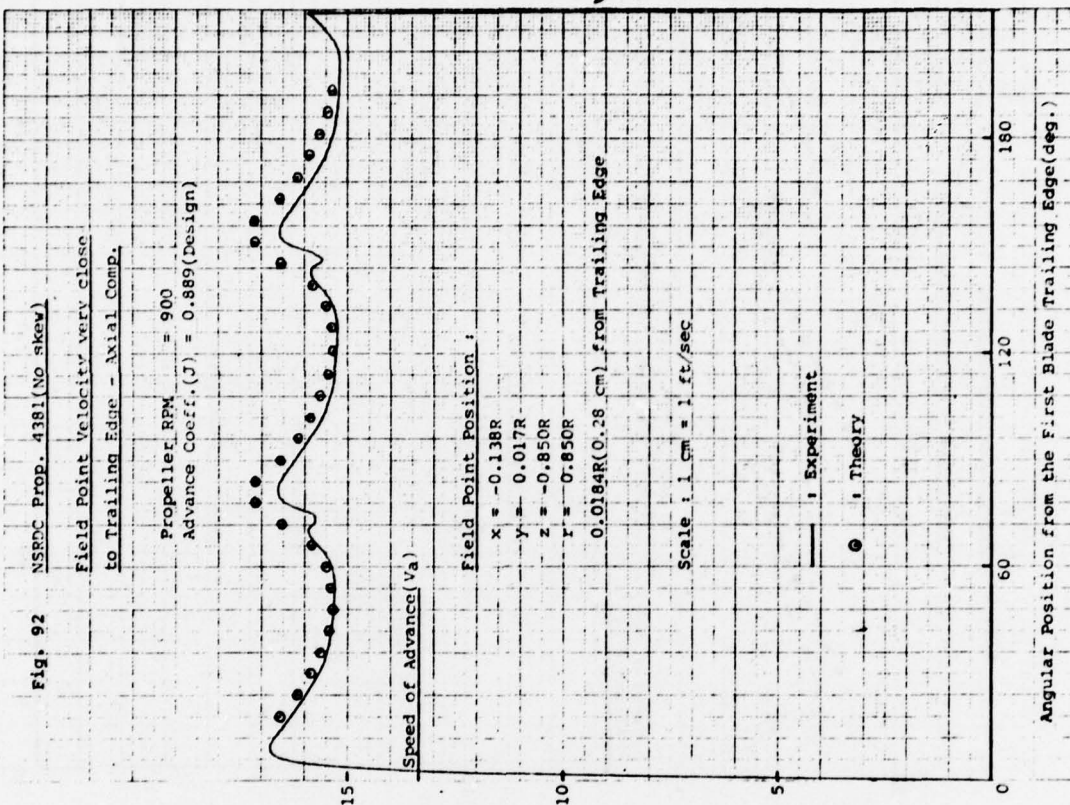
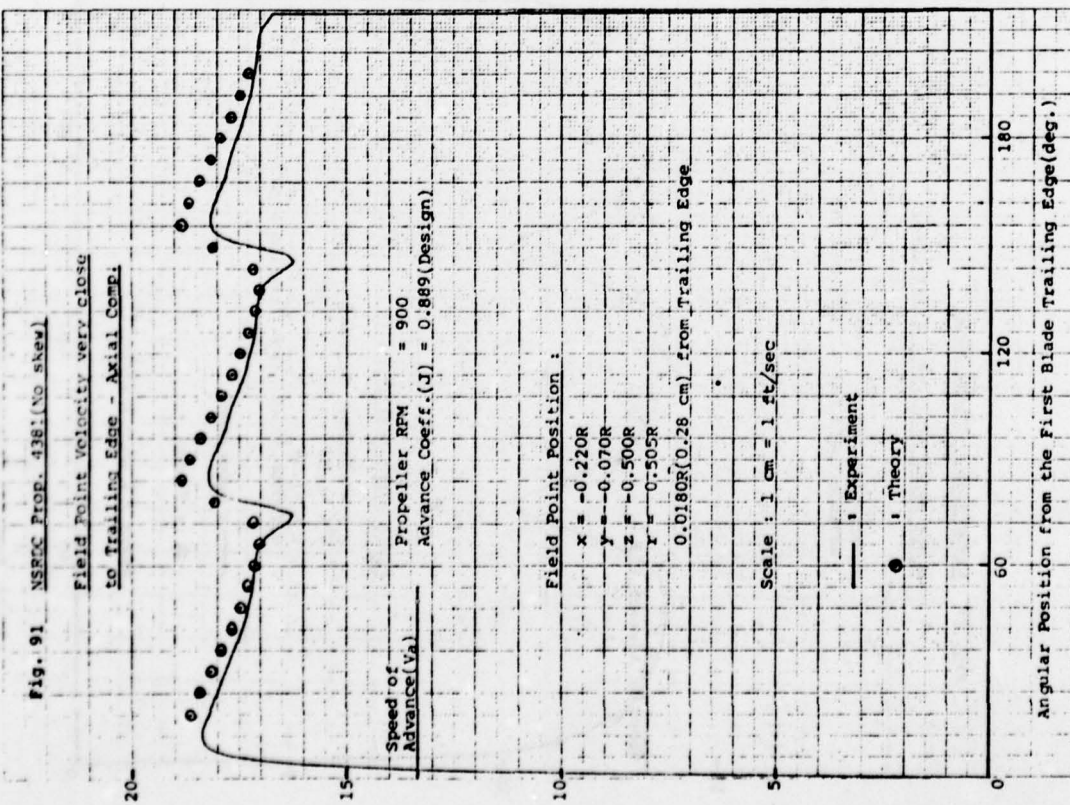


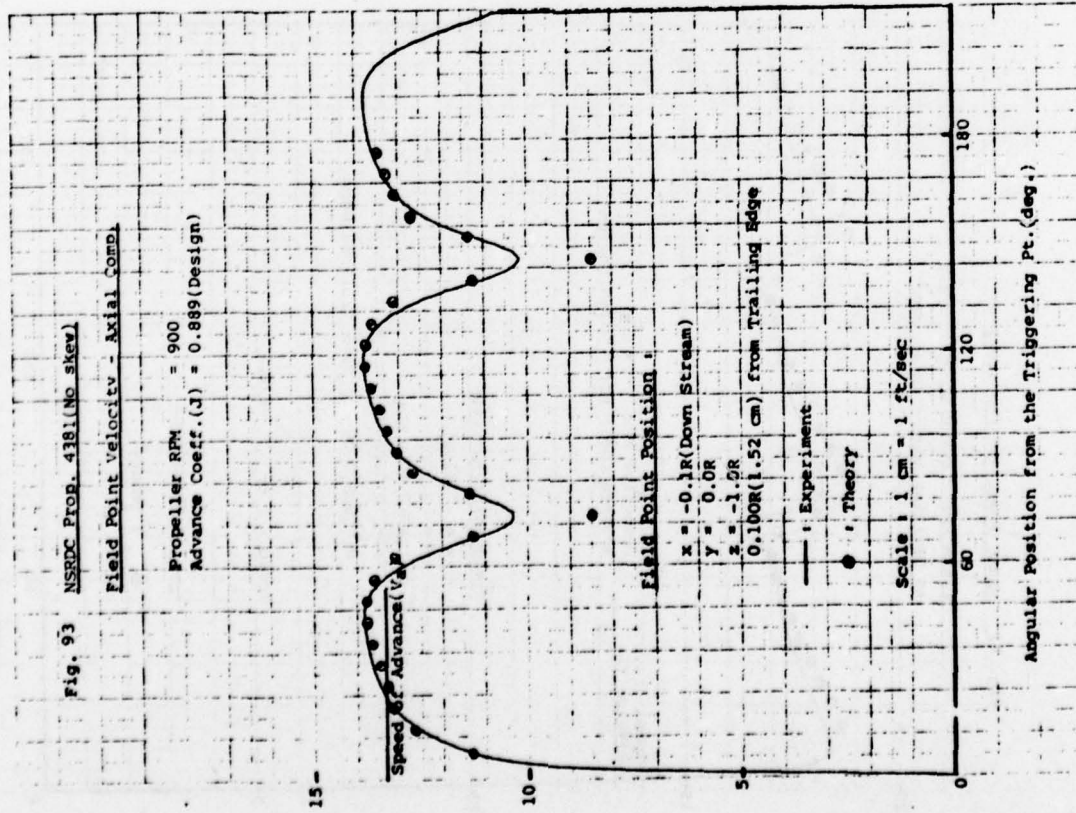
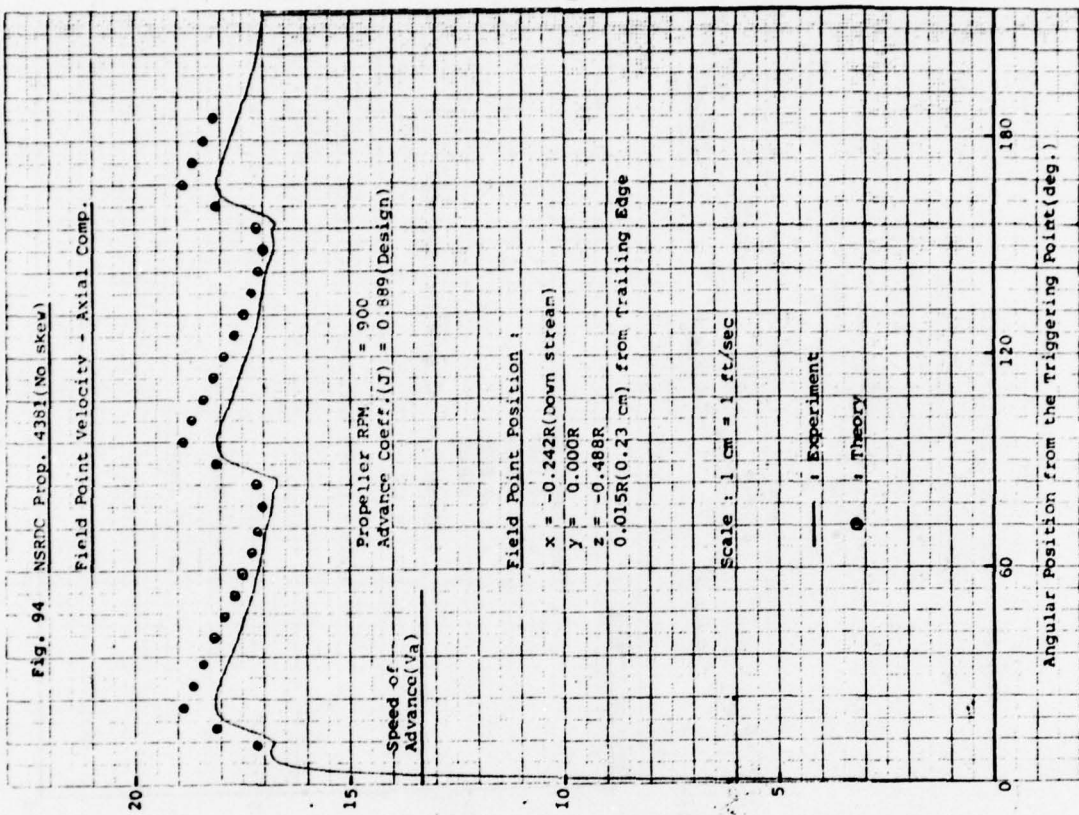
Fig. 86 Schematic Presentation of Modelling
of Vortex Wake System in PUF-2

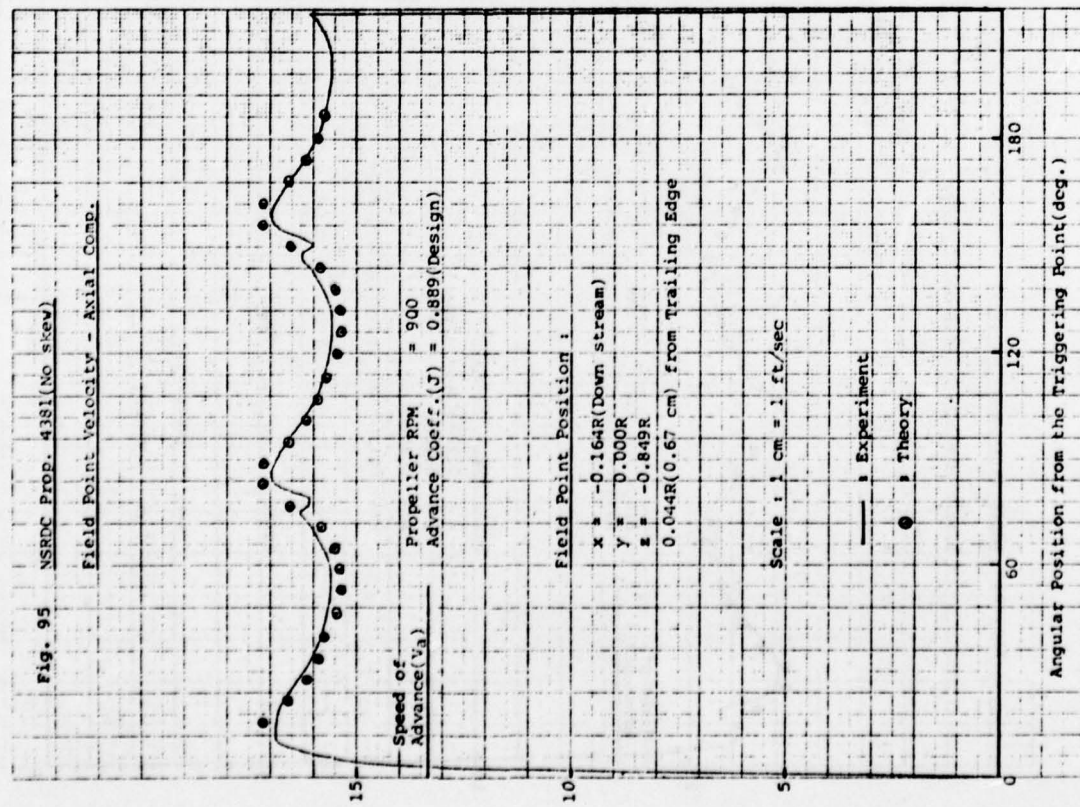
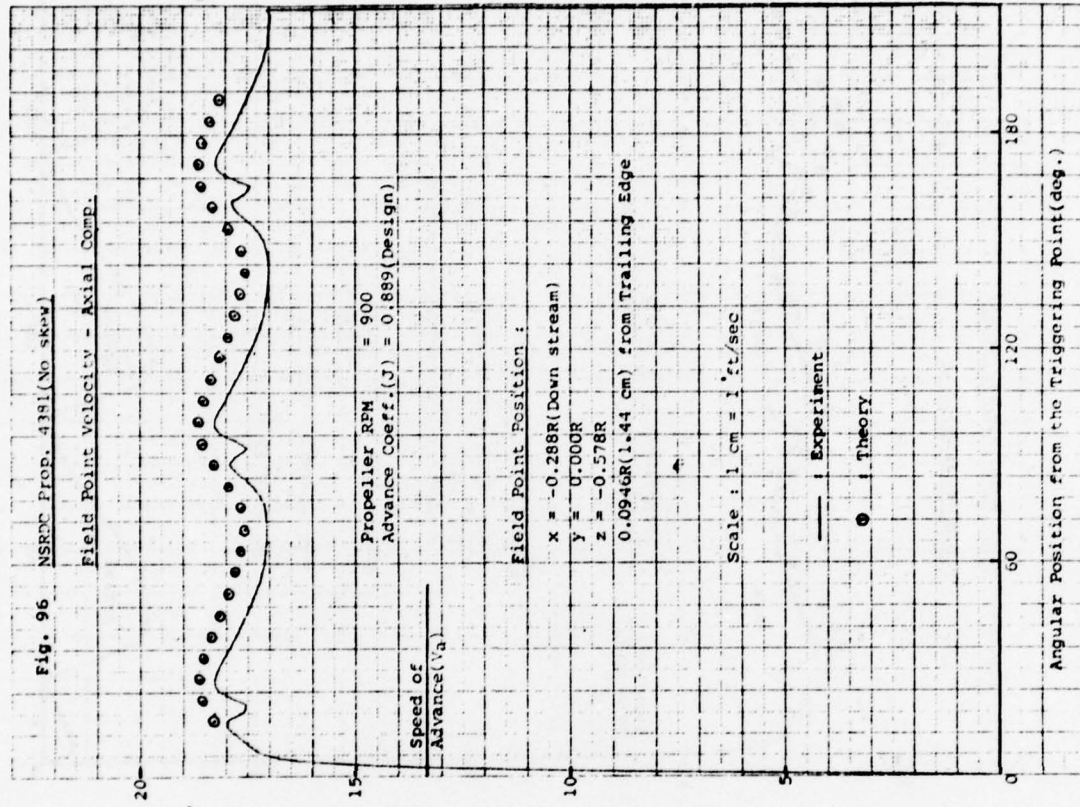


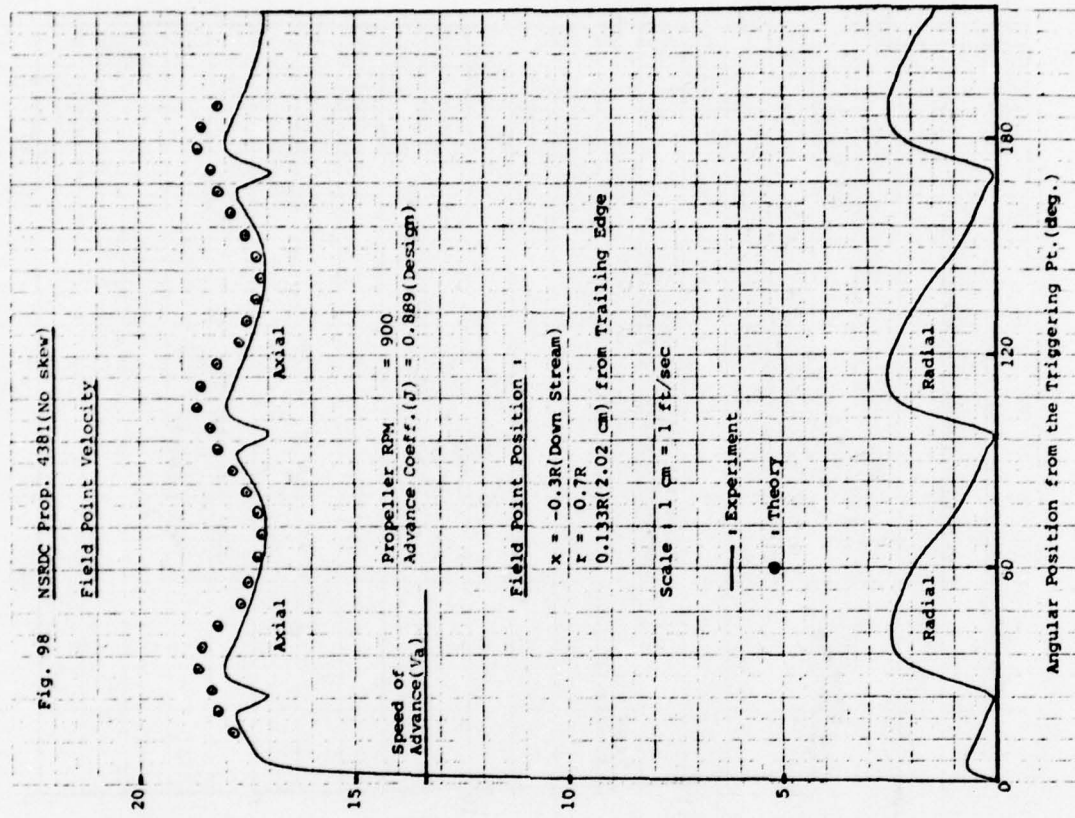
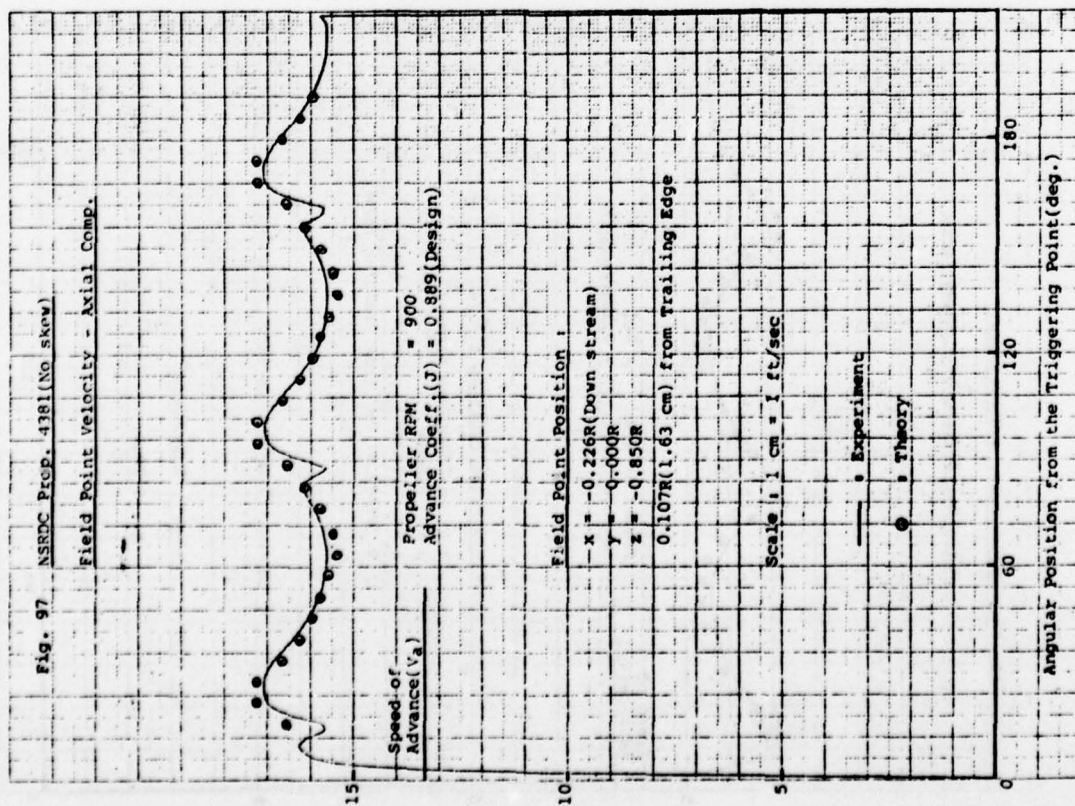


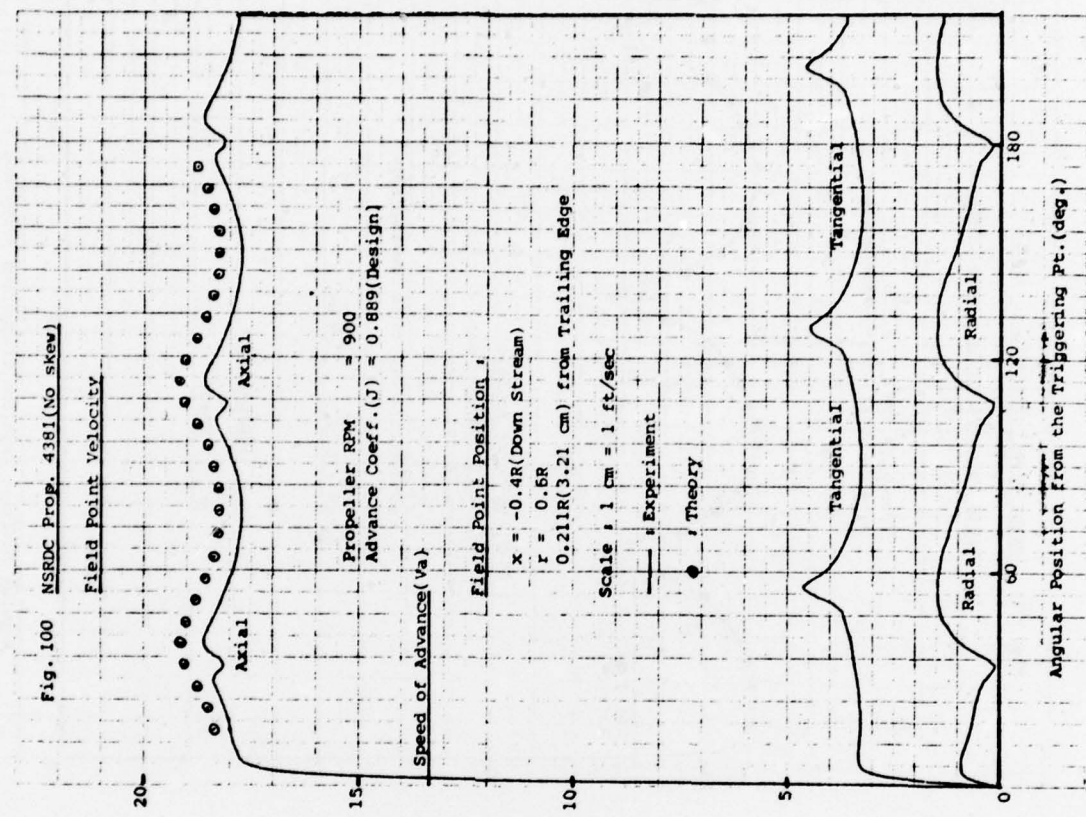
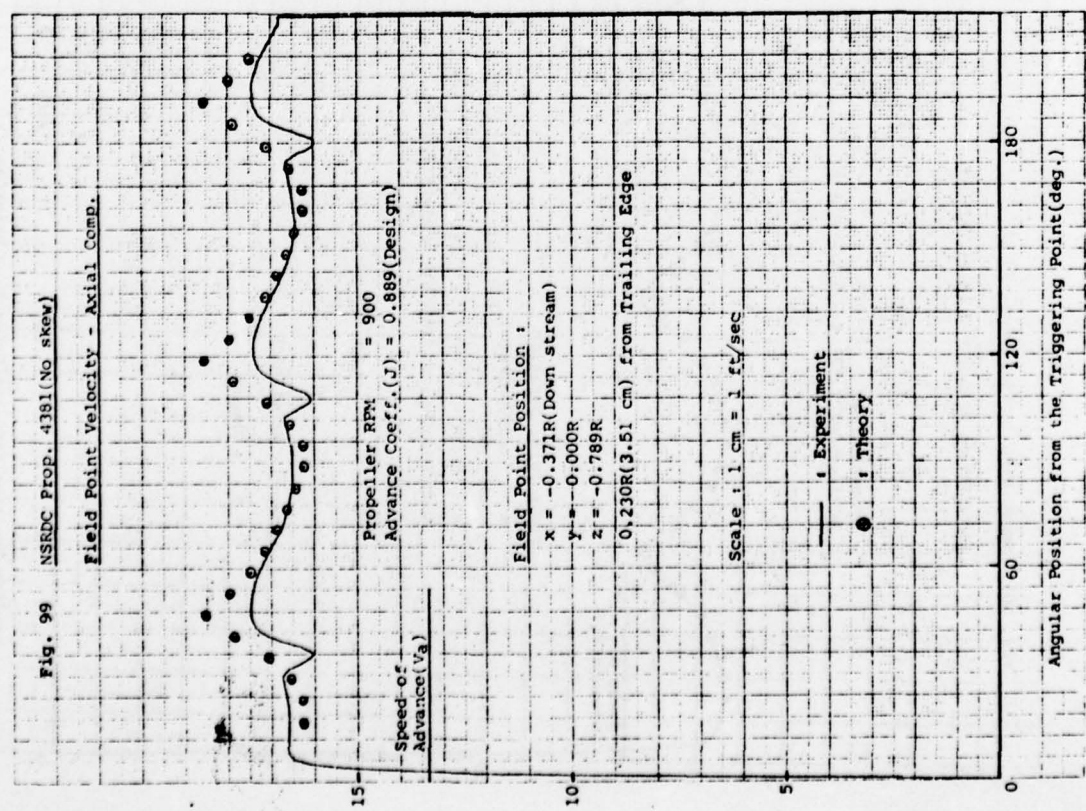


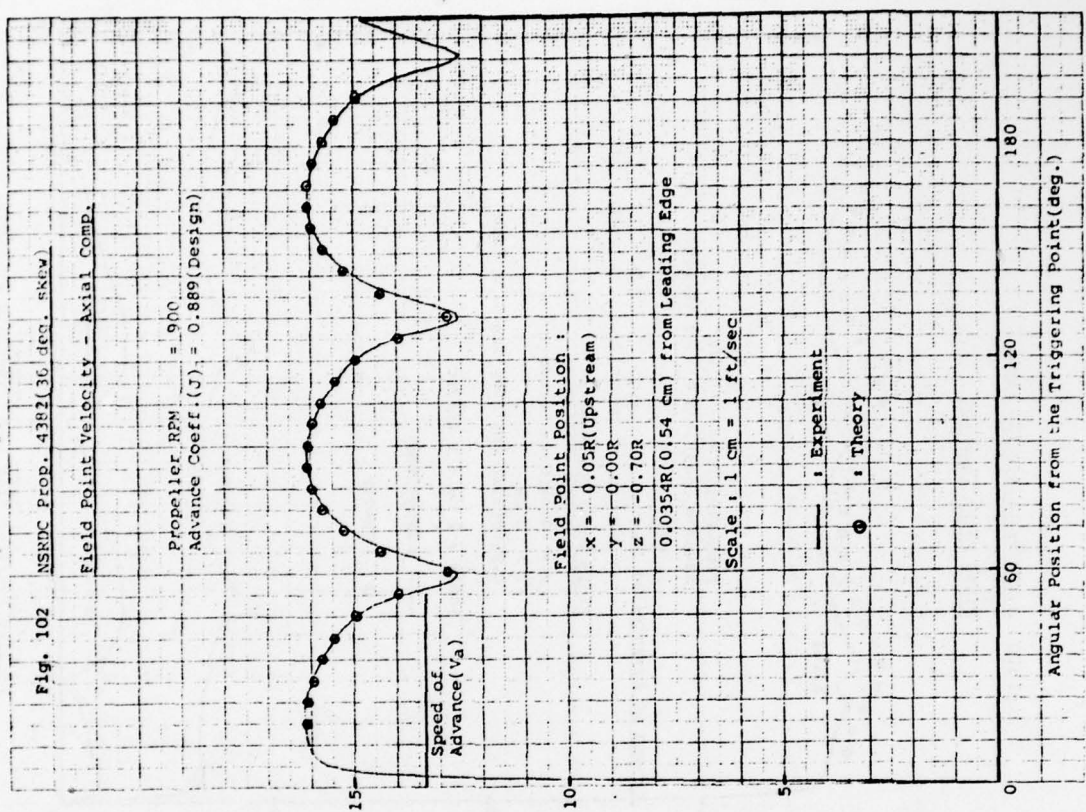
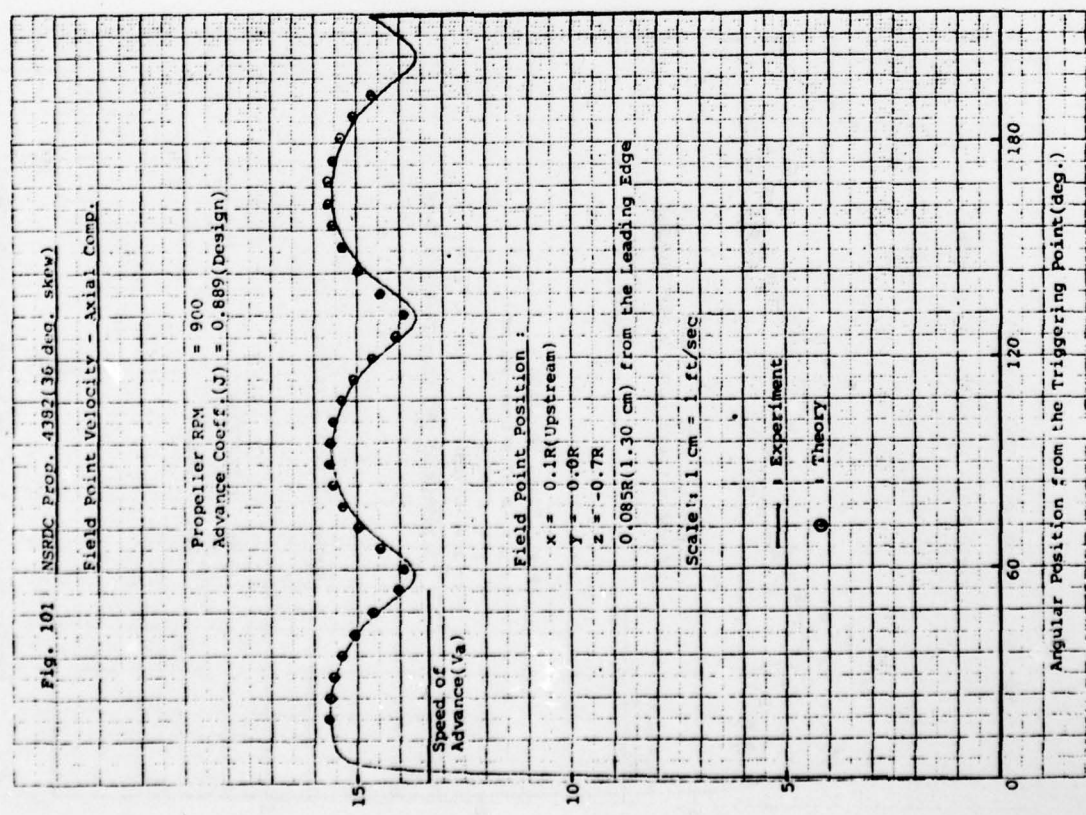


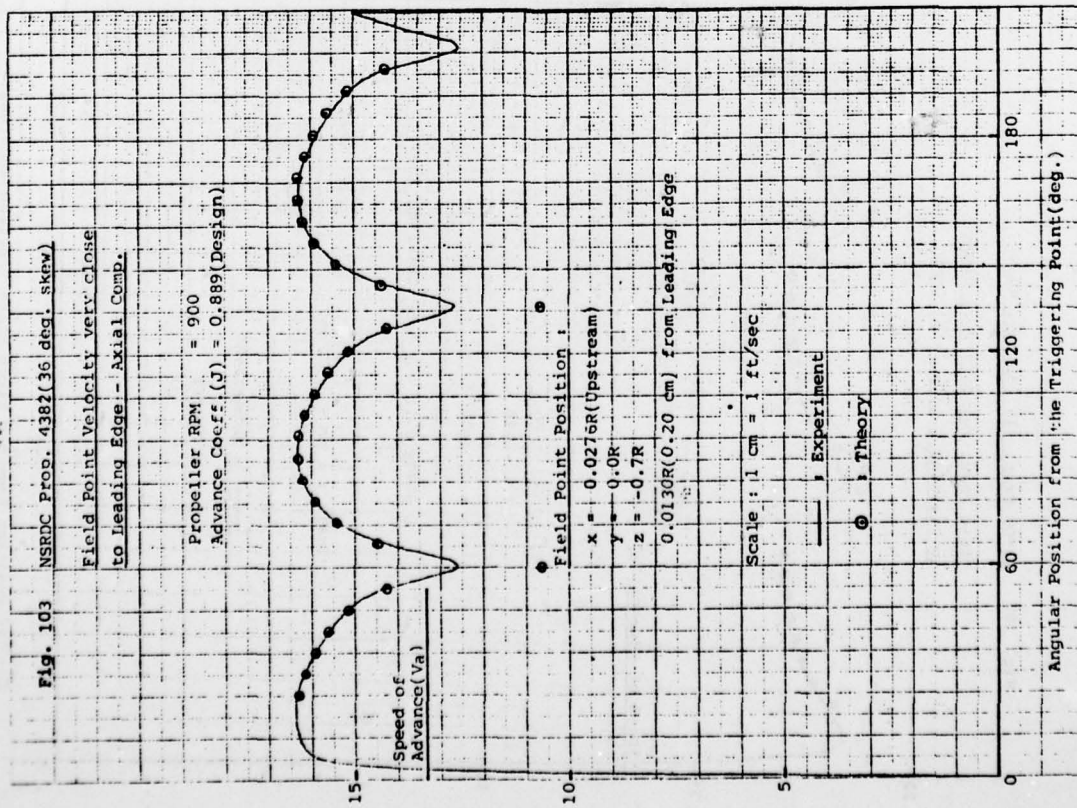
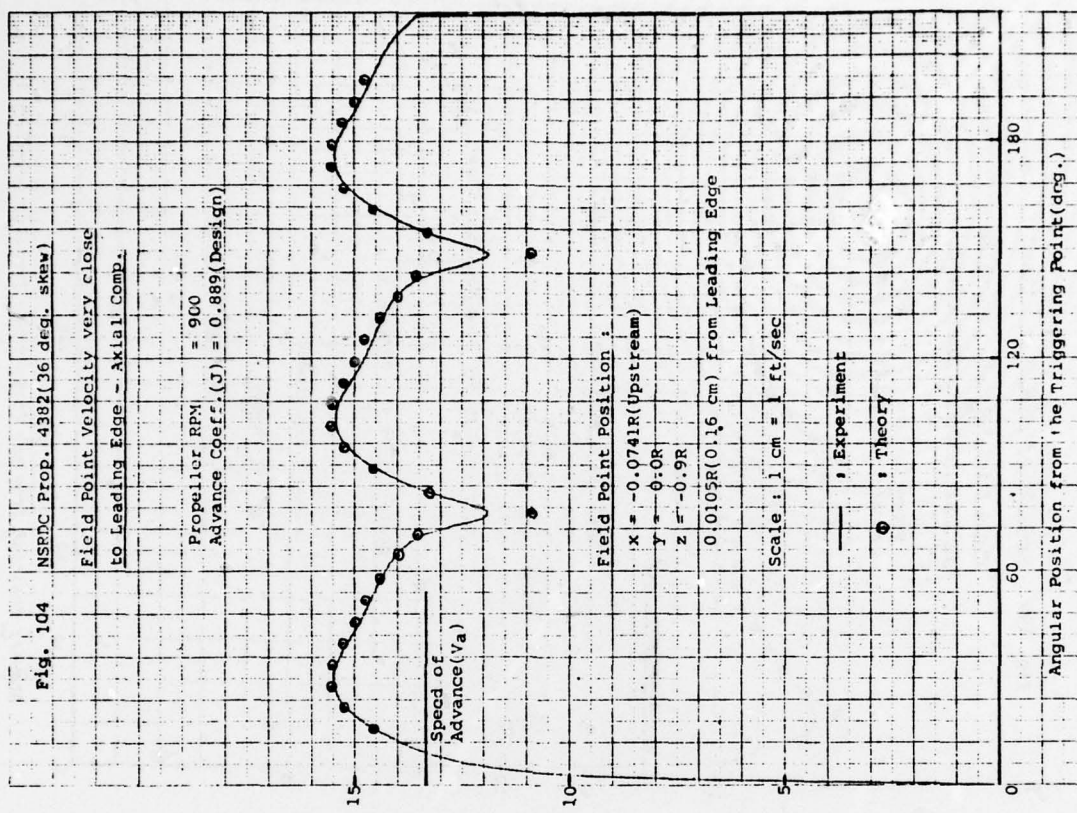


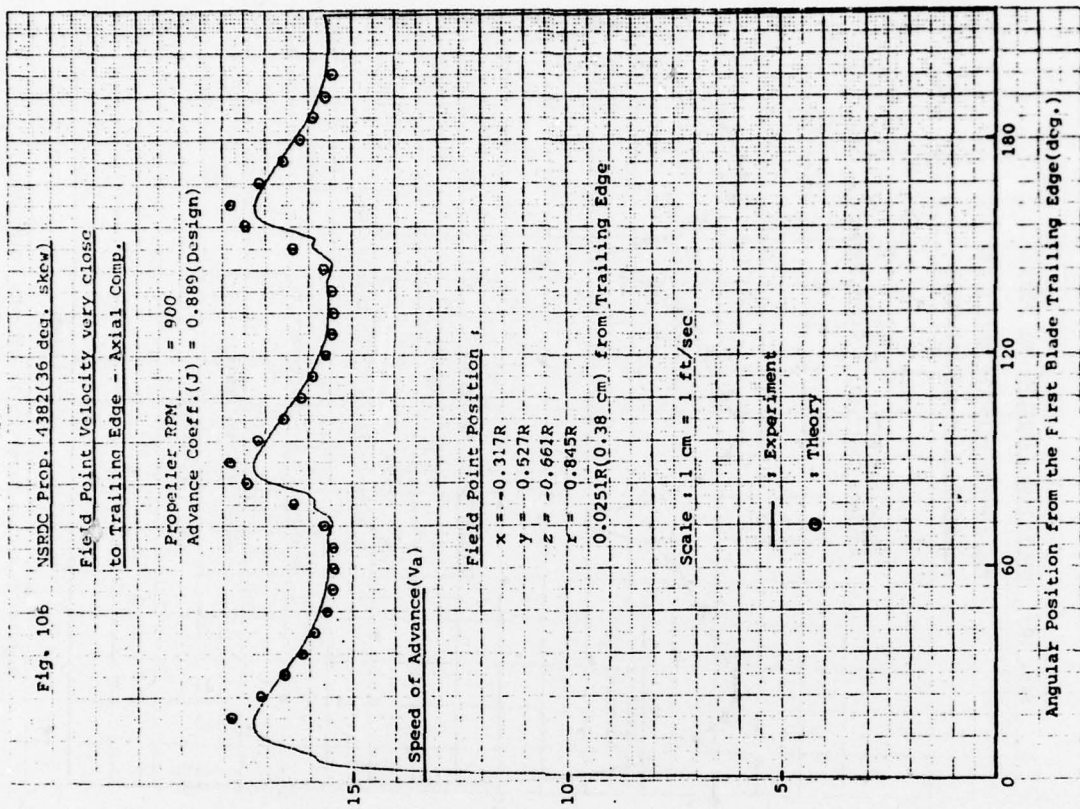
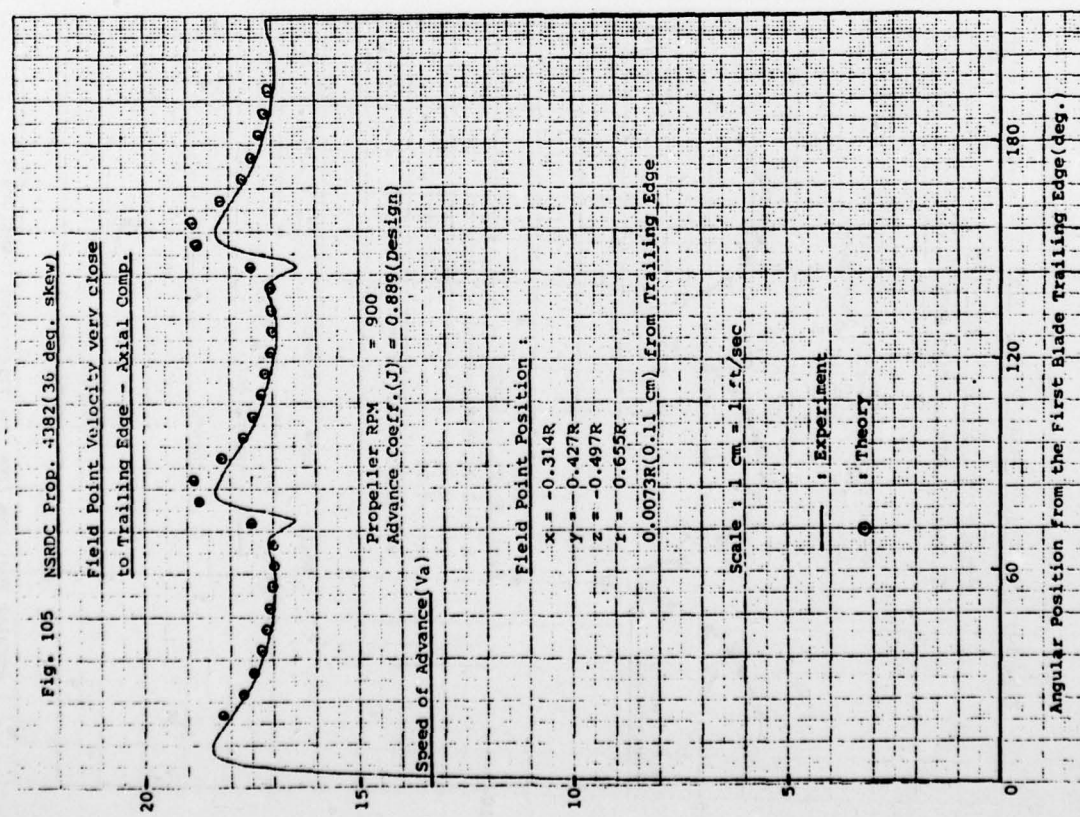


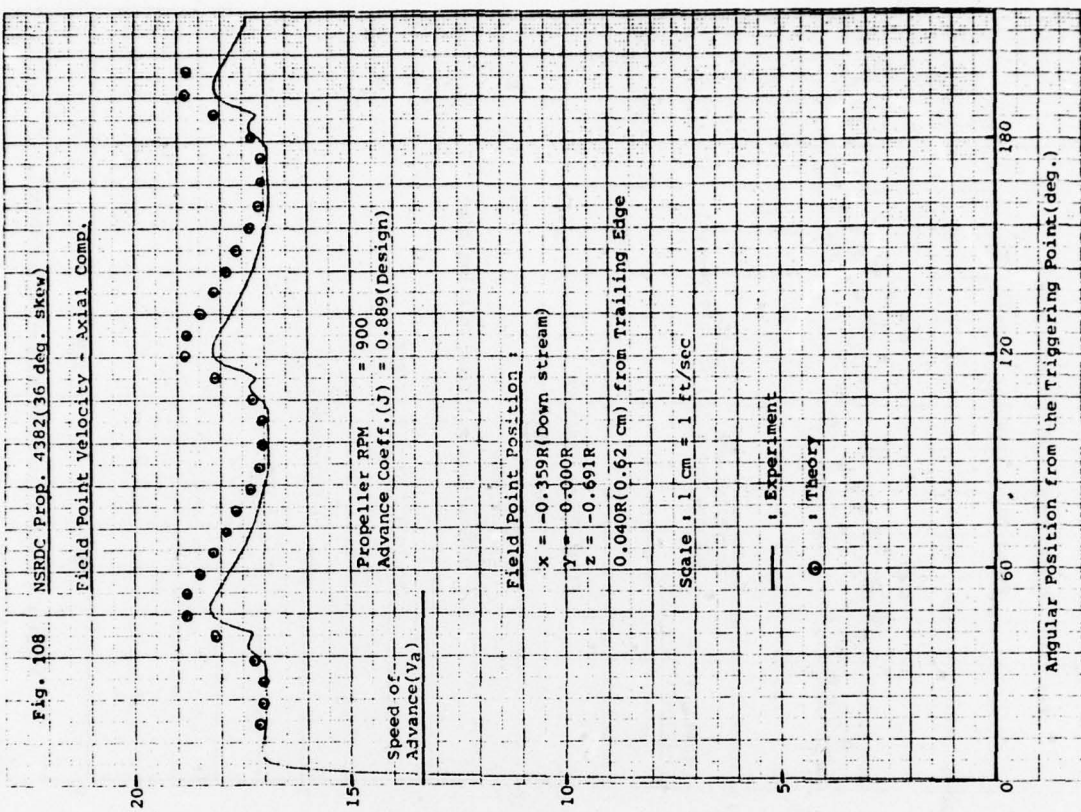
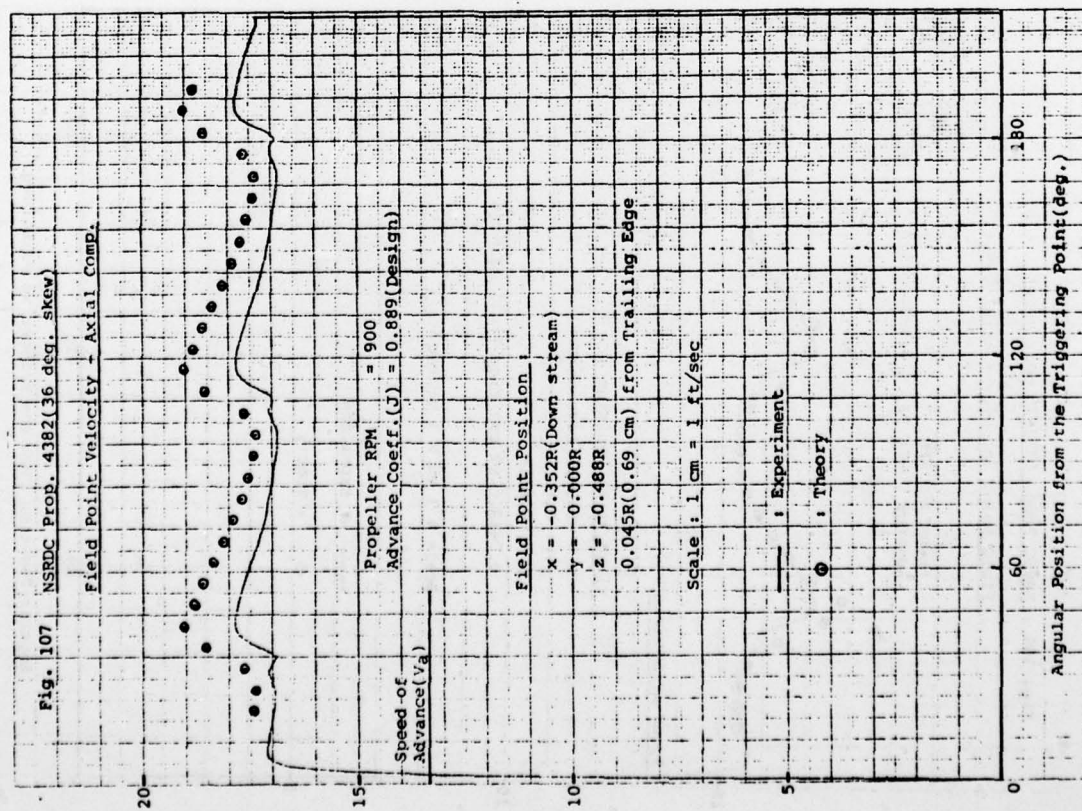


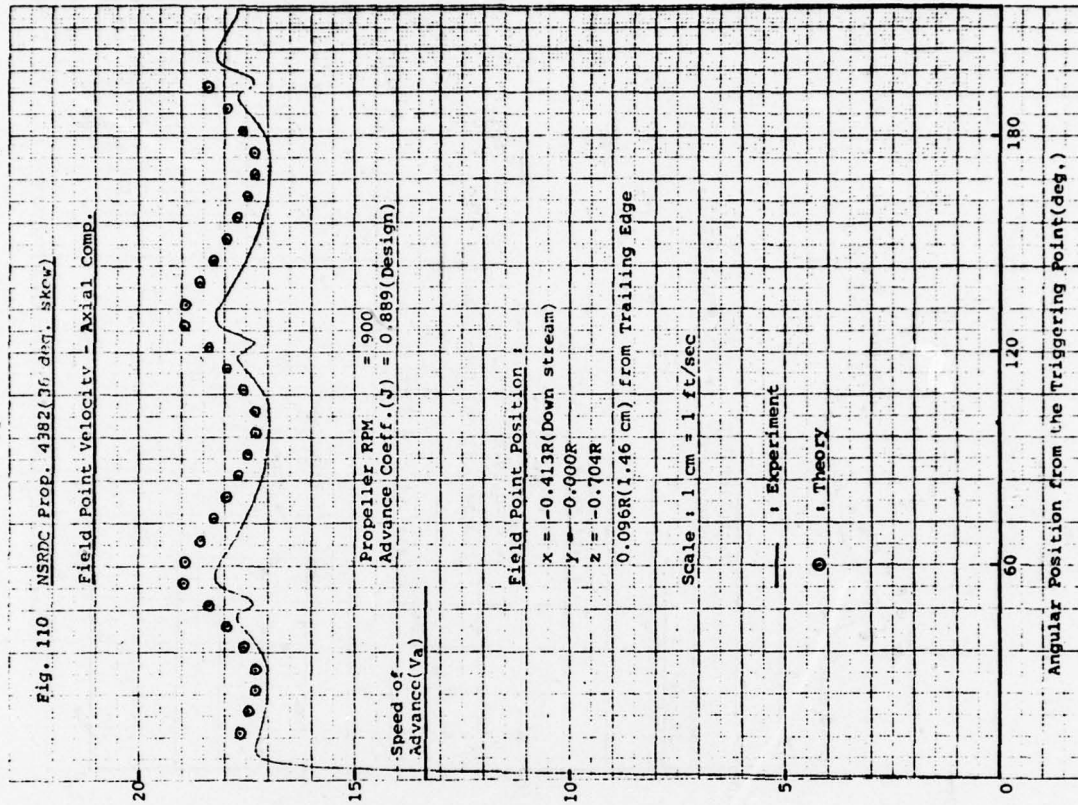
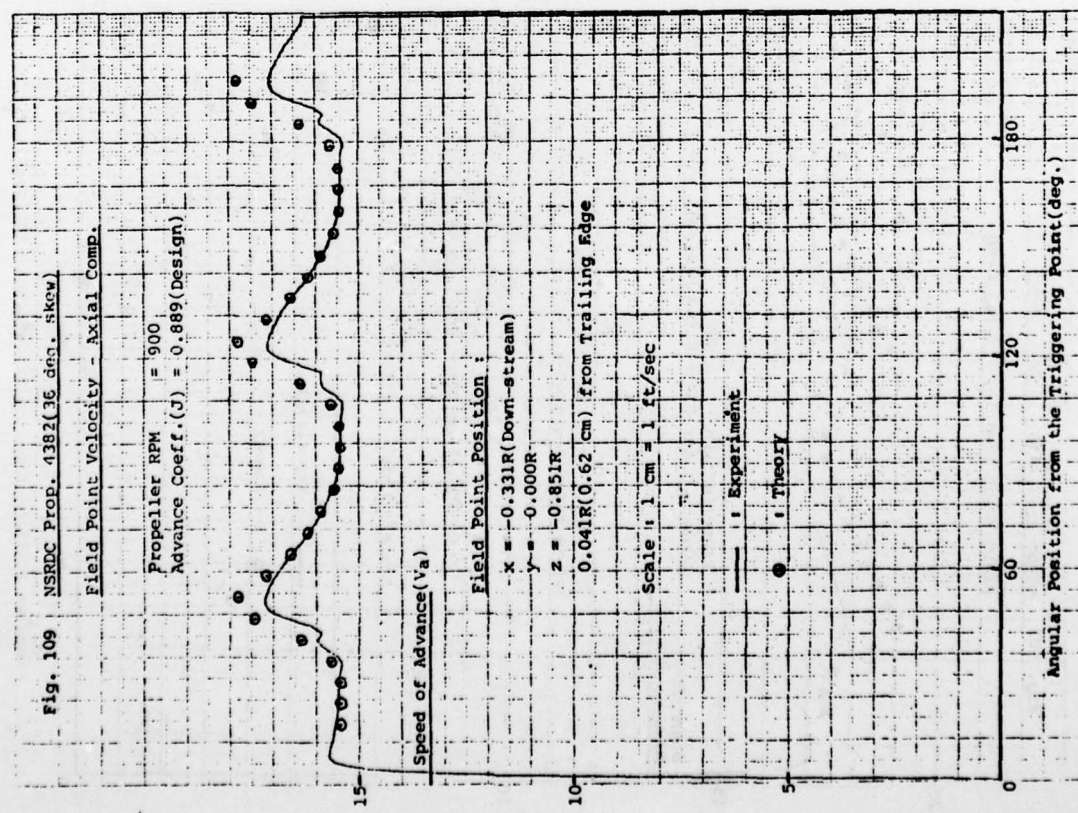


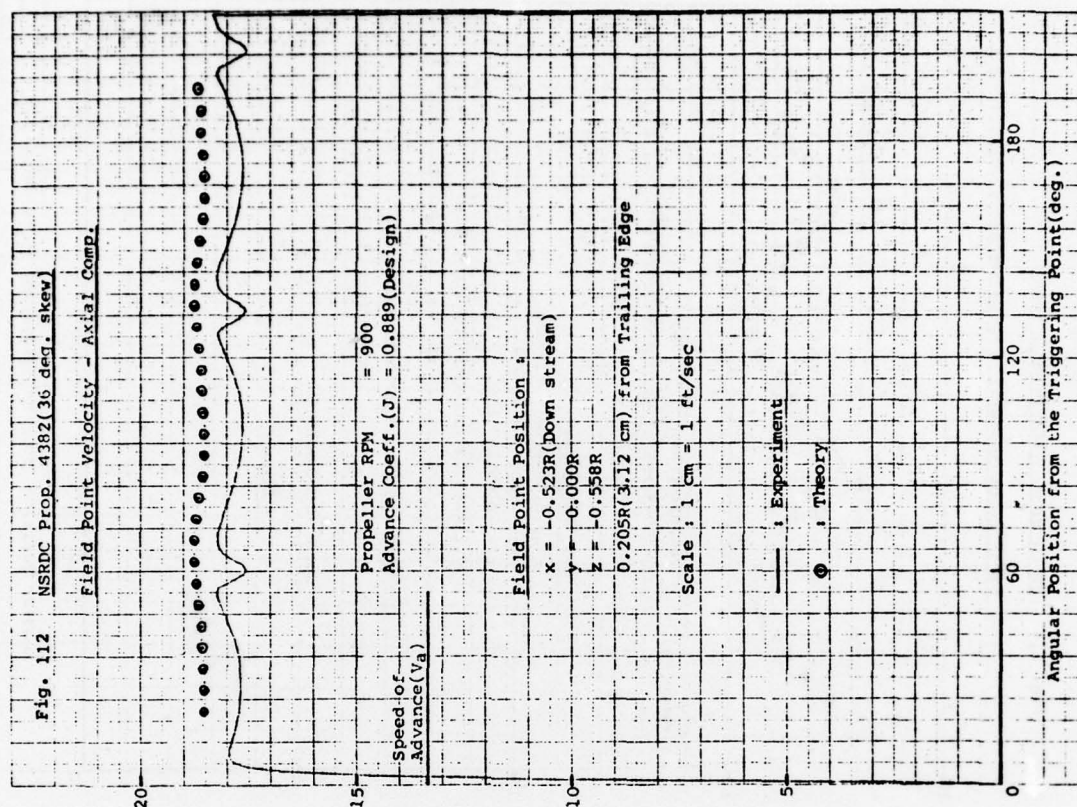
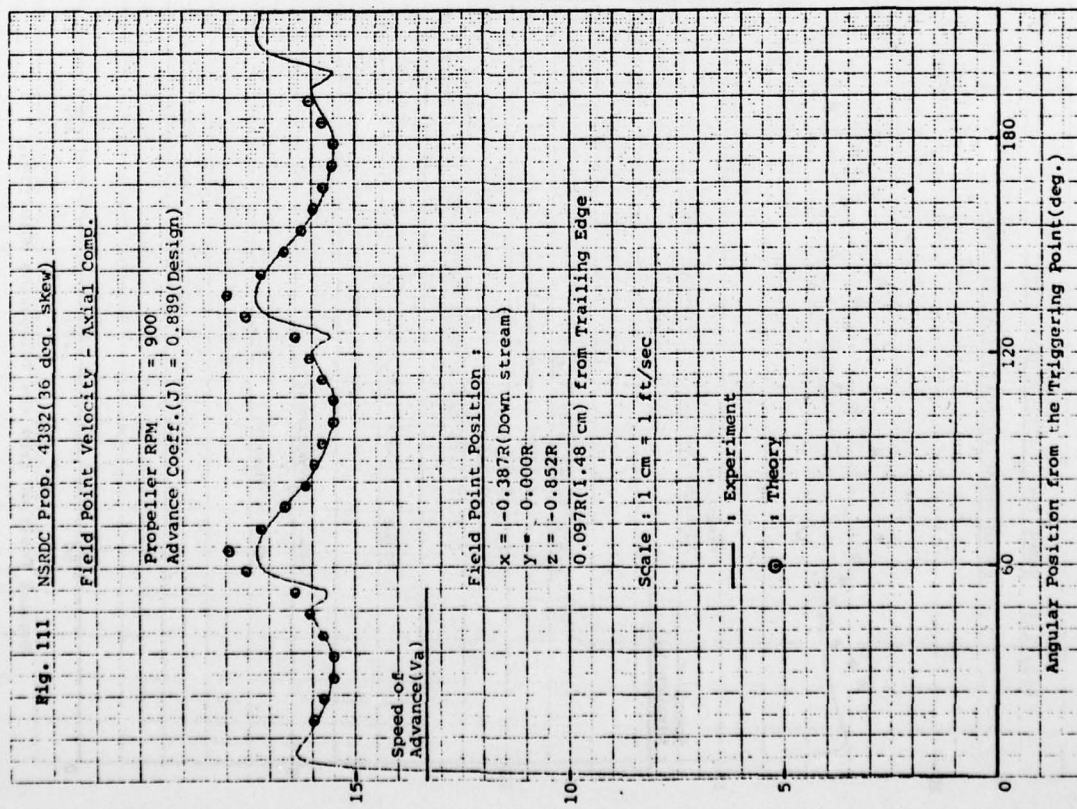


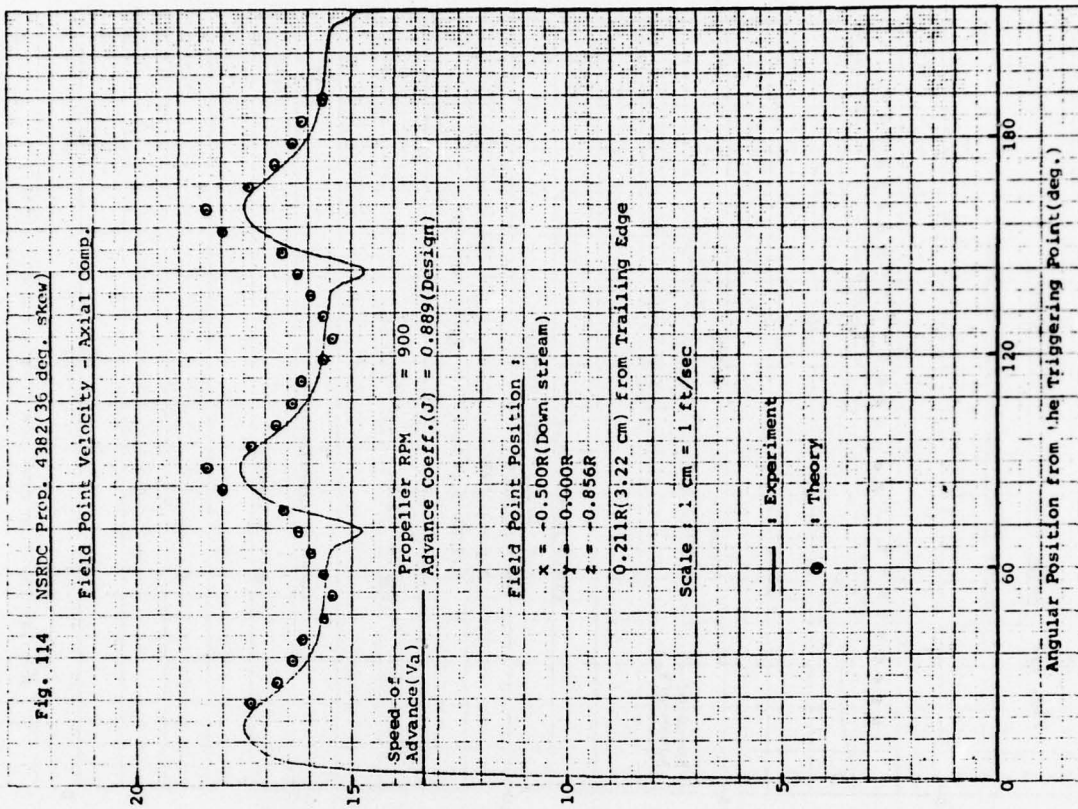
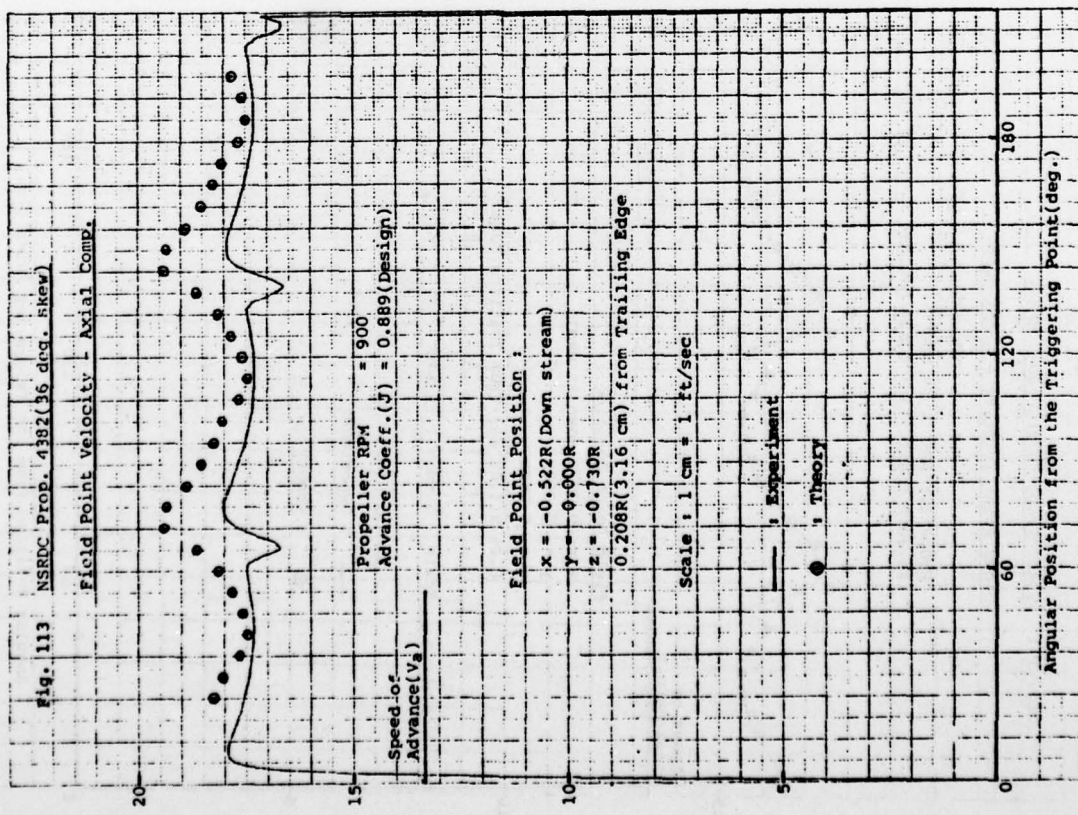


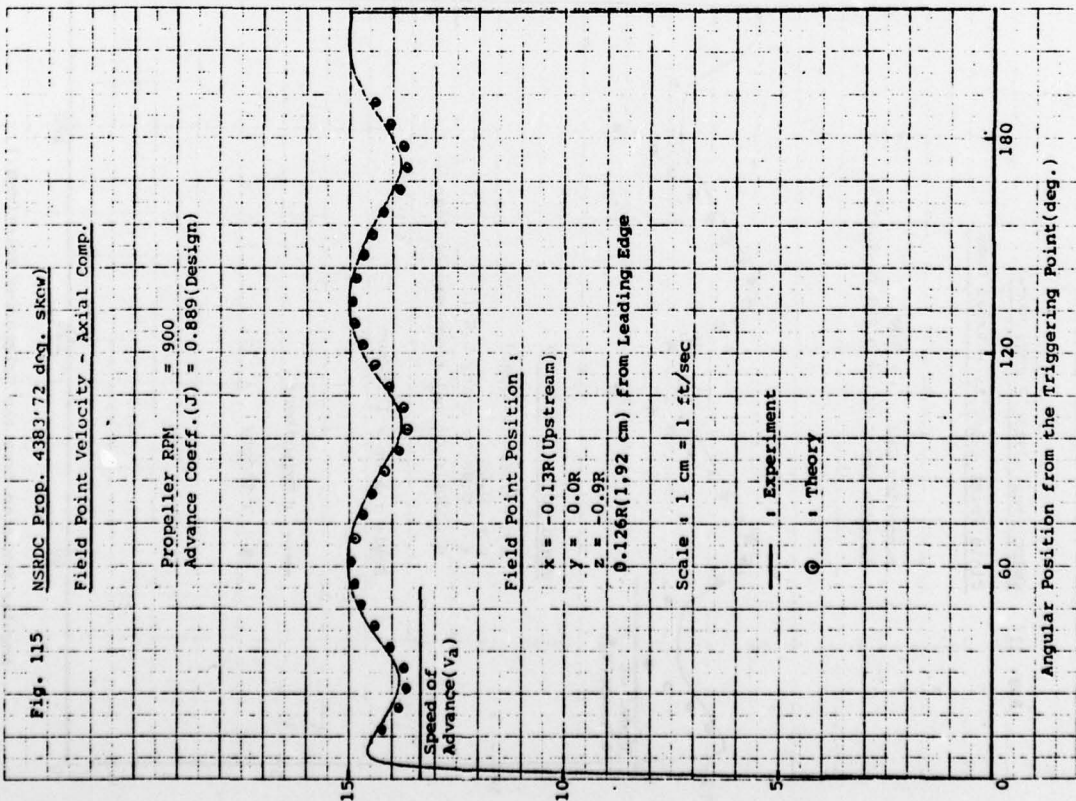
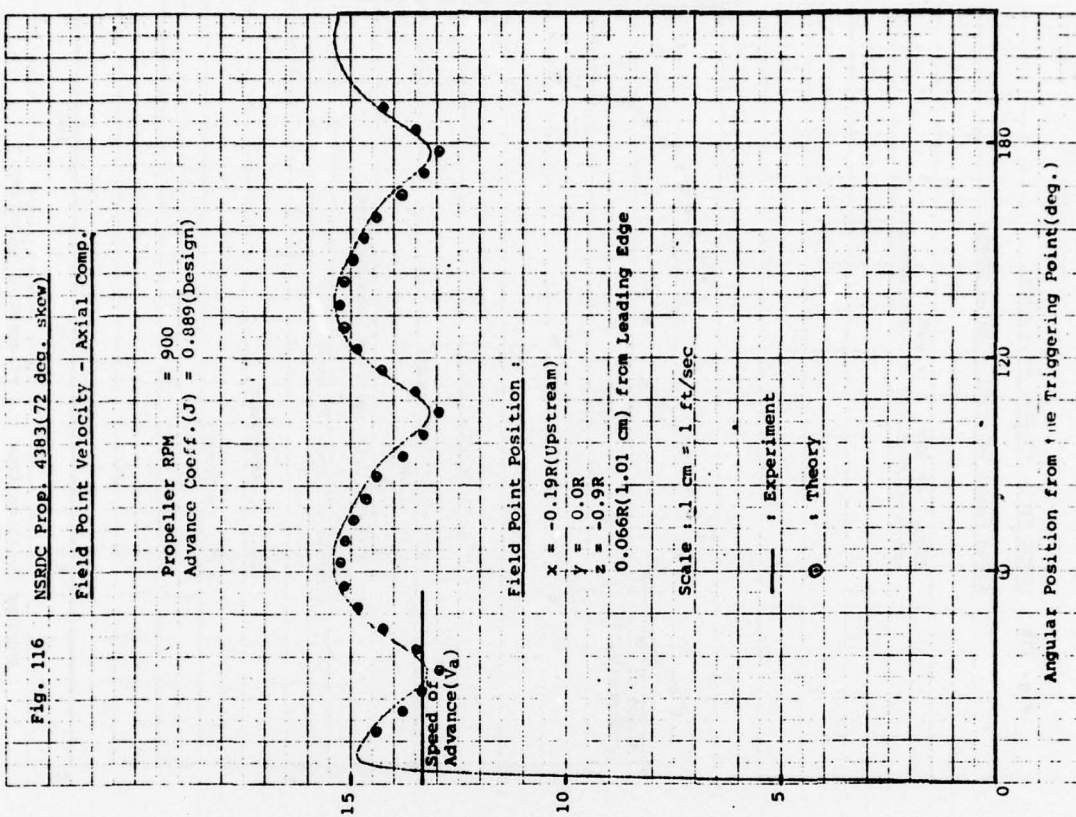


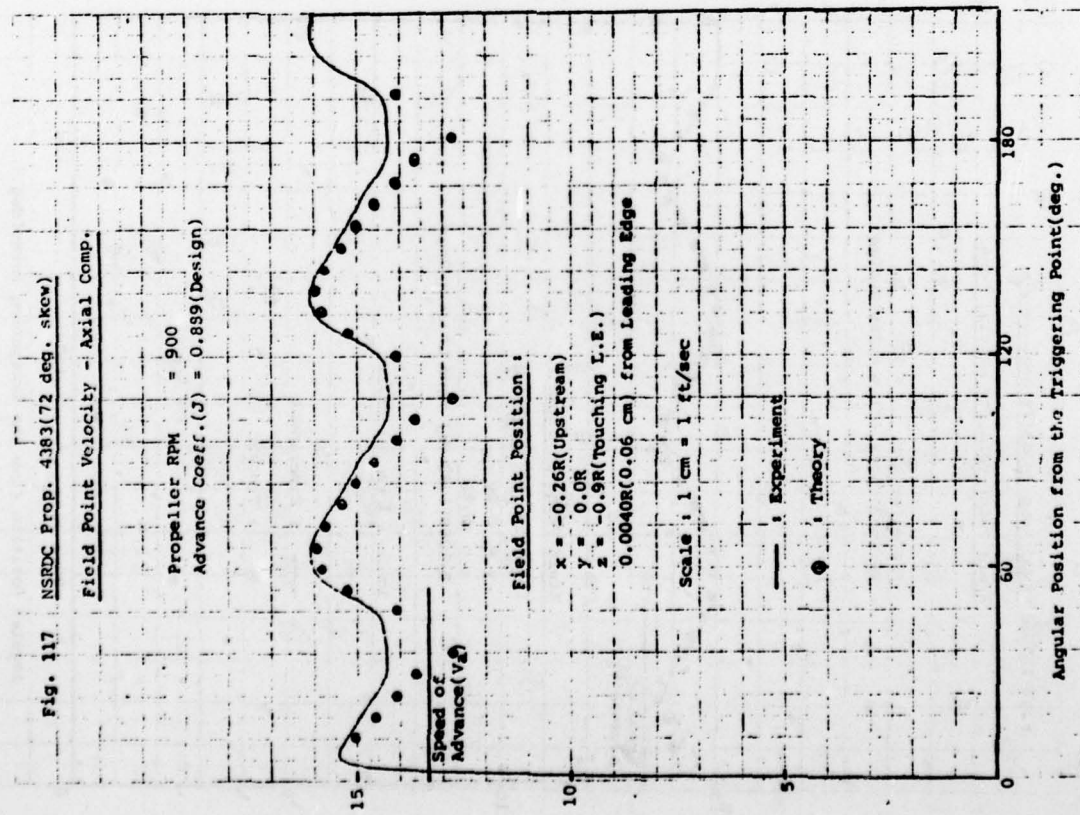
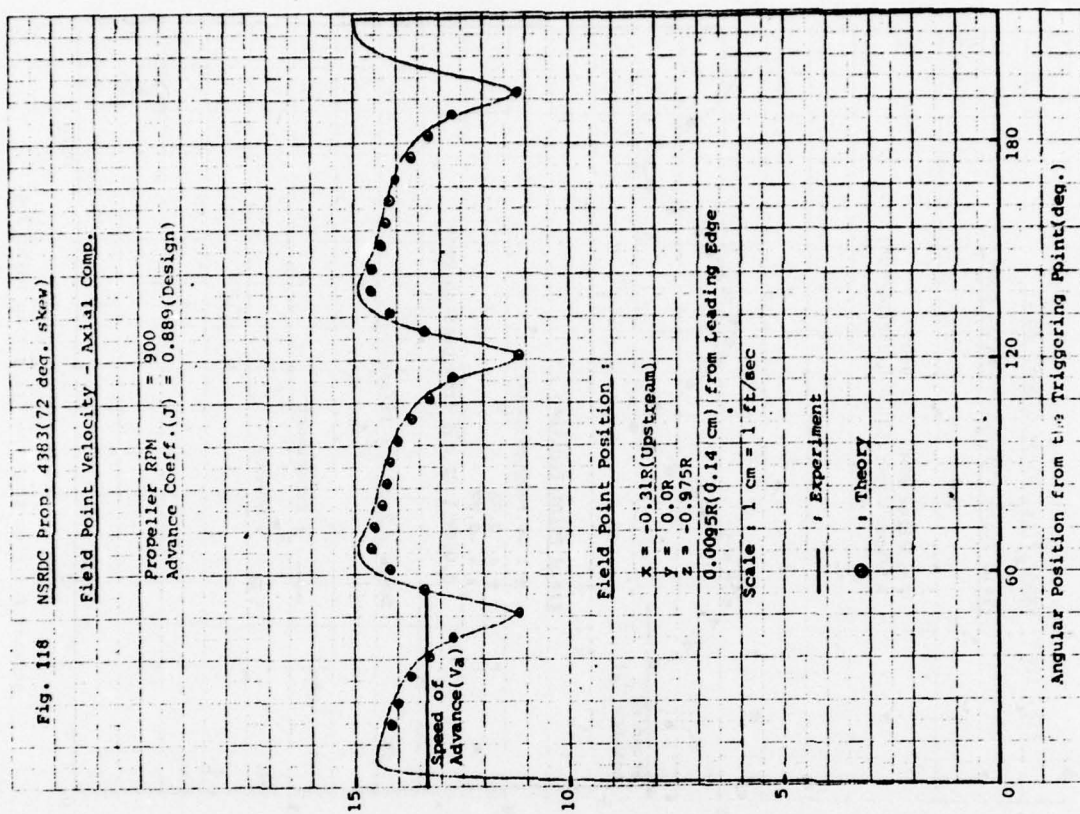


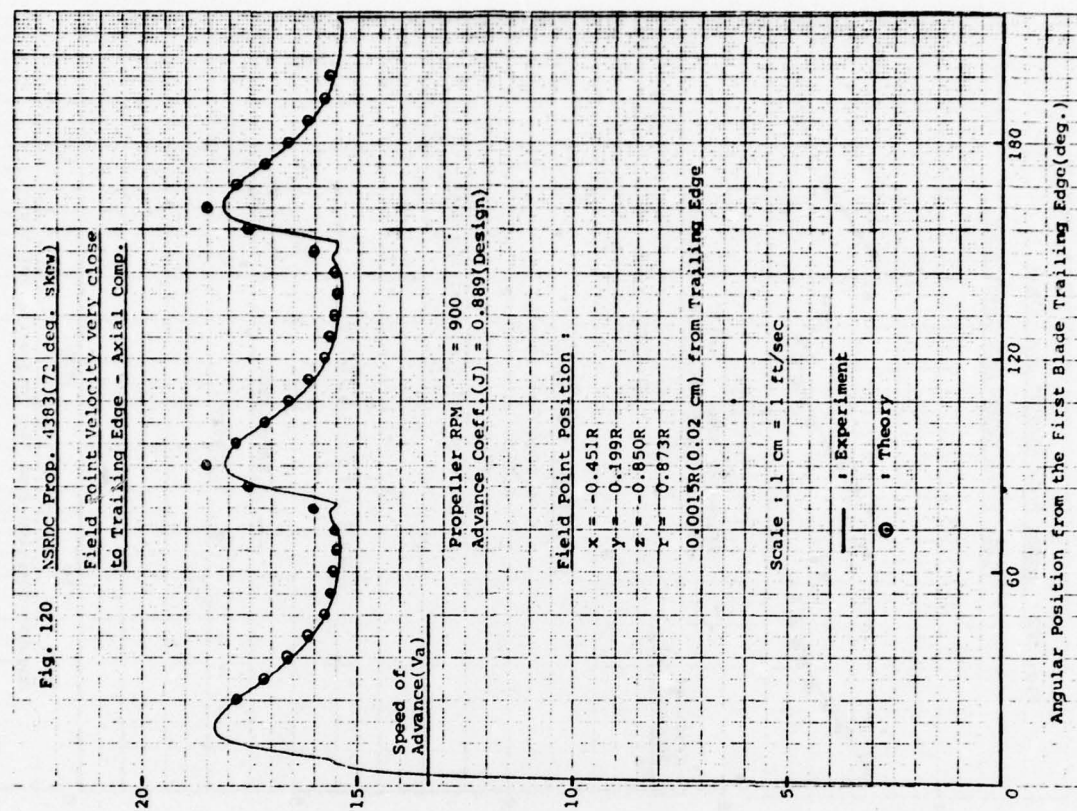
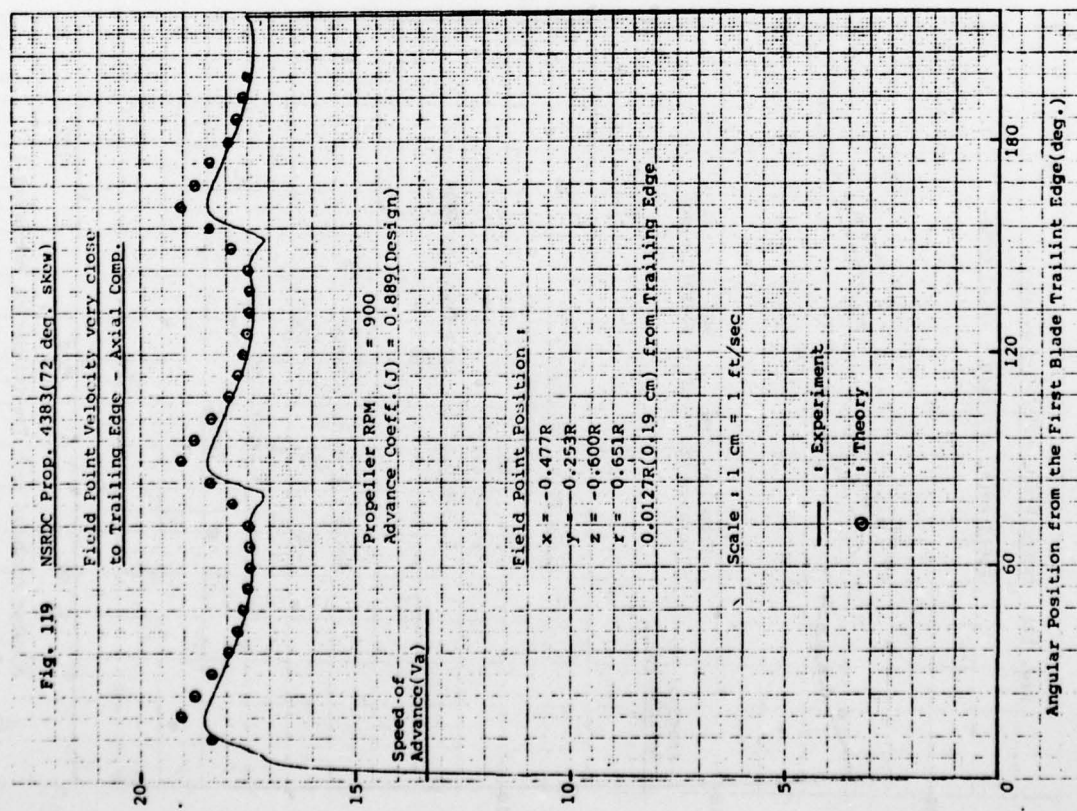


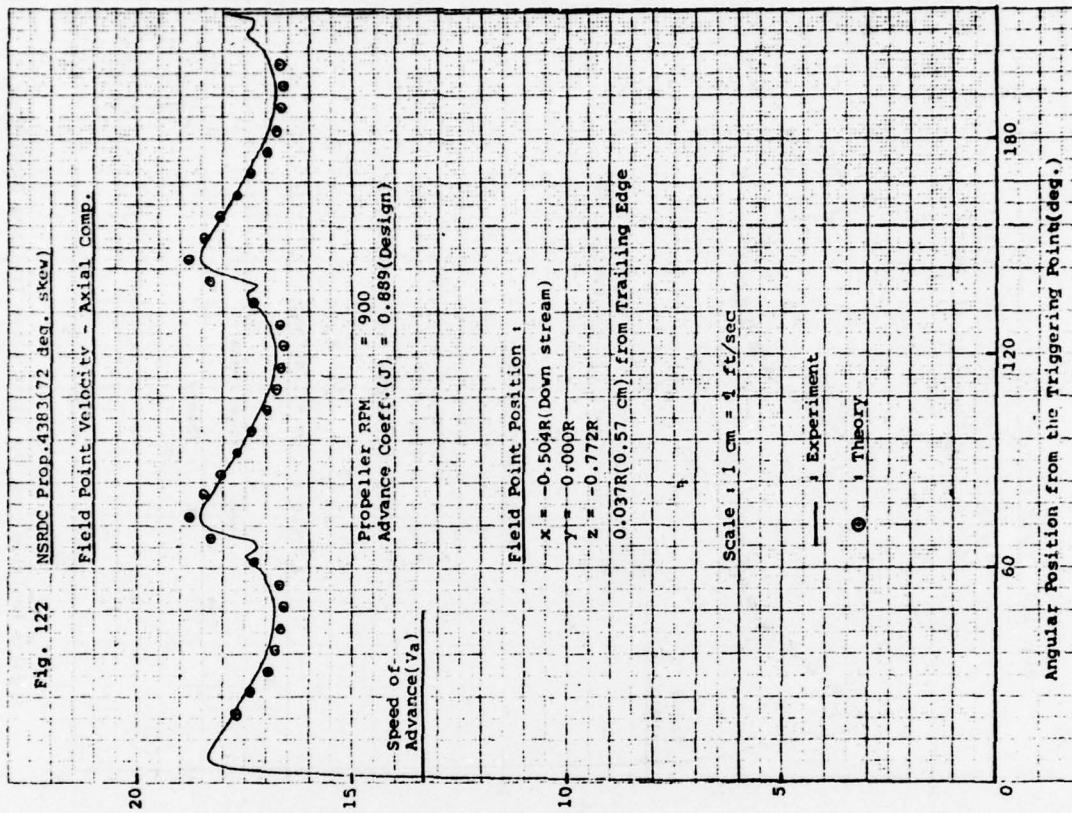
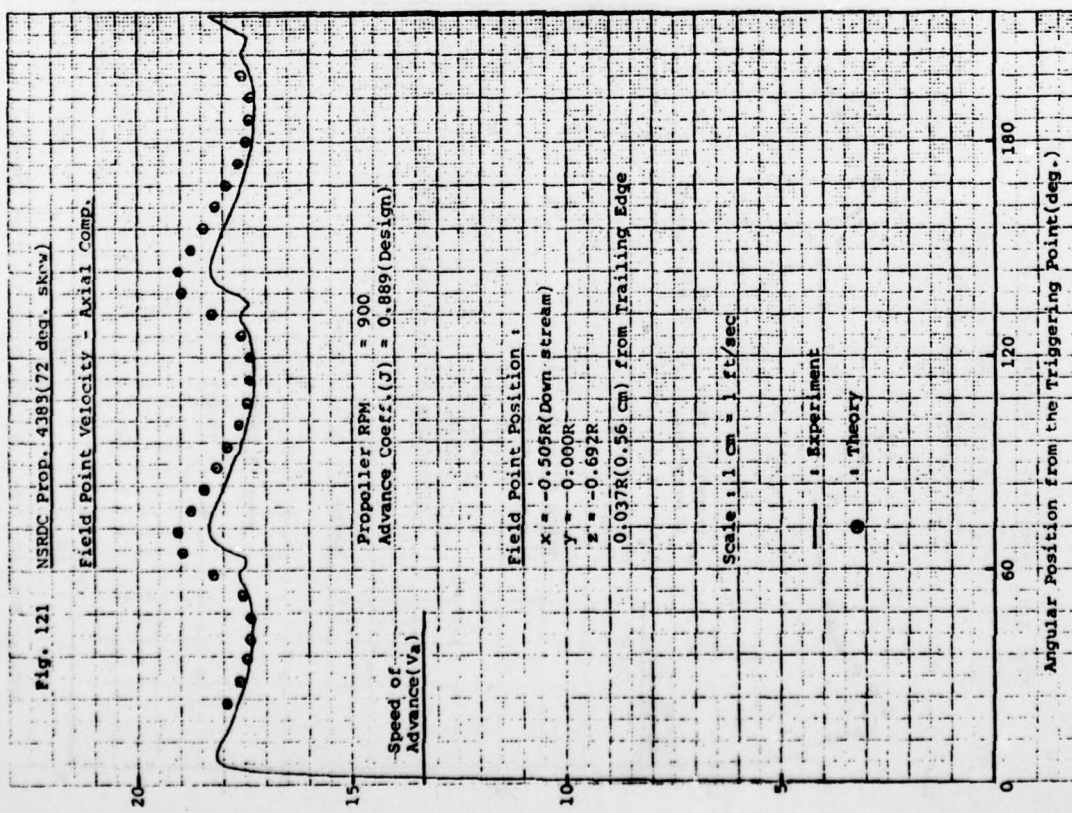


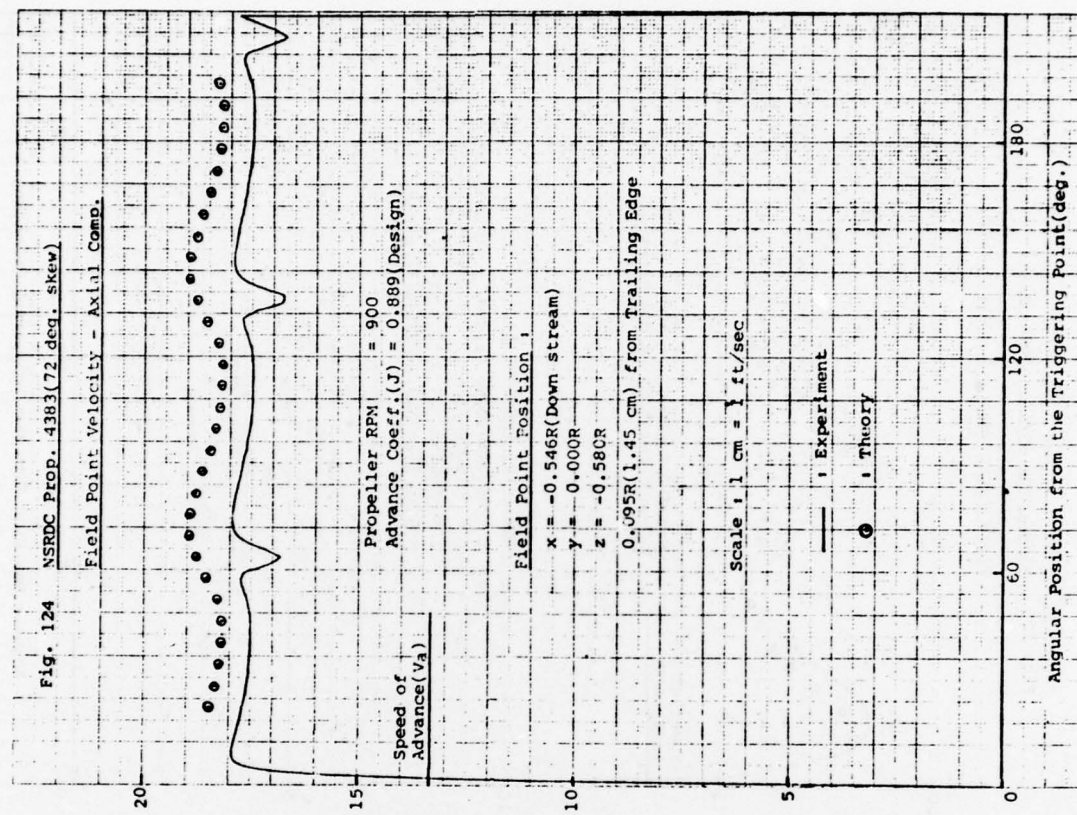
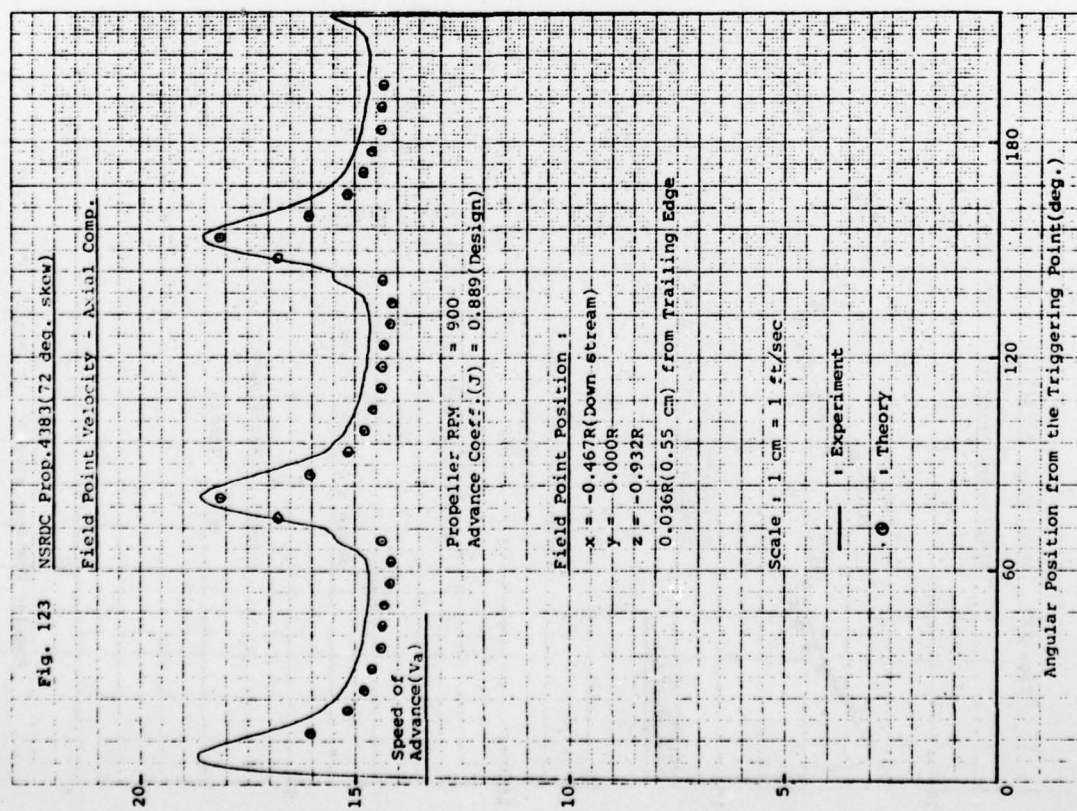


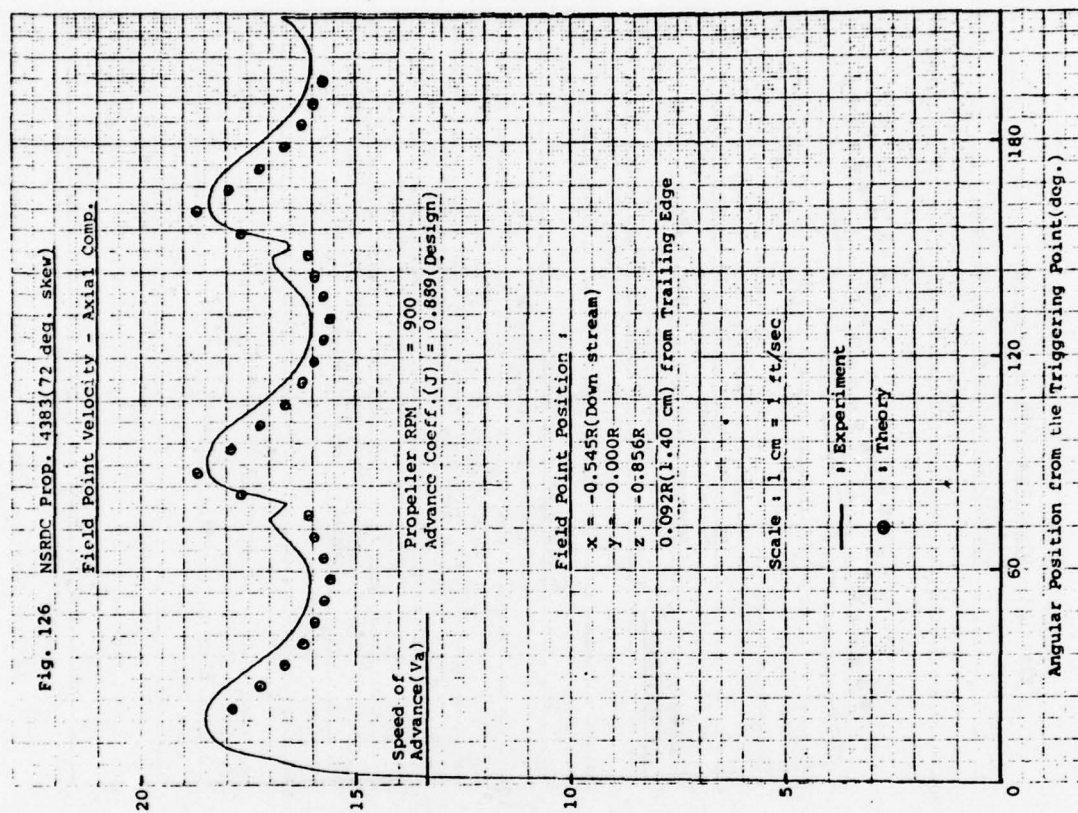
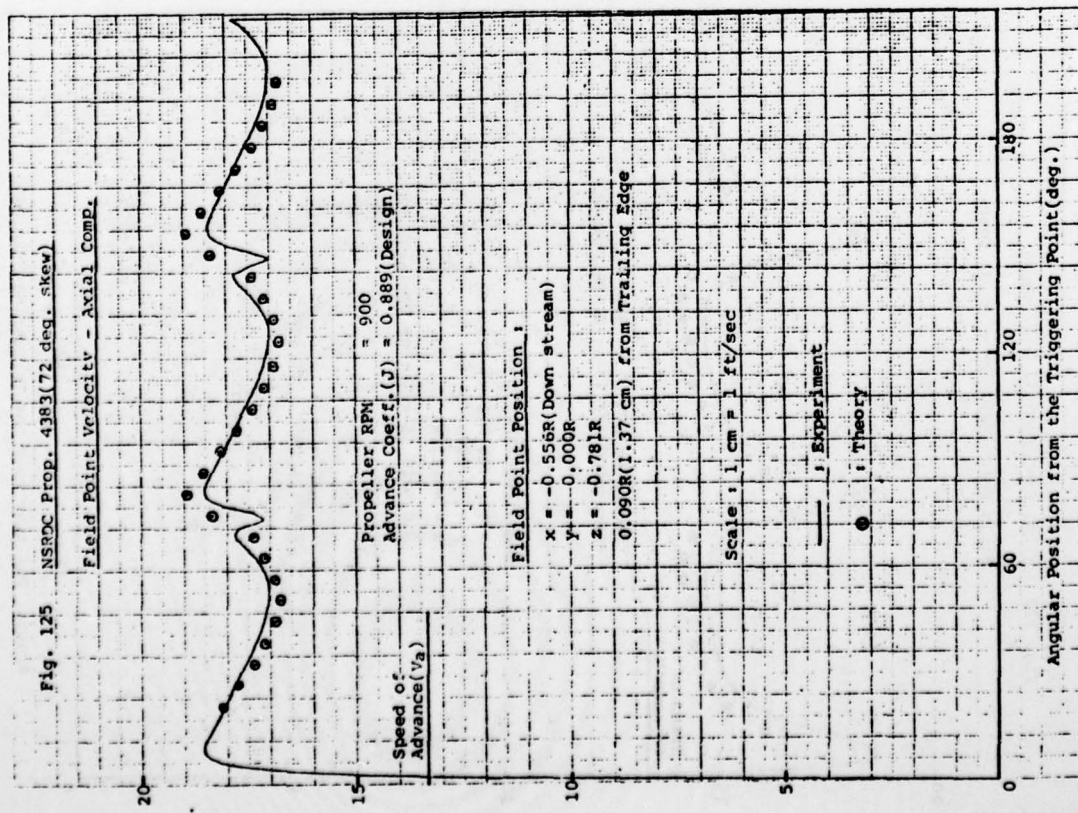


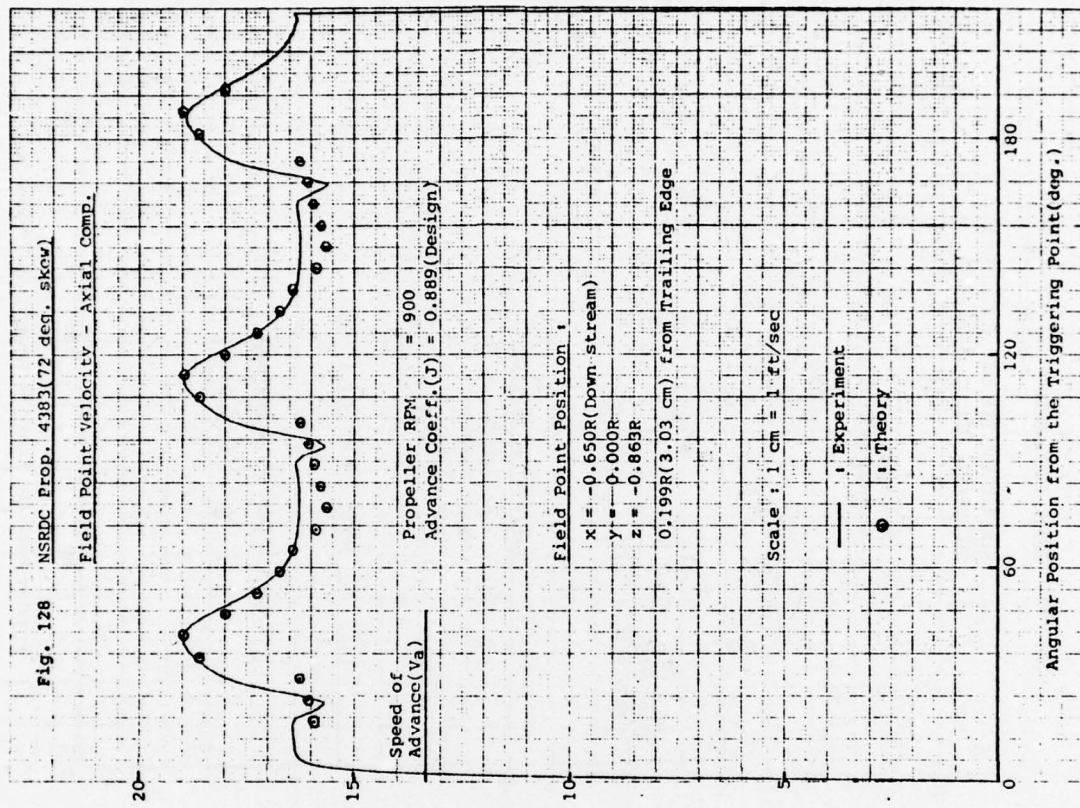
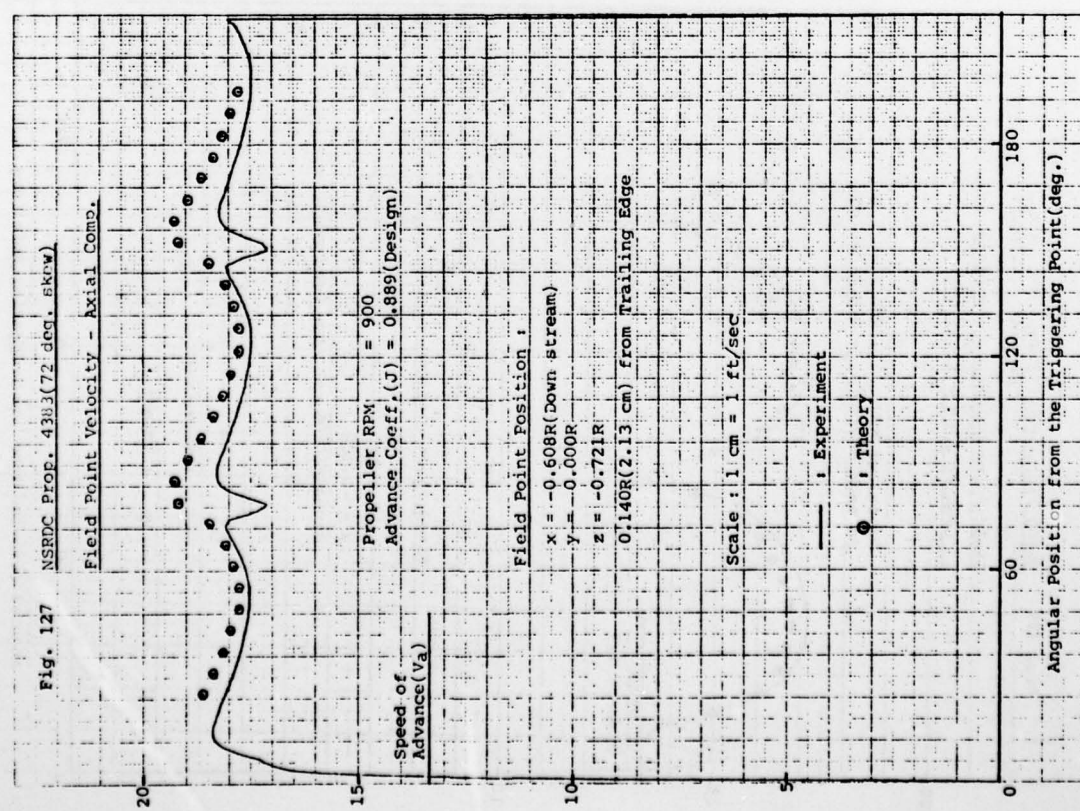


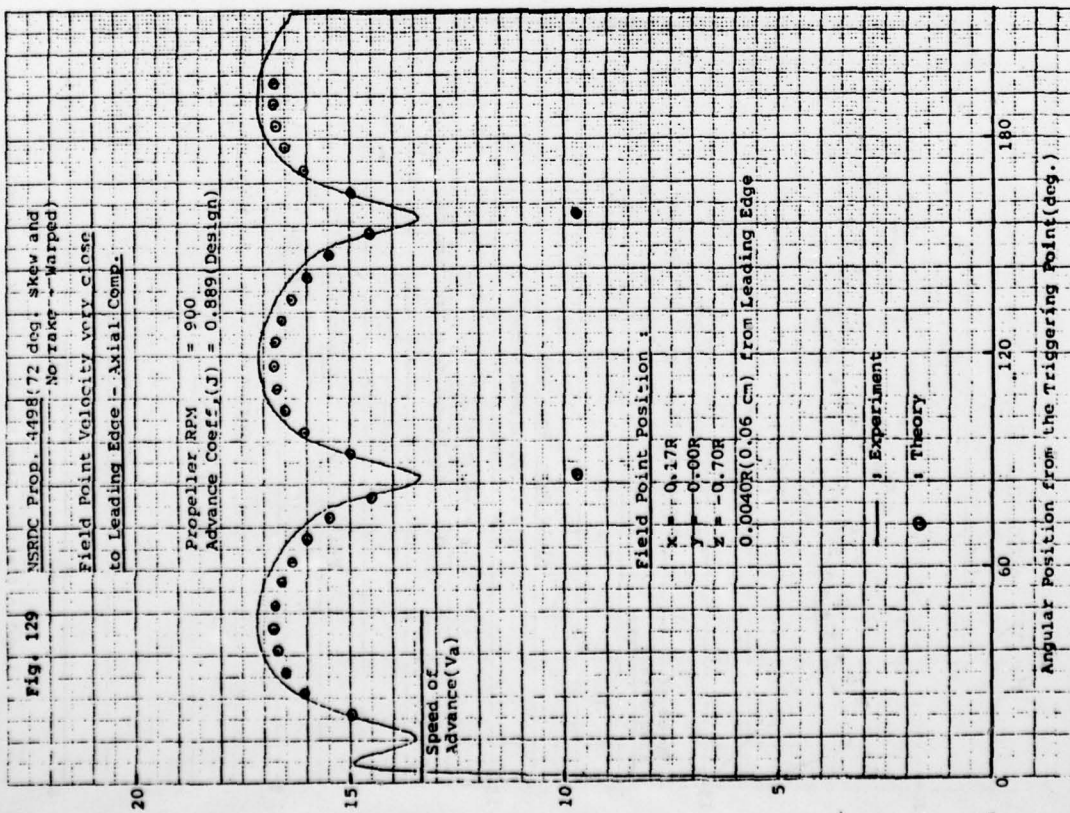
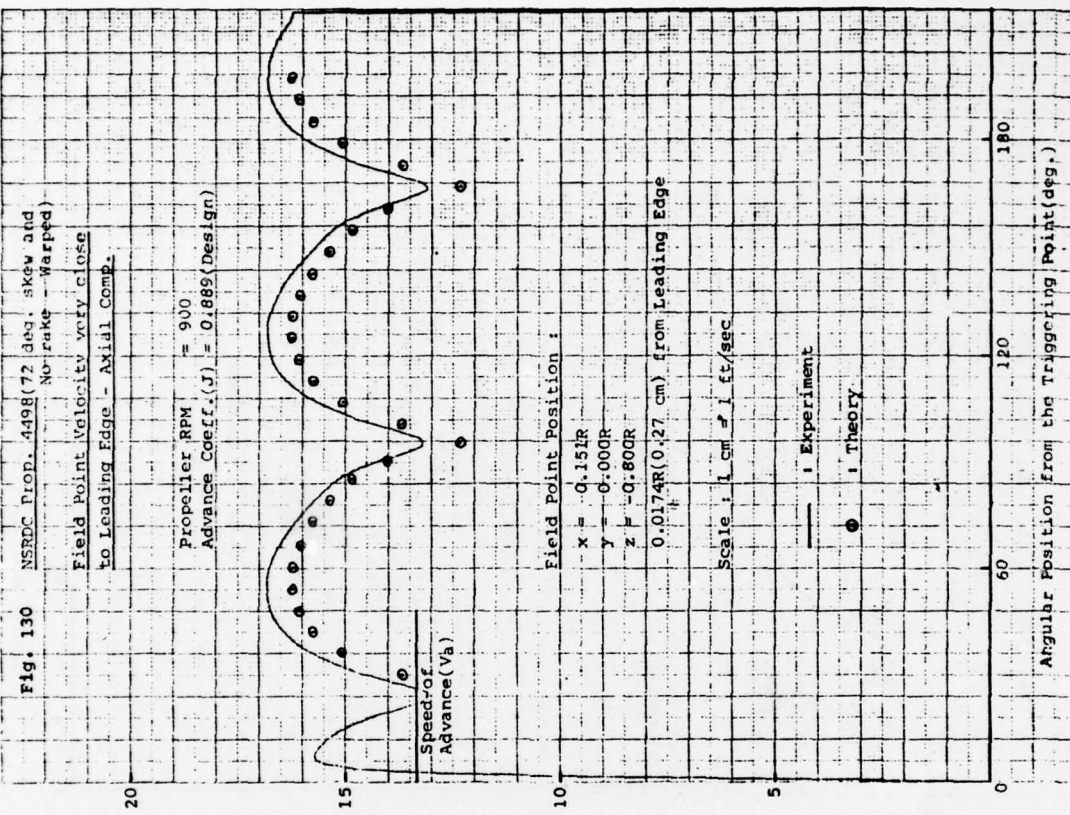












AD-A060 722 MASSACHUSETTS INST OF TECH CAMBRIDGE DEPT OF OCEAN E--ETC F/G 13/10
NUMERICAL AND EXPERIMENTAL METHODS FOR THE PREDICTION OF FIELD --ETC(U)
JUN 78 K MIN

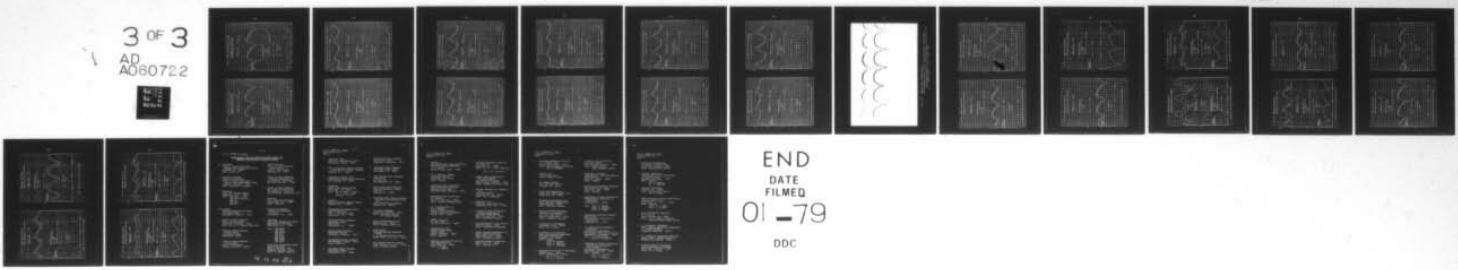
UNCLASSIFIED

OE-78-12

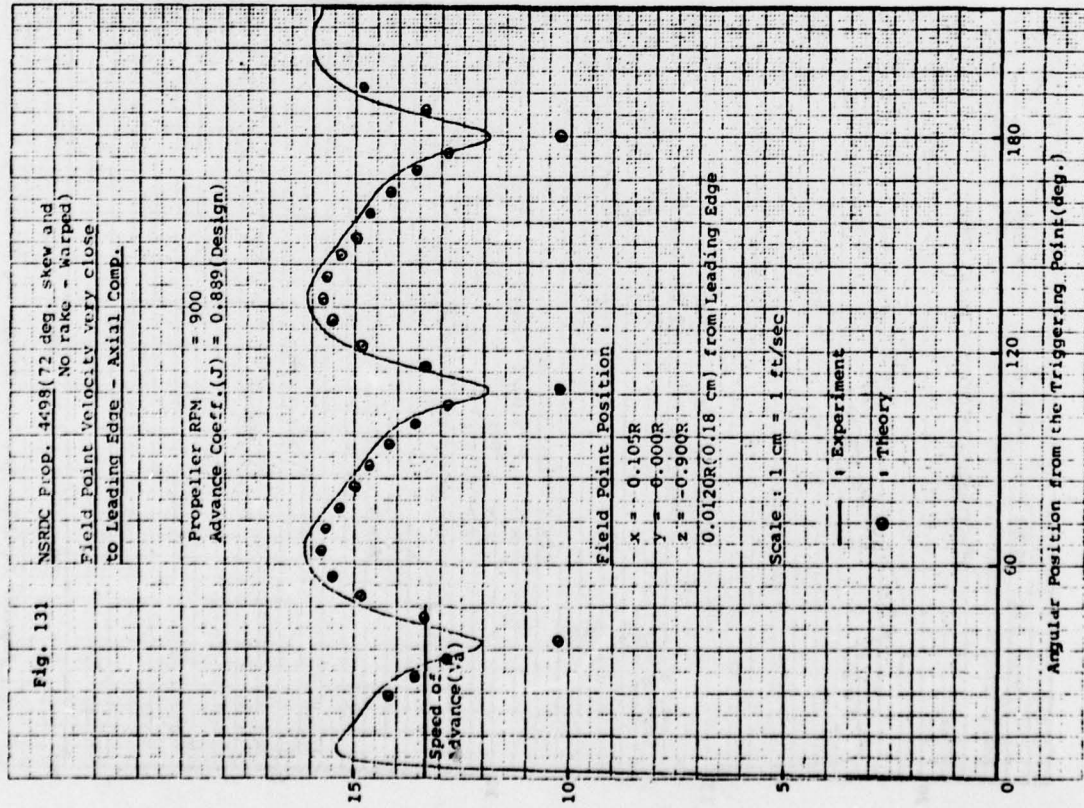
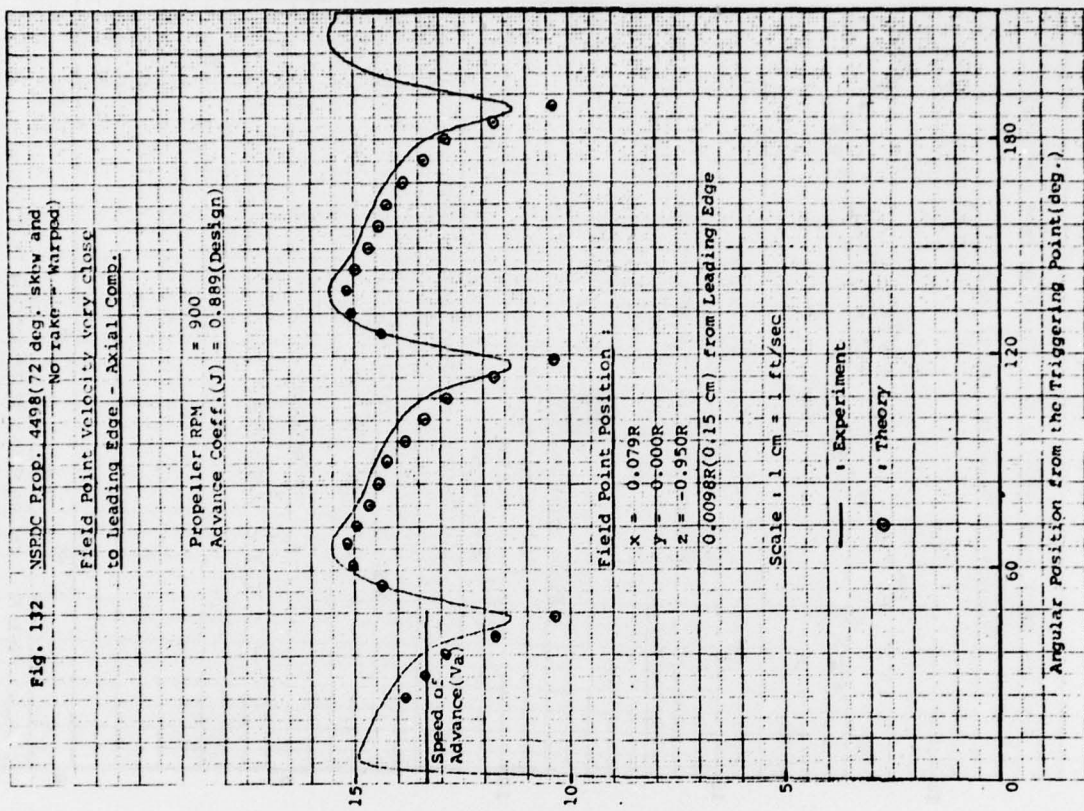
N00014-76-C-0357

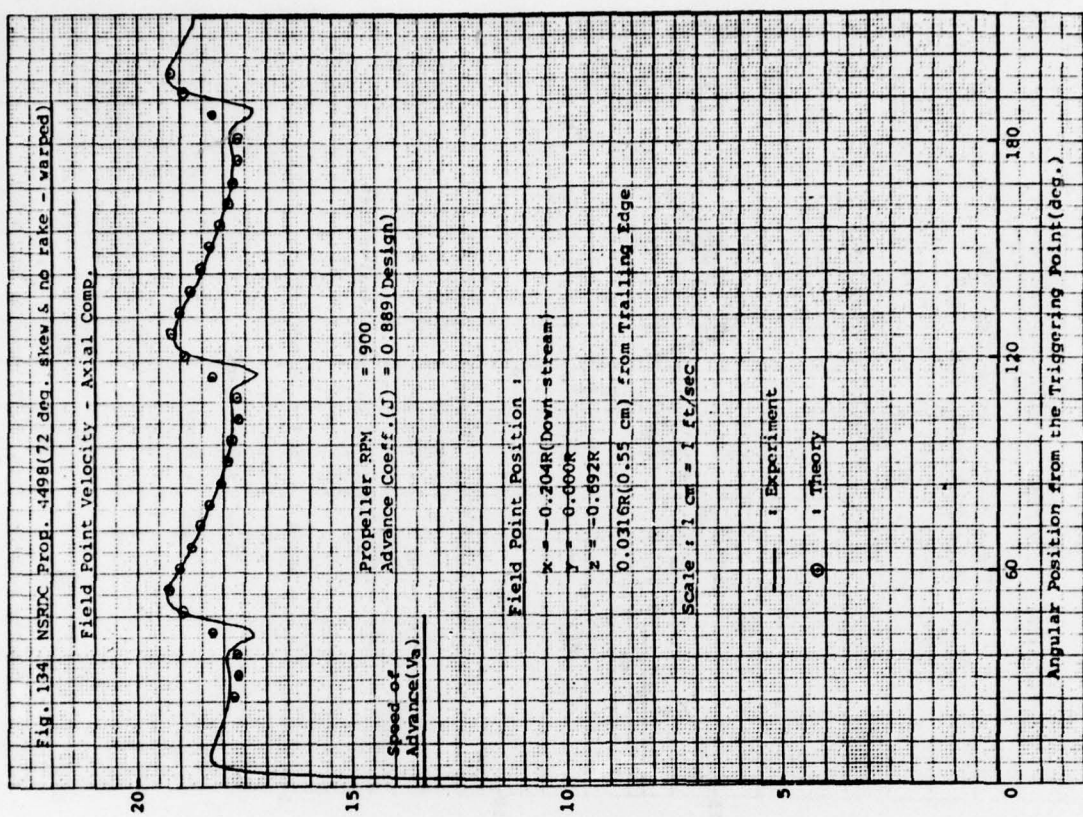
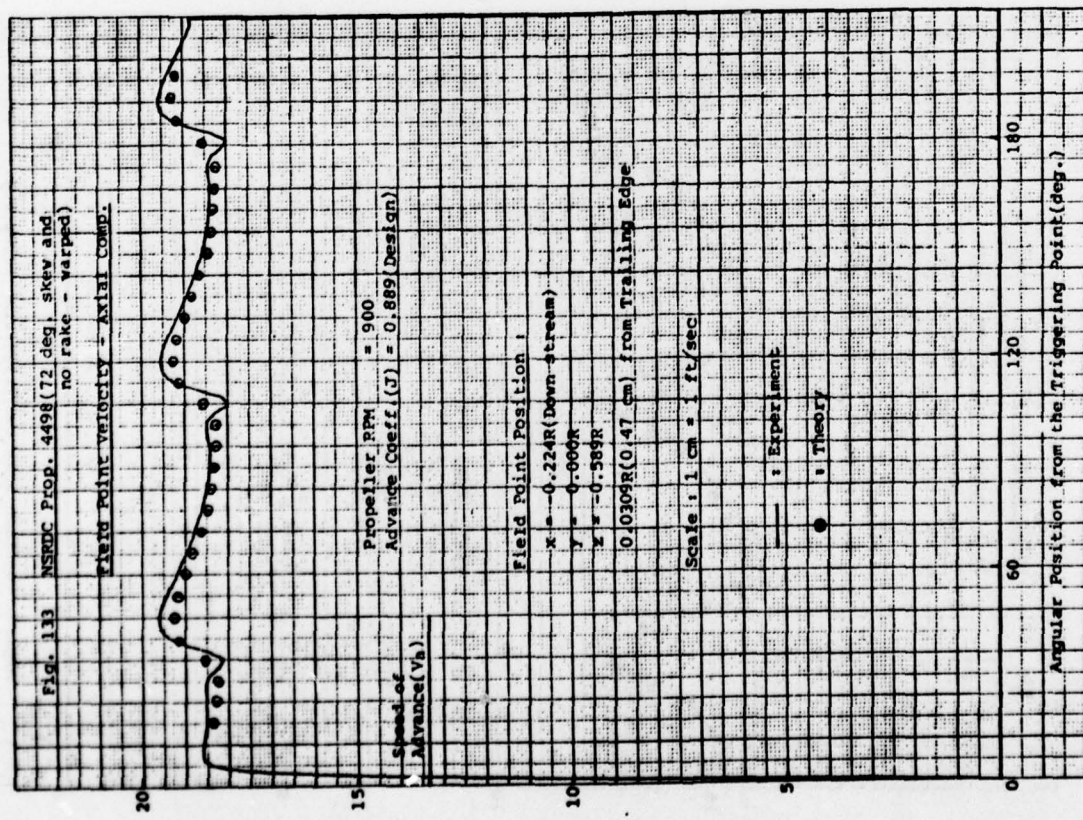
NL

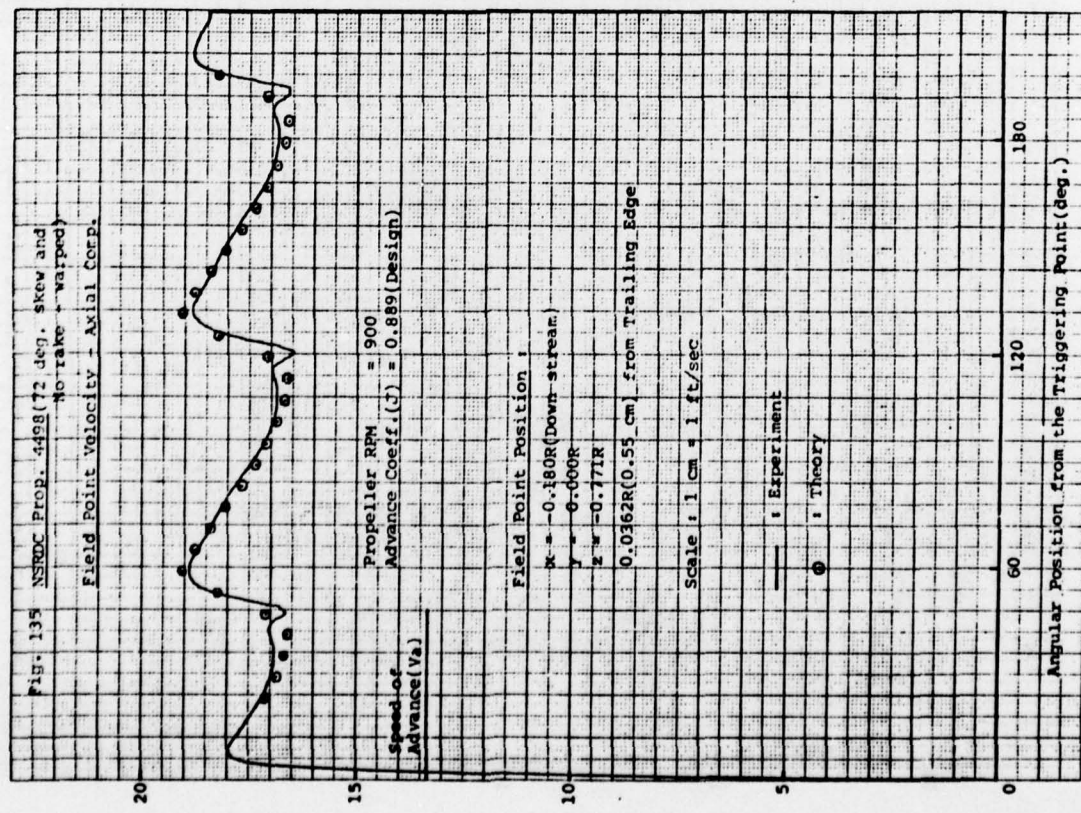
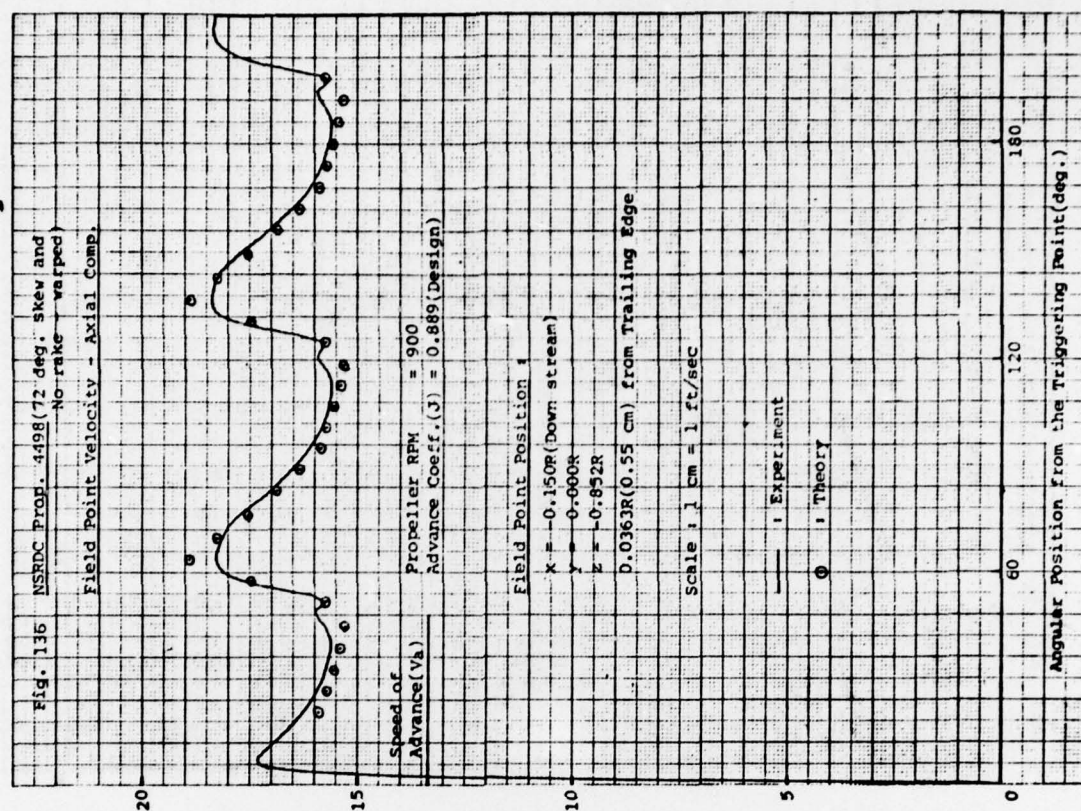
3 OF 3
AD
A060722

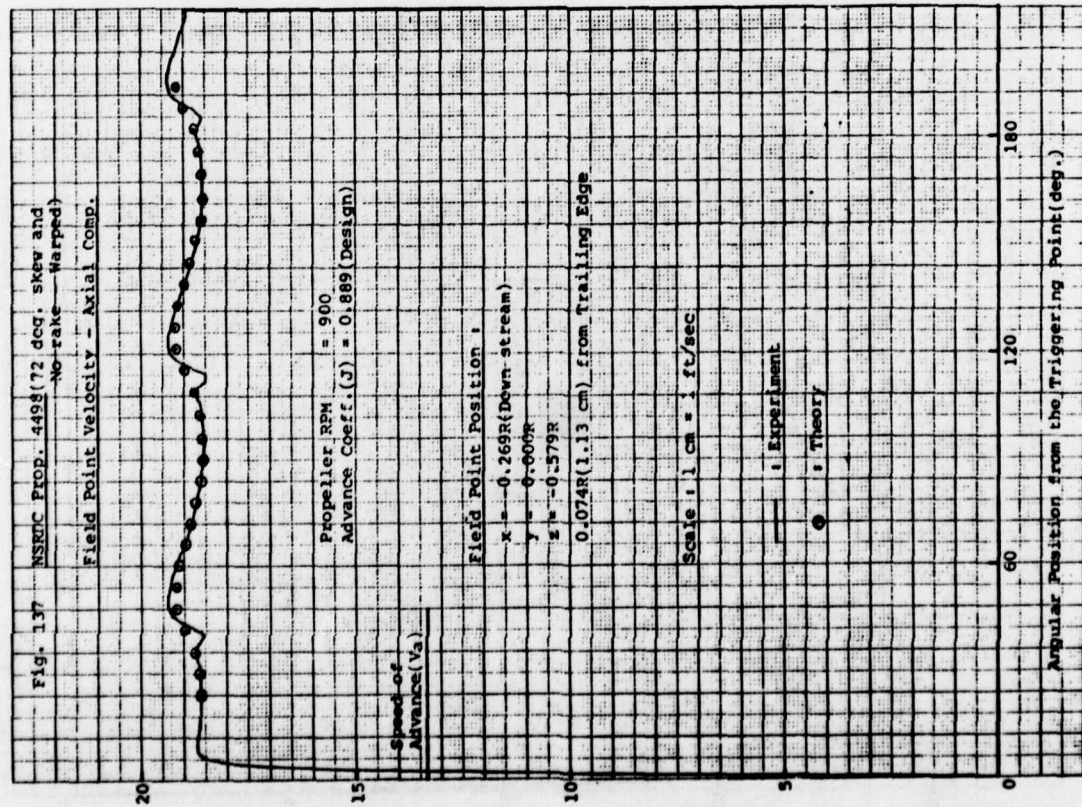
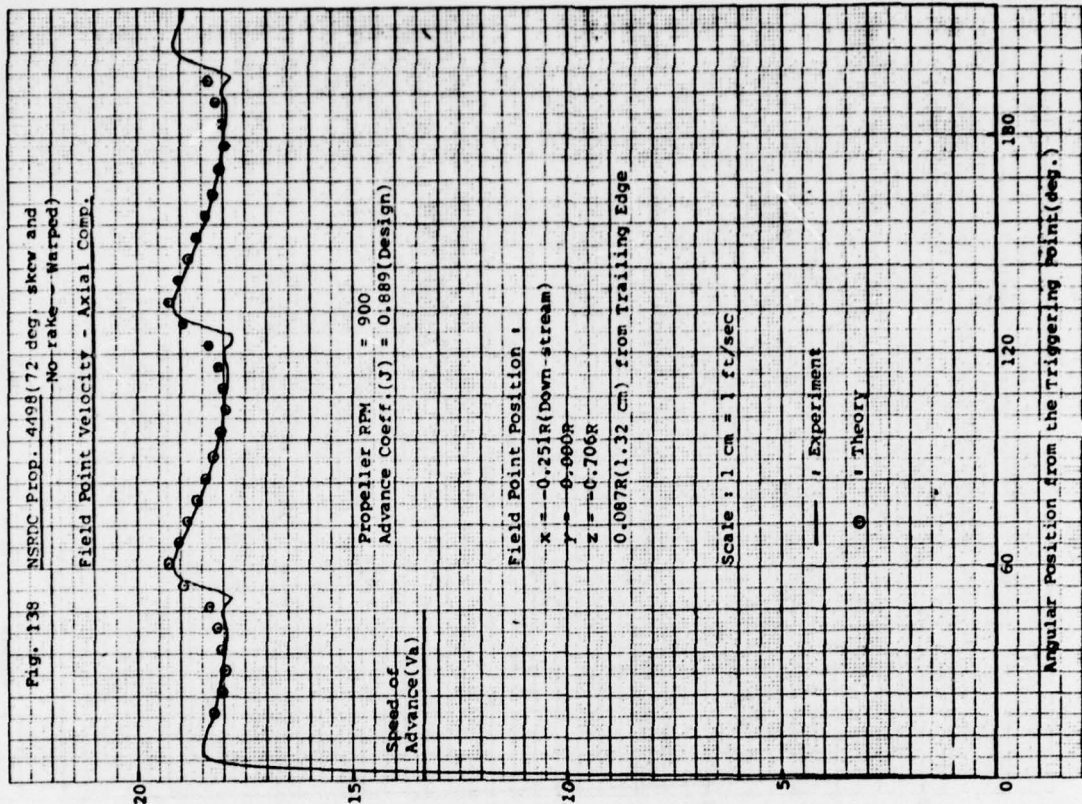


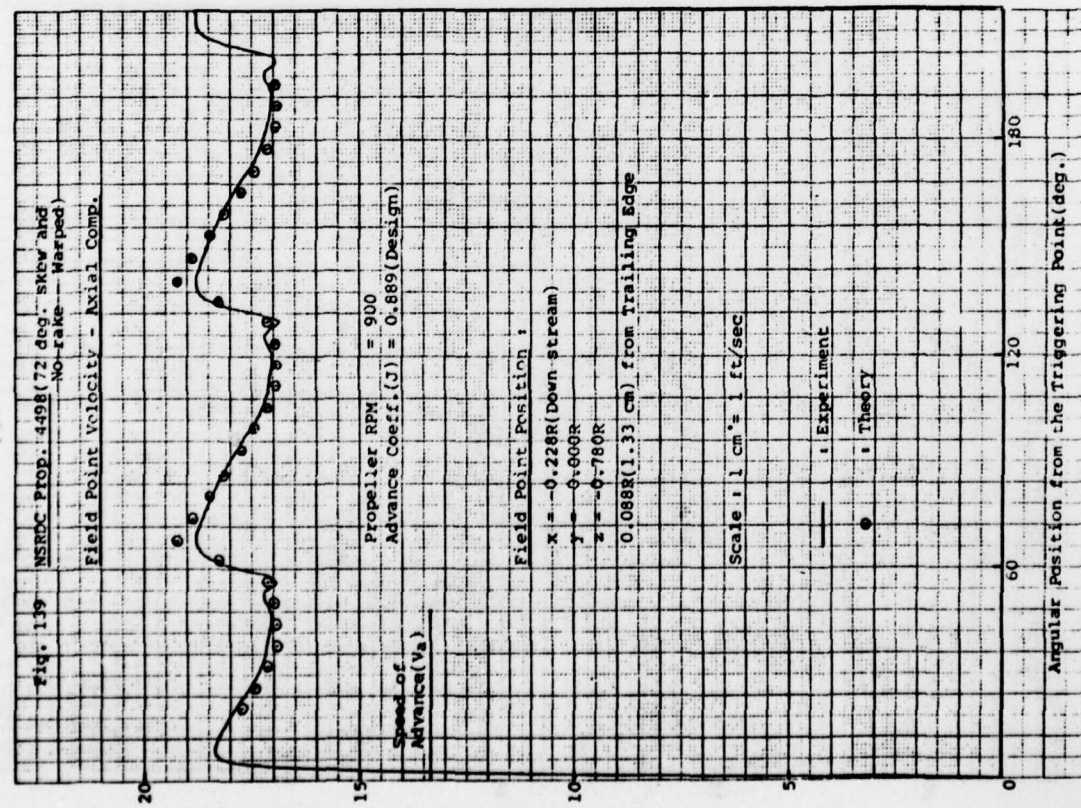
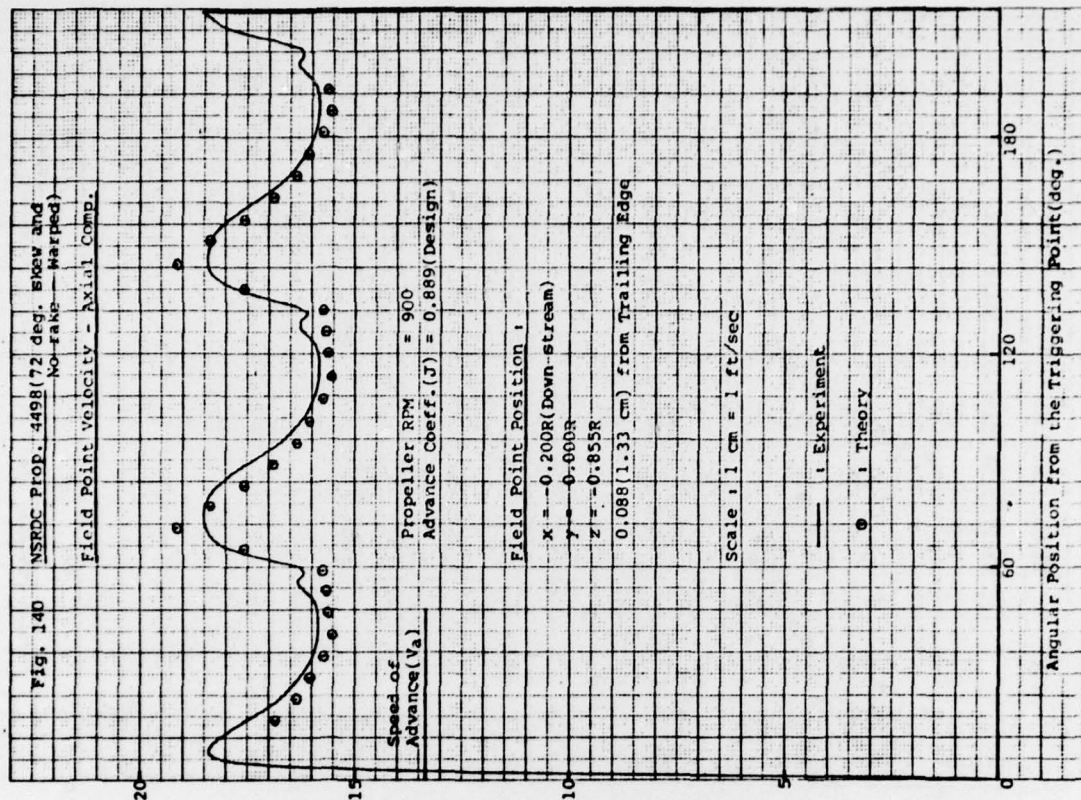
END
DATE
FILED
01-79
DDC

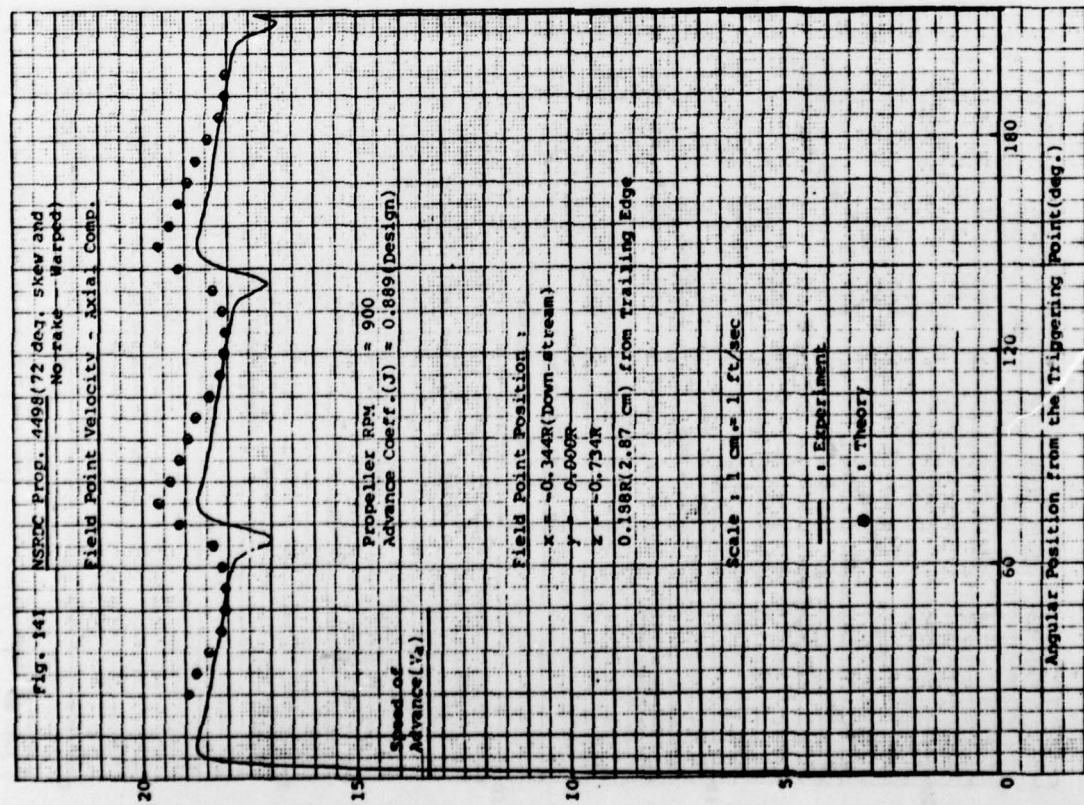
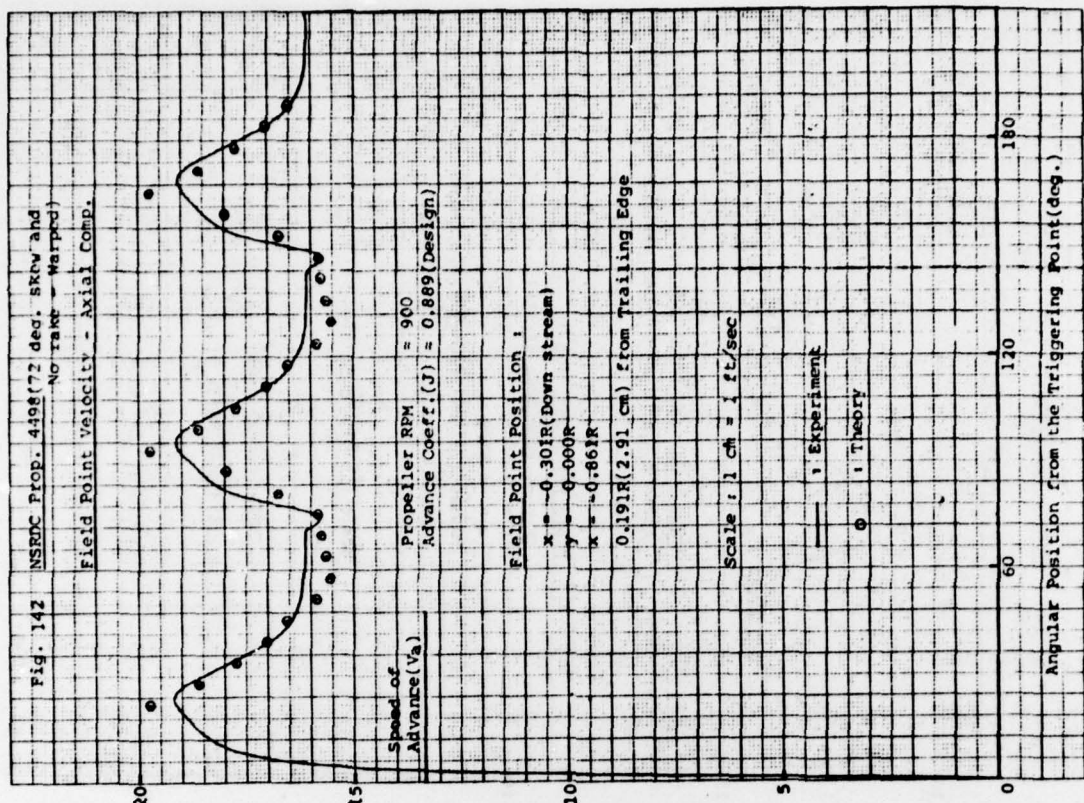












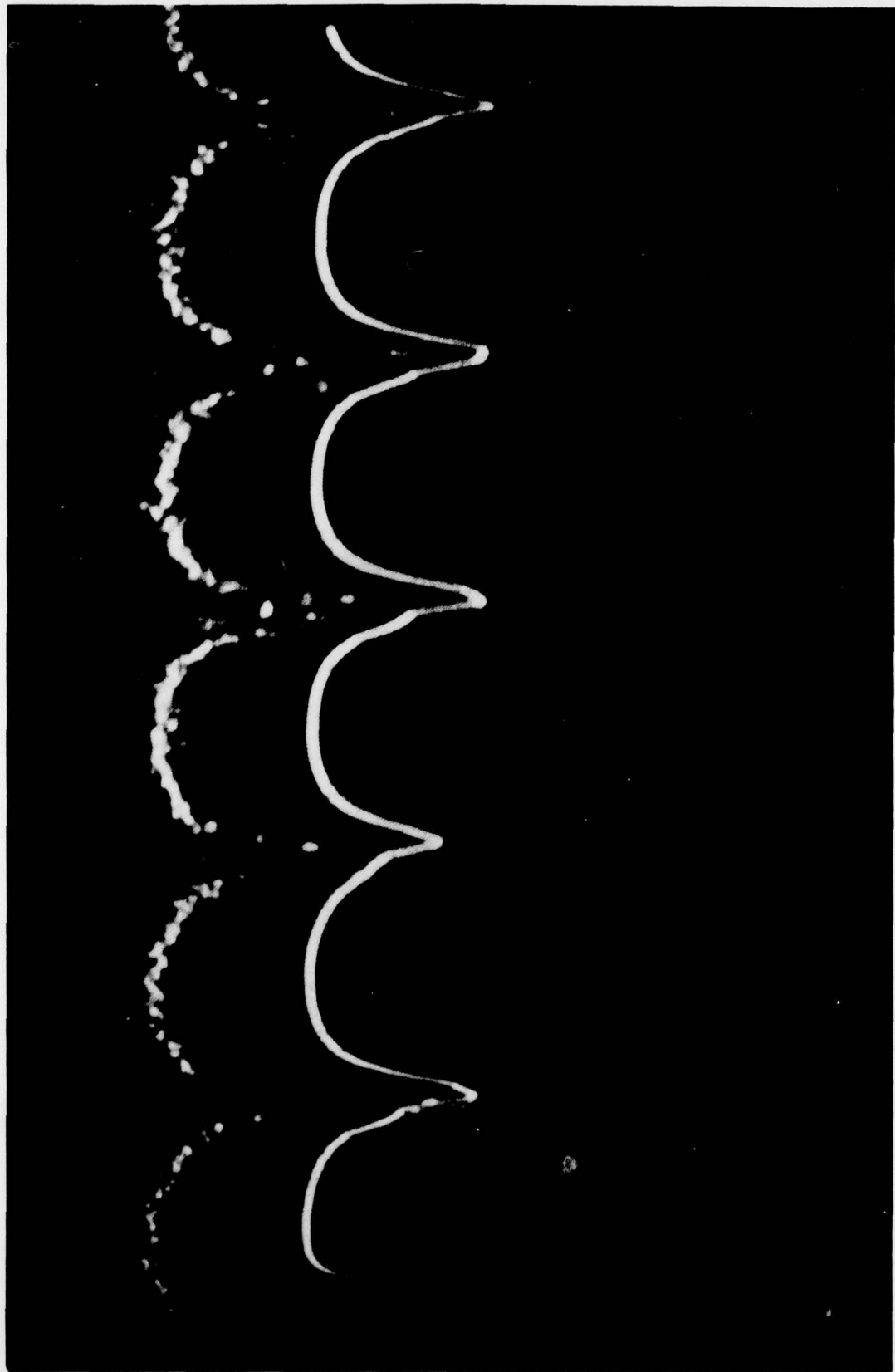
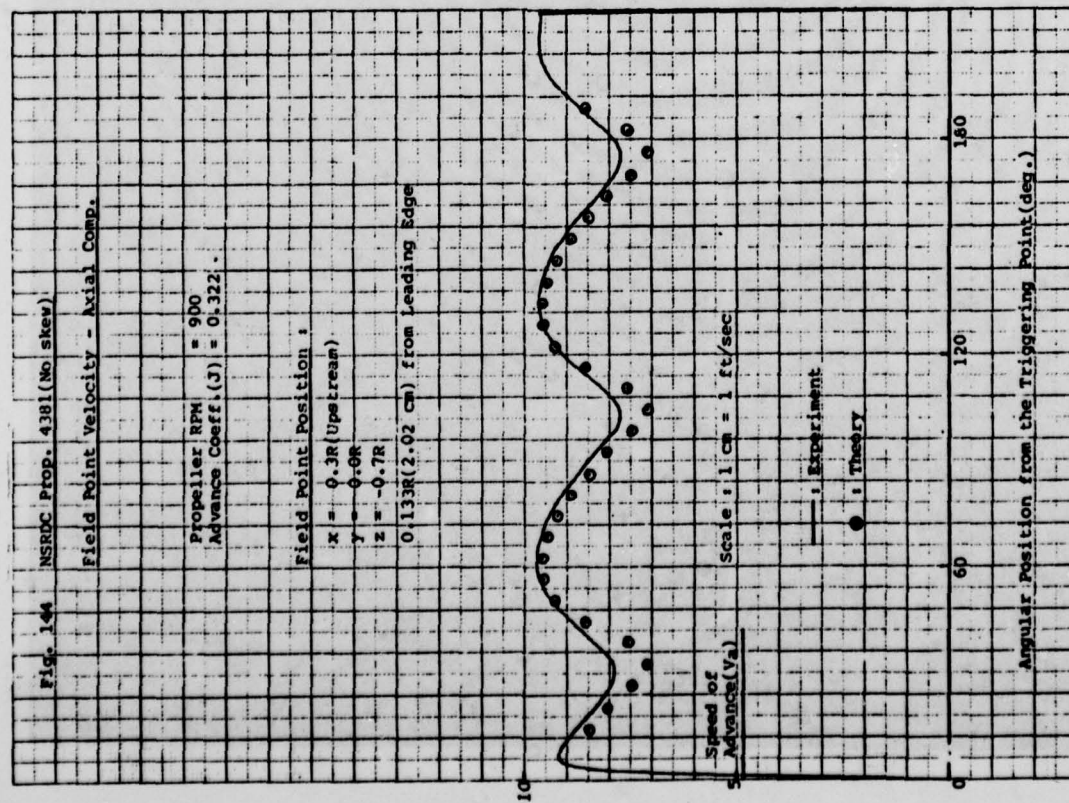
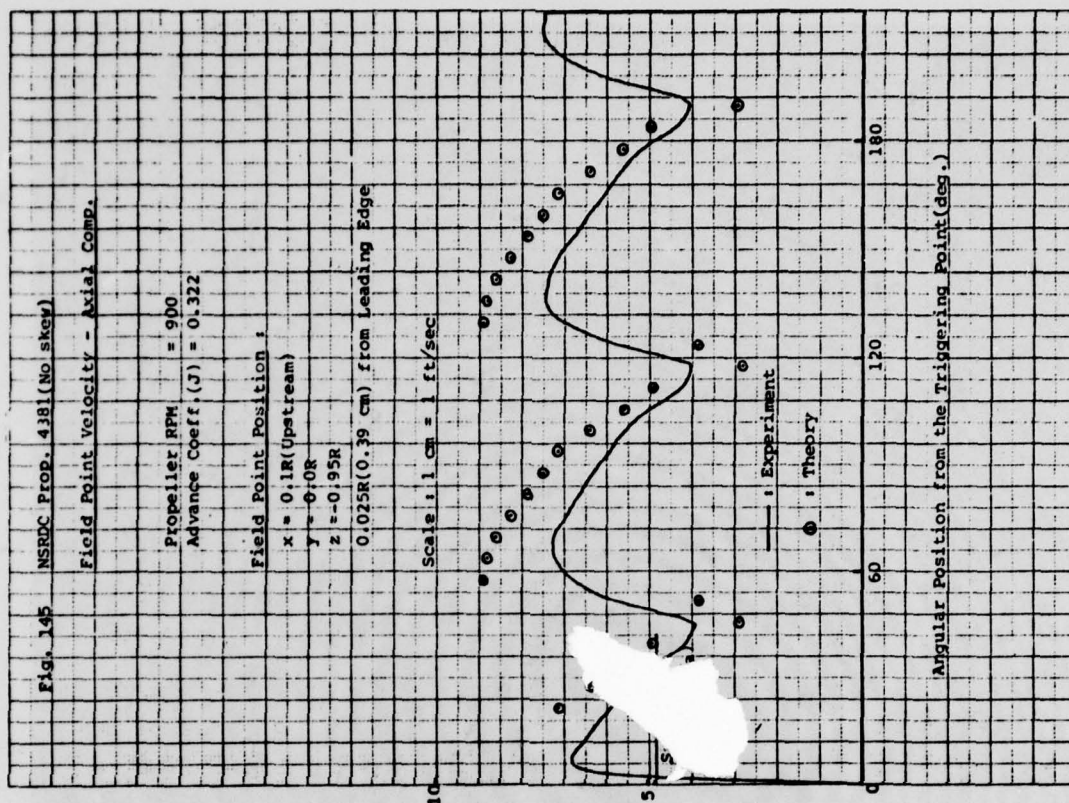
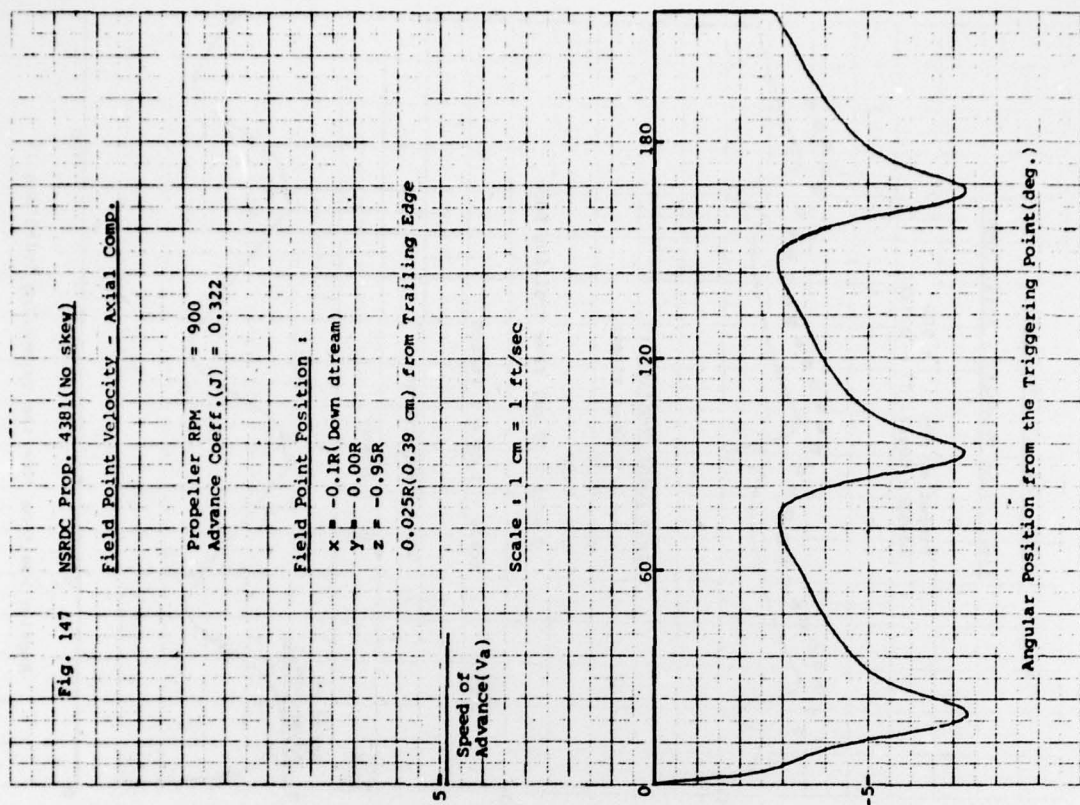
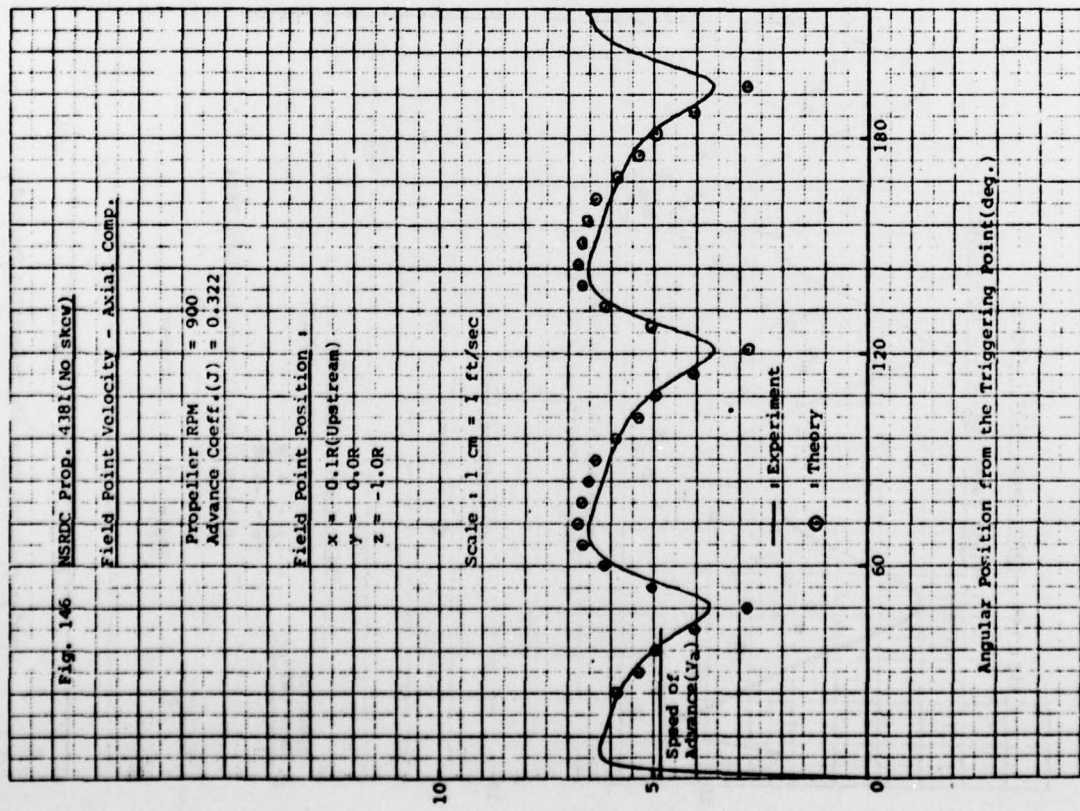
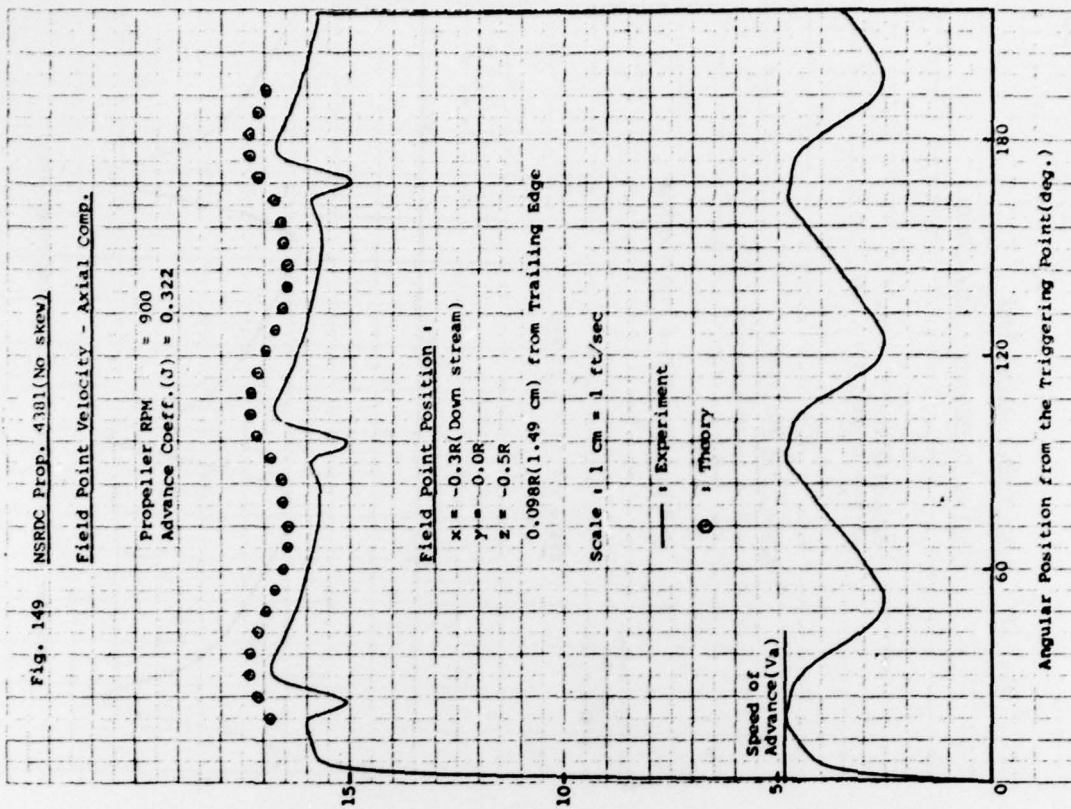
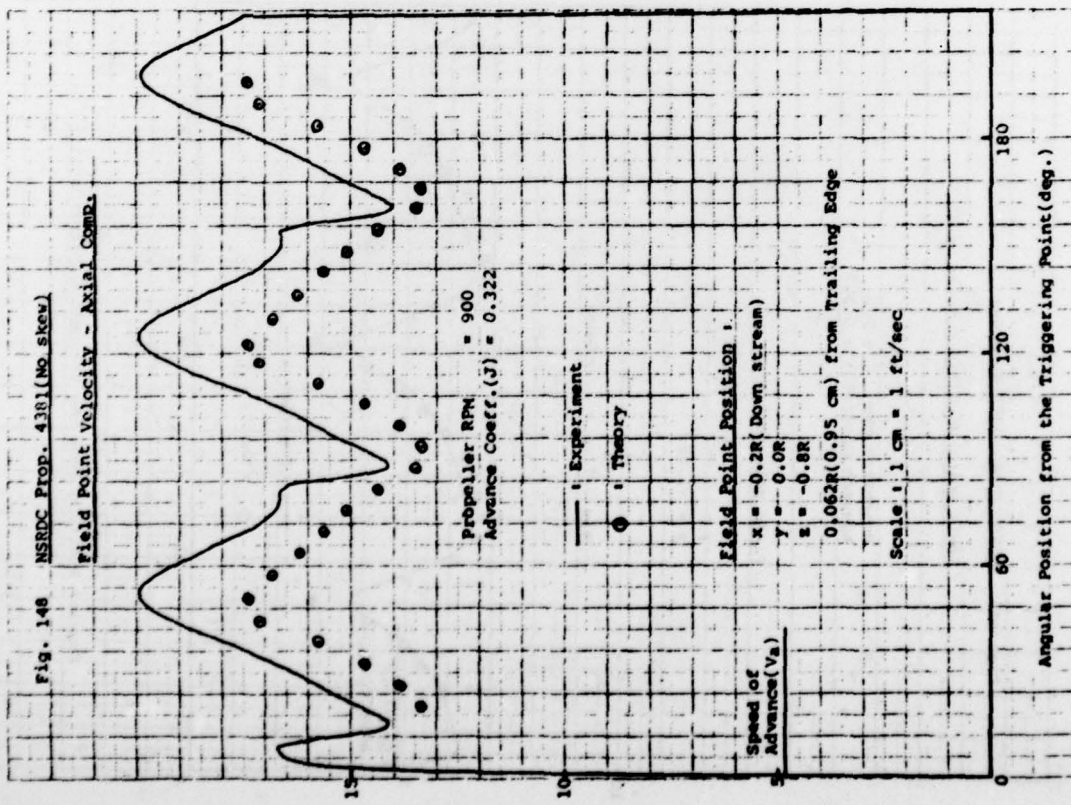
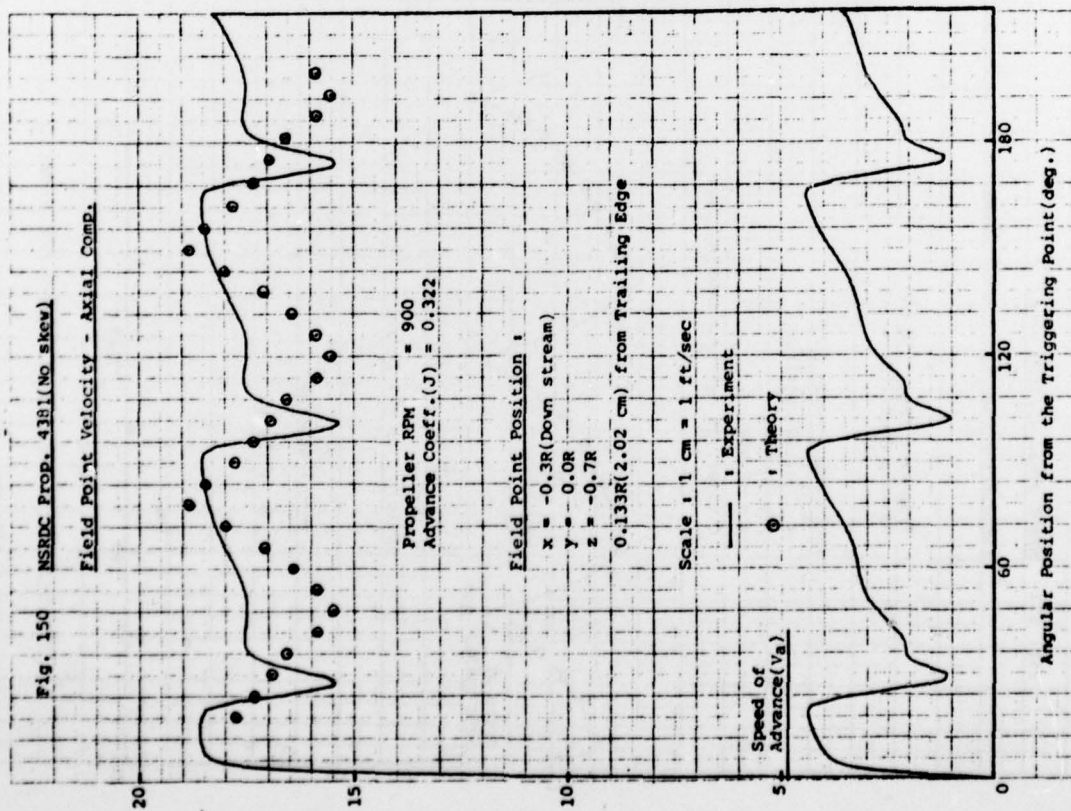
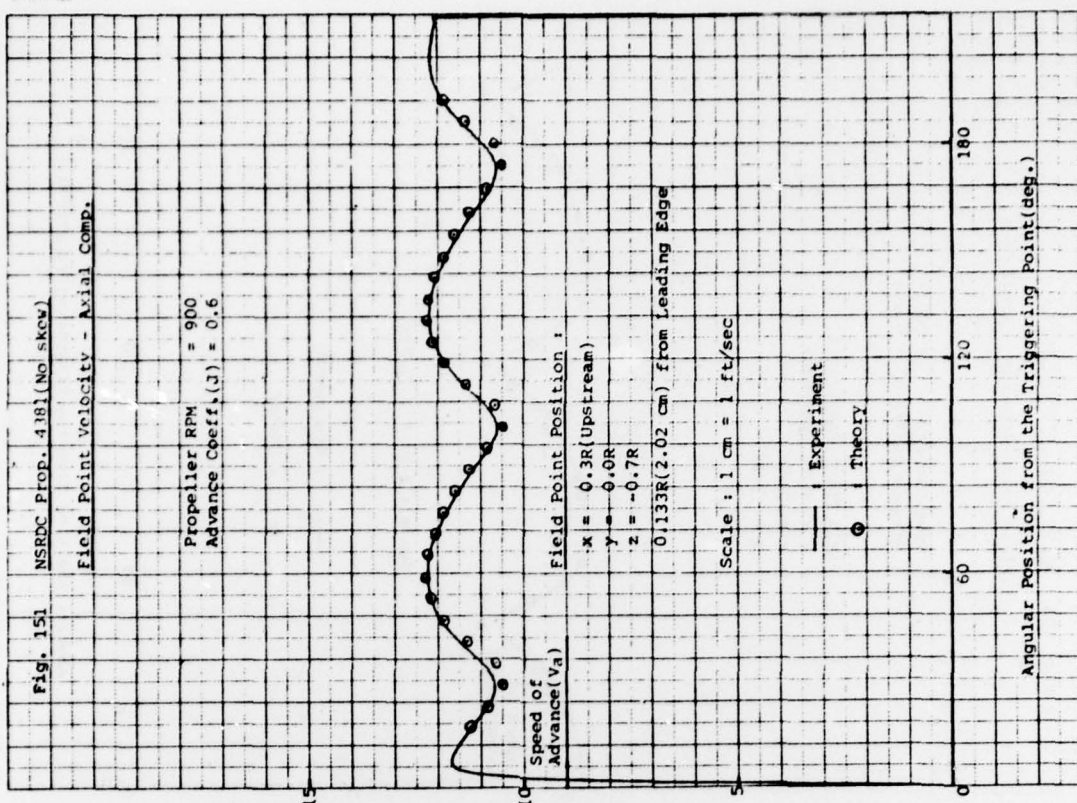


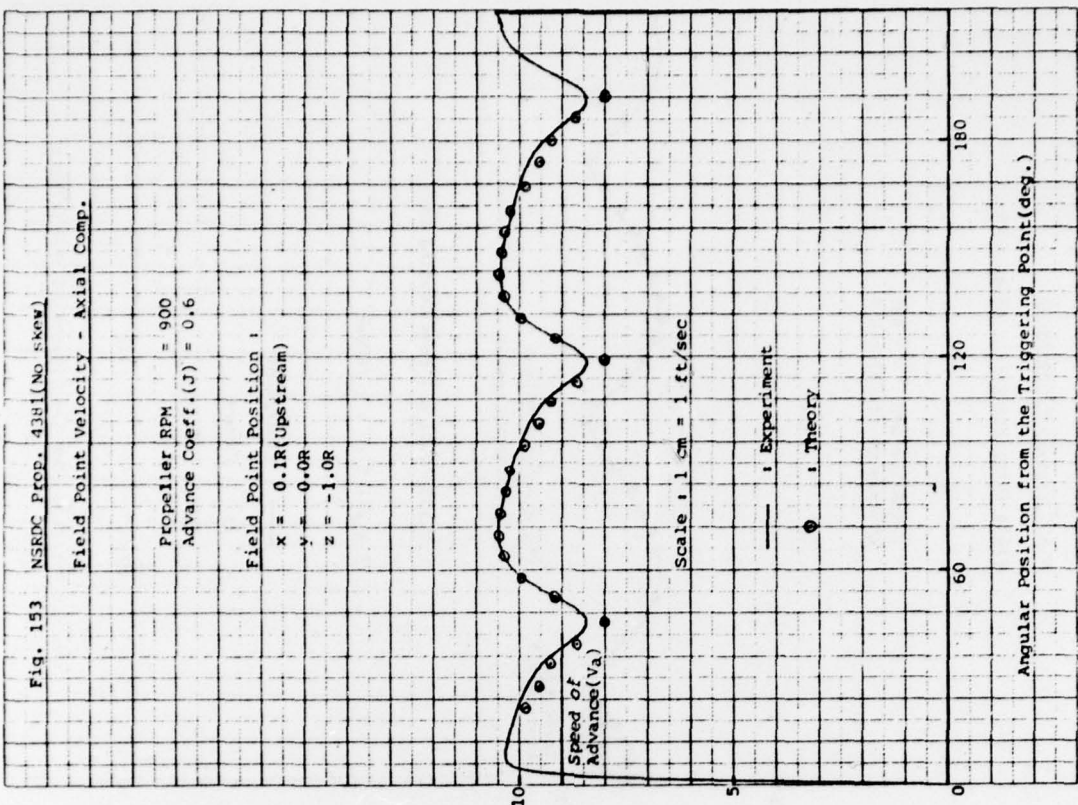
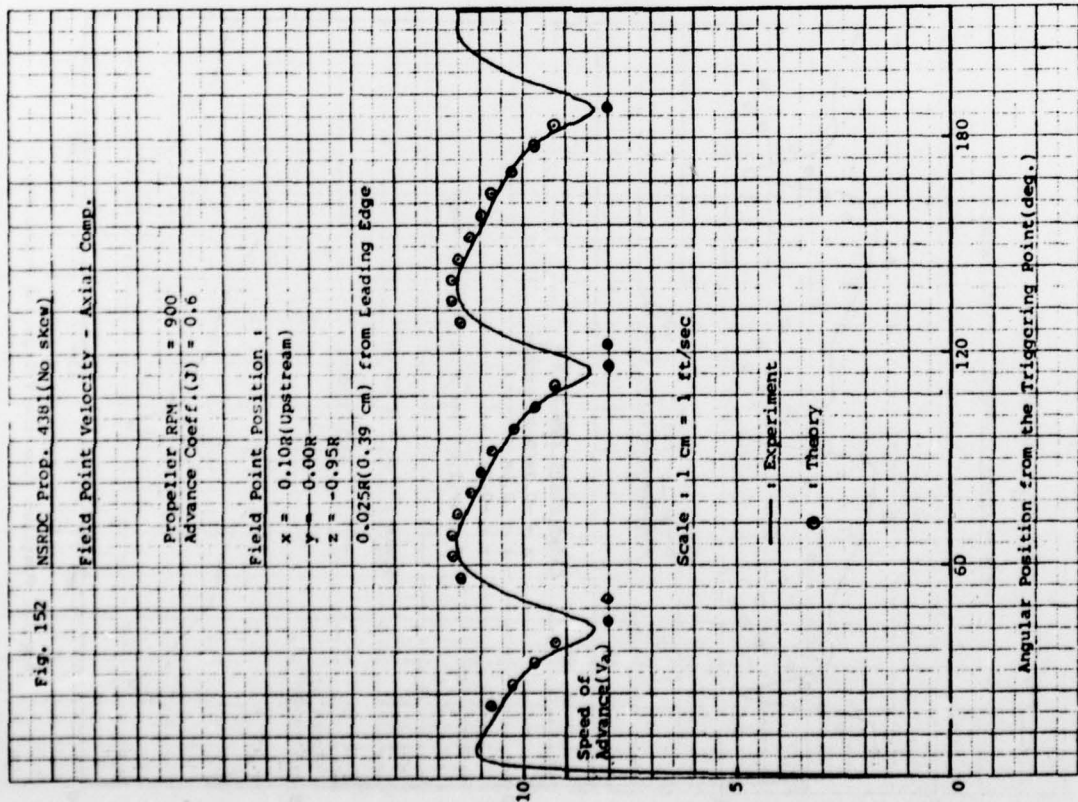
Fig. 143 NSRDC Prop. 4381(No skew)
Oscilloscope Trace of Field Point Velocity - Axial Comp.
Field Point Position : $x=0.2R$ (Upstream), $y=0.0R$, $z=-0.7R$
 $J = 0.889$ (Design), 1 div. = 3.81 ft/sec

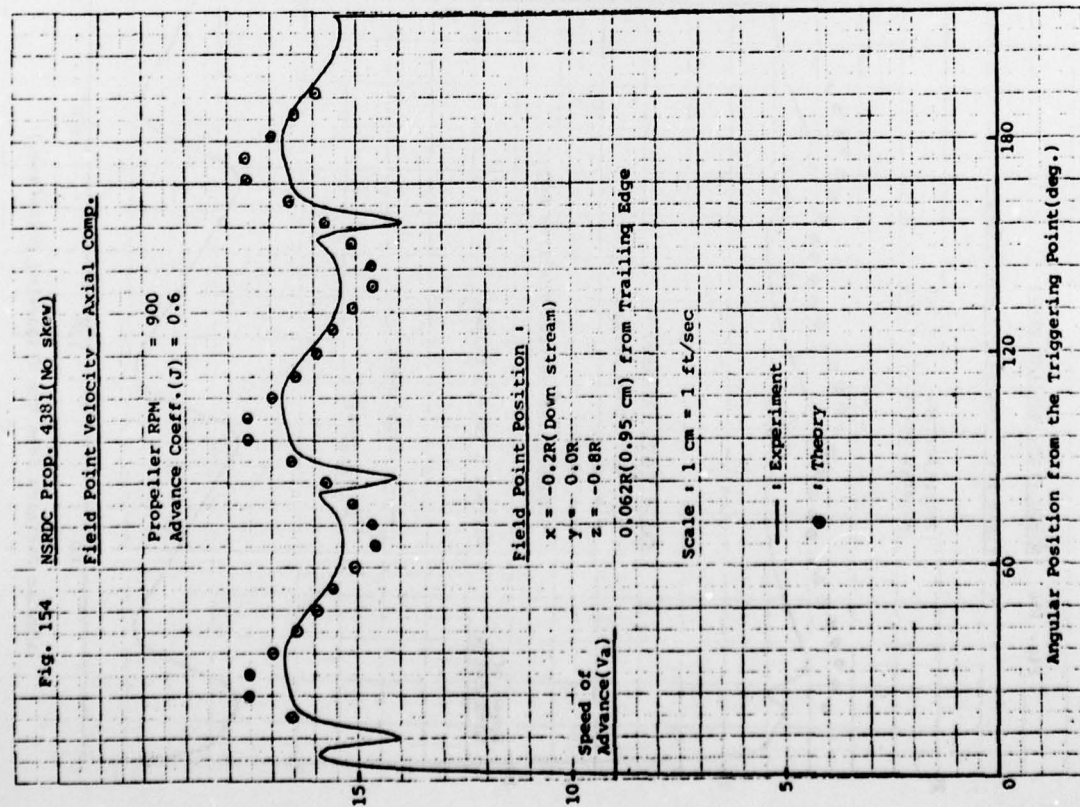
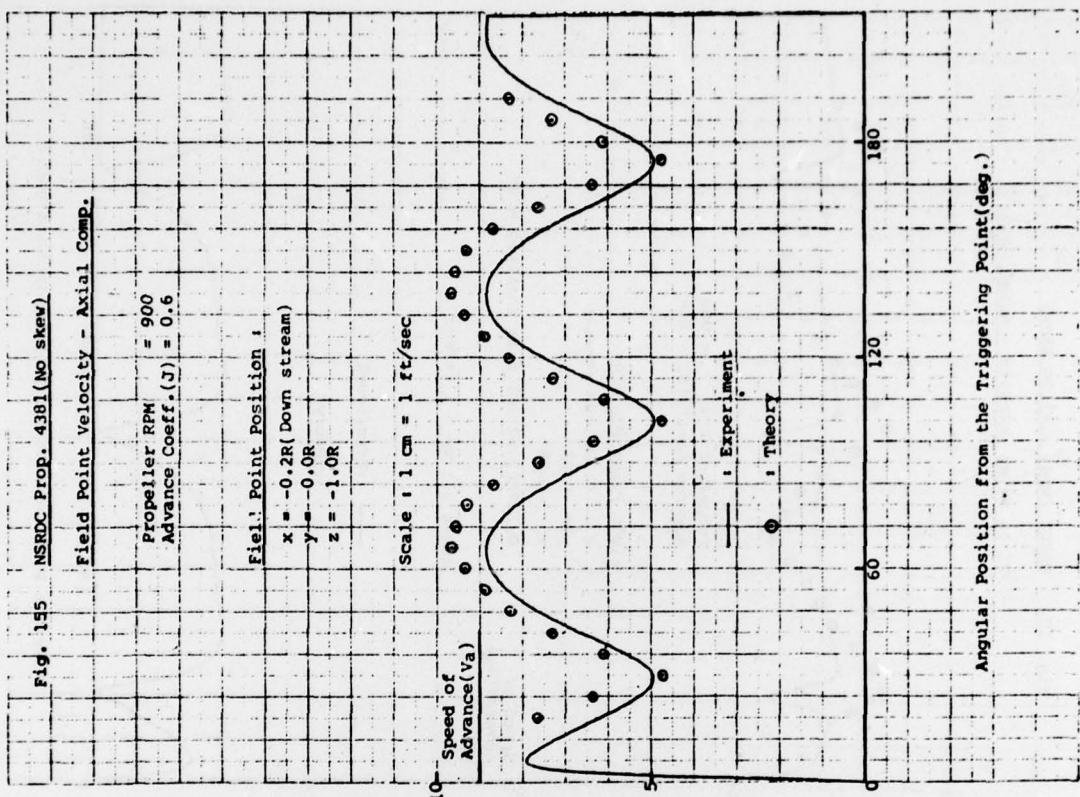


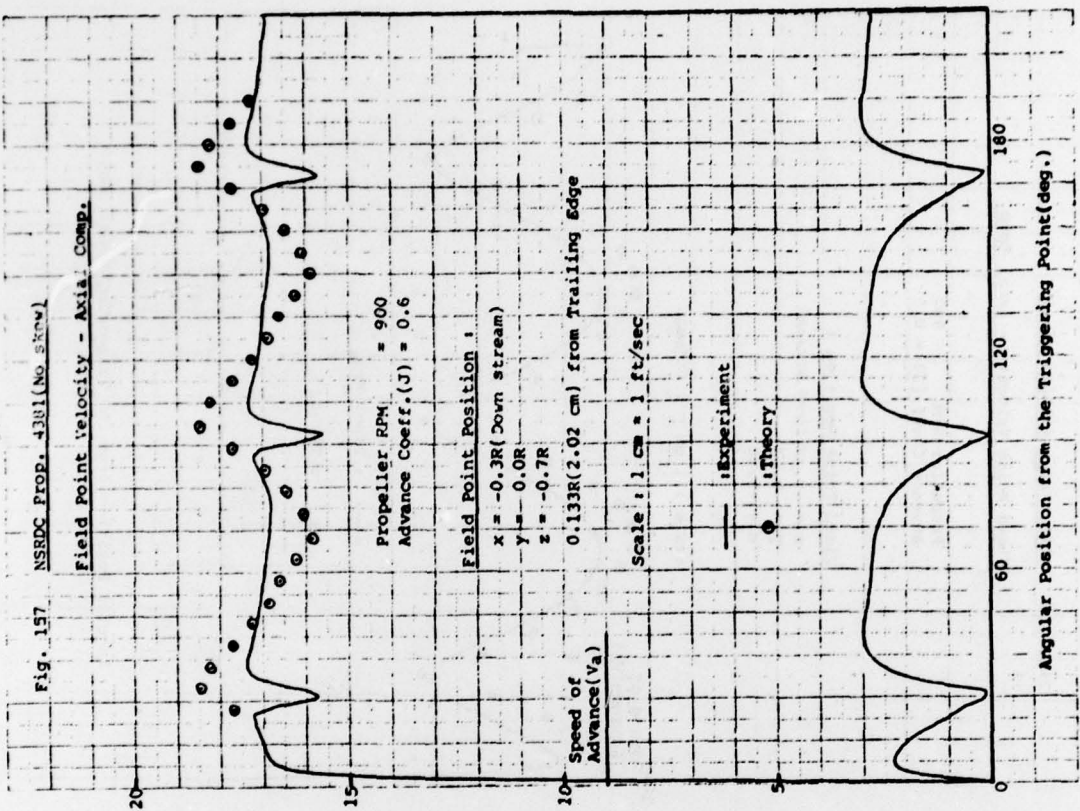
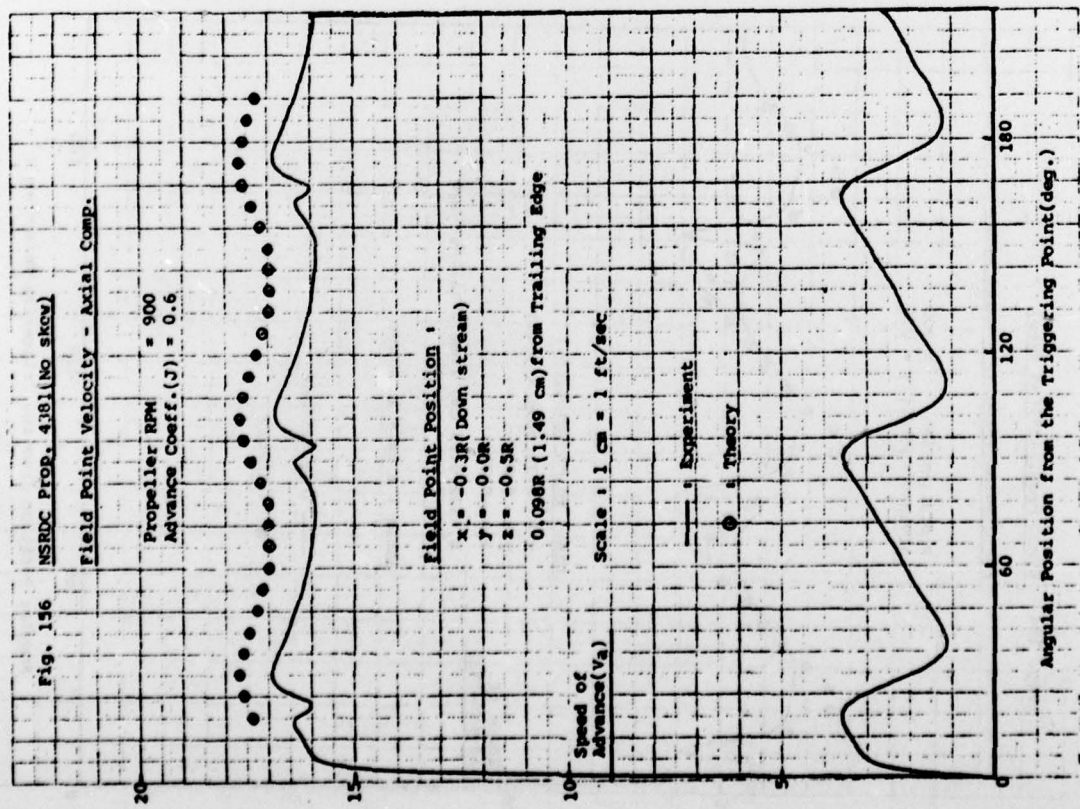












M.I.T. REPORT NO. 78-12

DISTRIBUTION LIST FOR REPORTS PREPARED UNDER THE
GENERAL HYDROMECHANICS RESEARCH PROGRAM

- 40 Commander
David W. Taylor Naval Ship
Research and Development Center
Bethesda, MD 20084
Attn: Code 1505
- 1 Officer-in-Charge
Annapolis Laboratory
David W. Taylor Naval Ship
Research and Development Center
Annapolis, Maryland 21402
Attn: Code 522.3 (Library)
- 7 Commander
Naval Sea Systems Command
Washington, D.C. 20362
Attn: SEA 09G32 (3 cys)
SEA 03512 (Peirce)
SEA 037
SEA 0322
SEA 033
- 12* Director
Defense Documentation Center
5010 Duke Street
Alexandria, Virginia 22314
- 1 Office of Naval Research
800 N. Quincy Street
Arlington, Virginia 22217
Attn: Mr. R. D. Cooper (Code 438)
- 1 Office of Naval Research
Branch Office
492 Summer Street
Boston, MA 02210
- 1 Office of Naval Research
Branch Office
536 S. Clark Street
Chicago, Illinois 60605
- 1 Chief Scientist
Office of Naval Research
Branch Office
1030 E. Green Street
Pasadena, CA 91106
- 1 Office of Naval Research
Resident Representative
715 Broadway (5th Floor)
New York, New York 10003
- 1 Office of Naval Research
San Francisco Area Office
760 Market St., Room 447
San Francisco, California 94102
- 1 Director
Naval Research Laboratory
Washington, D.C. 20390
Attn: Code 2027
- 1 Library of Congress
Science and Technology
Division
Washington, D.C. 20540
- 8 Commander
Naval Ship Engineering Center
Department of the Navy
Washington, D.C. 20362
Attn: SEC 6034B
SEC 6110
SEC 6114H
SEC 6120
SEC 6136
SEC 6144G
SEC 6140B
SEC 6148
- 1 Naval Ship Engineering Center
Norfolk Division
Small Craft Engr. Dept.
Norfolk, Virginia 23511
Attn: D. Blount (6660.03)

M.I.T. REPORT NO. 78-12
Distribution List
Page 2

- | | | | |
|---|---|---|--|
| 1 | Commander (ADL)
Naval Air Development Center
Warminster, Penna 18974 | 1 | Puget Sound Naval Shipyard
Engineering Library
Bremerton, Washington 98314 |
| 1 | Naval Underwater Weapons Research
& Engineering Station (Library)
Newport, R.I. 02840 | 1 | Long Beach Naval Shipyard
Technical Library (246L)
Long Beach, CA 90801 |
| 1 | Commanding Officer (L31)
Naval Civil Engineering Laboratory
Port Hueneme, CA 93043 | 1 | Pearl Harbor Naval Shipyard
Code 202.32
Box 400, FPO
San Francisco, CA 96610 |
| 1 | Commander
Naval Ocean Systems Center
San Diego, CA 92152
Attn: Dr. A. Fabuls (4007)
Dr. J. Hoyt (2501)
Library (13111) | 1 | Mare Island Naval Shipyard
Shipyard Technical Library
Code 202.3
Vallejo, CA 94592 |
| 1 | Library
Naval Underwater Systems Center
Newport, R.I. 02840 | 1 | Assistant Chief Design Engineer
for Naval Architecture (Code
250)
Mare Island Naval Shipyard
Vallejo, CA 94592 |
| 1 | Department of Transportation
Library TAD-491.1
400 - 7th Street, S.W.
Washington, D.C. 20590 | 1 | U.S. Naval Academy
Annapolis, Maryland 21402
Attn: Technical Library
Dr. Bruce Johnson |
| 1 | Charleston Naval Shipyard
Technical Library
Naval Base
Charleston, S.C. 29408 | 1 | Naval Postgraduate School
Monterey, CA 93940
Attn: Library, Code 2124 |
| 1 | Norfolk Naval Shipyard
Technical Library
Portsmouth, Virginia 23709 | 1 | Study Center
National Maritime Research
Center
U. S. Merchant Marine Academy
Kings Point, L.I., N.Y. 11024 |
| I | Philadelphia Naval Shipyard
Philadelphia, Penna 19112
Attn: Code 240 | 1 | U.S. Merchant Marine Academy
Kings Point, L.I., N.Y. 11024
Attn: Academy Library |
| 1 | Portsmouth Naval Shipyard
Technical Library
Portsmouth, N.H. 03801 | | |

M.I.T. REPORT NO. 78-12

Distribution List

Page 3

- 1 Library
The Pennsylvania State University
Applied Research Laboratory
P. O. Box 30
State College, Penna 16801
- 1 Bolt, Beranek & Newman
50 Moulton Street
Cambridge, MA 02138
Attn: Library
- 1 Bethlehem Steel Corporation
Center Technical Division
Sparrows Point Yard
Sparrows Point, Maryland 21219
- 1 Bethlehem Steel Corporation
25 Broadway
New York, New York 10004
Attn: Library (Shipbuilding)
- 1 Mr. V. Boatwright, Jr.
R & D Manager
Electric Boat Division
General Dynamics Corporation
Groton, Conn 06340
- 1 Gibbs & Cox, Inc.
21 West Street
New York, New York 10006
- 1 Hydronautics, Inc.
Pindell School Road
Howard County
Laurel, Maryland 20810
Attn: Library
- 2 McDonnell Douglas Aircraft Co.
3855 Lakewood Blvd.
Long Beach, CA 90801
Attn: J. Hess
T. Cebeci
- 1 Lockheed Missiles & Space Co.
P.O. Box 504
Sunnyvale, CA 94088
Attn: Mr. R. L. Waid, Dept 57-
74
Bldg. 150, Facility 1
- 1 Newport News Shipbuilding &
Dry Dock Company
4101 Washington Avenue
Newport News, Virginia 23607
Attn: Technical Library, Dept.
- 1 Nielsen Engineering & Research
Inc.
510 Clude Avenue
Mountain View, CA 94043
Attn: Mr. S. Spangler
- 1 Oceanics, Inc.
Technical Industrial Park
Plainview, L.I., N.Y. 11803
- 1 Society of Naval Architects
and Marine Engineers
ONE WORLD TRADE CENTER
New York, New York 10048
Attn: Technical Library
- 1 Sun Shipbuilding & Dry Dock Co.
Chester, Penna 19000
Attn: Chief Naval Architect
- 1 Sperry Systems Management Div.
Sperry Rand Corporation
Great Neck, N.Y. 11020
Attn: Technical Library
- 1 Stanford Research Institute
Menlo Park, CA 94025
Attn: Library G-021

M.I.T. REPORT NO. 78-12

Distribution List

Page 4

- 2 Southwest Research Institute
P. O. Drawer 28510
San Antonio, Texas 78284
Attn: Applied Mechanics Review
Dr. H. Abramson
- 1 Tracor, Inc.
6500 Tracor Lane
Austin, Texas 78721
- 1 Mr. Robert Taggart
9411 Lee Hwy, Suite P
Fairfax, VA 22031
- 1 Ocean Engr Department
Woods Hole Oceanographic Inst.
Woods Hole, MA 02543
- 1 Worcester Polytechnic Inst.
Alden Research Laboratories
Worcester, MA 01609
Attn: Technical Library
- 1 Applied Physics Laboratory
University of Washington
1013 N.E. 40th Street
Seattle, Washington 98105
Attn: Technical Library
- 1 University of Bridgeport
Bridgeport, Conn 06602
Attn: Dr. E. Uram
- 4 University of California
Naval Architecture Department
College of Engineering
Berkeley, CA 94720
Attn: Library
Prof. W. Webster
Prof. J. Paulling
Prof. J. Wehausen
- 3 California Institute of Technology
Pasadena, CA 91109
Attn: Aeronautics Library
Dr. T. Y. Wu
Dr. A. J. Acosta
- 1 Colorado State University
Foothills Campus
Fort Collins, Colorado 80521
Attn: Reading Room,
Engr. Research Center
- 1 University of Hawaii
Department of Ocean Engineering
2565 The Mall
Honolulu, Hawaii 96822
Attn: Library
- 1 Institute of Hydraulic Research
The University of Iowa
Iowa City, Iowa 52240
Attn: Library
- 1 Department of Ocean Engineering
Massachusetts Institute of
Technology
Cambridge, MA 02139
Attn: Prof. P. Mandel
Prof. M. Abkowitz
Prof. N. Newman
- 1 Engineering Technical Reports
Room 10-500
Massachusetts Institute of
Technology
Cambridge, MA 02139
- 2 St. Anthony Falls Hydraulic
Laboratory
University of Minnesota
Mississippi River at 3rd Ave, SE
Minneapolis, Minnesota 55414
Attn: Dr. Roger Arndt
Prof. E. Silberman
- 3 Department of Naval Architecture
and Marine Engineering-
North Campus
University of Michigan
Ann Arbor, Michigan 48109
Attn: Library
Dr. T. F. Ogilvie
Prof. F. Hammitt

M.I.T. REPORT NO. 78-12

Distribution List

Page 5

1 College of Engineering
University of Notre Dame
Notre Dame, Indiana 46556
Attn: Engineering Library

3 Davidson Laboratory
Stevens Institute of Technology
711 Hudson Street
Hoboken, New Jersey 07030
Attn: Library
Mr. J. Breslin
Mr. S. Tsakonas

2 Stanford University
Stanford, CA 94305
Attn: Engineering Library
Dr. R. Street

3 Webb Institute of Naval Architecture
Crescent Beach Road
Glen Cover, L.I., N.Y. 11542
Attn: Library
Prof. E. V. Lewis
Prof. L. W. Ward

1 Applied Research Laboratory
P. O. Box 30
State College, PA 16801
Attn: Dr. B. Parkin, Director
Garfield Thomas Water Tunnel

1 Dr. Michael E. McCormick
Naval Systems Engineering Department
U. S. Naval Academy
Annapolis, Maryland 21402

1 Dr. Douglas E. Humphreys (Code 794)
Naval Coastal Systems Laboratory
Panama City, Florida 32401

1 Florida Atlantic University
Ocean Engineering Department
Boca Raton, Florida 33432
Attn: Dr. S. Dunne